Design Of An Actinide Burning, Lead or Lead-Bismuth Cooled Reactor That Produces Low Cost Electricity

October 2002

Idaho National Engineering and Environmental Laboratory
Bechtel BWXT Idaho, LLC

Design of an Actinide Burning, Lead or Lead-Bismuth Cooled Reactor That Produces Low Cost Electricity

FY-02 Annual Report
October, 2002

Report compiled and edited by
P. E. MacDonald and J. Buongiorno

MIT Principal Investigators

Prof. Ron Ballinger -Material Studies
Prof. Ken Czerwinski –Polonium Technology
Richard Herron – Reactor Design
Chris Larson - Polonium Technology
Vaclav Dostal –Reactor Design
Dr. Pavel Hejzlar -Neutronics
Jeongyoun Lim-Materials
Prof. Mujid Kazimi -Reactor Design
Prof. Neil Todreas - **Project Leadership**

INEEL Principal Investigators

Dr. Jacopo Buongiorno, Reactor Design
Cliff Davis -Reactor Design
Dr. Steve Herring -Neutronics
Philip MacDonald - **Project Leadership**
Dr. Eric Loewen -Materials Studies
Dr. Kevan Weaver -Neutronics

Table of Contents

Executive Summary

The purpose of this collaborative Idaho National Engineering and Environmental Laboratory (INEEL) and Massachusetts Institute of Technology (MIT) Laboratory Directed Research and Development (LDRD) project is to investigate the suitability of lead or lead-bismuth cooled fast reactors for producing low-cost electricity as well as for actinide burning. The goal is to identify and analyze the key technical issues in core neutronics, materials, thermal-hydraulics, fuels, and economics associated with the development of this reactor concept. Work has been accomplished in four major areas of research: core neutronic design, plant engineering, material compatibility studies, and coolant activation. The publications derived from work on this project (since project inception) are listed in Appendix A. This is the third in a series of Annual Reports for this project, the others are also listed in Appendix A as FY-00 and FY-01 Annual Reports.

NEUTRONIC DESIGN

The major focus of the neutronic analyses performed at MIT in FY-02 was on the design of a core that can achieve excellent safety through self-controllability (as in the Integral Fast Reactor, IFR) and high transuranic destruction. The analyses were performed for metallic thorium-based fuel (Th-U-Pu-MA-Zr) in a once-through cycle assuming that the discharged fuel from the Actinide Burner Reactor (ABR) remains in temporary storage before multi-recycling is introduced. The major conclusions of these studies can be summarized as follows:

- Using thorium as the prime fertile material is an effective means to reduce the large reactivity swing occurring in fertile-free cores while still allowing a high net actinide destruction rate per MWth. In addition, thorium use increases the Doppler feedback in comparison with fertile-free fuels and reduces the coolant density reactivity coefficient. Both the Doppler and fuel thermal expansion feedbacks are negative and their values are comparable to those for the IFR fuel.
- The ABR destruction rate of actinides per MWth-yr is ~35% less than the destruction rate in the fertile-free critical ABR but only 20% less than in an accelerator-driven facility (due to the higher capacity factor in the ABR). This is a very appealing feature considering the simplicity of the proposed reactor versus the more complex accelerator-driven system.
- The discharged fuel from the ABR satisfies proliferation constraints for both the plutonium and uranium compositions. Plutonium isotopics are significantly degraded from that of the PWR spent fuel vector making it virtually weapons unusable. Also, the fraction of in-bred U-233 remains below 12% if depleted uranium is mixed with the thorium (~30wt% of uranium in the U+Th mixture).
- The high coolant void worth typical of liquid metal cooled fast reactors (especially those with minor actinide fuel) can be effectively mitigated by the employment of streaming fuel assemblies yielding a negative coolant void worth and a very small positive coolant temperature coefficient.
- The combination of reactivity coefficients satisfies the requirements of self-control throughout the cycle so that, in concert with the passive decay heat removal design, all transients without scram lead to an inherent shutdown without exceeding safe fuel and structural temperature limits.
- The fuel cycle cost of the once-through cycle is significantly higher than that of the multi-recycle scheme (about 30 versus 15 mills/kW-hr, best estimate). Therefore, considering fuel cycle economics and the small potential for reduction of long-term

radiotoxicity and heat load on the repository from the wastes of the LWR/ABR system, the once-through fuel cycle has to be discarded from future considerations.

- In comparison with an accelerator-driven facility, the fuel cycle cost of the ABR in the multi-recycle scheme is slightly smaller, but both the accelerator-driven facility and ABR fuel cycle costs are well above current LWR fuel cycle costs, even if lower bound values are used [the lower bound value for both the accelerator-driven facility and the ABR is about 9 mills/kW-hr versus about 3 mills/kW-hr for light water reactors (LWRs)].

In summary, the proposed design of the 7-year life core for burning transuranics from spent LWR fuel appears to be very promising and deserving of future refined analyses and optimization because it offers high consumption of actinides, excellent safety characteristics, and has the potential to have low electricity generation cost due to its modularity, simplicity, and high capacity factor. The only drawback is a high fuel cycle cost, which is inherent to all actinide burning systems because of the currently high fuel reprocessing costs.

PLANT ENGINEERING

The plant engineering work reported in this Annual Report includes: an evaluation of gas-lift pumping for the ABR, analyses of various reactor transients, improvement of the metal-fuel performance modeling, pump selection, heat exchanger design and accident analyses, an assessment of the supercritical steam cycle, an assessment of under-lead-bismuth eutectic (LBE) viewing technology, and a capital cost analysis.

Evaluation of gas-lift pumping. The feasibility of a gas-lift pump approach for the ABR was assessed. Gas-lift pumping of the LBE coolant in our case will require generation of a 53% void fraction in the chimney resulting in 2.3 m swelling of the liquid level. Such a large swelling of the liquid level would require design of a much longer vessel. The gas flow rate required to sustain a 53% void fraction in the chimney is 1.6 kg/s. The gas would be injected at the bottom of the chimney at a pressure of about 800 kPa (corresponding to the weight of the LBE column in the chimney). The pumping power would be about 5.1 MW versus 3.8 MW for a mechanical pump. Finally, the 1.6 kg/s helium mass flow rate corresponds to a 28 m^3/s volumetric flow and to a 3.8 m/s helium superficial velocity at the free liquid surface, enough to entrain considerable amounts of LBE, which would then have to be removed before the compressor inlet. These results clearly demonstrate that a gas-lift pump approach is not feasible for the ABR.

Analyses of Reactor Transients. The ATHENA code was used to determine the response of the ABR to a variety of transients, including pump trip, station blackout, reactivity insertion, heat exchanger tube rupture, turbine stop valve closure, steam line break, loss of feed-water preheating, and loss of coolant from the reactor cleanup system. The transients were simulated without reactor scram to demonstrate the safety margins inherent in the reactor design. The ABR design successfully met the identified cladding, fuel, and guard vessel temperature limits for each of the transients analyzed. The cladding temperature was always closer to its limit than the fuel and guard vessel temperatures. The most limiting transient is initiated by a station blackout. The station blackout coupled with a failure to scram produced a peak cladding temperature that was equal to the transient limit. The margin to the temperature limit during a station blackout increased to a more comfortable 24°C when a reactor scram was simulated. A steam line break does not result in significant overcooling in the actinide-burner reactor. The overcooling potential is limited by the small water inventory in the heat exchangers compared to the heat capacity of the lead-bismuth coolant. The transient initiated by a heat exchanger tube rupture resulted in the highest cover gas pressure of the cases evaluated. Because of the high pressure on the secondary side of the heat exchangers, a relief valve will be required to protect the reactor

vessel. The maximum pressure is governed by the relief valve capacity and set-point. It was set to open at 0.2 MPa in this analysis. Also, a loss-of-coolant accident (LOCA) sequence involving the coolant cleanup system was analyzed and the ABR was again found to be passively safe.

Metal-fuel Modeling. During FY-02 two major improvements were made to the metal-fuel model developed in this project during FY-01 and the revised model was benchmarked with metal-fuel irradiation data from the IFR development program. First, better constitutive equations for the irradiation creep and thermal creep of the cladding material HT-9 were added to the code. The second improvement consisted in allowing for non-constant temperature, dose, and linear heat generation rate during irradiation. The new version of the model can simulate the behavior of a metal fuel pin with arbitrarily changing operating conditions.

Pump Selection. The work in Section 3.4 illustrated that a centrifugal pump is capable of meeting the ABR pumping needs. Also, that these needs can be met by two pumps which will neatly fit within the 1.05 meter annular gap between the reactor vessel and the core chimney.

Heat Exchanger Design and Accident Analyses. The reevaluation of the heat exchangers reaffirmed that the 700 MWth of core power can be transmitted to the power cycle. The new design is a baffled, cylindrical shell and tube heat exchanger with a modular design. Eight cylindrical heat exchangers have replaced the two original kidney-shaped components identified in the FY-01 design. Each heat exchanger is 9.0 meters in length with an inside shell diameter of 1.0 meters. As before, the LBE coolant circulates on the shell side and the secondary coolant in the tubes, which have a triangular pitch. Three secondary-side heat exchanger variants are presented: superheated steam, supercritical steam, and supercritical CO_2. The worst-case heat exchanger accident with either a steam or CO_2 cycle was assessed. The hazardous result investigated was formation of lead oxide (PbO) in the primary coolant system, which could block or disrupt flow paths. We determined that reactions which could lead to lead oxide formation were too slow to result in significant oxide formation in the event of a tube rupture.

Supercritical Steam Cycle. An initial investigation of a supercritical steam cycle was performed to determine if it is desirable alternative to either the superheated steam or supercritical CO_2 power cycles. The net efficiencies obtainable with the supercritical steam cycle are competitive with those of the supercritical CO_2 power cycle. However, the balance of plant design with the CO_2 power cycle is much simpler.

Under-LBE Viewing. Toshiba has performed significant work in the development of a 3-D ultrasonic under-sodium viewer. No such work has been done with a lead-based coolant, but an under-lead ultrasonic viewer could be expected to have higher resolution, but somewhat lower range.

Supercritical-CO_2 Brayton Cycle. Work was performed during FY-02 to optimize the recuperator and develop preliminary designs for the main components used in the supercritical-CO_2 Brayton cycle. The need for effective recuperators led to consideration of compact heat exchangers. In order to accommodate the high pressure differential across the recuperator, the printed circuit heat exchangers manufactured by HEATRIC were selected. The most important factors for the performance evaluation were the heat exchanger geometry and flow arrangement. The diameter of the semicircular channels was selected as 1 mm. The heat conduction characteristic length was assumed to be equal to the plate thickness, even though it is likely to be smaller.

The precooler design is significantly simpler than the recuperator design. However, the same type of heat exchanger as for the recuperators is used. The precooler is designed to minimize the pumping power of the cooling water and the pressure drop on the gas side and still have an acceptable size.

The preliminary design of the turbo-machinery was also completed. The very encouraging finding is that the turbo-machinery size is miniscule compare to any other currently used fluid. It is about 30 times smaller than conventional steam turbines and about 5 times smaller than helium turbo-machinery. The preliminary efficiency calculation results are close to 92% efficiency (accounting for kinetic energy losses). The size of a 300 MW$_e$ turbine is about 1 m long and 0.8 m in diameter with approximately 5 stages. A similar evaluation was performed for the compressors giving on the order of 2 and 3 stages for the main and recompressing compressors respectively. Overall, the cycle components are compact and their design should not impose significant requirements on research and development.

Economic Analysis. A capital cost analysis for the ABR was performed. The basis for this analysis was the 1994 Advanced Liquid Metal Reactor (ALMR) capital cost analysis. The table to the right presents a realistic comparison of the capital costs of the ABR and the ALMR. (The plant type labeled F is a first-of-a-kind plant and the type labeled N is a nth-of-a-kind plant. The number (1 or 3) distinguishes between power plants with one or three power blocks.) The ALMR report was adjusted and scaled to account for differences between the two plants. Major differences include the absence of an intermediate heat transport loop in the ABR, difference in materials due to corrosion concerns, and the differences between the reactor vessels and heat exchangers. The findings were that there is some uncertainty in the ABR capital cost analysis due to the incomplete information available on the ALMR capital cost analysis. This uncertainty was quantified and a range of values for the capital cost of the ABR provided. In all but the worst cases the ABR is competitive with the ALMR plant, and in many cases has a capital cost advantage on a dollars per kilowatt-electric basis.

Comparison of ALMR and ABR capital cost (constant $F = 0.25$).

Plant Type	ALMR Total Cost (2002 $/kWe)	ABR Total Cost (2002 $/kWe)
F1	2,761	2,542
F3	2,120	1,991
N1	2,196	1,938
N3	1,801	1,661

MATERIAL STUDIES

LBE corrosion tests of several commercially available U.S. steels were performed at the INEEL during FY-02 in which measurements were taken of the interaction layer with respect to time, temperature, and alloy type to quantify the damage rates. Corrosion coupons of HT9, 410, 316L, F22, and iron with three different level of silica (1, 2 and 3wt.%) were tested at 550 to 700°C at time steps of 100, 300, 600, 700, and 1,000 hours inside corrosion cells made from hafnium stabilized zirconium alloy and 410 stainless steels. Various zirconium alloys were also tested for 100 to 1000 hours at 550 to 700°C. At low temperatures (<550°C) zirconium has good corrosion resistance to LBE due to the presence of an adherent oxide layer. At higher temperatures (650°C and above), the zirconium alloys are easily dissolved by the LBE. The oxygen potential was controlled within a range of about 10^{-27} to 10^{-40} atm, using solid carbon to remove excess oxygen as carbon dioxide and reduce any PbO formed. Scanning electron microscope (SEM), energy dispersive X-ray (EDX), and inductively coupled plasma (ICP) analyses were all performed on the samples to determine the depth of the interaction (corrosion) layer, and the composition of the

LBE and interaction layer. (Detailed results for Experiments 10 and 11 conducted at 550 and 650°C, respectively, in the Zirconium alloy cells are presented in this Annual Report.)

The pre-oxidized hafnium stabilized zirconium corrosion cells resulted in a liquid phase chemistry that affected the sample corrosion/disolution in the loop, especially during Experiment 11 (650°C). The zirconium in solution in the LBE slows down the corrosion of some of the alloys by forming a layer of zirconium compounds on the surfaces, and by consuming excess O_2. We observed that the interaction layer formation rates of the HT9 and 316-stainless steel at 550 and 650°C are best represented by a logarithmic fit to the data. The 316L stainless steel interaction layer formation rates at 550°C were relatively low, however, the 316L stainless steel had relatively large interaction layers at 650 C. This degradation of the 316L stainless steel seems to be connected to the mass transfer of the Ni, as indicated by the ICP results. The interaction layer formation rates of the F22 low alloy steel and the 410-stainless steel at both temperatures was approximately linear. The F22 low alloy steel exhibited the highest interaction layer formation rate at 550°C but the lowest rate at 650°C. This result is probably due to the presence of the zirconium/hafnium layers on the samples in the 650°C test.

During this past year the effort at MIT has been focused on the testing of selected refractory metals and initial testing of model Fe-Si alloys as part of an effort to develop a science-based alloy development program, the goal of which is to develop an advanced iron based alloy specifically optimized for Pb and Pb-Bi service. Two rotating electrode facilities have been built at MIT to conduct dynamic corrosion tests in Pb or Pb-Bi alloy coolants under isothermal conditions. The oxygen potential is controlled using the equilibrium reaction between H_2, H_2O and O_2 and a mixing and monitoring system. The systems are capable of operating at temperatures up to 1000°C.

The refractory metals tested at MIT exhibit very little degradation when exposed to liquid Pb or Pb-Bi. This is due to their very limited solubility as well as, in the case of tantalum, the formation of a very stable oxide film. The attack of pure iron by lead is quite severe and thus confirms the need for protective measure for the iron when operating at low oxygen potentials. The depth of the interaction layer on the Fe-1.24%Si alloy exposed to Pb for 100 hrs at 600°C under reducing conditions was about 20~28 μm. The Fe-2.25% Si alloy was exposed for 100 hours in molten lead at 600°C and the reaction with the Pb was very minor with no intergranular penetration observed. There was also some enrichment of the silicon on the surface. The surface layer for the Fe-3.82% Si material shows a more compact interaction layer when compared with those with lower silicon content. There is a very clear enrichment of silicon in the surface region.

An SEM micrograph of a Fe-1.24% sample tested in Pb-Bi eutectic (44.5% Pb, 55.5% Bi) for 100 hours indicated that bulk materials (mainly iron oxide formed during the heat-up period) were removed from the sample surface and incorporated into the deposited Pb-Bi layer leaving a compact but severely damaged interface between the Pb-Bi and bulk metal. The interaction layer of a Fe-2.55% Si alloy sample after exposure to Pb-Bi eutectic at 600°C for 100 hours consisted of a detached iron oxide layer with Pb-Bi at the interface with the metal. It is believed that the iron oxide formed during the heat process. Based on a comparison with the Pb case, it appears that Pb-Bi is more aggressive than Pb alone. The results of the Fe-Si series of tests show very promising behavior, especially in molten lead. It appears that, as expected, a silicon rich layer is formed on the surface during exposure due to the selective dissolution of the iron. Since the solubility of silicon is much lower than iron in Pb and Pb-Bi, we expect that the enriched layer will continue to grow during exposure and will limit further dissolution. If the oxygen potential

is high enough there will come a point where SiO_2 is stable and a protective oxide layer will form.

COOLANT ACTIVATION

In the coolant activation area the studies on polonium-hydride kinetics were completed. The kinetic constants for the polonium-hydride formation reaction were calculated and found to be roughly independent of temperature and increase with hydrogen concentration. Sorption of polonium on rare earth (i.e., praseodymium) foils was also explored as a means to remove polonium from the LBE coolant. The formation of a praseodymium oxide film on the surface of the foil greatly impairs sorption, and should be avoided. Conceptual design of a rare-earth filter that removes polonium with an efficiency of 92% is provided. Also polonium removal by alkaline extraction was investigated using tellurium as chemical surrogate. Preliminary experiments show that alkaline extraction can be rather effective in cleaning up LBE, as the tellurium concentration in the LBE was reduced by three to four orders of magnitude upon contact with molten sodium hydroxide at around 500°C. Furthermore, five candidate materials for the reaction crucible (which has to withstand high-temperature molten LBE and NaOH for up to 24 hours) were evaluated, i.e., graphite, alumina, nickel, nickel-chromium and zirconium. SEM and ICP analyses indicate that zirconium has the best compatibility for this application.

1. Project Overview

1.1. Background

While considerable design work has been done in the United States, Europe, and Japan on fast reactors, including actinide-burners, it has mostly been done for sodium cooled reactors. A lead-bismuth cooled fast reactor was considered in the United States in the 1950s. However, it was abandoned in favor of sodium cooling for two reasons:

(1) Lead-bismuth coolant at the temperatures of interest can be very corrosive to structural materials; and
(2) The doubling time of sodium cooled fast reactors can be significantly shorter than that of lead-bismuth cooled reactors as a result of the higher power density achievable in sodium cooled cores.

Whereas a short doubling time was considered an important performance characteristic in the 1950's, it is of little significance today, as we do not foresee a depletion of low cost uranium resources in the near future, and we have a significant inventory of actinides that can be burned in fast reactors. Regarding the material compatibility issue, the Russians addressed this issue and were able to deploy lead-bismuth cooled reactors for use in their most advanced nuclear submarines, the so-called "Alpha" class submarines, which are the fastest in the world. The Russians have built and operated seven lead-bismuth reactors in submarines and two on-shore prototypes. More recently, they have studied the design of a variety of lead and lead-bismuth reactors for electric power generation, some of which can operate with one core loading for many years and do not require any fuel reprocessing (however, much of the Russian heavy metal technology is not available in the West).

Elsewhere, very long-lived core, lead-bismuth cooled, fast reactors have continued to be investigated in Japan, Korea, and in the United States at the University of California at Berkeley. A lead-bismuth cooled, accelerator-driven, sub-critical actinide-burner is a possible candidate in DOE's Advanced Accelerator for Applications (AAA) project for burning the actinides and long-life fission products from spent light water reactor fuel. It is envisioned that the reactors investigated in this study could operate in concert with accelerator-driven facilities in a program to both burn the waste from the current generation of light water reactors and produce low-cost electricity. It should also be noted that there exists a synergy between the development of the accelerator-driven facilities and a lead or lead-bismuth cooled critical reactor system: they share similar coolant and fuel technologies with the result that either system can greatly benefit from improvements achieved for the other.

Recently the Generation IV Roadmap process selected the lead-cooled fast reactors as one of six candidates (with potentially improved sustainability, economics, safety and reliability, and proliferation resistance) that should be developed for future energy generation. The lead-cooled reactor systems of interest to the Generation IV Roadmap include small, long refueling interval, battery type plants of 50-150 MWe; modular systems of 300-400 MWe similar to those being developed in this project, and large monolithic plants of 1200 and greater MWe. The Generation IV Roadmap was also interested in lead-cooled plants with coolant temperatures sufficiently high to enter markets for hydrogen and process heat production.

Rationale for use of lead-alloy coolant. Liquid-metal cooled fast reactors have the following advantageous characteristics:

- Their heat transfer capability enables compact, high power-density cores. This attribute is essential to developing a relatively small (and economic) core.
- Their excellent capability for natural circulation, especially for lead-alloy cooled fast reactors with an open (loose pitch) core, provides important safety advantages and offers significant potential for heat transport system simplification.
- They have unique passive safety and autonomous operability characteristics attributable to the fast neutron energy spectrum, which enables:
    (a) A relatively high conversion ratio and weak fission product poisoning, thereby minimizing burnup reactivity loss and the associated need for active control and the potential for reactivity insertion accidents, and
    (b) Favorable neutronic (when properly designed) and thermo-structural feedback characteristics allowing passive adjustment of the fission power generation to the system heat rejection.

Among the different liquid metals, the choice of lead or lead-bismuth for the reactor coolant in a fast reactor offers enhanced safety and reliability. The advantages of lead-alloy over sodium as a coolant are related to the following basic material characteristics: chemical inertness with air and water; higher atomic number; low vapor pressure at operating temperatures; and high boiling temperature. The basic properties of lead, lead-bismuth, and sodium are compared in Table 1.1[1].

Table 1.1. Basic characteristics of liquid metal coolants.

Coolant	Mass #	Neutron Absorption Cross Section (mb)	Melting Point (°C)	Boiling Point (°C)	Chemical Reactivity (with air and water)
Pb-Bi	~208	3.82	125	1670	Inert
Pb	207	2.75	327	1737	Inert
Na	23	2.35	98	883	Highly reactive

These basic properties lead to the following potential advantages for lead-bismuth coolant:

- Harder neutron spectrum and better reflection properties (with little moderation), which results in an improved neutron economy, especially when burning actinides from spent LWR fuel, and makes it possible to get a good conversion ratio even without blankets (neutron economy is vital to achieving long core lifetimes while minimizing burnup reactivity loss and excessive control requirements).

- High boiling temperature (1670°C) and high heat of vaporization of lead and lead-bismuth coolants (versus 883°C for sodium), which eliminates boiling and related loss of cooling as a realistic accident scenario.

- Significantly lower reactivity (in fact, negative reactivity with certain designs) associated with hypothetical voiding of the coolant. The positive reactivity effect of coolant voiding is a concern with sodium-cooled fast spectrum systems.

- No energetic reactions with air and water (eliminating fires and the necessity of employing an intermediate heat transport loop, thereby reducing plant capital costs).

---

[1] Thermophysical properties of pure lead, Pb-Bi eutectic and sodium from [Lyon 1952, Kutateladze 1958], cross sections from [BNL 2000].

- Possibility of using relatively high outlet temperatures and high efficiency heat transfer cycles. With proper control of the coolant chemistry and choice of cladding and structural materials, it is likely that relatively high coolant temperatures can be obtained; in addition, there is potential for coupling of the reactor to other energy conversion and distribution systems of the future.

- High solubility of the actinides in the coolant, which prevents re-criticality events upon core melting.

Because lead or lead-bismuth have not been used as reactor coolants outside of Russia and much of the Russian technology is unavailable in the West, important technology issues (e.g., structural material corrosion, coolant chemistry control, filtration of impurities, coolant activation) must be addressed. There are also other disadvantages to the use of lead or lead-bismuth for cooling an actinide fast reactor in addition to the material compatibility problems. These include: high material cost; higher melting temperature (125°C for lead-bismuth versus 98°C for sodium); the production of Po-210 and lead toxicity. But probably most important, the relative cost of the various design alternatives that have been proposed earlier must be substantially improved.

1.2. Project Objectives and Organization

The purpose of this Idaho National Engineering and Environmental Laboratory (INEEL) and Massachusetts Institute of Technology (MIT) Laboratory Directed Research and Development (LDRD) project is to investigate the suitability of lead-bismuth cooled fast reactors for producing low-cost electricity as well as for actinide burning. The goal is to identify and analyze the key technical issues in core neutronics, materials, thermal-hydraulics, fuels, and economics associated with the development of this reactor concept. The goal is also to identify the most promising approach for designing such a reactor.

The INEEL and MIT are carrying out this investigation in a cooperative, coordinated manner in four discipline-based areas (core neutronic design, material compatibility studies, coolant activation, and plant engineering). The distribution between INEEL and MIT lead responsibilities in these disciplinary areas is as follows:

(1) Neutronics — MIT has examined core designs to achieve the two limiting objectives— maximum actinide consumption and minimization of electricity cost while the INEEL and MIT together have examined a core designed to optimize both objectives simultaneously.
(2) Plant Engineering — The INEEL has assessed the transient plant performance while MIT has assessed steady state plant performance. In both cases, the focus has been on determining the maximum allowable plant power and the associated plant capital cost for the following plant system options: primary coolant under natural versus forced-circulation; and a steam, helium or supercritical carbon dioxide secondary coolant system. The INEEL has also analyzed the fuel performance and the reactor vessel and guard vessel structural behavior.
(3) Structural Materials — INEEL is performing circulation corrosion studies while MIT is performing static autoclave studies with spinning test sections. Further, INEEL's studies focus on commercially available materials while MIT focuses on more advanced materials.
(4) Coolant Activation — MIT has been obtaining fundamental chemical data characterizing polonium removal from a lead-bismuth primary coolant due to the formation of H_2Po and rare earths. The INEEL has focused on the development of an alkaline extraction technology for removal of polonium from a lead-bismuth primary coolant.

The project has been active in disseminating its results through preparation of topical reports and technical papers in journals and technical conferences. These publications are listed in Appendix A. This is the third Annual Report.

1.3. Current Research Direction

This research project investigates the suitability of lead-bismuth cooled fast reactors for producing low-cost electricity as well as for actinide burning. While these two goals are the primary thrust in the development of a conceptual design, proliferation resistance and safety are also important aspects to be incorporated in the design process. Thus, this concept will address all objectives of the Generation IV program: favorable economics, proliferation resistance, enhanced safety and waste minimization.

A brief description and schematic figures of the current most promising design is presented below to familiarize the reader with the concept that is being developed. The concept strives for balance between the actinide destruction rate, economic electric power generation, and excellent safety characteristics. Our FY-01 Annual Report (MacDonald and Buongiorno 2001) discusses the dilemmas, constraints, and design strategy that lead to this design.

A schematic of the reactor primary coolant system and the reactor vessel auxiliary cooling system (RVACS) (the decay-heat removal system) is illustrated in Figure 1.1. The whole primary circuit operates at atmospheric pressure and is contained within a single vessel. This results in an integrated, more compact system and essentially eliminates the possibility of any type of loss-of-coolant accident (LOCA) because the primary coolant does not flow in external pipes. The annulus between the core barrel and the reactor vessel is used to accommodate the heat exchangers and the circulation pumps.
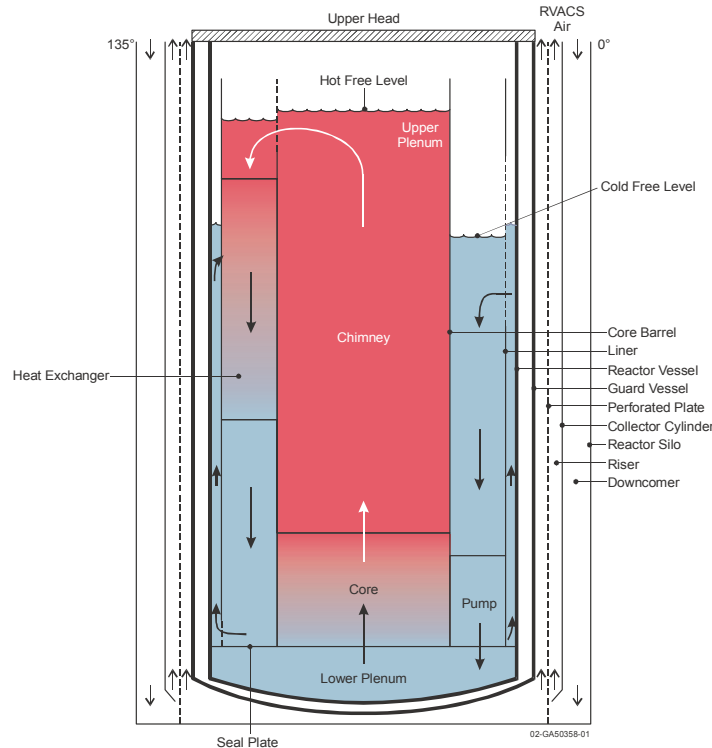
Figure 1.1. Layout of the reactor with the circulation scheme for the primary coolant and for the reactor vessel auxiliary cooling system (RVACS).

Circulation of the primary coolant within the pool is based on a dual-free-level approach. The primary coolant flows from the core outlet to the hot free level. From there it flows through the intermediate heat exchanger and surfaces again at the cold free level, from which it is pumped down to the core inlet. This circulation scheme prevents dragging of gas bubbles into the core in the case of a heat-exchanger-tube-rupture event, which could otherwise cause undesirable reactivity perturbations.

A guard vessel surrounds the main reactor vessel and is welded to the reactor compartment. Both the guard vessel and the reactor compartment are sealed thus effectively forming the reactor containment. In a hypothetical loss-of-primary-heat-sink event, the residual heat is removed by the RVACS passive decay heat removal system, i.e., the decay heat is discharged through the vessel and the guard vessel to air in natural circulation on the outer surface of the guard vessel. The gap between the vessel and the guard vessel is filled with liquid lead-bismuth to enhance heat transfer. Also a perforated cylinder is placed around the guard vessel to increase the heat transfer surface to the air. The RVACS is a completely passive system and for the reference dimensions of the vessel, it can safely remove the decay heat from a 700-MWth core without violating the temperature limits of the fuel, cladding and vessel.

The core employs 157 streaming fuel assemblies as illustrated in Figure 1.2, fueled with a metal alloy of thorium, uranium, zirconium, plutonium, and minor actinides. These fuels enable achievement of satisfactory actinide burning rates, and exhibit adequate reactivity coefficients. As shown in both Figures 1.1 and 1.2, the space between the core barrel and the vessel is used to place 8 modular heat exchangers and reactor coolant pumps. The heat exchangers are designed with the lead bismuth flow on the shell side and high-pressure CO_2 or steam inside the tubes.
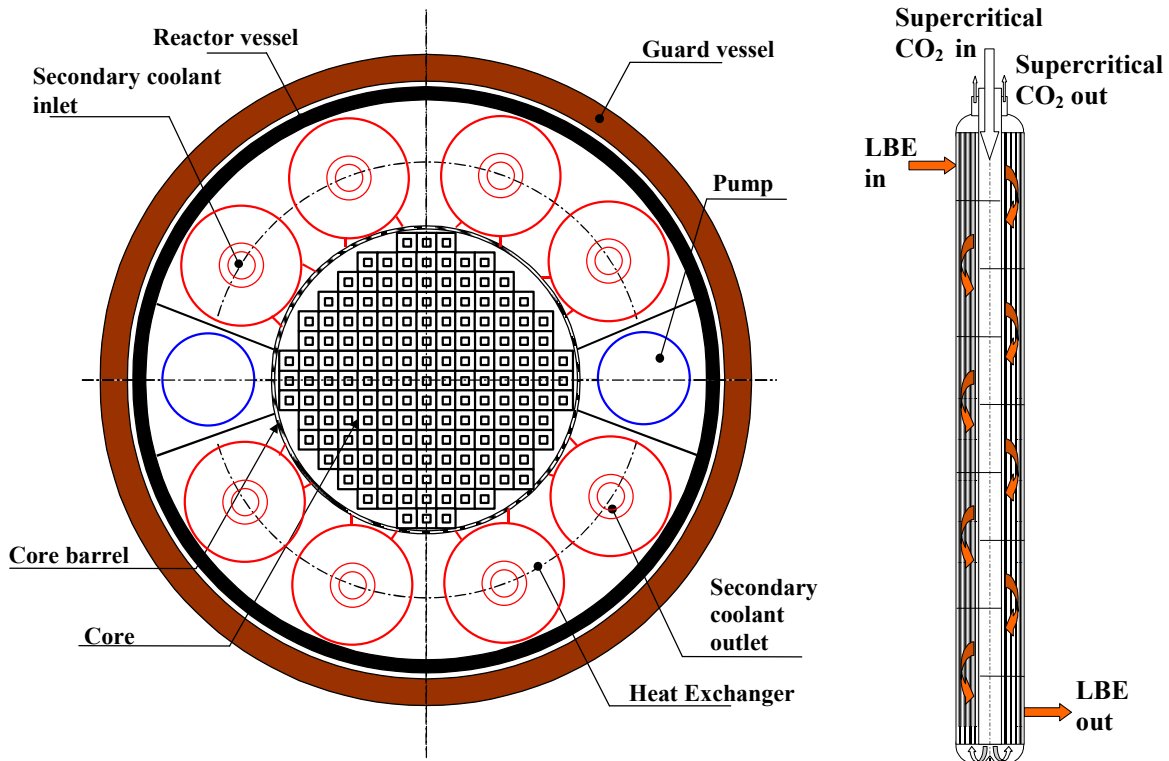
Figure 1.2. Top view of the vessel with core and heat exchanger layout and cross-section view of one heat exchanger showing the coolant flow paths.

Figure 1.3 shows the Brayton power cycle with supercritical CO_2 working fluid. The pressures, temperatures, enthalpies, entropies, and densities in Figure 1.3 are listed by numbered location in Table 1.2 and Table 1.3 lists the important reactor system design parameters. This cycle achieves high cycle efficiency (44.6%) at relatively low temperatures compatible with the cladding temperature constraints and is significantly simpler than the Rankine cycle. The proposed cycle employs a split recuperator design with flow recompression to avoid a negative pinch point. Only about half of the total flow enters the main compressor to proceed to the low temperature recuperator. The main stream is merged with the recompressed stream prior to entering the high temperature recuperator. The total mass flow is then heated in the high temperature recuperator and subsequently in the intermediate heat exchangers. Following the expansion in the high and low-pressure turbines, the working fluid enters the high temperature recuperator and, subsequently, the low temperature recuperator. After leaving the low temperature recuperator the flow is split. About half of the flow is recompressed in the recompression compressor. The remaining flow is cooled in the pre-cooler prior to entering the main compressor.
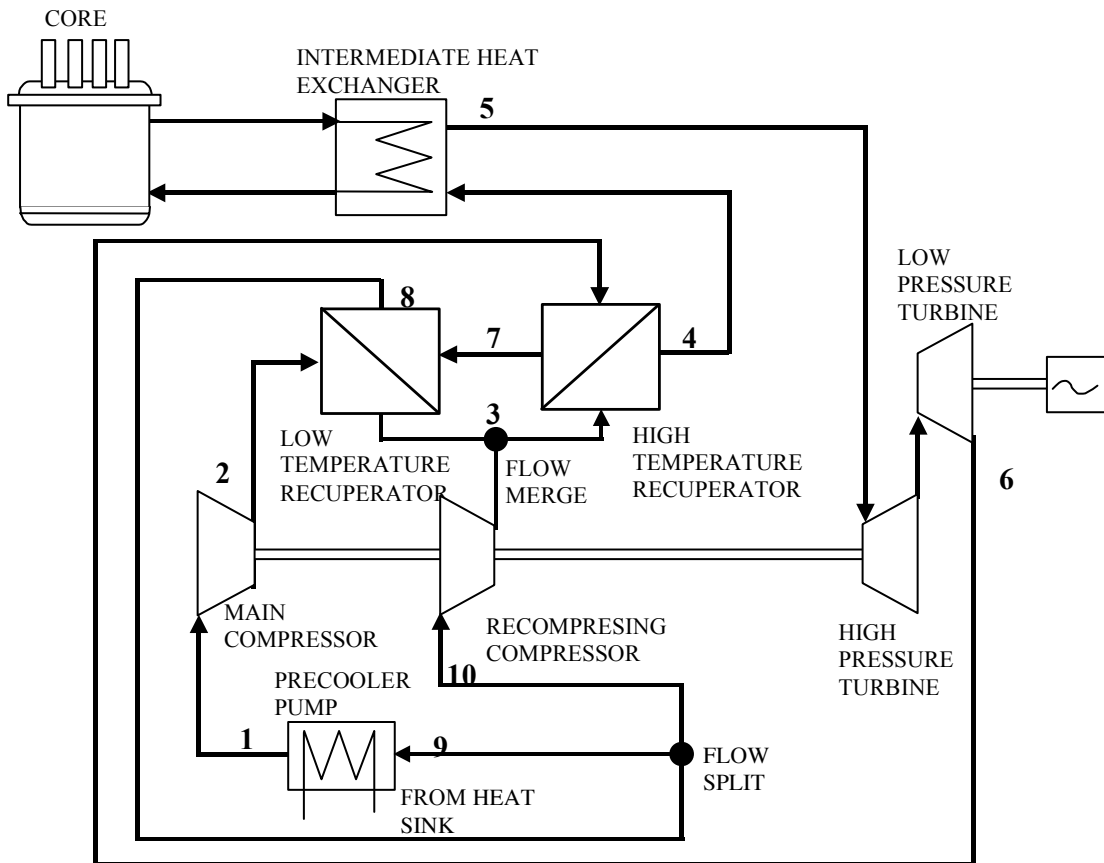
Figure 1.3. Brayton power cycle with supercritical CO_2.

The rest of this FY-02 Annual Report will describe our current analyses and evaluations of this design.

Table 1.2. Pressures, temperatures, enthalpies, entropies, and densities in Figure 1.3 listed by numbered location.

Location	Pressure (kPa)	Temperature (°C)	Enthalpy (kJ/kg)	Entropy (kJ/kgK)	Density (kg/m3)
1	7600.00	32.00	315.08	1.376	557.5
2	19000.00	63.62	336.89	1.387	681.97
3	18971.50	156.41	537.95	1.923	297.3
4	18943.04	408.02	861.67	2.520	146.2
5	18864.11	550.00	1035.94	2.753	117.61
6	7627.95	445.53	920.952	2.777	56.04
7	7616.49	161.54	597.23	2.205	102.7
8	7605.07	68.87	478.61	1.8975	162.7

Pressure ratio	2.5
Recompression fraction	0.41
Compressor efficiency	0.82
Turbine efficiency	0.87
Cycle Efficiency	**44.6**

Table 1.3. Reference reactor design parameters.

Core electric power			312 MW$_e$
Core thermal power			700 MW$_{th}$
Cycle efficiency			44.6 %
Core inlet temperature			467°C
Core outlet temperature			555°C
Reactor vessel geometry	Guard vessel	Outer diameter	6.15 m
		Inner diameter	5.65 m
		Wall thickness	25 cm
	Vessel	Outer diameter	5.55 m
		Inner diameter	5.45 m
		Wall thickness	5 cm
	Liner-to-vessel gap		7.5 cm
Fuel pin	Fuel outer diameter		5.48 mm
	Cladding inner diameter		6.32 mm
	Cladding outer diameter		7.52 mm
	Cladding thickness		0.6 mm
	Fuel heated length		1.3 m
	Fission-gas plenum height		2.47 m
	Cladding material		HT-9, EP-823, or ODS martensitic/ferritic steels
	Gap bond		liquid Pb
Core geometry	Number of positions (1 external and 5 internal rows are voided) in assembly		21 x 21
	Pitch to diameter ratio (square pitch)		1.3
	Number of fuel assemblies		157
	Core equivalent outer diameter		2.92 m
	Number of rods per fuel assembly		312
	Fuel assembly pitch		206.3 mm
	Core Barrel Outer Diameter		3.20 m
	Core Barrel Thickness		20 mm
Fuel type			U-Th-Pu-MA-Zr metal

2. Results of FY-02 Reactor Core Neutronics Studies

2.1. MIT FY-02 Results (Dr. Pavel Hejzlar)

2.1.1. Neutronic Design for Self-Controllability

2.1.1.1. Objective

The key objective is to design a self-controllable reactor core so that its response to Anticipated Transients Without Scram (ATWS) leads always to a safe shutdown state without exceeding the limits assuring core integrity. Key design features to be pursued include:

- Establishing the design limits that ensure core integrity and assure that these limits are not exceeded during accidents,
- Relying on inherent safety features, in particular neutronic feedbacks (Doppler coefficient, fuel expansion, coolant density change, radial expansion), and heat transfer mechanisms (e.g., natural convection and radiation) to achieve a safe shutdown state, and
- Relying on passive safety features (examples are enhanced thermal expansion materials, gas expansion modules, and other passive reactivity feedback mechanisms) to assist the inherent feedbacks in the achievement of a self-controllable reactor state during ATWS scenarios.

Note that conventional active safety systems can also be used, but they will not be credited for self-control, i.e., the reactor has to be able to achieve a safe shutdown state without reliance on the active safety systems. Because inherent features provide the highest degree of confidence due to their assured functioning independent of human or machine errors, the primary thrust of the design effort will be directed to maximum reliance on such features.

This work is a continuation of last years work reported by Hejzlar in Section 3.5.4 of our FY-01 Annual Report (MacDonald and Buongiorno 2002). For the convenience of the reader, all of the work is reported here, including some results from our FY-01 Annual Report.

2.1.1.2. Reactivity Feedback Ratios Criteria for Self-Controllable LBE-Cooled Core.

The design of our Actinide Burning Reactor (ABR) follows the approach adopted for the Integral Fast Reactor (IFR) design [Wade and Hill, 1997], which defines the state of the art of fast breeder reactors with passive safety features and satisfies the above objectives. A self-controllable reactor, such as the IFR, needs: (1) to be capable of dissipating decay heat with reliance on natural phenomena and (2) to exhibit a combination of reactivity feedbacks that lead to an inherent reactor shutdown without reliance on reactor scram. The former requirement is satisfied through reliance on the heat storage capacity of a large pool to absorb the initial decay power peak, design measures to promote natural circulation through the core and thus effectively transport the heat to the vessel wall, and finally a large surface area vessel with heat transfer augmentation and enhanced natural convection of air flow to dissipate decay heat to the ambient air. A plant design having these features is described in our FY-01 Annual Report (MacDoanld

and Buongiorno) and in Section 1 above. The purpose of the neutronics analyses covered here is to design a core to satisfy the latter requirement.

The neutronics constraints affecting safety are primarily the reactivity feedbacks that control the passive shutdown characteristics in compliance with the top-level requirement for self-controllability of the reactor, imposed by the objective to attain excellent safety comparable to that of the IFR. Self-controllability requires that, in a quasi-static reactivity balance sense, the reactor is inherently shut down to a safe state under the most restricting anticipated transients without scram. There are three external paths through which the core can be compromised – (1) coolant core inlet temperature, (2) coolant flow rate and (3) externally induced reactivity changes, either due to control rod motion or seismically induced core geometry changes. These all-encompassing paths are embodied in three generic anticipated transients without scram [Wade and Fujita, 1989]: (1) Unprotected Loss of Flow (ULOF), Unprotected Loss of Heat Sink (ULOHS), and Unprotected Transient Overpower (UTOP).

Wade and Hill [1997] derived criteria for passive self-regulation in the IFR from the neutronics viewpoint. The three paths that encompass all possible initiators affecting the core reactivity are changes in primary-coolant pumping power, primary-coolant inlet temperature, and control rod position. They showed that for sufficiently large margins between the operating point and safety limits, one can design a core with reactivity feedback ratios that assure passive self-regulation if the following ranges for the reactivity coefficients (expressed in terms of measurable integral reactivity parameters) are met:

1. **Loss-of-flow, S1**: $A/B \leq 1$, where A is the net power reactivity coefficient in cents and B represents the power/flow coefficient of reactivity in cents/100% power/flow, which controls the asymptotic temperature rise in an unprotected loss of flow transient. In the case of natural circulation at full power, this criterion can be relaxed.

2. **Loss-of-heat sink, S2**: $1 \leq \dfrac{C\Delta T_c}{B} \leq 2$, where C characterizes the inlet temperature coefficient of reactivity in cents/°C and ΔT_c is full-power, steady-state coolant temperature rise. The term ensures inherent balanced response to an unprotected loss of heat sink transient and coolant inlet freezing.

3. **Transient overpower, S3**: $\dfrac{\Delta \rho_{TOP}}{|B|} \leq 1$, where $\Delta \rho_{TOP}$ is the reactivity vested in a single control rod.

The above three safety criteria (S-criteria) were adopted as top-level constraints for the core neutronic design and are discussed in more detail by Hejzlar in Section 3.4 of our FY-01 Annual Report [MacDonald and Buongiorno 2001]. Because the S-criteria are determined by values and signs of reactivity coefficients, the latter will be required to fall within the ranges that satisfy these three criteria.

If a reactor meets the above conditions, the rise of coolant temperature above its normal full-power, full-flow conditions never exceeds ΔT_c and thus cladding failure does not occur even if control rods fail to scram. The above criteria require that a core is designed in such a way that the changes in coolant temperature rise have a larger reactivity effect than variations of burnup and fuel temperature and that the worth of one control rod used for reactivity compensation is relatively small compared to reactivity variations from anticipated changes in temperature rise across the core. Note that the above criteria were derived for a sodium-cooled reactor, based on

an outlet temperature margin to prevent sodium boiling ($\sim 2.5\Delta T_c$) and the margin to structural material damage of $\sim 1.5\Delta T_c$. Because the coolant conditions of the ABR are different, the above three criteria are re-derived as discussed below. The parameters affecting the criterion limits are compared for sodium and LBE coolants in Table 2.1, where the key margins entering the derivations are in bold type.

The LBE coolant has a much larger margin to boiling than sodium, however, the margin to structural damage is much smaller since the temperature limit is the same for both coolants. Therefore, the key constraint determining maximum coolant temperature rise is derived from the cladding limit of 725°C and the high boiling point of LBE does not bring any benefit in terms of S criteria. In terms of core coolant temperature rise, the margin to cladding damage is higher for the ABR core because of a significantly smaller ΔT_c. In terms of the absolute temperature difference, this margin is slightly higher for the IFR core. The margin to freezing of the coolant inlet is more than twice as high for the ABR core due to its higher core inlet temperature and smaller ΔT_c.

Table 2.1 Comparison of key parameters for a typical sodium-cooled IFR and a LBE-cooled ABR.

	IFR (sodium)	ABR (LBE)
Coolant inlet temperature (°C)	350	461
Coolant outlet temperature (°C)	500	552
Core coolant temperature rise, ΔT_c (°C)	150	92
Coolant boiling point (°C)	892	1670
Margin to boiling in terms of ΔT_c (°C), δT_{out}	392°C ~ 2.5ΔT_c	1118°C ~ 12ΔT_c
Coolant freezing point (°C)	97.8	125
Margin to freezing in terms of ΔT_c, δT_{in}	**250°C ~ 1.5ΔT_c**	**336°C ~ 3.6ΔT_c**
Conservative margin to freezing based on IFR approach	**2/3*250°C~ ΔT_c**	**2/3*336°C ~2.4ΔT_c**
Temperature limit to cladding structural damage	725°C	725°C
Margin to cladding damage in terms of ΔT_c, δT_{out}	**225°C~ 1.5ΔT_c**	**173°C~ 1.9ΔT_c**
Conservative margin to cladding damage based on IFR approach	**2/3*225~ ΔT_c**	**2/3*173°C~1.25ΔT_c**

To follow the IFR work [Wade and Hill, 1997], where more conservative values for the margins to cladding damage and freezing (~2/3 of actual margin) were adopted for derivation of the A, B, and C coefficients, the same reduction of the margins was used in deriving the criteria for the LBE-cooled reactor. Two thirds of actual margins, based on the IFR approach, are also listed in Table 2.1.

Criterion S1 ensures that the asymptotic coolant temperature rise in an unprotected loss of flow transient remains within acceptable limits, in our case the cladding damage limit. Asymptotically, a stable steady state under natural circulation flow is established if the design ensures that the negative feedbacks reduce the power to the level that can be just removed by natural circulation. The asymptotic limit on coolant outlet temperature under natural circulation flow can be derived from a reactivity balance to be [Wade and Chang, 1988]

$$\delta T_{out} = \frac{A}{B}\Delta T_c \tag{2-1}$$

Adopting the conservative limit of 1.25 ΔT_c for maximum coolant outlet temperature, the inequality

$$\frac{A}{B}\Delta T_c \leq 1.25 \Delta T_c \qquad (2\text{-}2)$$

must be satisfied. Hence:

$$\frac{A}{B} \leq 1.25. \qquad (2\text{-}3)$$

As aforementioned, **criterion S2** ensures an inherent balanced response to an unprotected loss of heat sink transient and coolant inlet freezing. In unprotected loss of heat sink (ULOHS) scenarios, heat rejection to the balance-of-plant is lost causing the inlet temperature to increase (at constant flow) accompanied by a negative reactivity insertion from the higher coolant temperature. As a result, the power is reduced, introducing positive reactivity insertion from the fuel temperature feedback, but the net effect is a power reduction if the reactivity feedbacks from the fuel temperature are less than those induced by the coolant temperatures. Asymptotically, outlet temperature is equal to inlet temperature as power goes to zero and inlet temperature change can be derived from a reactivity balance as [Wade and Chang, 1988]

$$\delta T_{in} = \frac{A+B}{C}, \qquad (2\text{-}4)$$

while the outlet temperature change gives

$$\delta T_{out} = \left(\frac{1+A/B}{C\Delta T_c /B} - 1\right)\Delta T_c. \qquad (2\text{-}5)$$

Since the maximum increase of outlet temperature must not exceed the margin to cladding damage, i.e., conservatively $1.25\Delta T_c$, the lower limit of Criterion S2 can be derived from the inequality

$$\left(\frac{1+A/B}{C\Delta T_c /B} - 1\right)\Delta T_c \leq 1.25\Delta T_c. \qquad (2\text{-}6)$$

Rewriting the equation, we obtain:

$$\frac{C\Delta T_c}{B} \geq \frac{1+A/B}{2.25}. \qquad (2\text{-}7)$$

Conservatively, the maximum allowed A/B is 1.25 for this transient with a coolant temperature increase. Substituting for A/B=1.25 yields

$$\frac{C\Delta T_c}{B} \geq 1.0, \qquad (2\text{-}8)$$

which is the same limit as for the IFR design.

For the chilled temperature scenario, the reactivity increase from a lower inlet temperature due to overcooling from the balance-of-plant side leads to a power increase that is compensated by the reactivity fuel temperature feedback. It can be derived [Wade and Chang, 1988] that the asymptotic state for the outlet temperature is:

$$\delta T_{out} = \left(\frac{C\Delta T_c / B}{1 + A/B} - 1 \right)(-\delta T_{in}) \tag{2-9}$$

Since inlet temperature change must satisfy the margin to freezing, one can write:

$$\left(\frac{C\Delta T_c / B}{1 + A/B} - 1 \right)(2.4\Delta T_c) \leq 1.25\Delta T_c \text{, and after recasting} \tag{2-10}$$

$$\frac{C\Delta T_c}{B} \leq 1.5\left(1 + \frac{A}{B}\right) \tag{2-11}$$

or for a conservatively low A/B=0.2 for this type of transient:

$$\frac{C\Delta T_c}{B} \leq 1.8. \tag{2-12}$$

Thus the S2 criterion for the ABR design is:

$$1.0 \leq \frac{C\Delta T_c}{B} \leq 1.8, \tag{2-13}$$

which provides about the same range for the design of individual reactivity coefficients as the IFR criterion.

Finally, the **S3 criterion** will be evaluated. The asymptotic coolant outlet temperature in an overpower transient after the rise in core inlet temperature due to the balance-of-plant heat removal limit, can be derived [Wade and Chang, 1988] as:

$$\delta T_{out} = \left(\frac{\Delta\rho_{TOP} / B}{-C\Delta T_c / B} \right)(\Delta T_c) \tag{2-14}$$

Limiting the asymptotic core outlet temperature by the conservative cladding damage constraint yields:

$$\left(\frac{\Delta\rho_{TOP} / B}{-C\Delta T_c / B} \right)\Delta T_c \leq 1.25\Delta T_c, \tag{2-15}$$

or: $$\frac{-\Delta\rho_{TOP}}{B} \leq 1.25\left(\frac{C\Delta T_c}{B} \right)_{min} \tag{2-16}$$

12

Using the minimum value of $C\Delta T_c/B = 1$ yields the conservative limit for the S3-criterion:

$$\frac{\Delta\rho_{TOP}}{B} \leq 1.25 \tag{2-17}$$

A similar derivation can be performed for the lead-cooled core, where the coolant inlet and outlet temperatures and the cladding limit are the same as for the LBE-cooled core, but the margin to coolant freezing is reduced. Table 2.2 summarizes the S criteria for IFR, LBE-cooled, and lead-cooled reactors for the assumed operating conditions listed therein.

Table 2.2 Comparison of S-criteria for various coolants.

	IFR Na-cooled	ABR LBE-cooled	ABR Lead-cooled
Coolant inlet temperature (°C)	350	461	461
Core coolant temperature rise, ΔT_c (°C)	150	92	92
Coolant freezing point (°C)	97.8	125	327
Temperature limit to cladding structural damage	725°C	725°C	725°C
Conservative margin to freezing	ΔT_c	$\sim 2.4\Delta T_c$	ΔT_c
Conservative margin to cladding damage	ΔT_c	$1.25\Delta T_c$	$1.25\Delta T_c$
S1 criterion	$\frac{A}{B} \leq 1$	$\frac{A}{B} \leq 1.25$	$\frac{A}{B} \leq 1.25$
S2 criterion	$1 \leq \frac{C\Delta T_c}{B} \leq 2$	$1 \leq \frac{C\Delta T_c}{B} \leq 1.8$	$1 \leq \frac{C\Delta T_c}{B} \leq 2.7$
S3 criterion	$\frac{\Delta\rho_{TOP}}{\|B\|} \leq 1$	$\frac{\Delta\rho_{TOP}}{B} \leq 1.25$	$\frac{\Delta\rho_{TOP}}{B} \leq 1.25$

Note that the lead cooled reactor has a significantly larger range in the direction of coolant freezing for the S2—criterion than the LBE-cooled core for the same core temperature rise and core inlet temperature. Although contra-intuitive at first glance, since the margin to freezing is smaller for lead coolant, the larger S2 range is valid. This is because in accidents with overcooling of coolant entering the core at constant pump flow, the reactivity increase from negative temperature feedbacks is compensated by a power increase leading to a core outlet temperature rise. Since the core outlet temperature is limited to be below the cladding damage constraint, a smaller difference between core inlet temperature and freezing point actually provides more scope for reactivity feedbacks entering the $C\Delta T_c/B$ term to comply with the core outlet temperature rise limit resulting from core inlet overcooling scenarios. Moreover, overcooling accidents are not of concern (except at plant startups) in the preferred design with a supercritical CO_2 (S-CO_2) cycle because the cycle cannot operate without the recuperators and thus does not employ their bypass. The lead cooled concept with a S-CO_2 cycle is more attractive because lead is significantly less corrosive than LBE offering a higher temperature limit for structural materials – a benefit not accounted for in Table 2.2 data. In addition, it is substantially cheaper than LBE and much less polonium is generated in lead, which will simplify the design of polonium removal systems.

2.1.1.3. Evaluation of Core Radial Expansion Coefficient

The quantitative judgment of self-controllability based on the three S-criteria requires the knowledge of the following reactivity coefficients and parameters:

- Doppler coefficient,
- Fuel thermal expansion coefficient,
- Coolant temperature coefficient,
- Core radial expansion coefficient,
- Rod driveline expansion coefficient, and
- Maximum control rod worth.

The first three coefficients were evaluated by Hejzlar in our FY-01 Annual Report [MacDonald and Buongiorno 2001]. The other three coefficients are discussed in this report. The reactivity feedback from radial expansion of the core is a very important feedback that is typically dominant for mitigating the consequences of unprotected transients. Obtaining an accurate core radial expansion coefficient requires an extensive effort and its magnitude has always been associated with the largest amount of uncertainty, especially in cases where assembly bowing occurs. Evaluation of the core expansion coefficient will be the focus of this section.

Core Radial Expansion Phenomenon and State-of-the Art Modeling

Reactivity changes from core radial expansion and bowing depend strongly on the core design and are typically negative, but can also be positive if the design is not carried out properly. To achieve a negative feedback, the motion of the active core zones of fuel assemblies must be limited to outward displacement as the core heats up from increased power. The desired displacement is typically achieved through various core constraints. The principles of such restraint concepts, used also in the FTR and CRBR, are schematically illustrated in Figure 2.1. The constraints necessitate minimum radial gap clearances between assemblies, but the gap must also provide sufficient space to accommodate creep, both thermal and irradiation induced, swelling effects, and adequate tolerance for easy refueling during shutdown. The limited-free-bow core restraint is typically preferred for radial expansion of liquid metal cooled
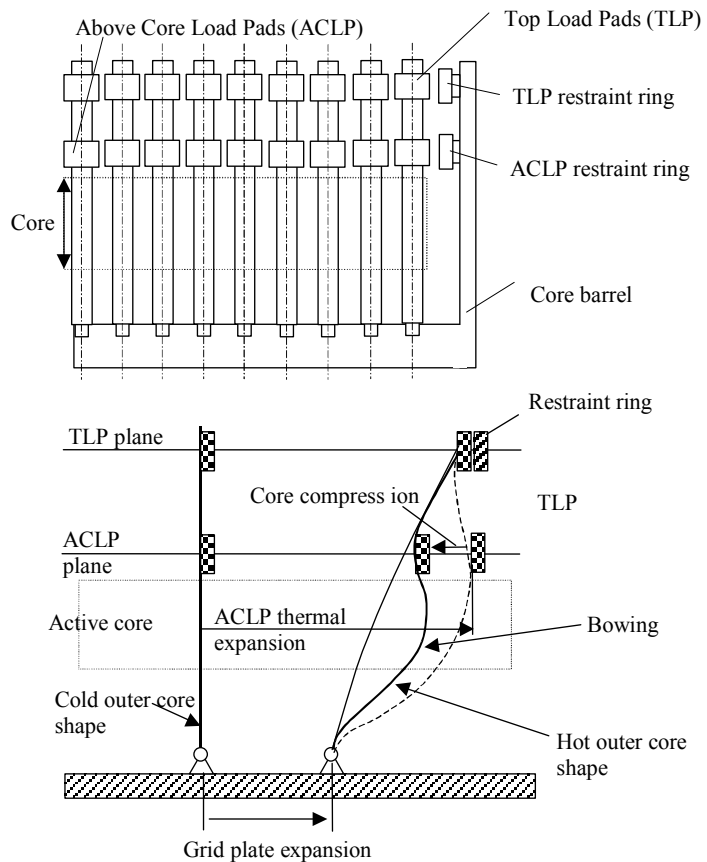
Figure 2.1 Limited free bow concept and radial core expansion phenomenon (adapted from Royl et al. 1992].

cores.

The constraints shown in Figure 2.1 employ above-core load pads (ACLP) - a continuous network of contacting load pads - above the core, which allows radial movement of the fuel assemblies in the above-core plane up to the ACLP restraint ring. Similarly, the top load pads (TLP) in the plane above the gas plenum of the outer fuel assemblies are restrained from further radial expansion by the TLP restraint ring. In this manner, the allowable bowing is well defined within the restraint rings. At zero power, the assemblies are in a stright position or bent slightly outward from creep. As power is increased during startup, lateral temperature gradients develop, resulting in the core expansion from thermal dilatation of the ACLP and outward bowing of the core periphery. The support of the bending forces leads to a compressive force in the ACLP and core compression, as indicated in Figure 2.1. Stiff load pads are necessary to prevent excessive core compression that would offset a significant fraction of the overall expansion effect. As power is further increased, the top sections of the fuel assemblies bow outward resulting in negative reactivity insertion with increasing power until the TLP restraint ring is contacted. The negative reactivity insertion due to the core radial expansion/bowing is controlled by the ACLP average temperature. The core outlet temperature is a good approximation. As the transient progresses, the core support structure starts to heat up (indicated by grid plate expansion on Figure 2.1) due to delayed core inlet temperature increase, resulting in a further negative reactivity feedback.

Calculations of the core radial expansion feedback are quite complex, since elastic and inelastic bowing of assemblies, which are subject to temperature dependent boundary conditions at their nozzle support, ACLP, and TLP and subject to thermal and inelastic bowing deformations, have to be calculated. The design parameters that need to be considered involve grid plate temperature, core temperature rise, restraint ring temperature, grid plate and restraint ring thermal expansion coefficients, duct material properties (thermal expansion, swelling, creep), nozzle support conditions, core axial and radial location, assembly radial thermal gradient, ACLP location and compressibility, and gaps at the ACLP and TLP elevations. Moreover, each assembly operates at different power and is subject to different temperature gradients. Analytical models for one fuel assembly were developed [Wigeland and Moran 1986] to study uncertainties in the calculations. More detailed models use the SASSYS/SAS4A codes [Dunn et al. 1985, Tentner et al. 1985] to calculate the axial profile of the outer shape of the active core region incorporating temperature differences across the assemblies and other local effects [Wigeland 1986]. This model was extended to account for an additional restraint ring included at the elevation of the ACLP, used in some earlier reactors, such as FFTF, and the results compared to an empirical correlation derived from tests on FFTF [Wigeland 1987]. Excellent agreement was achieved, confirming that the detailed modeling of local effects affecting bowing and radial expansion, as employed in SASSYS/SAS4A, can predict core radial expansion reactivity feedback reliably.

Simplified Approach for Assessment of Core Radial Expansion in ABR using MCNP

Although the SASSYS/SAS4A system is capable of good predictions of core radial expansion, it was not used to evaluate this reactivity feedback in the proposed ABR concept. Rather a simplified approach has been developed for two reasons:

(1)   Accurate modeling of core bowing/expansion response to power/flow changes requires knowledge of the detailed core design with all its fuel assembly details, core support structures, load pads, and restraint rings. This information is not fully available at this conceptual design stage.

(2)   Streaming central and peripheral channels allow significant directional neutron streaming making the use of diffusion theory on which the SASSYS/SAS4A code is based questionable.

Therefore, a simplified approach using the MCNP4C code, which solves the full neutron transport equation more rigorously thereby describing the directional neutron streaming, was selected to evaluate the core radial expansion coefficient. The calculations assumed that the core design employs a limited-free-bow core restraint that allows a well-defined core expansion resulting in a reactivity reduction from power/flow increases.   The core radial expansion coefficient is calculated by comparing the reactivity of the radially expanded core with that of the reference core at nominal operating conditions. The expanded core and the core radial expansion coefficient were modeled as follows:

1. Uniform expansion of the whole core is assumed, i.e., the core support plate, ACLP, and TLP are assumed to be subjected to the same temperature change, resulting in an increase of rod pitch, which is identical at each core level. Hence, all pins remain parallel, but their pitch is opened.
2. The sealed boxes of streaming channels expand their radial dimensions in proportion to the same temperature increase.
3. A thermal expansion coefficient of 2×10^{-5} °C^{-1}, typical of HT-9 steel at temperatures representative of the ABR core outlet, is used for all structural materials (assumed constant).   The expanded dimensions are calculated for a sufficiently large temperature difference of 600°C. This large ΔT is significantly higher than the increase allowable in the reactor core, but was selected this high to achieve reactivity changes significantly higher than MCNP statistical error. Note that except for changes in radial dimensions, all other parameters in the MCNP input remain identical.
4. The total value of the uniform core radial expansion coefficient is obtained by subtracting the reactivity of the reference core from that of the expanded core and dividing by the temperature difference of 600°C to obtain the linearized value per °C.
5. The value obtained from step 4 is divided by 2 to obtain the radial expansion coefficient controlling reactivity changes in the early phases of the transient, i.e., only the upper part of the core is assumed to expand early in the transient.

The MCNP4C results using the above approach are summarized in Table 2.3. The value of the core radial expansion coefficient of -0.185¢/°C corresponds well with the value of -0.156c/°C claimed for the LBE cooled STAR-LM reactor under development at ANL [Sienicky and Petkov, 2002].

Table 2.3. Radial expansion coefficient for the optimized core design.

Case	k_{eff}	α_R (¢/°C)[**]
Reference configuration	0.9999± 0.0002	
Radially expanded core	0.9938± 0.0002	
Total uniform radial expansion coefficient		-0.37±0.01
Core radial expansion coefficient		-0.185±0.01

[**]Linearized value between high (reference +600°C) and reference temperatures assuming constant coefficient of thermal expansion of 2×10^{-5} m/m [Wigeland and Moran 1986], i.e., typical values for grid plate and load pad stainless steel materials in LMRs.

Finally, it is expected that the simplified approach will yield conservative results, based on the comparison of another simplified approach with the detailed model analysis performed by Wigeland [1986]. The simple model in this reference calculated reactivity feedback using a feedback coefficient in conjunction with changes in temperature of the grid support and ACLP, similarly as in the simplified model above. Including other effects, such as subassembly bowing and the potential for clearances to occur between subassemblies in the ACLP region resulted in a significantly greater negative reactivity feedback from radial core expansion.

Verification of the Simplified Approach on an IFR Core Design

To verify the capability of the simplified MCNP model to predict the core radial expansion coefficient, the sodium-cooled Advanced Liquid Metal Reactor (ALMR) core design has been modeled using the approach outlined above and the results compared to Oda's reported values [1993]. The ALMR is a 840MWth core using U-TRU-Zr fuel (10wt% Zr) in two regions with different TRU loadings - 21.79wt% in the outer core region and 16.14% in the inner region. The core has 391 assemblies – 192 fuel assemblies, 114 reflector assemblies, 66 shield assemblies, 10 control assemblies, 6 gas expansion module assemblies (GEM), and 3 ultimate shutdown assemblies. The core configuration is shown in Figure 2.2. Gas expansion modules were not modeled and were replaced by regular reflector assemblies. The data used in the model setup are summarized in Oda's Tables 5.1-1 through 5.1-5 of [1993].
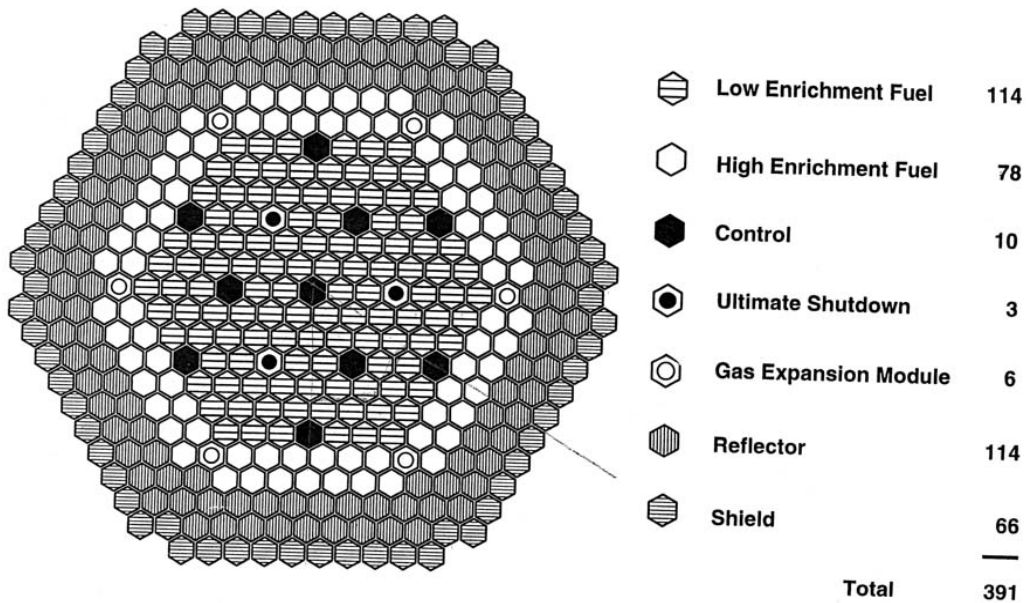
Figure 2.2. Baseline core configuration of the ALMR burner core (from Oda 1993).

The cross section of the MCNP4C 1/6th model of the core is shown in Figure 2.3. Because no details were given regarding the structures outside the core, the grid plates and inlet modules were modeled in a simplified manner. The details of the structures were left out due to the lack of the design information and to reduce the amount of time consuming tedious work. Also, the composition of the TRUs (Pu and MA vectors) was not specified, hence typical vectors from PWR spent fuel at 33MWd/kgHM were assumed.

17

Coolant
Shield assemblies
Reflector
Control assemblies
Fuel assemblies
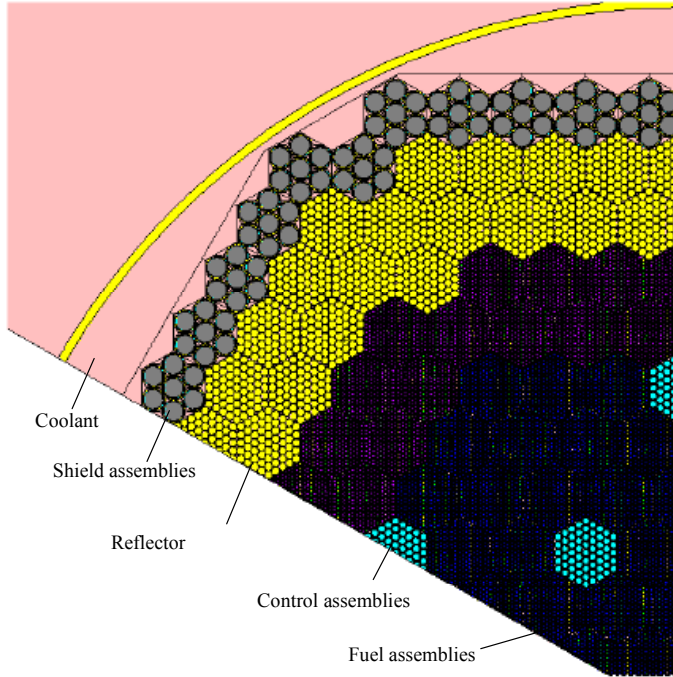
Figure 2.3. Layout of the 1/6th ALMR core as modeled by MCNP.

The calculations were performed in the following manner. First, the reference k_{eff} was calculated using the reference core dimensions. Secondly, the core was radially expanded using the linear coefficient of thermal expansion for HT-9 ($2x10^{-5}$ m/m/°C) for a temperature 600°C above the reference temperature. The expansion was performed uniformly by expanding both the lower grid plate and top load pads by the same distance, so that fuel rods retain parallel geometry. All other dimensions not associated with core expansion were kept fixed at a reference value. The results are summarized in Table 2.4.

Table 2.4. Core radial expansion coefficient for the ALMR design

Case	k_{eff}	Core radius (cm)	Total uniform α_R (¢/K)[**]	Uniform Rdk/dR
Reference configuration	1.0355± 0.0003	98.09		
Radially expanded core[*]	1.0307± 0.0003	99.27	**-0.29±0.01**	**-0.52**
Value from [Oda,1993]			**-0.35**	**-0.577**

[**]Linearized value between high (reference +600°C) and reference temperatures assuming constant coefficient of thermal expansion of $2x10^{-5}$ m/m [Wigeland and Moran 1986], i.e., typical values for grid plate and load pad stainless steel materials in LMRs and total β_{eff} = 0.00328.

The reported value of the uniform radial expansion coefficient is about ~17% higher than the MCNP results using the simplified model. Due to the lack of sufficient information, the results carry large uncertainty and can serve only as ballpark numbers. Hence the predicted value from the simplified MCNP model can be considered to be in satisfactory agreement with the reported uniform core radial expansion coefficient. If all the out-of core structures are modeled, the leakage and absorption in these structures would increase upon expansion and would further increase reactivity reduction yielding more negative values closer to the reported results. Because the model provides a conservative core radial expansion coefficient and the results agree with the IFR values reported by IFR designers, the simplified approach for core radial expansion coefficient estimation is considered sufficient for the purposes of these conceptual studies.

2.1.1.4. Comparisons Of the ABR and IFR Reactivity Feedback Coefficients and S-Criteria

The reactivity feedback coefficients and all three S-criteria for the ABR are compared against typical IFR values in Table 2.5. The Doppler coefficient, fuel thermal expansion coefficient, and coolant density coefficients for the ABR were reported by Hejzlar in Section 3.4 our FY-01 Annual Report [MacDonald and Buongiorno 2001]. The control rod driveline expansion coefficient was taken conservatively to be zero, consistent with the IFR reference case. The ABR has a smaller Doppler coefficient than the IFR because of the harder spectrum. In addition, the difference between fuel core-average and coolant core-average temperatures is less in ABR than for the IFR due to the smaller pin linear power. The thermal hydraulic calculations [Dostal et al. 2002] show that this temperature difference is only 90°C versus 150°C for IFR. This is on top of the small radial temperature increase inside the fuel pins due to the high conductivity of the metallic fuel. As a result, the value of the net power reactivity coefficient A, which accounts for the Doppler feedback and fuel thermal expansion, is small, making the ratio A/B about half of that of IFR, i.e., in the desirable direction for ULOF transients.

Table 2.5. Expressions for reactivity coefficients and values of the reactivity feedback coefficients and S-criteria for the Na-cooled IFR and LBE-cooled ABR.

	Doppler	Fuel expansion	Coolant temper.	Rod driveline	Radial expansion	Coolant ΔT (K)	Fuel ΔT(K)
Expressions for reactivity coefficients [Wade and Chang 1988]							
A (¢) =	(α_D	+ α_e)					x ΔT_f
B (¢) =	(α_D	+ α_e	+ α_{Co}	+ 2α_{RD}	+ 2 α_R)	x ΔT_c/2	
C (¢/K) =	(α_D	+ α_e	+ α_{Co}		+ α_R)		
Typical IFR reactivity coefficients for individual components for1800MWth core [Wade and Fujita 1989]							
	-0.12	-0.09	+0.18	~0	-0.22 (α_R)	150	150
Calculated reactivity coefficients for IFR: A=-31¢, B=-35¢, C=-0.25¢/K							
Calculated criteria for IFR: S1: A/B = 0.88<1, S2: CΔT_c/B = 1.1, which is between 1 and 2.							
ABR reactivity coefficients for individual components (700MWth core)							
	-0.07	-0.06	+0.04	~0	-0.18[*]	92	90
Calculated reactivity coefficients for optimized ABR: A= -12¢, B= -22¢, C= -0.28¢/K							
Calculated criteria for ABR: S1: A/B = 0.55<1.25, S2: CΔT_c/B = 1.20, which is between 1 and 1.8.							

[*]Calculated using simplified approach from Section 2.1.2.3. An estimate from the IFR value, corrected for LBE coolant based on a comparison of sodium and LBE cooled compact cores by Hill et al. (1999), where the LBE –cooled core of the same size and arrangement exhibits 18% smaller α_R than its sodium-cooled counterpart and accounting for different β_{eff} in the optimized ABR would yield 0.23, i.e., 0.22 (0.82) 0.0036/0.0028=0.23.

To satisfy all three criteria, a large value of the power/flow coefficient of reactivity, B, is desirable. This coefficient includes, in addition to fuel temperature feedback, coolant temperature and core radial expansion coefficients. The LBE-cooled burner has a very small coolant temperature coefficient, which leads to a higher B. However, the smaller core coolant temperature rise, smaller core radial expansion feedback, and smaller fuel temperature coefficient reduce the B value, hence B in the ABR design is smaller than for the IFR core. Finally, the inlet temperature coefficient of reactivity, C, is comparable to that in the IFR, since the smaller positive value of the coolant temperature coefficient, which is beneficial, approximately compensates the negative effect of the smaller core radial expansion coefficient. The bottom row of Table 2.5 shows that both the first and second criteria are satisfied. In comparison with IFR,

the actual values of these criteria are farther from the limits, providing more design space for changes of reactivity feedbacks with burnup.

Finally, the S3 criterion needs to be evaluated. The original core design by Hejzlar reported in our FY-01 Annual Report [MacDonald and Buongiorno 2001] had 25 control rods. The maximum reactivity excess during the 8 year cycle, reached at 2EFPYs, was calculated to be 8$ = 800¢. Thus the S3 criterion,

$$\frac{\Delta \rho_{TOP}}{|B|} = \frac{800 / 25}{20} = 1.6 > 1.25 \qquad (2\text{-}18)$$

is not satisfied, even not accounting for the larger control rod worth in the location of peak neutron flux. Therefore, design modifications are necessary to improve reactor response to overpower transients. The options to achieve compliance with the S3 criterion will be pursued next.

2.1.1.5. Modified core design with reduced control rod worth

Since the peak reactivity during a cycle is primarily determined by TRU composition, which is fixed, there are two approaches for the improvement of UTOP performance. The first alternative is to increase the number of control rods. This is easy to accomplish in the ABR design with streaming assemblies because there is an empty space in the central assembly region where control rods can be placed. Another possibility to satisfy the UTOP criterion would be to make the B coefficient more negative. This is feasible by increasing streaming and pushing the coolant temperature coefficient towards negative values. However, this would require more space for the core region. Because no additional space for additional streaming channels is available in a vessel of fixed dimensions, as dictated by the transportability constraint, a core design with an increased number of control rods was adopted.

The new core layout with 49 control rods is shown in Figure 2.4. Control rods were placed in fuel assemblies with the highest power in the region of higher enrichment. The average control rod worth is 8$/49 = 0.16$. Based on neutron flux peaking of 1.2, the maximum control rod worth can be estimated not to exceed 0.22$ and the S3 criterion to yield:
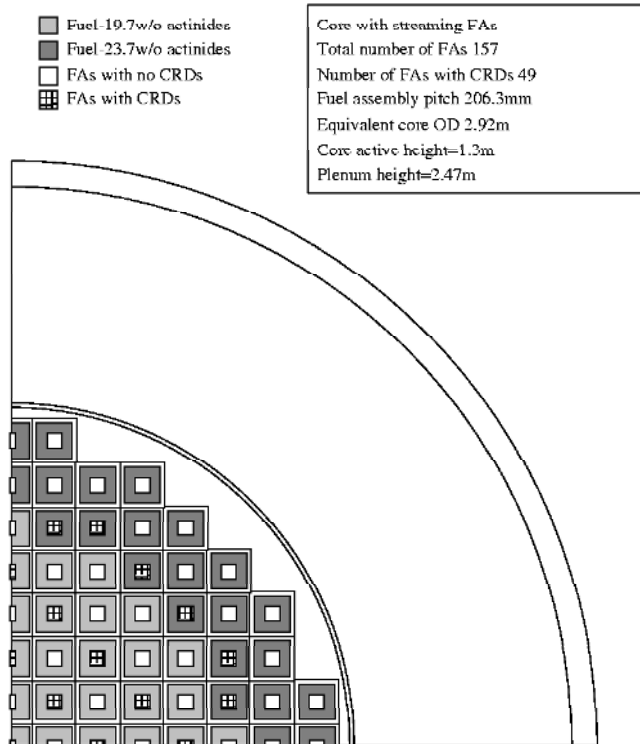
Figure 2.4. Core layout for the optimized core design with an increased number of control-rods.

20

$$\frac{\Delta\rho_{TOP}}{|B|} = \frac{220}{20} = 1.1 < 1.25 \, . \tag{2-19}$$

Hence, 49 control rods (in 1/3 of the fuel assemblies) should be sufficient for containment of the UTOP scenario. This expectation will have to be confirmed through more rigorous analysis of the modified core design.

2.1.2. Neutronic Performance Of The Modified Reference Core Design

2.1.2.1. Power Distribution At Beginning-Of-Life

Core power and flux distributions at beginning-of-life with the control rod inserted to reach criticality are shown in Figures 2.5 and 2.6, respectively; the axial power profile is plotted in Figure 2.7. Note the slightly smaller power at the core top due to the presence of control rods in the upper half of the core. Overall, the peaking is very small. The small power peaking is due to the flat neutron flux profile across the core, as can be observed from Figure 2.6, and enrichment zoning where fresh fuel is placed in core peripheral assemblies. The flat neutron flux profile is a consequence of a large mean free path and very strong neutronic coupling.
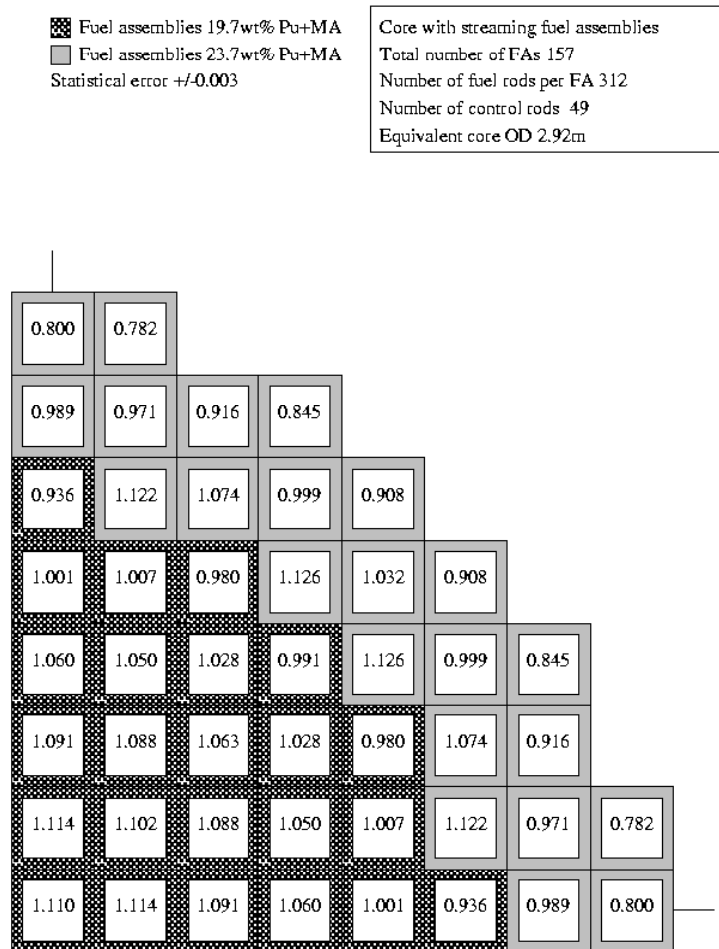
Figure 2.5. Power distribution at beginning-of-life (control-rods in).

21
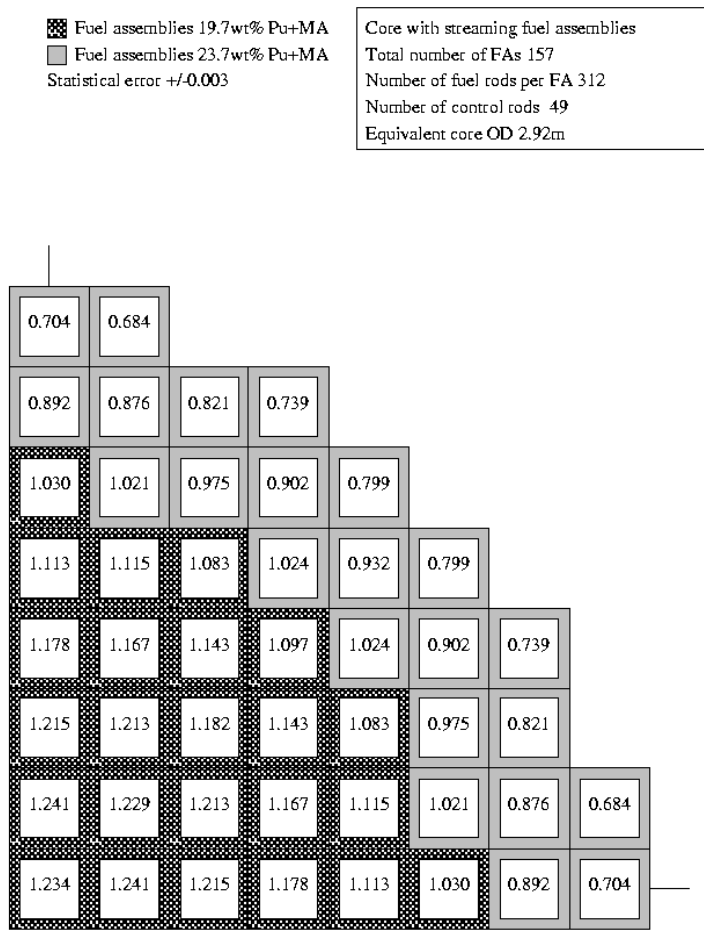
Figure 2.6. Neutron flux distribution at beginning-of-life (control-rods in).

Core with 157 FAs at BOL
H=130cm
Th-U(30%)-Pu-MA-Zr fuel
49 CRDs in
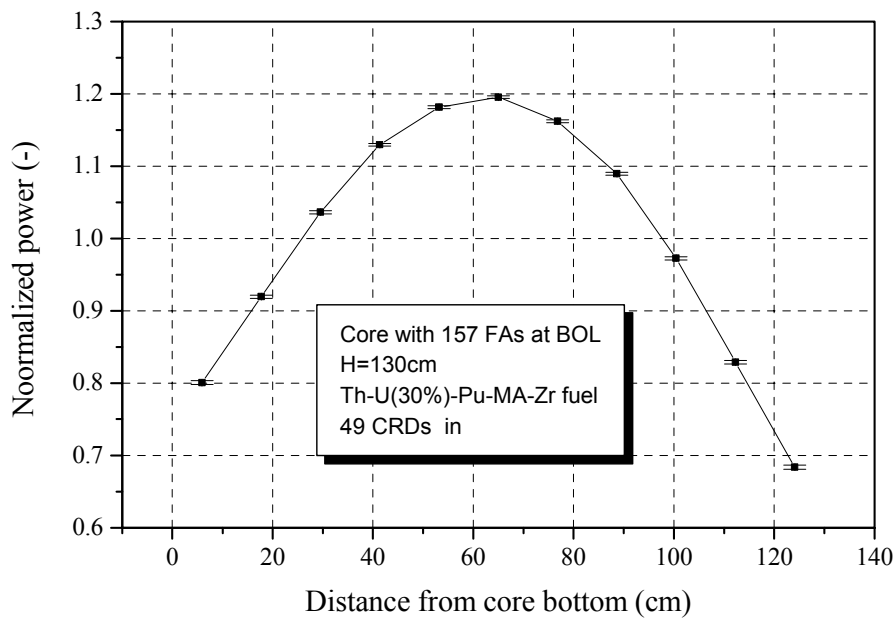
Figure 2.7. Axial power peaking at beginning-of-life.

2.1.2.2. Burnup Performance

All the burnup calculations were performed using Monte Carlo Neutron Photon Transport (MCNP)-based burnup codes. All the codes used ORIGEN2.1 [Croff 1980] to perform the depletion calculations. The coupling between MCNP and ORIGEN2.1 has been attained through the newly MIT-developed code MCODE [Xu et al. 2002]. MCODE has been used for most of the calculations; other MCNP-ORIGEN2.1 codes, such as the INEEL-developed MOCUP [Moore et al. 1995] and LANL-developed MONTEBURNS 1.0 [Poston and Trellue 1999] were also used for comparison. All codes used the MCNP4C [Briesmeister 2000] version of MCNP.

Because MCODE, which was primarily used for burnup calculations of the ABR core, is the new MCNP-ORIGEN coupling code, currently not available through the RSICC distribution center, a brief description of the code with focus on differences from MOCUP and MONTEBURNS will be provided. More information is given in Xu et al. [2002]. MCODE differs from MOCUP and MONTEBURNS in three major techniques affecting the MCNP-ORIGEN coupling and depletion procedure:

1. Power/flux normalization
2. ORIGEN depletion for constant flux option, and
3. MCNP-ORIGEN coupling method.

Power/flux normalization.   Since all the tallies in MCNP are normalized per fission source neutron, the flux values need to be multiplied by a constant factor to yield the required power level. MOCUP does not provide automatic generation of this factor and leaves its supply to the user. MONTEBUNRS employs for flux multiplication factor (FMF) the method recommended in MCNP, i.e., FMF=$(P\bar{\nu})/(Q\,k_{eff})$, where P = total power of the entire system (watts), $\bar{\nu}$ = average number of fission neutrons per fission event, Q = average recoverable energy (excludes neutrinos) per fission event (Joules/fission) and k_{eff} = eigenvalue of the system. The changes of recoverable energy with the composition of actinides during burnup require some effort in the determination of this value. Scaling by k_{eff} for non-critical systems (mostly the case in burnup calculations) also carries uncertainties, since although fission rates scale well with k_{eff}, one-group fluxes may not. The issues associated with Q and k_{eff} have been discussed in detail in Zhao et al. [2000].

MCODE employs a more rigorous and conceptually-transparent approach by obtaining the flux multiplication factor based on an energy balance as follows:

$$\text{FMF} = \frac{P}{\sum_{i=1}^{n}\sum_{j=1}^{m_i} N_{ij}\left[\int \sigma_{ij,f}(E)\phi_i(E)dE\right]V_iQ_j} \qquad (2-20)$$

where P = total power of the system

N_{ij} = the number density of actinide j in active cell i

$\sigma_{ij,f}(E)$ = fission cross section of actinide j in active cell i

$\phi_i(E)$ = spatial-average neutron spectrum in active cell i

V_i = volume of active cell i

Q_j = recoverable energy for actinide j calculated from an equation consistent with the ORIGEN2 formulation

m_i = total number of actinides in active cell i

n_i =total number of fissile cells

Equation (2-20) takes only a negligible fraction of CPU time since all quantities involved are readily available during the computational process and is fully compatible with the ORIGEN2 depletion scheme.

ORIGEN Depletion at constant flux option. There are two modes of depletion in ORIGEN, either constant power (IRP in ORIGEN) or constant flux (IRF in ORIGEN), which implies that either power or flux will be constant for each active cell within the time-step. MOCUP and MONTEBURNS use the constant flux depletion option in ORIGEN, MCODE provides both IRP and IRF options, depending on the user's choice. In reality the overall power of the system is usually maintained at a certain level under steady state operations. The constant-power depletion mode can ensure a certain energy production for a given time-step. However, the constant-flux depletion mode cannot guarantee the desired energy production because flux varies during ORIGEN burnup throughout the step at constant power. To ensure a given constant power under IRF depletion, the time-step-average flux is applied through an internal burnup corrector in ORIGEN, proposed by Hejzlar in Zhao et al. [2000], as follows:

1. Extract one-group cross sections and flux values from MCNP output
2. Calculate the flux multiplication factor and obtain beginning-of-time-step flux values
3. Execute a trial ORIGEN run with constant beginning-of-time-step flux values
4. Compute the ratio of energy production between rated power and the trial ORIGEN run (average to beginning-of-time-step ratio)
5. Use the average to beginning-of-time-step ratio to correct beginning-of-time-step flux values
6. Re-run ORIGEN with adjusted constant time-step-average flux to obtain final results.

The CPU time running ORIGEN twice per time-step is negligible compared to the MCNP running time, while the accuracy of calculations is improved.

MCNP-ORIGEN coupling method. The coupling between MCNP and ORIGEN deals with the issue of what MCNP-calculated cross sections and fluxes to supply to ORIGEN2 to obtain the best results. Note that the cross sections and fluxes undergo continuous changes during the time-step (macro-step) between two MCNP calculations. MOCUP uses the beginning-of-time-step values. In MONTEBURNS, the mid-time-step approach is deployed, i.e., the middle-of-time-step values are extracted to build the transition matrices to represent the entire time-step.

MCODE provides the option to run in two modes – predictor (P) and predictor-corrector (PC). Predictor mode uses the cross sections and flux values from the beginning of time steps in the same way as MOCUP. In the PC mode, burnup depletion is calculated twice, first using the spectra corresponding to the isotope vector at the beginning of the step to predict isotope composition at the end of the step. The end-of-step vectors are then used in MCNP to evaluate end-of-step fluxes and cross sections, which are supplied to ORIGEN2 to calculate corrected end of time step values. Average number densities from these two calculations are taken as the end-of-step material compositions for the next time step. This standard predictor-corrector algorithm [Kang and Mosteller 1983] is also the preferred algorithm for burnup calculations for all licensing-level reactor physics codes, such as CASMO-4 and HELIOS.

It is obvious that the simple and computationally straight-forward and fastest approach adopted in MOCUP is the least accurate approximation of the three. MCODE in PC mode is the most accurate, especially in cases with strongly non-linear behavior of transition matrices, but the

computationally most intensive approach. MONTEBURNS is a compromise between these two codes offering better accuracy than MOCUP and CPU savings compared to MCODE. However, if eigenvalues at the end of time-steps are required, MONTEBURNS needs to invoke an additional MCNP run per step and its CPU savings disappear. On the other hand, MCODE achieves fairly good eigenvalue histories even at large time-steps and with reduced requirements on statistical precision, which allows substantial CPU reduction.

Because the MCODE-PC approach is the most rigorous method and was shown to yield most accurate results at longer time steps in PWR burnup benchmark studies [Xu et al. 2002], and because of its ease of use and transportability across platforms, it was selected for the best estimate burnup analyses of the ABR core.

Burnup Comparison using MCODE, MOCUP and MONTEBURNS and Code Choice

Burnup calculations of the detailed 1/8th 157FA-core model were performed using all three MCNP-based aforementioned burnup codes. Because the neutron flux across the core is relatively flat and the neutron migration area is large, only two core regions were modeled assuming that each entire region is exposed to a constant region-average neutron flux. Sixty-two fission products and 37 actinides were tracked in MCODE and MOCUP in each region throughout the entire burnup period. MONTEBURNS automatically draws into MCNP the key fission products and actinides based on their fractional importance. If any of the following values: atom fraction, weight fraction, fraction of absorption, and fraction of fission are greater than the value of the "fractional importance", the isotope is included in all transfers from ORIGEN to MCNP through the remainder of the run. The fractional importance was assigned to be 0.1%. All the codes used the same ENDF VI libraries for actinides and the same combination of ENDF-VI and ENDF-V libraries for the fission products, depending on library availability for a particular isotope.

A relatively large number of neutron histories was chosen (300,000 in MOCUP and MONTEBURNS and 600,000 in some MCODE runs) to attain a small MCNP statistical error. The maximum error on neutron flux was less than 0.2%. The error on reaction rates varied from nuclide to nuclide; most of the errors were less than 0.5% and the largest error for the nuclides with very low number density was 1.2%. The time step for the MCNP updates of the cross sections varied between 100 and 400 days.

Figure 2.8 compares the burnup curves calculated for the new core configuration using MONTEBURNS, MCODE and MOCUP. In the interest of clarity, error bars are shown only on the MCODE curve. All the MCODE runs were performed using the flux normalization with the internal
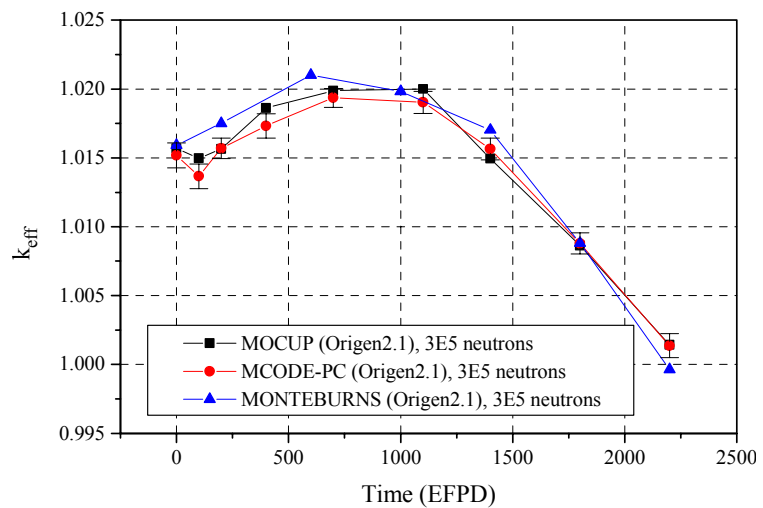
Figure 2.8. Comparison of reactivity burnup curves for 3 MCNP-based burnup codes.

predictor corrector method on macro-step average flux. The "MCODE-PC" curve was calculated with MCODE having the predictor corrector option method turned on. All the codes were run on the same personal computer with 300,000 neutron histories per step using ORIGEN2.1 and MCNP4C. The following observations and conclusions can be made:

1. MCODE and MOCUP results have smaller k_{eff} than that of MONTEBURNS early during burnup (up to 1000 EFPDs), while there is a good agreement at end-of-life.
2. There is a significant difference in the reactivity trend between MONTEBURNS and the other two codes at the end of the first burnup step where the reactivity calculated by MONTEBURNS is increased while the other codes exhibit a small reduction. This can be attributed to the method by which fission products and actinides are brought into MCNP during depletion. MCODE and MOCUP track all isotopes (specified by the user) from beginning-of-life, while MONTEBURNS brings in the isotopes whose weight exceeds a user-predefined importance fraction. Because MONTEBURNS carries less fission products at the end of the first step, the reactivity penalty from fission product captures is smaller. Even though the importance of individual fission products during early burnup is small, the effect of the sum of all fission products on reactivity is noticeable (0.6% of neutron absorptions at the end of the 1st step) resulting in a small reactivity reduction. Another aspect contributing to this discrepancy is the larger time step used by MONTEBURNS because MONTEBURNS does not provide freedom to specify variable time steps throughout the burnup process.

Figure 2.9 compares the MCODE runs in pure predictor and predictor-corrector modes, both with doubled neutron histories to reduce statistical error. The benefit of the predictor-corrector method can be clearly observed, as the unrealistic overshoots and undershoots at times with large curvature changes are eliminated and the burnup curve is smoother.
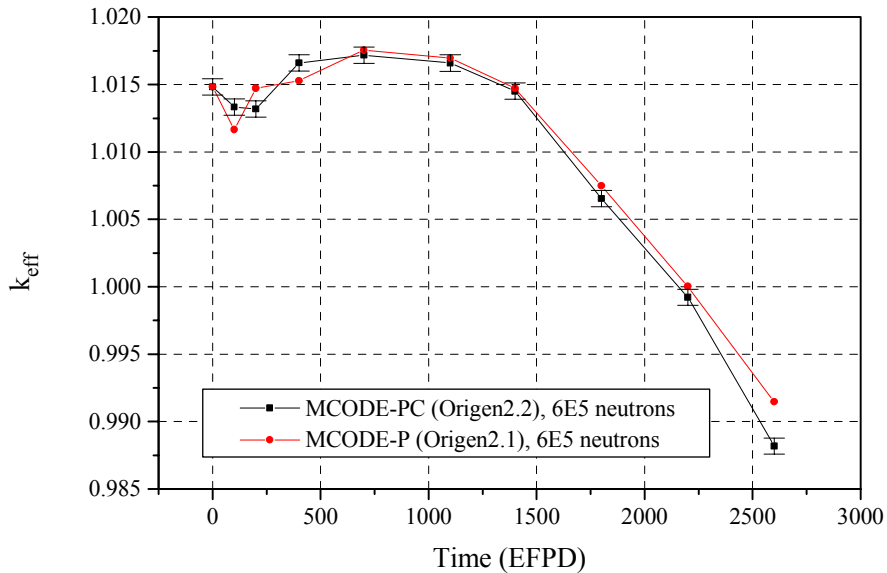
Figure 2.9. Effect of predictor corrector method and improved ORIGEN2.2.

Discrepancies in the mass balance of the fission products have been identified in ORIGEN2.1 for fuels having high transuranic loadings. These discrepancies have been brought to the attention of the code author who provided an updated version with an improved logic for fission product yield tracking. The new version is designated ORIGEN2.2. The difference between the two ORIGEN2 versions can be also seen on Figure 2.9. The ORIGEN2.1 burnup curve agrees well

with the ORIGEN2.2 results until about 2200 EFPDs when it starts to diverge towards higher k_{eff} values. This is because of the higher importance of the fissions from bred-in higher actinides, which did not yield fission products in the original ORIGEN2.1 code, leading to less absorptions in the fission products and thus to higher reactivity. This discrepancy was not seen in earlier LWR benchmarks because most fissions occur in the U-235 and Pu-239 and the contributions from minor actinides are negligible. For fast reactors with large contributions from fissions of even higher minor actinides and high minor actinide loadings, the difference can become appreciable.

Another important parameter significantly affecting the accuracy is the size and distribution of the neutron source. This is especially pertinent to large systems, such as this reactor core. Comparison of the curve "MCODE-PC (Origen2.1), 3E5 neutrons" (3000 neutrons source) on Figure 2.8 with the curve "MCODE-P (Origen2.1), 6E5 neutrons" (6000 neutrons source) on Figure 2.9 shows that the former curve with a smaller number of histories reaches appreciably higher peak reactivity. Since the cases with more neutron histories are more accurate, a 6000-neutron source was selected for final burnup studies. It was also found that a well-distributed neutron source is necessary. This was achieved by running 1000 cycles prior to initiation of the burnup calculations to generate a well-distributed 6000-neutron source, which was then used in the burnup calculations. The same neutron source was invoked in each burnup step. A significant drawback of MONTEBURNS is its inability to start MCNP runs from a previously established neutron source file. Because the source point needs to be specified in the MCNP input, it is difficult to start the run from a well distributed neutron source and 6000-source MONTEBURNS runs starting with fewer original source points were found to yield even higher peak reactivity than the curve "MCODE-PC (Origen2.1), 3E5 neutrons".

MCODE with the predictor-corrector (PC) method turned on and ORIGEN2.2 was adopted for the best estimate calculations because it yields the more accurate results for burnup curves with significant curvature changes, pertinent to this case. Moreover, detailed and rigorous benchmark calculations of MOCUP against CASMO4 on ultra-high burnup LWR lattices at MIT showed that MOCUP tended to over-predict reactivity at higher burnup. The major reason for this discrepancy was identified to be inaccurate prediction of actinide number densities due to the accumulation of small inaccuracies in cross section calculations at the beginning of step, where the spectrum is less representative than for the mid-step conditions. MONTEBURNS with the mid-point strategy was found to yield results significantly closer to those of CASMO4. On the other hand other MIT investigations found that MONTEBURNS tended to over-predict reactivity for fuels with a high fraction of americium because it altered the branching ratio between stable and excited states.

Uncertainties in Minor Actinide Libraries

Because there are significant uncertainties on the cross section data for the minor actinides, which constitute a non-negligible fraction of the TRU loading, the sensitivity of the reactivity burnup curve to different libraries was investigated. Figure 2.10 compares the development of k_{inf} versus burnup using MCODE-PC for two runs of the same case. The first run uses ENDF-VI libraries, the second JEF2.2 libraries.
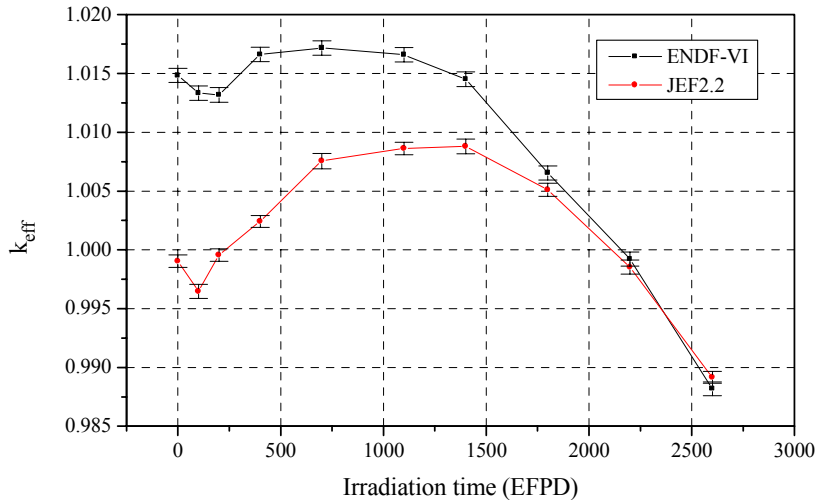
Figure 2.10. The effect of the MCNP library choice on the burnup curve.

The difference in the MCNP results using ENDF-VI and JEF2.2 is remarkable considering that the input data are identical except for library calls. Clearly, the calculations performed for high actinide loadings in hard spectrum reactors have a large uncertainty caused by uncertainties in the nuclear data. One-group actinide cross sections edited from MCNP4C at beginning-of-life are compared in Table 2.6. The statistical uncertainties are also listed and are less than 1%. Therefore, differences between the two libraries larger than 1% are of interest, but primarily those above 10%, which are shaded to emphasize the actinides with the largest differences. The discrepancies for some actinides are huge. The most striking example is the Am-242 ground state where the difference is more than 1000%.

Exploring the reasons for this large disagreement, one is led to conclude that the ENDF-VI cross-section has problems. MCNP4C does not provide this cross section in the basic data set and the one used in the calculations comes from the high flux reactor set of libraries (HFIRXS) generated from ENDF-VI basic data by INEEL for ORNL. Plotting the (n,γ) cross section for this nuclide (see Figure 2.11) shows that the ENDF-VI cross section for this nuclide, which is an earlier evaluation by Benjamin and McCrosson from 1975, was measured only up to 0.01MeV. Since most neutrons in hard spectrum systems are between energies 0.1 and 1MeV, the effective cross section from the MCNP tally is close to zero, which does not reflect reality, but rather the lack of data. JEF2.2 comes from the June 1982 evaluations by Conde and agrees exactly with JENDL3.2. Although, this nuclide is unimportant in reactivity calculations due to its short half-life, ENDF-VI needs better data for Am-242.
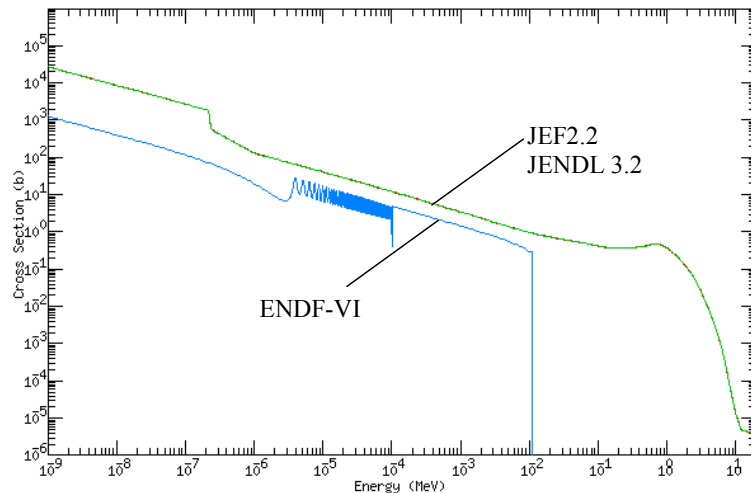
Figure 2.11. (n,γ) cross section plot for Am-242 ground state.

28

Table 2.6. JEF2.2 and ENDF-VI one-group BOL cross sections in outer core region

Nuclide	Xsection designation	JEF Xsection value	Statistical error	ENDF Xsection value	Statistical error	ENDF-JEF %
Th232	SNF[*]	8.13E-03	0.0041	8.42E-03	0.004	3.42
	SNG[*]	2.71E-01	0.0027	2.53E-01	0.0027	-7.02
U234	SNF	3.88E-01	0.0029	3.66E-01	0.0029	-5.96
	SNG	4.83E-01	0.0126	5.02E-01	0.0142	3.75
U235	SNF	1.60E+00	0.0026	1.61E+00	0.0025	0.63
	SNG	3.89E-01	0.003	3.96E-01	0.003	1.82
U236	SNF	1.03E-01	0.0033	9.56E-02	0.0033	-7.27
	SNG	4.39E-01	0.0063	3.32E-01	0.0068	-32.17
U238	SNF	3.71E-02	0.0039	3.60E-02	0.0039	-3.23
	SNG	2.14E-01	0.0029	2.17E-01	0.0029	1.25
Np237	SNF	3.70E-01	0.003	3.49E-01	0.003	-6.02
	SNG	1.12E+00	0.0031	1.14E+00	0.003	2.12
Pu238	SNF	1.15E+00	0.0025	1.11E+00	0.0025	-3.35
	SNG	3.88E-01	0.004	5.44E-01	0.0034	28.73
Pu239	SNF	1.69E+00	0.0024	1.67E+00	0.0024	-1.44
	SNG	3.29E-01	0.0032	3.08E-01	0.0033	-6.71
Pu240	SNF	4.21E-01	0.0028	3.98E-01	0.0028	-5.79
	SNG	3.88E-01	0.0035	3.63E-01	0.0035	-7.04
Pu241	SNF	2.16E+00	0.0026	2.16E+00	0.0026	-0.06
	SNG	4.61E-01	0.0032	2.98E-01	0.0039	-54.61
Pu242	SNF	3.02E-01	0.003	2.81E-01	0.003	-7.56
	SNG	3.36E-01	0.0055	3.21E-01	0.0059	-4.66
Am241	SNF	2.83E-01	0.0032	2.74E-01	0.0031	-3.43
	SNG	1.50E+00	0.0028	1.23E+00	0.0029	-21.39
Am242m	SNF	2.71E+00	0.0026	3.29E+00	0.0027	17.51
	SNG	4.09E-01	0.0028	2.46E-01	0.0037	-66.23
Am242	SNF	2.72E+00	0.0026	2.19E-01	0.0063	-1138.43
	SNG	4.99E-01	0.0029	3.23E-02	0.0062	-1444.84
Am243	SNF	2.20E-01	0.0033	2.14E-01	0.0032	-2.75
	SNG	1.26E+00	0.0036	1.07E+00	0.0036	-17.76
Cm242	SNF	6.56E-01	0.0026	1.54E-01	0.0033	-326.26
	SNG	3.32E-01	0.0049	2.00E-01	0.0072	-65.79
Cm243	SNF	2.89E+00	0.0029	2.29E+00	0.0031	-25.97
	SNG	1.55E-01	0.0077	1.72E-01	0.0055	9.85
Cm244	SNF	4.86E-01	0.0029	4.52E-01	0.0029	-7.53
	SNG	4.61E-01	0.0121	6.55E-01	0.0068	29.64
Cm245	SNF	2.29E+00	0.0027	1.95E+00	0.0028	-17.20
	SNG	2.33E-01	0.0033	2.41E-01	0.0032	3.33
FISSILE	SNF	1.31E+00	0.0025	1.29E+00	0.0024	-1.57
	SNG	6.19E-01	0.003	5.55E-01	0.0031	-11.53
FERTILE	SNF	5.37E-02	0.0031	5.15E-02	0.0031	-4.36
	SNG	2.66E-01	0.0029	2.53E-01	0.0029	-4.87
ACTINIDE	SNF	2.87E-01	0.0026	2.82E-01	0.0025	-1.99
	SNG	3.31E-01	0.0029	3.09E-01	0.003	-7.09

[*] SNF=σ_f, SNG=σ_c

On the other hand, Am-242m is an important isotope significantly affecting the reactivity burnup curve. The JEF2.2 library yields a 66% larger capture cross-section and 17% smaller fission cross section. Figure 2.12 plots the (n,γ) cross section for this nuclide. JEF2.2 uses a 1982 evaluation by Conde, the ENDF-VI 1978 evaluation by Mann, Benjamin and Howerton. JEF2.2 is closer to JENDL3.2. The plot confirms why the edited one group capture cross sections differ. Although all the major libraries agree well in thermal spectra, there is a large disagreement in hard spectra, which is largest exactly in the energy range applicable to lead-alloy cooled systems.
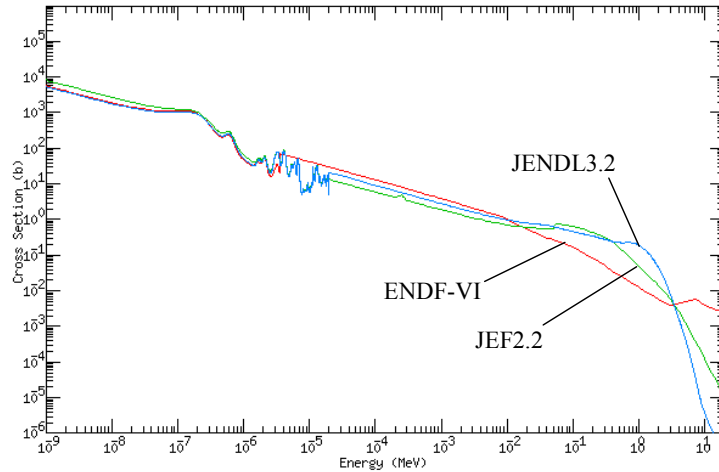
Figure 2.12. (n,γ) cross section plot for Am-242 meta state.

But even the more common nuclides, such as Pu-241 or Pu-238, which one would expect to have very good agreement, are in question. Especially, the 55% smaller ENDF-VI Pu-241 capture cross section compared to JEF2.2 is bothersome. Examining the cross section curves on Figure 2.13 shows that the disagreement arises at high energies, exactly in the range of the neutron peak of a hard spectrum system. The bottom line of Table 2.6 shows that the effective capture cross section of the actinide mix from this benchmark is about 7% higher

Figure 2.13. (n,γ) cross section plot for Pu-241.

than that of ENDF-VI, thus burnup calculations in hard spectrum systems with JEF2.2 libraries will show higher conversion ratios and flatter burnup curves. And this is exactly what happens in Figure 2.10. Most of the cross section discrepancies occur at high energies. The need for improved data and libraries for minor actinides and re-evaluation of other actinides, e.g. Pu-238, Pu-241 at higher energies becomes evident.
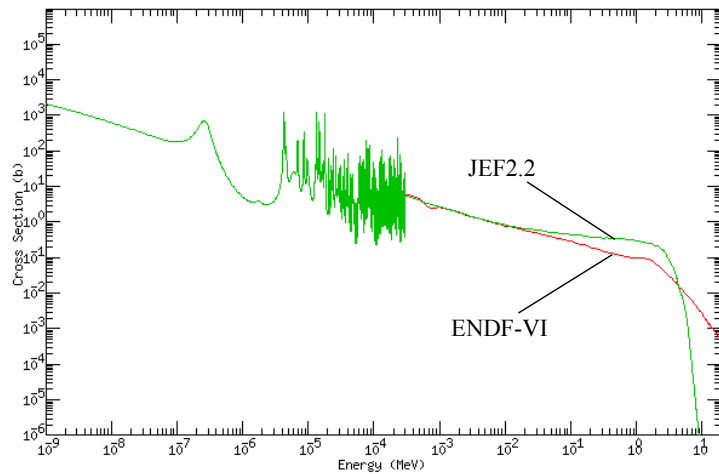
Figure 2.10 shows that the reactivity burnup curve can be flatter with smaller peak reactivity excess, if the JEF2.2 cross-sections are closer to reality. Because good experimental data to benchmark the nuclear data for the minor actinides is not available and the ENDF-VI cross section set yields a larger reactivity swing and peak reactivity excess (and thus higher control rod worth necessary for compensation), the ENDF-VI libraries were used for the burnup calculations in this report. Note that cycle length is not appreciably affected by library use.

30

Cycle Length and Transuranics Destruction Rate

The trace of k_{eff} as a function of irradiation time obtained by MCODE-PC using the ENDF-VI libraries was shown on Figure 2.10. It can be observed that reactivity-limited irradiation time is about 6.3 EFPYs, or 7 years assuming a 90% capacity factor. The maximum excess reactivity of 1.7%Δk/k, or 5.6$, is reached at ~2 EFPYs. The maximum control rod worth will be discussed below, but it is expected that 49 CRDS will yield sufficiently low individual worth to satisfy the requirements on fuel and cladding temperature limits in an unprotected overpower transient (withdrawal of one control rod without scram). The discharge burnup in the inner core region is 120MWd/kgHM, which is well within the established experience for metallic U-Pu-Zr fuels [Hill et al. 1999].

The consumption rate of the individual transuranic isotopes per EFPY is 0.23kg/EFPY. In comparison with the fertile-free actinide burner investigated earlier during this project [Hejzlar et al. 2000, 2001], the TRU destruction rate per MWth is about 36% less. Hence, the penalty of introducing fertile U-238 to denature bred-in U-233 is relatively small with respect to the effectiveness of the actinide burning and relatively high TRU burning rates can still be achieved. It is instructive to compare this TRU consumption rate with that of an ATW. The accelerator-driven facility designers report destruction of 220kgTRU/y per 840MWt in ATW, or 0.262 kg/y per MWt [Beller et al. 2001]. This compares with 0.23kg/EFPY, or 0.21 kg/y assuming 90% capacity factor for this ABR design. Thus, the destruction rate per year is about 80% of that of ATW. This is a relatively high destruction rate considering the presence of fertile materials and comparing the simplicity of the reactor to the complex accelerator-reactor tandem configuration. Further improvement is possible because a capacity factor of 95% should be attainable in a reactor refueling once in 7 years. A higher capacity factor is an expected advantage of a critical reactor over an accelerator driven system. This is because: (1) the capacity factor of two systems, the accelerator and the subcritical target, which must concurrently maintain operation is less than the capacity factor of one system and (2) current large accelerators experience frequent trips. The latter reason is a key issue to be resolved in further accelerator development because in current high-power accelerators the time between failures is measured in hours or tens of hours, [Eriksson and Piaszczyk 1998].

Finally, it needs to be noted that the above ABR destruction rates pertain to transuranics, i.e., the isotopes with higher atomic number than uranium. However, actinides in the thorium chain, primarily Pa-233, are also generated, hence the net actinide destruction rate will be lower. The difference is small (less than 2%) because of the small amount of Pa-233 and Pa-231. Uranium-233 is not counted as a waste, because it is valuable fissile material, which can be used after separation in LWRs to improve resource utilization. Thus, one possible scenario is a symbiotic operation of ABRs with LWRs by recycling separated uranium from ABRs for use in LWRs, where it would have to be blended with natural uranium due to its relatively high enrichment. Because about 4 tonnes of 12% enriched uranium is discharged from an ABR each 7 years, about 15 ABR units could supply one 1000MWe PWR after blending with natural uranium to about 4% enriched fuel.

Figure 2.14 shows that the 12% proliferation limit on uranium containing U-233 [Forsberg et al. 1999] is reached at about 6 EFPY, which corresponds to the end-of-life. Thus denaturing by 30w/o natural uranium is sufficient. Multiple recycling of spent ABR fuel is not evaluated. Once this option is introduced in the future, the content of the U-238 in the total uranium would have to be further increased to ~40% to satisfy the proliferation index at equilibrium, as shown by Hejzlar in our FY-01 Annual Report [MacDonald and Buongiorno 2001].

Figure 2.14. Proliferation index for fissile uranium.

The plutonium isotopics are significantly degraded from that of the PWR spent fuel vector making it virtually weapons unusable – see Figure 2.15. Especially noteworthy is the very high content of Pu-238 (~6wt%) – a result of β⁻ decay of the Np-238, which is generated upon neutron capture in the Np-237. Also, the fractions of other even numbered isotopes are very high, i.e., 35 and 7wt% for the Pu-240 and Pu-242, respectively.

Figure 2.15. Plutonium vector in the outer core region for fuel with 30w/o U

2.1.2.3. Reactivity Feedbacks and Control Parameters

Doppler Coefficient

The Doppler coefficient of the modified core design was calculated using MCNP4C with the JEF2.2 temperature dependent cross section libraries. The JEF2.2 libraries were selected for this purpose due to the availability of the consistent temperature cross-sections for the minor actinides. Although, the reactivity values for the hard spectrum core differ using the JEF2.2 libraries from those using the ENDF-VI libraries, as shown in the previous section, the value of the Doppler coefficient is not appreciably affected by library use, since it is a relative value

between temperatures. Also, the differences in cross-sections occur primarily at high energies, where there are no resonances. A comparison of the ABR Doppler coefficients obtained from the JEF2.2 and ENDF-VI libraries (using UTXS temperature dependent libraries [Abdelrahman and Abdurrahman 1998]) showed good agreement. The JEF2.2 results at beginning-of-life are shown in Figure 2.16. Because of the limited number of temperatures available in the library set, only two points could be obtained. MCNP-calculated points are linearized average values between two temperatures and assume β_{eff}=0.0030, as calculated in the next section.
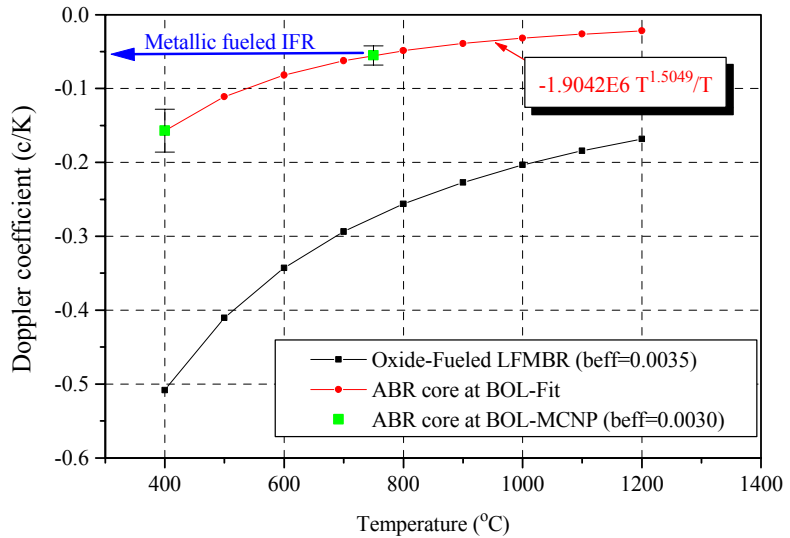
Figure 2.16. Comparison of Doppler coefficient with oxide fueled LFMBR.

In typical LMFBRs, the Doppler coefficient is described by a law of the type [Salvatores 1986]:

$$T \frac{dK_D}{dT} = A T^{-\alpha}, \tag{2-20}$$

where A and α are constants. In practice the Doppler coefficient in a 1200MWe LMFBR with PuO_2/UO_2 fuel varies from ~ -1.2pcm/°C at 400°C to ~ -0.5pcm/°C at 1200°C [Salvatores 1986]. Substituting these values into Equation (2-20), the unknown constants can be calculated to match the Doppler coefficients at temperatures of 400°C and 1200°C. This procedure yields the constants. A = -0.01737 and α = 0.11765. Using Eq.(2-20) with these constants and an LMFBR delayed neutron fraction of 0.0035 yields the Doppler coefficients shown in Figure 2.16 on the curve "Oxide-Fueled LMFBR". A similar fit to MCNP4C–calculated values was performed for an actinide burner core (curve "ABR core at BOL-Fit") yielding constants A = -1.9042E6 and α = 1.5049 to obtain the Doppler coefficient directly in ¢/°C.

The Doppler coefficient for the ABR fuel is negative and about 3 times smaller than that for the oxide core. The smaller magnitude of the Doppler coefficient is consistent with metallic-fueled cores, such as the IFR for plutonium burning where Hill et al. [1995] reported a value of the Doppler coefficient of ~ - 0.05¢/°C. Because the criteria for self-controllability favor small negative Doppler feedback to mitigate the power rise from cooldown scenarios, the small negative Doppler coefficient is preferable to provide, in combination with the negative prompt fuel thermal expansion coefficient and negative coolant void worth, inherent reactor shutdown in the whole spectrum of unprotected accidents.

The Doppler coefficient varies with burnup both due to changes in the fuel composition and due to variations in the effective delayed neutron fraction. Figure 2.17 shows the Doppler coefficients at two temperatures calculated at beginning-of-life, middle of life (B=45MWd/kgHM), and near the end-of-life (B = 75 MWd/kgHM). The JEF2.2 libraries were used in all cases and the fission products that had temperature dependent libraries available were Doppler broadened as well. Note that the burnup shown is core-average burnup and the peak burnup is higher. Except for the case at end-of-life, which exhibits a less negative value at low-temperature and has high uncertainty, the data show that the dependence of the Doppler coefficient on burnup is not significant and can be approximated by the equation given on Figure 2.16.
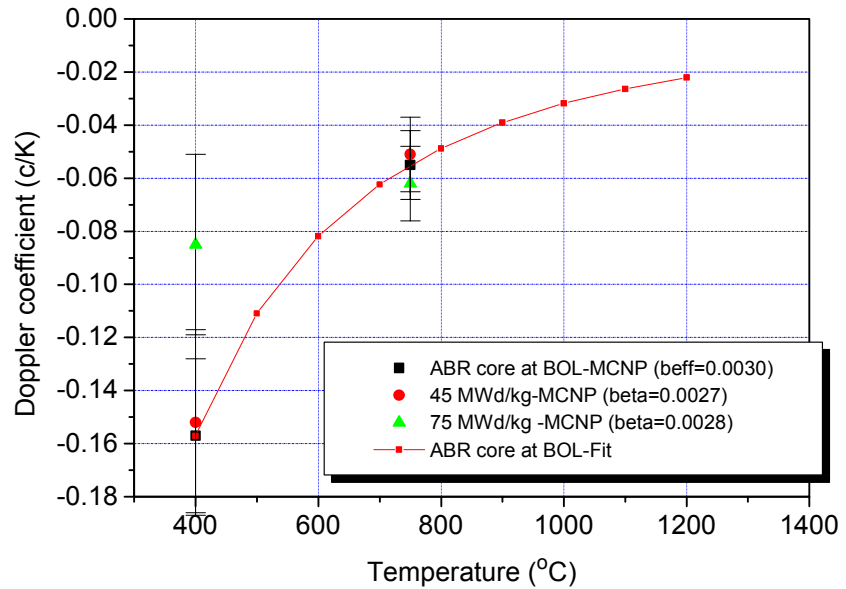
Figure 2.17. Doppler coefficients at various burnups

Fuel Thermal Expansion Coefficient

A full core model was used to calculate the thermal expansion effect. All dimensions and concentrations throughout the core were kept fixed, except for the fuel, which was assumed to elongate its height into the upper gas plenum and increase its diameter. Fuel density change leads to changes in the number densities. To eliminate the effects of fuel temperature variation on other reactivity-related aspects, such as the Doppler coefficient and scattering fuel properties, the fuel temperature was held constant in all calculations. Thus, the analysis yields only the effect of thermal expansion of the fuel. The details of the model were described by Hejzlar in the FY-01 Annual Report [MacDonald and Buongiorno 2001]. The MCNP4C calculations for the modified core design yielded the same value of fuel thermal expansion coefficient as for the original core, i.e., 0.06±0.02c/K.

The above value is applicable to fresh and low burnup fuel, because the calculations assumed an open gap between the fuel and the cladding allowing free movement of the fuel in both the radial and upward axial directions. The lead bond was assumed to be squeezed up into the gas plenum upon fuel expansion. For metallic fuel, after 1 or 2% burnup the metal becomes bound to the cladding and axial expansion is controlled by coolant temperature, not fuel temperature, thus the thermal expansion coefficient cannot be counted as part of the fuel temperature feedback and is taken as zero. It will also be responsible for a reactivity decrease from core heat up, but on a different time scale.

Reactivity changes with coolant density at beginning-of-life, middle-of-life, and end-of-life are plotted in Figure 2.18. In the end-of-life case, a search for criticality through control rod positioning was not performed, hence the eigenvalue at the reference density is above 1.0. The coolant void reactivity worth is negative for the case of voiding of all coolant in the core (see the zero-density point on Figure 2.18) while maintaining coolant outside the core at reference density. If the coolant density is decreased homogeneously throughout the core, reactivity slightly

Figure 2.18. Reactivity response to coolant density changes.

increases for densities down to 6g/cc. The maximum reactivity insertion remains less than 1$ (0.85$). The reactivity peak is the largest at beginning-of-life; and smaller at higher burnups (0.48$ and 0.56$ at middle-of-life, and end-of-life, respectively) due to reduced threshold fissions of the Np-237 and Am-241, which are the principal minor actinides in the initial loading and are gradually transmuted to actinides with higher fission cross sections at lower energies that do not exhibit threshold behavior. Because the largest reactivity insertion occurs at the beginning-of-life, further discussion will be focused on this conservative case.

First, it is important to note that the density of 6g/cc, where the peak reactivity occurs, cannot be effectively reached by coolant heat up, because the density at the boiling point of 1670°C is 8.7g/cc, which corresponds to a reactivity insertion of +0.46$. But even this high temperature cannot be reached because the core structural material and fuel melts at lower temperatures. Assuming that the maximum allowable coolant temperature is equal to the transient cladding temperature limit, i.e. 725°C, the minimum density from the coolant temperature changes is 9.85 g/cc, corresponding to a very small reactivity insertion of 0.08$, or 0.04¢/°C. This is almost 5 times less than the 18¢/°C value cited for a sodium cooled IFR core.

Finally, it is to be noted that although a higher positive coolant temperature coefficient may be feasible from the self-controllability viewpoint, the philosophy adopted for this design was to keep the maximum reactivity insertion below 1$ to constrain power surges during hypothetical scenarios of gas or steam ingress of bubbles into the core, such as from ruptured tubes of the intermediate heat exchanger, when coolant densities in the core might be below those corresponding to the melting point.

Effective Delayed Neutron Fraction
The effective delayed neutron fraction was calculated using the MCNP4C model of the full core to yield at beginning-of-life:

$$\beta_{eff} = \frac{k - k_p}{k} = \frac{1.00191 - 0.99889}{1.00191} = 0.0030 \pm 0.0002 \qquad (2\text{-}21)$$

where k is the eigenvalue obtained with all the neutrons, i.e., both prompt and delayed, and the k_p is the eigenvalue computed using prompt neutrons only. Note that MCNP4C accounts for the different spectra of delayed and prompt neutrons. For consistency, identical libraries accounting for unresolved resonances (61c) were used and the effect of delayed neutrons in prompt criticality calculations was turned off through the TOTNU card.

The above calculations did not incorporate the effect of photo-neutrons produced outside the fuel. Some of these photo-neutrons are produced by delayed gamma rays contributing to the delayed neutron population. Also, some delayed neutrons will be multiplied by the (n,2n) and (n,3n) reactions in the large mass of coolant. However, it is expected that the contribution from photo-production and (n,xn) reactions to the total effective yield will be small.

Table 2.7 compares the β_{eff} of the optimized ABR design at three different burnups with the effective delayed neutron fraction of other fast reactors. At higher burnups, the β_{eff} is slightly reduced as the amount of fissile plutonium decreases and the higher minor actinides with smaller delayed neutron yields build up. The decrease is small, as it is compensated by more fissions from the bred-in U-233, which has a higher delayed neutron yield.

The delayed neutron fraction is less than the values for mixed oxide cores, and also less than the β_{eff} for a conventional metal-fueled IFR core. The streaming core contains a smaller weight fraction of fertile isotopes (U and Th), hence less neutrons are absorbed and fissioned in these nuclides than in an IFR core. Because neutrons from fertile fissions provide an appreciable contribution to the overall neutron population and because yields of delayed neutrons from fissions of these isotopes are high, the delayed neutron fraction is reduced in low fertile content fuel. In addition, increased neutron leakage out of the core in the optimized streaming core is responsible for an increased loss of delayed neutrons, which are more likely to be absorbed in structural materials outside the core in comparison with prompt neutrons. Thirdly, higher actinides, in particular Am-241, have small delayed neutron yields, contributing to a reduced β_{eff}. Therefore, the optimized core exhibits a smaller delayed neutron fraction than in a conventional IFR. On the other hand, a significant improvement in comparison to the pure actinide burner and minor actinide burner designs, investigated earlier, can be observed. Thus, the effect of fertile isotopes proved to be beneficial.

Table 2.7 Comparison of β_{eff} with various fast reactor designs

Reactor	Fuel	β_{eff}	Reference
Super Phenix (France)	UO₂-PuO₂	0.004	Waltar and Reynolds [1981]
CDFR (UK)	UO₂-PuO₂	0.003	Waltar and Reynolds [1981]
SNR-2 (Germany)	UO₂-PuO₂	0.004	Waltar and Reynolds [1981]
Conventional IFR core	Metallic U-Pu-Zr fuel	0.0034	Hill et al. [1995]
Pure Pu burner core	Metallic Pu-28Zr + Hf-26Zr fuel	0.002	Hill et al. [1995]
Pure MABR	Pu-Ma-Zr	0.0021	
Optimized ABR-BOL	**U-Th-Pu-MA-10Zr**	**0.0030±0.0002**	
Optimized ABR-MOL	**U-Th-Pu-MA-10Zr**	**0.0027±0.0002**	
Optimized ABR-EOL	**U-Th-Pu-MA-10Zr**	**0.0028±0.0002**	**-**

Control Rod Worth and Driveline Expansion

Because the reactivity swing is relatively small, the total control rod worth is low, and all the control rods are inserted from the top, the design must ensure that the rod worth is less than β and that ejection of more than one rod is prevented. Therefore, each of the 49 control rods has one control-rod with a separate drive. The maximum control-rod worth is a key parameter, which determines the reactor response to overpower transients and thus needs to be calculated with reasonable accuracy.

The average control-rod worth can be calculated using the peak reactivity excess at 700EFPDs from the ENDF-VI burnup curve on Figure 2.10. The peak reactivity excess at that time is 5.6$, hence the average inserted worth of one control rod is 5.62/49 = 0.12$. The maximum control-rod worth can be estimated by assuming that its location is in the assembly with the peak flux using a neutron flux peaking of 1.234 from Figure 2.6. Per one-group perturbation theory, taking control rod worth proportional to flux squared yields 0.17$. However, this is only an approximate estimate since neutron flux peaking may be different at 700EFPDs, when the peak reactivity occurs and neutron importance at a particular location can be different. To calculate a more realistic maximum control-rod worth, a more rigorous approach was adopted. Using MCNP4C input with the fuel composition at 700EPFD (corresponding to a core-average burnup of 28.5MWd/kgHM), all 49 control rods were inserted into the core to a height that yields criticality (49cm from the core top). The neutron flux and power distributions were calculated to identify the control-rod location exposed to the highest neutron flux. Figures 2.19 and 2.20 show the power and flux distributions, respectively. The results are summarized in Table 2.8. Both peak flux and power occur in the central assembly, thus the control rod in the central box of this assembly will have the highest worth. Then the control rod at this location was withdrawn and the core eigenvalue calculated. By comparing reactivities prior and post control-rod withdrawal, the maximum control-rod worth was calculated. The change of peaking due to control-rod withdrawal is also shown to quantify the magnitude of local power peaking

▨ Fuel assemblies 19.7wt% Pu+MA	Core with streaming fuel assemblies	
▨ Fuel assemblies 23.7wt% Pu+MA	Total number of FAs 157	
Statistical error +/-0.003	Number of fuel rods per FA 312	
	Number of control rods 49	
	Equivalent core OD 2.92m	
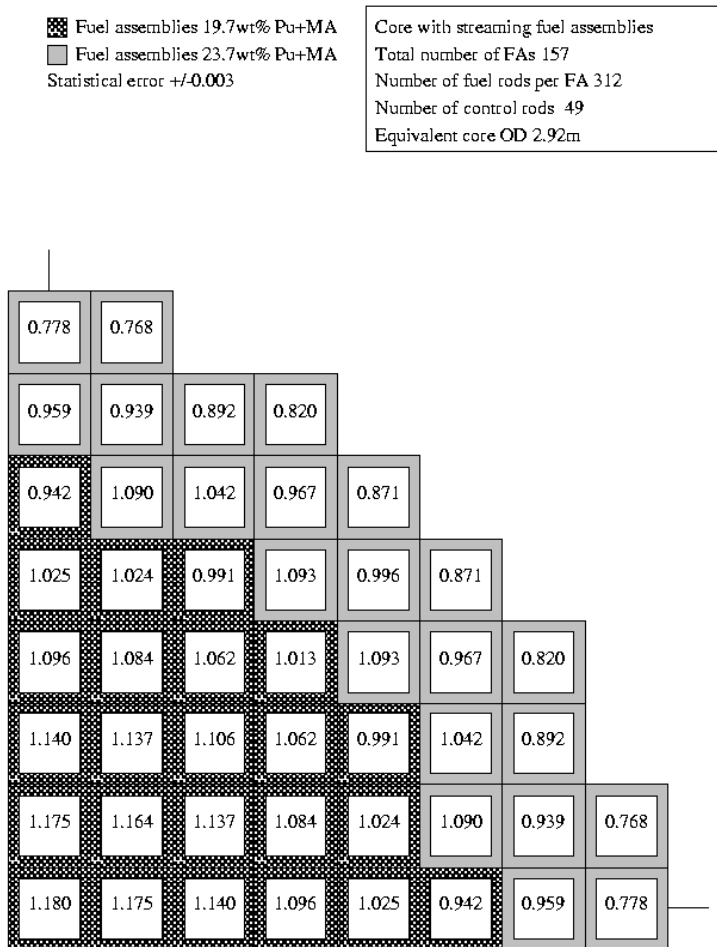
Figure 2.19. Power peaking at the time of reactivity peak (700EFPDs).

37

increase after the control-rod with the maximum worth is withdrawn.

Table 2.8. Maximum control-rod worth.

Statepoint	k_{eff}	Radial power peaking
Reference case at 700 EFPDs	0.9993±0.0002	1.180±0.003
After control-rod withdrawal at 700EFPD	0.9999±0.0002	1.204±0.002
Maximum control-rod worth at 700EFPD	0.20$±0.06$	N/A
Control-rod worth at end-of-life	~0	N/A
Control-rod worth at beginning-of-life	0.17$±0.06$	N/A

Table 2.8 shows that the value of control-rod worth is 15% higher than the crude estimate above, but because of a large statistical uncertainty, it lies within the uncertainty range. A higher control-rod worth is not surprising, since the control-rod is located in the core center where the neutron importance is the highest and the flux peaking at this location is slightly larger than at beginning-of-life. The maximum control rod worth calculated by the more tedious and time-consuming approach using a detailed MCNP model was adopted for use in the evaluation of the S3 criteria. The control rod worth varies during the cycle. Beginning-of-life control rod worth calculated by the above rigorous method is given in the last line of Table 2.8. At the end-of-life, all the control-rods are pulled out of the core and the maximum inserted rod worth is about zero.

The results from Table 2.8 confirm that the maximum control-rod worth remains well below 1$. Thus, ejection of one control-rod does not lead to prompt criticality. Moreover, to eliminate control rod ejection of control-rods that are lighter than the heavy LBE coolant, a system of control-rods moving from the top into the central void region were employed. This eliminates design complications and prevents control-rod expulsion by the LBE coolant, which has a 5 times higher density than boron carbide. In the case of a hypothetical decoupling of a control-rod from its drive, the rod will drop by gravity into the fuel assembly central voided region and shut down the reactor. The only credible accident is thus an inadvertent control rod withdrawal, which can be handled by the inherent reactor reactivity response, if the S3 criterion is satisfied.

The control-rods in the central box depend on cooling by radiation and gas natural
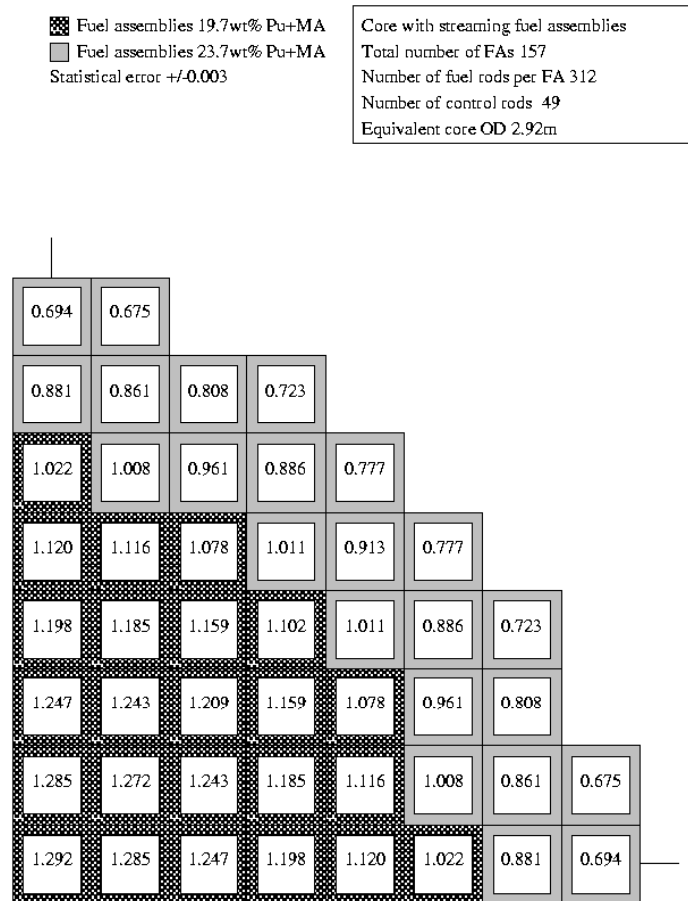
Figure 2.20. Neutron flux assembly peaking at the time of reactivity peak (700EFPDs)

convection between the rod array and the box wall, which is cooled on the other side by the LBE flow. Because these cooling modes have inherently low heat transfer rates, the feasibility of control-rod cooling by radiative and convective heat transfer to the central box wall needs to be established early in the design stage. Boron carbide control rods are primarily heated by neutrons. MCNP calculates a neutron heating of the boron carbide in the core region of 750W/m per absorber pin (finger). Considering the additional heating in the HT-9 cladding of the control rods, we will assume that 1000W/m needs to be removed from the control-rod fingers.

A simple conservative analysis will neglect convection contributions and multidimensional radiation effects. Then the heat flux by radiative heat transfer can be estimated from the radiation equation between two infinite plates:

$$q'' = \frac{\sigma \left(T_{rod}^4 - T_{wall}^4 \right)}{1/\varepsilon_{rod} + 1/\varepsilon_{wall} - 1.0} \tag{2-22}$$

This equation is plotted for a fixed box wall temperature of 550°C and emissivities typical for HT-9 steel in Figure 2.21 as a function of control-rod cladding temperature. Because the control fingers have a small diameter and a relatively large pitch, nearly their entire circumference can see the cooled wall of the central streaming channel. Nevertheless, we will conservatively assume that only 2/3rds of the control-rod finger periphery directly sees the walls. Then the required heat flux to dissipate the linear heat rate of 1000W/m is, for a 5mm OD, only 96kW/m^2. Figure 2.21 shows that this heat flux can be radiated to the cooler wall at a control-rod cladding temperature of 1100°C. Since the melting

Figure 2.21. **Radiative heat flux versus control-rod clad temperature.**

point of boron carbide is 2350°C and the melting point of steel is 1450°C, the cooling of control rods is feasible, especially if the convection contribution and 3-D view factors are considered. Also, it is possible to use control-rod cladding material with a higher temperature melting point. Thus, it can be concluded that although more detailed calculations are necessary in the future, the above conservative estimate confirms the feasibility of cooling the control fingers through radiation and convection in the central box enclosure.

Another important parameter affecting reactivity feedback involves reactivity changes introduced by the control rod driveline expansions. The control rod guide tubes penetrate the coolant above the core, which upon heatup transfers the heat to the control rod drivelines and these thermally expand further into the core, reducing reactivity. Although the time scale is slower than the fuel temperature feedback because the heat transfer path goes though cladding, coolant, and control-rod guide tube with gas gap, the feedback needs to be considered. During transients with a power increase, control-rod driveline expansion leads to a reactivity reduction while in cool-down scenarios an increase in reactivity can occur.

A schematic of control-rods with their drivelines and key dimensions for the situation of the maximum control-rod insertion (at 700EFPDs) is shown in Figure 2.22. If the drivelines are made of stainless steel with a linear expansion coefficient of 12×10^{-6} m/m/°C (a typical value), the elongation of the top-entry control-rod drives for a temperature change of +500 °C can be calculated to be +3.8cm – see Figure 2.22. This scenario was simulated through inserting all 49 control-rods into the core by this amount yielding the multiplication factors shown on the right side of Figure 2.22. The reactivity is reduced by 0.5\$ resulting in a control-rod driveline expansion coefficient of -0.1 ± 0.01¢/°C.

Figure 2.22. Schematic of a control-rod with its driveline showing the thermal expansion after heatup to 500°C. The values for stainless steel are on the right and the values for Invar are on the left.

An alternative material with much smaller thermal expansion coefficient is Invar® Fe64/Ni36 alloy, which has a coefficient of thermal expansion of 1.2×10^{-6} m/m, resulting in an expansion of only +0.38cm and a correspondingly smaller control-rod driveline expansion coefficient of –0.01¢/K, as indicated on the left side of Figure 2.22.

2.1.2.4. Self-Controllability Characteristics for the Modified Core Design

Once all reactivity feedbacks have been established, reactivity coefficient ratios can be calculated and compared to the S-criteria for a self-controllable reactor. Individual reactivity coefficients and coefficient ratios for the modified ABR design at beginning-of-life, middle-of-life, and end-of-life are compared against the typical ratios of a metallic fueled IFR in Table 2.9.

Table 2.9. Self-controllability characteristics for modified ABR design.

	Doppler	Fuel expansion	Coolant density	Rod driveline	Radial expansion	Coolant ΔT (K)	Fuel ΔT(K)
Expressions for reactivity coefficients [Wade and Chang 1988]							
A (¢) =	$(\alpha_D$	$+ \alpha_e)$					x ΔT_f
B (¢) =	$(\alpha_D$	$+ \alpha_e$	$+ \alpha_{Co}$	$+ 2\alpha_{RD}$	$+ 2\,\alpha_R)$	x $\Delta T_c/2$	
C (¢/K) =	$[\alpha_D$	$+ \alpha_e$	$+ \alpha_{Co}$		$+\ \alpha_R)]$		
Typical IFR values for1800MWth core [Wade and Fujita 1989]							
	-0.12	-0.09	+0.18	~0	-0.22 (α_R)	150	150

IFR values for α_{RD}=~0¢/K: A=-31¢, B=-35¢, C=-0.25¢/K; **A/B = 0.88<1, CΔT_c/B = 1.1** $\in \langle 1;2 \rangle$

IFR values for α_{RD}=-0.078¢/K: A=-31¢, B=-47¢, C=-0.25¢/K; **A/B = 0.7<1, CΔT_c/B = 0.8** $\notin \langle 1;2 \rangle$

	Doppler	Fuel expansion	Coolant density	Rod driveline	Radial expansion	Coolant ΔT (K)	Fuel ΔT(K)
Values for optimized ABR with fertile fuel (700MWth core)							
BOL	-0.055	-0.06	+0.03	-0.01(-0.1[†])	-0.18[**]	92	90
MOL	-0.051	~0[*]	+0.02	-0.01(-0.1[†])	-0.18	92	90
EOL	-0.085	~0[*]	+0.04	~0	-0.18	92	90

	A(¢)	B(¢)	C(¢/K)	$\Delta\rho_{TOP}$(¢)	S1:A/B	S2:CΔT_c/B	S3:$\Delta\rho_{TOP}$/B
BOL	-10	-22 (-30)	-0.27	17	**0.47** (0.35)	**1.14** (0.82)	**0.69** (0.57)
MOL	-5	-19 (-27)	-0.21	20	**0.24** (0.17)	**1.03** (0.71)	**1.06** (0.73)
EOL	-8	-19	-0.23	~0	**0.41**	**1.11**	**~0**
Required range for optimized ABR					**<1.25**	**1.0≤ ≤1.8**	**<1.25**

[*]Metallic fuel bound to clad and axial expansion is controlled by coolant temperature, not fuel temperature, thus thermal expansion coefficient is taken to be zero.

[**]Core radial expansion coefficient was evaluated only at beginning-of-life, because the changes with burnup are expected to be less than the uncertainties of the simplified model.

[†]Values in parentheses are for stainless steel. The base values are for low-expansion Invar® Fe64/Ni36 alloy.

The S1 criterion is easily satisfied throughout the cycle. The satisfaction of the S2 criterion depends on the control rod driveline design. The IFR analyses assumed a control rod driveline expansion coefficient of zero in the cited references [Wade and Chang 1988, Wade and Fujita 1989]. If a zero value is used, both the ABR and IFR easily satisfy the S2 criterion. Stainless steel drivelines give a reactivity coefficient of driveline expansion of –0.1 ¢/K for the ABR and, if this value is incorporated into the calculations (see values in parentheses in Table 2.9), the lower limit of the S2 criterion at beginning-of-life and middle-of-life cannot be satisfied. It is to be noted that if the IFR value of –0.078¢/K [Wade et al. 1997] for control-rod driveline expansion[*] is used in the calculations for the IFR case, the S2 criterion would also fall below the 1.0 limit by about the same amount as for the ABR – see alternative set of reactivity ratios for IFR. Although the negative control-rod driveline expansion feedback is a good safety feature in transients/accidents leading to coolant temperature increase, it hurts in the scenarios with coolant inlet temperature reduction and challenges the lower limit for the inlet temperature coefficient of reactivity. At end-of-life, when all the control-rod drives are withdrawn from the core and the control-rod driveline expansion does not affect the reactivity, the S2 criterion is easily satisfied.

---

[*] This is the smallest value for a very low reactivity burnup swing of 0.45$ only (Case 1 in the above reference).

To reduce the reactivity feedback from control-rod driveline expansion, two possible approaches can be pursued. The first approach is the application of double entry control rods proposed by Hejzlar et al. [2000, 2001], which can be easily designed in such a way that the net reactivity change upon driveline expansion is zero or slightly negative if needed. This is because top-entry control-rod drives are inserted into the core while bottom-entry control-rod drives are withdrawn from the core upon driveline heatup. Because bottom-entry control rods need to be submerged in coolant to rely on buoyancy forces for inherent shutdown in case of hypothetical rod decoupling from the drive, the core design is more complex and hence allows for less fuel pins in the core. The second approach is to employ a special alloy with a small thermal expansion coefficient as the driveline material. The most promising candidate is the Invar® Fe64/Ni36 alloy, which has about a 6 times smaller coefficient of thermal expansion than stainless steel. Using the Invar® alloy significantly increases the coolant inlet temperature coefficient of reactivity, C, so that the S2 criterion is satisfied. This can be observed from the base values in bold type generated for Invar®.

The S3 criterion is satisfied throughout the cycle. It is to be noted these calculations carry a large uncertainty because the minor actinide cross sections are uncertain, and thus uncertainty in peak reactivity during burnup, as demonstrated on Figure 2.10. If JEF2.2 libraries are used, the maximum control rod worth would be even smaller (~ 0.11\$), yielding $\Delta\rho_{TOP}/B=0.40$.

It can be concluded that the above set of reactivity coefficients having small negative fuel temperature feedback together with a small positive coolant temperature reactivity coefficient, small negative control-rod driveline expansion coefficient, and negative core radial expansion coefficient exhibits excellent self-regulating characteristics, making possible reactor inherent shutdown in major transients without scram. This is proved by the analyses of a number of unprotected transients using the ATHENA code in Section 3.2 of this Annual Report.

2.1.3. Decay Heat Calculation

The transient analyses of the new optimized ABR that relies on natural convection for decay heat removal depends on our knowledge of the decay heat after shutdown. The ANS5.1 decay heat curve cannot be used because it is valid for LWRs and gives non-conservative results for fuels with higher actinide content [Smith 2001]. Therefore, a decay heat curve must be calculated for this specific core with a high transuranic loading. The following approach was used to calculate the decay heat of the optimized ABR:

1. Burnup of the reference ABR core with two different enrichment regions was calculated using MONTEBURNS.
2. To obtain conservative results, the fuel composition at the end of the seventh step (rather than at the end of the 6th step, i.e. time of actual discharge) was extracted for each region to be decayed in ORIGEN2.1. This composition corresponds to burnups of 126 and 104 MWd/kgHM for the inner and outer core region.
3. New ORIGEN2.1 libraries, generated by MONTEBURNS reflecting one-group cross sections averaged over each region for all the important fission products and actinides at the end of the 7th step were extracted and supplied to ORIGEN2.1.
4. ORIGEN2.1 was executed to calculate the decay power separately for each region. The individual decay powers were then summed up to provide the total decay heat.

The results are plotted in Figure 2.23, which also compares the decay heat curve against the ANS curve for LWRs. It can be observed that the ABR decay heat is lower early after shutdown and above the ANS curve later. An interesting observation is that there is higher decay heat in the outer core, which has lower burnup, than in the inner core, after 63,000 seconds. This is due to the higher decay heat from the actinides, which become more important than the decay heat from the fission products. Note that the ABR decay heat curve carries an uncertainty caused by the lack of accuracy for some of the ORIGEN2.1 data. For example ORIGEN2 assumes that actinides above Pu-240 have the same fission product yield as plutonium. Because these calculations were performed prior to the availability of the updated ORIGEN2.2, some fission products from minor actinide fissions may be missing. Also, not all 1500 isotopes from ORIGEN2 could be updated with accurate one group cross sections. Finally, it is noted that ORIGEN2 gives conservative results compared to more accurate codes for long-term decay heat calculations [Smith 2001], such as SAS2H.
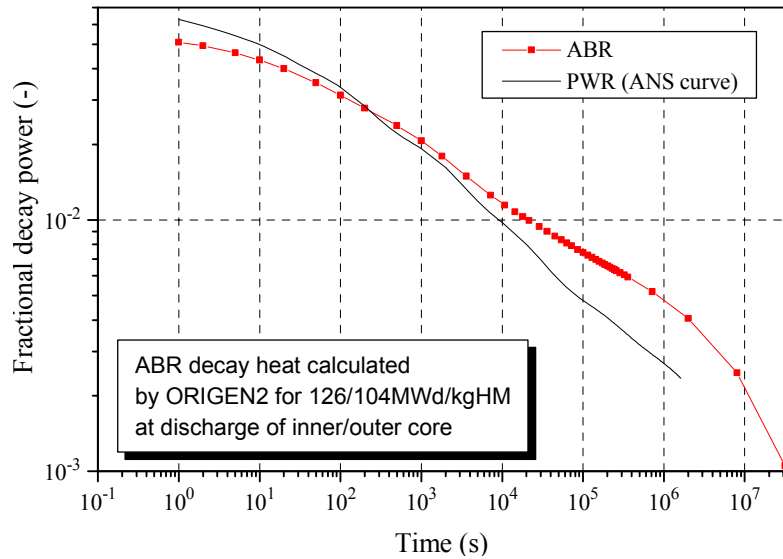
Figure 2.23. Comparison of optimized ABR decay heat curve with ANS decay heat for LWRs.

2.1.4. Fuel Cycle Cost Assessment

So far, the key efforts were directed at the design of the ABR burner to maximize actinide destruction rate and achieve excellent safety. This section will focus on the assessment of the fuel cycle cost, to incorporate the entire fuel cycle into the design. This is especially important because reprocessing of spent LWR fuel and of ABR fuel is known to be costly and the fuel cycle costs can affect the design strategy. Especially, it is of interest to quantify the difference between fuel cycle costs for the once-through and multi-recycle schemes to confirm or dispute the expectation of higher fuel cycle costs of the multi-recycle scheme.

The two options of incorporating an LBE-cooled fast critical reactor (ABR) into the fuel cycle to reduce transuranics from LWR spent fuel are shown in Figure 2.24. The heavy metal flows are based on the burnup calculations of the current reference design. Note the following three points:

- The multi-recycle option allows the elimination of virtually all transuranics while the once-through concept destroys only about 32% of the TRUs initially loaded; the remaining 68% is transferred to interim storage or a repository.

Multi-Recycle Scheme – Heavy Metal Material Balances On 7-Year Basis

Spent Pu-MA-U-Th-Zr+FPs fuel, **15.84MT heavy metal (7.97MT Th, 4.0MT U, 2.81MT TRU)**

1.13 MT
Th

Reprocessing facility

4.18 MT
Pu+MA

Pu-MA-
U-Th-Zr

Fabrication

ABR
700 MWth

Spent LWR
fuel storage

Th,U, Zr

U+Pu+MA+FP,Zr

136 MT HM
1.36MT TRU
134.5MT U

13.0 MT
Th+U
3.9MT U

4.18 MT TRU
17.2 MT HM
9.1MT Th
3.9MT U

1.36 MT TRU
burned

LLFPs

SLFPs

LWR

134.6 MT U

Repository

ABR = LBE cooled Actinide Burning Reactor
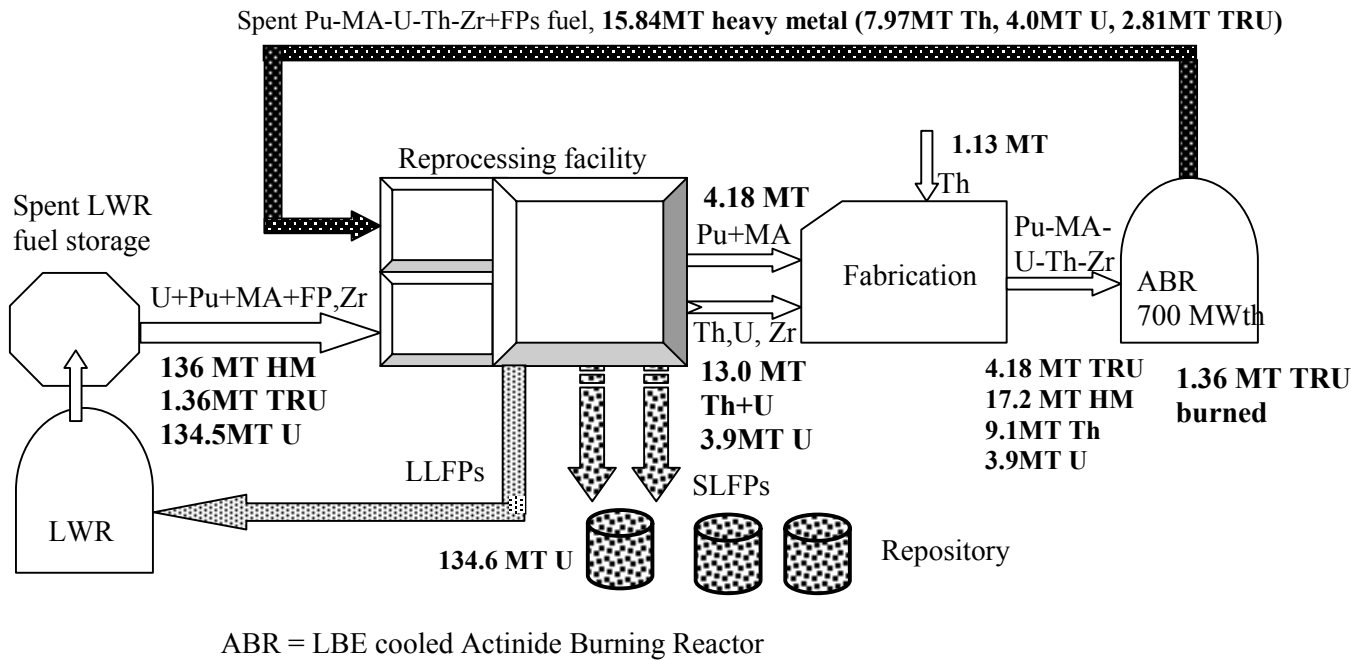
Once-Through FR Cycle Scheme– Heavy Metal Material Balances On 7-Year Basis

4.18 MT TRU
17.2 MT HM
9.1MT Th
3.9MT U

9.1 MT
Th

Reprocessing facility

4.18 MT
Pu+MA

Pu-MA-
U-Th-Zr

418 MT HM
4.18MT TRU
413.8MT U

Fabrication

ABR
700 MWth

Spent LWR
fuel storage

U+Pu+MA+FP,Zr

U, Zr

fuel

3.9MT U

FPs

409.9 MT U

Spent fuel – Pu+MA+U+Th+Zr+FPs

15.84MT HM (7.97MT Th, 4.0MT U, **2.81MT TRU)**

LWR

Storage and/or
repository
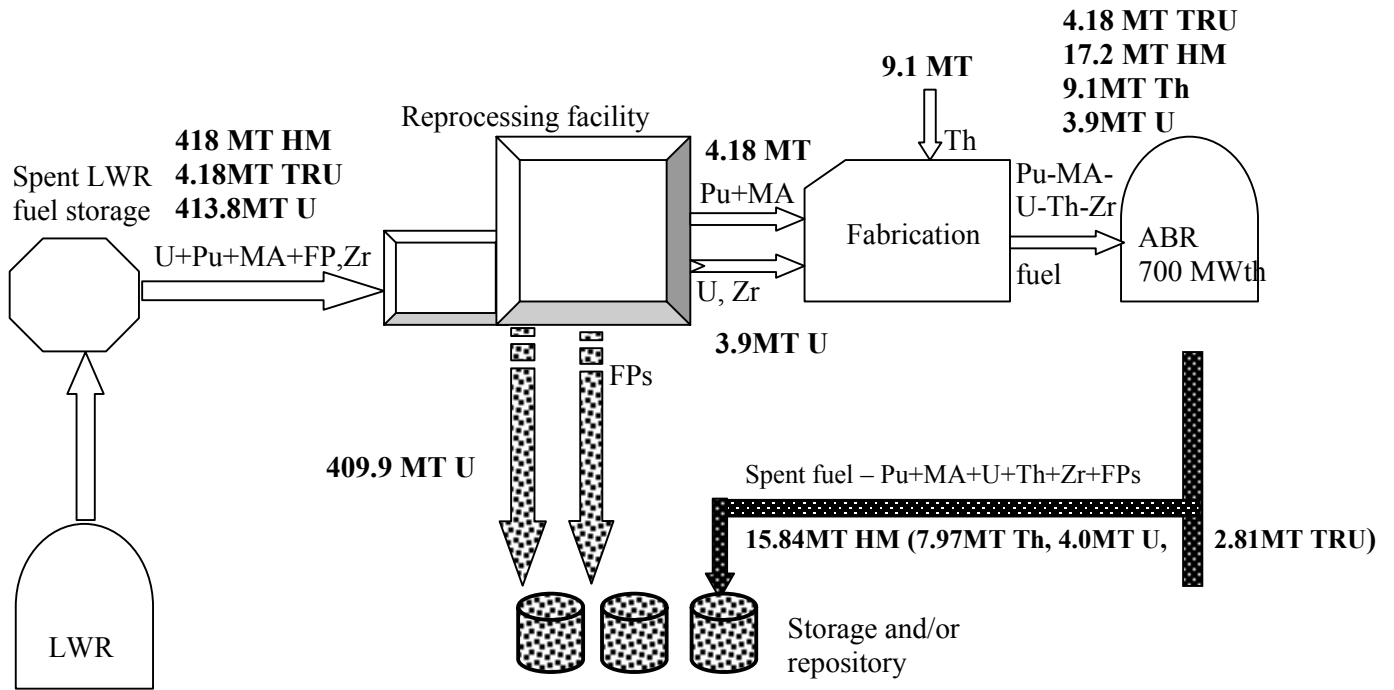
Note: ~ 3 x higher LWR spent fuel removal rate per ABR

Figure 2.24. Fuel cycle schemes and mass flows for LBE cooled fast burners.

- The once-through option consumes (per 1 ABR pass of 7 years) 3 times more TRUs from the LWR spent pool inventory (4.18 MT vs 1.36MT), hence 3 ABRs will have to be run in parallel in the multi-recycle option, if the basis for comparison is the same amount of TRUs removed from the spent LWR fuel inventory pools per unit time.

- The ABR calculations were not optimized for the multi-recycle option, hence the mass flows are just illustrative. Of particular concern is the uranium composition, which with multi-recycling will increase the U-233 content, requiring an increase of natural uranium denaturant in the ABR loading, hence reducing the TRU burnup capabilities. The U-233 content limit can probably be relaxed on the basis that the ABR will be at the same site as the reprocessing facility and diversion is difficult. The multi-recycling scheme where U-233 remains below 12% in the equilibrium core will require larger heavy metal flows, increasing the fuel cycle costs, thus the comparison shown here is optimistic for this mode.

Two approaches were used for the fuel cycle cost estimates. In the first approach, the unit costs are based on the accelerator-driven facility capital and O&M cost estimates published in Smith et al. [1999] using the same procedure for cost evaluation as Driscoll and Kim [2000]. In the second approach costing guidelines adopted for the Generation IV Roadmap project [Generation IV Roadmap, 2002] were employed. In both cases, a simplified estimate that assumes that the spent LWR fuel reprocessing, fabrication, and ABR fuel reprocessing occur at the same time just prior to fuel loading to the ABR (no lead time) is used, which is sufficient for comparative purpose at this stage. A comparison with accelerator-driven facility fuel cycle cost is also made.

2.1.4.1. Approach Using Accelerator-Driven Facility Data

Table 2.10 extracts capital and operating costs for the reprocessing and fabrication plants involved in extraction of the TRU waste from the LWR spent fuel, fabrication of the ABR fuel, and reprocessing of the latter, using the Smith data. To maintain consistency with the capacity of the reprocessing facility for which the cost estimate is given (175 MTHM/yr from LWR spent fuel), the unit costs are evaluated for 9 ABR units running in parallel, which consume about 170MTHM/yr (136MTHM per 7 years x 9 units=174.9MTHM/yr). The costs shown are for the last (eighth) module deployed to maximize the advantage of learning-curve savings. Up-front design costs and discounted back-end decommissioning costs are neglected, hence the unit costs in Table 2.10 should be optimistic (on the low-end side).

The unit costs in Table 2.10 were calculated as:

$$\$/kg\,(TRU\ or\ HM) = \frac{0.1 \times Capital\ Cost + Operating\ Cost}{1000 \times MT\,(TRU\ or\ HM)/yr}, \qquad (2\text{-}23)$$

where the metric tones (MT) in the denominator were taken from the ABR flow balance rather than from the reference accelerator-driven facility. Thus, *the important assumption adopted in this analysis is that the capital and operating cost of the fuel reprocessing and fuel fabrication complex (with LWR heavy metal throughput that is the same as for the reference accelerator-driven complex) is the same as that of the latter complex.* The main difference from an accelerator-driven facility cycle is that only TRUs are recycled in the system while the ABR recycles TRU with fertiles, where most of the heavy metal consists of Th and uranium.

Table 2.10. Processing plant parameters and mass flows for unit calculation costs.

	Units	LWR REPRO	FUEL FAB	ABR REPRO
The reference accelerator-driven facility reprocessing and fabrication facility				
Heavy metal flows	MTHM/yr	175	0	0
TRU flows	MTTRU/yr	1.82	8.3	6.514
Multi-recycle scheme				
1 ABR unit – flows per 7-year cycle				
Heavy metal flows	MTHM/8yrs	136	17.2	15.84
TRU flows	MTTRU/8yrs	1.36	4.18	2.81
10 ABR units – per year basis				
Heavy metal flows	kgHM/yr	174.9	22.1	20.4
TRU flows	kgTRU/yr	1.7	5.4	3.6
Capital cost[*]	$10^6$$/yr	594.8	280	495
O&M cost[*]	$10^6$$/yr	50.4	80.7	27.6
Unit cost per kgTRU	$/kgTRU	62840	20226	21340
Unit cost per kg HM	$/kgHM	628	4915	3786
Once-through scheme				
1 ABR unit – flows per 7-year cycle				
Heavy metal flows	MTHM/8yrs	418	17.2	0
TRU flows	MTTRU/8yrs	4.18	4.18	0
9 ABR units – per year basis				
Heavy metal flows	kgHM/yr	537.4	22.1	0.0
TRU flows	KgTRU/yr	5.4	5.4	0.0
Capital cost[*]	$10^6$$/yr	594.8	280	495
O&M cost[*]	$10^6$$/yr	50.4	80.7	27.6
Unit cost per kgTRU	$/kgTRU	20446	20226	0
Unit cost per kg HM	$/kgHM	204	4915	0

[*] From Smith et al. [2000]

There is significantly less TRU flow in the ABR reprocessing and fabrication columns for the ABR complex than for the ATW, but significantly higher total heavy metal flow rates. How this difference affects the capital and operating cost could not be quantified from the limited information in the Smith et al. report. Less TRU flow will require less measures to prevent criticality and less activity for shielding. Both these aspects will lead to both capital and O&M cost reduction. On the other hand higher heavy metal flows will tend to increase the cost, although one needs to consider that accelerator-driven facility fuel contains 70% zirconium, which will have to be reprocessed and refabricated. Also note that zirconium is three times lighter than heavy metals, hence the volumetric flow, which is determining for sizing the components, will most likely be even less favorable for an accelerator-driven plant. Accounting qualitatively for these considerations, the capital and O&M costs of the whole complex were assumed to be the same as those of the accelerator-driven facility.

The cost per 1kg of TRU fed to the fabrication facility to run 9 ABRs is compared for both cycles in Table 2.11. It was calculated from the relation:

$$\text{Cost} = [C_{RL} M_{TRU\text{-}LWR} + C_{FB} M_{TRU\text{-}FAB} + C_{RB} M_{TRU\text{-}REP}]/ M_{TRU\text{-}FAB} \tag{2-24}$$

where

C_{RL} = unit cost of TRU recovery from LWR ($/kgTRU)
$M_{TRU-LWR}$ = TRU mass flow through LWR reprocessing branch (kg)
C_{FB} = unit cost of burner fuel fabrication ($/kgTRU)
$M_{TRU-FAB}$ = TRU flow through fabrication facility (kgTRU)
C_{RB} = unit cost of heavy metal recovery from burner ($/kg TRU)
$M_{TRU-REP}$ = TRU flow through ABR reprocessing branch (kgTRU)

Note that to obtain the unit costs, normalization is performed with respect to the TRU throughput through the fabrication facility: i.e. per kg of TRU loaded into the ABR. The total energy produced in a 700MWth reactor during 7 years (7 EFPYs) assuming 45% efficiency and 90% capacity factor is:

(0.9) 7 (365) 24 (1000) 0.45 (700) = 1.7384E10 kW-hr

Dividing the total cost (unit cost x total mass flow through the fabrication facility) and adjusted per 1 ABR unit by the above number yields a fuel cycle cost (direct cost only, without carrying charges), which is also shown in Table 2.11 in mills per kW-hr. The once-through scheme gives a cost benefit of ~30%.

Table 2.11. Cost per 1kg of TRU fed to fabrication facility to run 9 and 27 ABRs (per the same amount of TRU removed from LWR spent fuel inventory).

Multi-recycle scheme (27ABRs)				
Unit costs	C_{RL}[$/kgTRU]	C_{FB}[$/kgTRU]	C_{RB}[$/kgTRU]	Total costs
	62,840	20,226	21,340	
Flows *	$M_{TRU-LWR}$ [kgTRU]	M_{HM-FAB}[kgTRU]	M_{HM-REP} [kgTRU]	
	1,749	5,374	3,613	
Unit cost [$/kgTRU]	20,446	20,226	14,346	**55,018**
Per 27 ABRs [$/kgTRU]	21,030	20,804	14,756	**56,589**
Cost in mills/kW-hr (700MWth, 45% efficiency, 7 Years, Capacity factor 0.9**)** **11.9**				
Once-through scheme (9 ABRs)				
Unit costs	C_{RL}[$/kgTRU]	C_{FB}[$/kgTRU]	C_{RB}[$/kgTRU]	
	20,446	20,226	N/A	
Flows*	$M_{TRU-LWR}$ [kgTRU]	M_{HM-FAB}[kgTRU]	M_{HM-REP} [kgTRU]	
	5,374	5,374	0	
Unit cost [$/kgTRU]	20,446	20,226	0	**40,670**
Cost in mills/kW-hr (700MWth, 45% efficiency, 7Years Capacity factor 0.9**)** **8.8**				

*Per 9 ABRs per year.

The assumption of the same capital and O&M cost for the reference accelerator-driven facility and ABR reprocessing plants based on the same LWR heavy metal throughput does not account for the different mass flows in the ABR fuel reprocessing branch, which may have appreciably different costs due to mass flow differences. Hence, *another assumption was made today basing the cost per kg of TRU equal to that of the reference accelerator-driven facility.* The results for one ABR are shown in Table 2.12. Now the situation is reversed, with the fuel cycle costs of the multi-recycle scheme about 50% less than for the once-through cycle.

47

Table 2.12. Cost per 1kg of TRU fed to fabrication facility to run 1 ABR and 3 ABRs (per the same removed TRU from LWR spent fuel inventory)

Multi-recycle scheme				
Unit costs	C_{RL}[\$/kgTRU]	C_{FB}[\$/kgTRU]	C_{RB}[\$/kgTRU]	
From Driscoll and Kim	60400	13100	11840	
Flows *	$M_{TRU\text{-}LWR}$ [kgTRU]	$M_{HM\text{-}FAB}$[kgTRU]	$M_{HM\text{-}REP}$ [kgTRU]	
	1749	5374	3613	
Unit cost [\$/kgTRU]	19652	13100.00	7959	**40711**
Per 3 ABRs [\$/kgTRU]	19652	13100.00	7959	**40711**
Cost in mills/kW-hr (700MWth, 45% efficiency, 7EFPYs)				**8.81**
Once through scheme				
Unit costs	C_{RL}[\$/kgTRU]	C_{FB}[\$/kgTRU]	C_{RB}[\$/kgTRU]	
From Driscoll and Kim	60400	13100	11840	
Flows*	$M_{TRU\text{-}LWR}$ [kgTRU]	$M_{HM\text{-}FAB}$[kgTRU]	$M_{HM\text{-}REP}$ [kgTRU]	
	5374	5374	0	
Unit cost [\$/kgTRU]	60400	13100	0	**73500**
Cost in mills/kW-hr (700MWth, 45% efficiency, 7EFPYs)				**15.91**

*Per 7 year cycle basis. The accelerator-driven facility costs are on a per year basis, hence future calculations will have to be revised to account for higher carrying charges in this long life reactor, but for comparative purposes it is sufficient now to use only direct costs as both ABR schemes have the same refueling time and are handled on the same basis.

The results show that on a per kgTRU basis the multi-recycling scheme is better by a factor of about two. This is due to the three times larger TRU or heavy metal throughput from the LWR spent fuel through the reprocessing facility. In a once-through cycle, much more TRU is reprocessed per path and only 1/3rd is burned; the rest goes to an interim storage. One can also view it as unnecessarily reprocessing more fuel than is actually burned. In a multi-recycling scheme, reprocessing of burned ABR fuel adds to the expenditures, but because the TRU to heavy metal ratio is much less (1:5 in comparison to 1:1 in LWR fuel), there is less heavy metal flow associated with this reprocessing branch, effectively reducing heavy metal flow through the LWR reprocessing branch. The overall effect is a smaller unit cost.

The other plausible base for comparison is cost per the (same) amount of TRU removed from the spent LWR fuel inventory. To achieve the same LWR TRU destruction rate as one ABR with multi-recycling, ~3 ABRs with a once-through fuel cycle must be run in parallel. This increases the total cost 3 times since the mass flows are tripled, but the unit cost per kg remains the same.

2.1.4.2. Approach using Generation IV Fuel Cycle Cost Guidelines

Recently, the Generation IV Roadmap Fuel Cycle Cross Cut Working Group published unit cycle process costs to be considered for economic calculations of advanced fuel cycles [Generation IV Roadmap, 2002]. The costs are based on consensus values developed by an OECD-NEA Expert Group on Trends in the Nuclear Fuel Cycle and somewhat modified to account for the deliberations of the OECD-NEA Expert Group on Comparison of Fast Reactors and Accelerator Driven Systems in Advanced Fuel Cycles. Key values applicable to the ABR and accelerator-driven facility are extracted in Table 2.13. Note that only major cost components are included; spent fuel transport, repository costs or credits, interim storage costs, and thorium cosst are neglected in this simplified evaluation, as their effect on the total fuel cycle cost is small in comparison to the cost of reprocessing and fabrication of the ABR fuel. Besides the nominal

values, lower and upper bounds per the Generation IV roadmap recommendations are also included. The unit costs for a critical ABR were taken to be the same as those recommended for fast reactor TRU fuels, because the composition of the ABR fuel is very close to that of IFR TRU fuel, except for thorium, which replaces most of the uranium in the IFR TRU fuel. But the difference between the cost of uranium and thorium is not sufficiently significant to affect the results of these ballpark analyses.

Table 2.13. Unit Costs for Advanced Fuel Cycles per Gen IV Roadmap Recommendations.

Component	Lower bound	Nominal cost	Upper bound	Unit
Critical ABR				
Reprocessing of LWR UOX fuel	500	800	1100	$/kgHM
Fabrication of ABR TRU fuel	1400	2600	5000	$/kgHM
Reprocessing of ABR TRU fuel	1000	2000	2500	$/kgHM
Sub-critical accelerator-driven system				
Reprocessing of LWR UOX fuel	500	800	1100	$/kgHM
Fabrication of ABR TRU fuel	5000	11000	15000	$/kgHM
Reprocessing of ABR TRU fuel	5000	12000	18000	$/kgHM

The fuel cycle cost can be expressed in mills per kW-hr levelized as of the start of irradiation:

$$FCC = \frac{C}{8.766\ pL\eta T}\frac{xT}{1-e^{-xT}}\ \text{mills/Kw-hre} \tag{2-25}$$

where C = cost per kg of heavy metal of burner fuel as of the start of irradiation,
η = thermodynamic efficiency (45%),
p = specific power in kW/kgHM,
L = capacity factor, assumed 0.95,
T = in-core residence time, assumed 7years, and
X = discount rate, e.g., 0.1/yr.

The values of cost (C) together with the fuel cycle cost results per Equation (2-25) are summarized in Table 2.14. The results using the fuel cycle expert group data recommended by the Generation IV roadmap report give a higher fuel cycle cost than the estimate based on the accelerator-driven facility costs. Because of the large uncertainties with the application of the accelerator-driven facility costs, which were developed for fertile-free fuels, to the fuels containing fertile material, the costs from Table 2.14 are considered as a more reasonable estimate than the assessments from Tables 2.11 and 2.12. Based on the fuel cycle cost viewpoint, the once-through scheme is not tenable because it has double the fuel cycle cost in comparison with the multi-recycling scheme. As mentioned above, the very high fuel cycle cost of a once-through scheme comes from the three times larger heavy metal throughput from the LWR spent fuel through the reprocessing facility while burning only a small fraction of TRUs per path. Moreover, the radiotoxicity and heat load of the spent ABR fuel in a once-through scheme are significantly higher than that of the spent LWR fuel, thus although the TRU mass from the spent LWR fuel is significantly reduced, the radiotoxicity of the spent fuel from a LWR/ABR system would not be reduced if the radiotoxicity of the spent ABR fuel using the once-through cycle is considered. Therefore, the once-through fuel cycle has to be discarded from future considerations and focus needs to be shifted to the multi-recycle scheme. In addition, an increase of burnup using more batches in a staggered batch fuel management scheme will be pursued to increase the burnup and further reduce the fuel cycle costs.

Table 2.14. ABR Fuel cycle cost estimate using Generation IV Roadmap recommendations.

ABR parameters: L=0.95, T=7years, η=0.45, p=40.7kW/kgHM			
Multi-recycle scheme			
Material Flows [kgHM/7 years]: M_{HM-LWR} = 136000, M_{HM-FAB} = 17200, $M_{HM-ABRrep}$ = 0			
	Lower bound	Nominal	Upper bound
Total unit cost, C [$/kgHM loaded in ABR]	6274.4	10767.4	16000.0
Levelized cost per Eq. (2-23) [mills/kW-hr]	8.6	14.8	22.0
Once-through scheme			
Material Flows [kgHM/7 years]: M_{HM-LWR} = 418000, M_{HM-FAB} = 17200, $M_{HM-ABRrep}$ = 15840			
Total unit cost, C [$/kgHM loaded in ABR]	13551.2	22041.9	31732.6
Levelized cost per Eq. (2-23) [mills/kW-hr]	18.6	30.3	43.6

2.1.4.3. Comparison With Accelerator-Driven Facility Fuel Cycle Costs

Even for the best case with the multi-recycle scheme, a fuel cycle cost of 14.8mills/kW-hr is too high to compete in the current electricity market. Because the ABR design has the additional mission of actinide burning, it is meaningful to compare its fuel cycle cost with the ATW, which has actinide partitioning and transmutation as a primary mission. The accelerator-driven system has 8 units of 840MWt each to burn 169 MT of heavy metal from spent nuclear fuel per year. The accelerator-driven facility parameters and mass flows using recent data by Beller et al. [2001] are given in Table 2.15, together with the fuel cycle cost estimate using the Generation IV Roadmap recommendations and capital and O&M cost data from Smith et al. [2000]. First, it is noted that the nominal fuel cycle cost value agrees well between both approaches. Secondly, it can be observed that the ABR fuel cycle cost in the multi-recycling scheme is slightly below that of the ATW. Thirdly, the fuel cycle costs of both the accelerator-driven facility and ABR are well above current LWR fuel cycle costs, even if lower bound values are used. The need to reduce the reprocessing and fabrication costs of TRU fuels is evident, if both economical electricity generation and actinide burning goals are to be achieved. Future evaluations should also take into account the credit for reduction of LWR fuel disposal costs, which may be high in Europe and Asia, where the cost can be up to 2000$/kg of heavy metal disposed.

Table 2.15. Accelerator-driven facility fuel cycle cost estimate

Accelerator-driven facility parameters: L=0.70, T=1years, η=0.37, p=1145kW/kgTRU Material Flows [kgTRU/yr]: $M_{TRU-LWR}$ = 169000, $M_{TRU-FAB}$ = 5870, $M_{TRU-ATWrep}$ = 4110			
Using Generation IV Roadmap recommendations			
	Lower bound	Nominal	Upper bound
Total unit cost, C [$/kgTRU loaded to ATW]	22896.1	42434.4	59272.6
Levelized cost per Eq. (2-23) [mills/kW-hr]	9.3	17.2	24.0
Using capital cost and O&M cost from Smith et al. [2000] (see Table 2.10) per Eq. (2-21)			
Total unit cost, C [$/kgHM loaded to ABR]		50371	
Levelized cost [mills/kW-hr]		19.4	

2.1.5. Conclusions and Future Work

The concept of a Pb-Bi cooled critical reactor that can destroy actinides from spent LWR fuel while maintaining excellent safety has been proposed and evaluated from the neutronics viewpoint. The analyses were performed for metallic thorium-based fuel (Th-U-Pu-MA-Zr) in a

once-through cycle assuming that the discharged fuel from the ABR remains in temporary storage before multi-recycling is introduced. The major focus of the neutronic analyses in FY-02 was on the design of a core that can achieve self-controllability, as in the IFR. The major conclusions can be summarized as follows:

- Using thorium as a major fertile material is an effective means to reduce the large reactivity swing occurring in fertile-free cores while still allowing high actinide destruction rate per MWth. In addition, thorium use increases the Doppler feedback in comparison with fertile-free fuels and reduces the coolant density reactivity coefficient.
- The ABR destruction rate of actinides per MWth-yr is ~35% less than the destruction rate in the fertile-free critical ABR and only 20% less than in an accelerator-driven facility (due to the higher capacity factor in the ABR). This is a very appealing number considering the simplicity of the proposed reactor versus the more complex accelerator plus reactor system.
- The high coolant void worth typical of minor actinide fuels can be effectively mitigated by the employment of streaming fuel assemblies. Using streaming fuel assemblies with one row of peripheral streaming channels and a central streaming region results in a negative coolant void worth and a very small positive coolant temperature coefficient, which provides very good potential for a design with self-regulation characteristics, similar to the IFR. The streaming assemblies also reduce the power and neutron flux peaking, and thus peak fast fluence.
- The discharged fuel from the ABR satisfies proliferation constraints for both the plutonium and uranium compositions. Plutonium isotopics are significantly degraded from that of the PWR spent fuel vector making it virtually weapons unusable. The 12% proliferation limit on fissile uranium with U-233 content is satisfied if depleted uranium is mixed with thorium with ~30wt% of uranium in the U+Th mixture.
- Both the Doppler and fuel thermal expansion feedbacks are negative and their values are comparable to those for the IFR fuel.
- The combination of the reactivity coefficients satisfies requirements of self-control throughout the cycle so that, in combination with the passive decay heat removal design, all transients without scram lead to inherent shutdown without exceeding safe fuel and structural temperature limits. This has been proven by ATHENA analyses of all major unprotected transients in a separate section.
- All our neutronic analyses are subject to relatively high uncertainties because of the uncertainties in the cross section data at high neutron energies for the minor actinides. More accurate cross section measurements for these nuclides are needed for the more advanced detailed design stage of hard-spectrum actinide burning systems, both critical and accelerator driven.
- The fuel cycle cost of the once-through cycle is significantly higher that that of the multi-recycle scheme. Therefore, considering fuel cycle economics and the small potential for reduction of long-term radiotoxicity and heat load on the repository from the wastes of the LWR/ABR system, the once-through fuel cycle has to be discarded from future considerations.
- In comparison with the ATW, the fuel cycle cost of the ABR in the multi-recycle scheme is slightly smaller, but both the accelerator-driven facility and ABR fuel cycle costs are well above current LWR fuel cycle costs, even if lower bound values are used.

In summary, the proposed design of the 7-year life core for burning transuranics from spent LWR fuel appears to be very promising and deserving of future refined analyses and optimization because it offers high consumption of actinides, excellent safety characteristics, and has the

potential to provide low electricity generation costs due to its modularity, simplicity, and high capacity factor. The only drawback is a high fuel cycle cost, which is inherent to all actinide burning systems at the currently high fuel reprocessing costs.

Future work will focus on the following key areas:

- Replacement of lead-bismuth with lead because: (1) coolant freezing is not of concern in conjunction with use of a supercritical CO_2 balance of plant and the design with its set of reactivity coefficient ratios satisfying the self-controllability criteria makes it possible to avoid coolant inlet temperatures that would lead to coolant freezing, (2) polonium issues are substantially mitigated, (3) lead is less corrosive to structural materials than lead-bismuth, (4) lead is substantially cheaper than LBE, and (5) lead is abundant allowing a large scale deployment of reactors while bismuth resources are limited. The effect of the coolant replacement on the neutronics analyses will be small and beneficial due to the smaller absorption cross section of the lead in comparison with the bismuth. This is expected to reduce the coolant temperature reactivity coefficient and increase somewhat reactivity-limited achievable burnup.
- Transition to multi-recycle fuel cycle. To prove the feasibility of high actinide burning while achieving excellent safety characteristics was a major goal of the first two years of this project. All analyses have been performed for a once-through fuel cycle, which was found to be economically unattractive, after fuel cycle cost data for the advanced fuel cycle became available. In the next phase, it is necessary to optimize the core for multi-recycling of discharged ABR fuel and prove that the excellent safety features are retained for the equilibrium cycle.
- Reduction of fuel cycle cost. Although the ABR fuel cycle cost is slightly smaller than that of ATW, it is still well above the LWR fuel cycle cost. The most effective way to reduce fuel cycle cost is through introduction of cheaper advanced reprocessing technologies, which are beyond the scope of this project, but fuel cycle cost can also be reduced through the ABR neutronic design, primarily by increasing discharge burnup. Therefore, core design and loading optimization will be pursued to explore use of an increased number of batches (smaller fraction refueled per cycle) to increase burnup and thus reduce fuel cycle cost.
- Supercritical-CO2 balance –of-plant. Future investigations should include a detailed design of the supercritical-CO_2 balance-of-plant and analyses of the coupled reactor – balance-of-plant system to prove that the threat of coolant freezing scenario – the main reason for preferring LBE against lead in most lead-alloy cooled concepts - can be eliminated.

2.2. FY-02 INEEL Results – A Qualitative Assessment of Sodium and Lead-Bismuth (Dr. Kevan Weaver)

In previous work, a comparison of Na and LBE coolants in a fast reactor was performed. Using a pin cell, the results published by Weaver in Section 3.2 of our FY-01 Annual Report (MacDonald and Buongiorno 2001) show that:

- The rate of TRU destruction for either coolant is similar for the parameters used (~ 1g/MWd for the fertile-free cases, and ~ 0.5-0.9 g/MWd for the fertile cases).

- However, for equivalent parameters (i.e., TRU loading, P/D, etc.), the LBE cooled cases destroyed up to 5 times more actinides per path through the core than similar sodium cooled cases, and up to 2 times more in the fertile cases. Fluence limits on cladding may not allow for such long in-core residence times.
- The sodium coolant produces a softer spectrum, which decreases the fission-to-capture ratio.
- In order to attain the same reactivity-limited burnup, or effective-full-power days of operation as the lead-bismuth cooled cases, the sodium-cooled cases require a higher beginning-of-life TRU loading.
- The amount of plutonium and its isotopics were degraded in all cases; where the even numbered isotopes (Pu-238, -240, and -242) had higher fractions than at beginning-of-life (resulting in high decay heat and spontaneous neutron rates).

In addition, the use of a tighter or looser lattice will also affect the neutronic performance of the fuel. Tighter lattices will result in a harder spectrum, but may reduce the heat removal capability of the coolant. As well, the choice of coolant will also affect the performance. A qualitative comparison of the pitch to diameter ratio (square) and coolant versus the infinite multiplication factor was performed using a pin cell model. The plutonium and minor actinide constituents are shown in Table 2.16, with the remaining constituents being Zr (fertile free), UZr, ThZr, UN, or ThN.

By only changing the pitch to diameter ratio, qualitative conclusions can be drawn about the fuel performance based on the coolant used. Figures 2.25 through 2.29 show the differences based on coolant.

There are several points to consider with respect to the figures:

Table 2.16. Beginning-of-life TRU composition for all 20 wt% Pu+MA.

Isotope	wt%
Pu-238	0.32%
Pu-239	9.28%
Pu-240	4.16%
Pu-241	1.60%
Pu-242	0.64%
Plutonium Total	16%
Np-237	1.72%
Am-241	1.80%
Am-243	0.36%
Cm-244	0.12%
Minor Actinide Total	4%

1. The steeper slope of the Na cooled cases indicates that sodium cooled lattices iare more sensitive to P/D. As the work presented here is based on square lattices, it would be expected that hexagonal pitch lattices would favor neither. Indeed, the curves indicate that the beginning-of-life reactivity for a typical tight sodium cooled lattice (P/D equivalent of 1.01) corresponds approximately to an LBE-cooled lattice with a P/D of 1.18. Thus,

Figure 2.25. K-infinite versus P/D for non-fertile fuel.

tight sodium-cooled lattices are equivalent in terms of reactivity excess at beginning-of-life to looser LBE lattices.

2. A higher beginning-of-life reactivity is usually an indication of higher burnup potential. However, an optimal lattice for LBE coolant favors looser pitch to keep the pressure drop reasonably small, while a sodium-cooled lattice needs to be relatively tight to keep the coolant void worth in check. By decreasing the P/D, the actual difference in beginning-of-life excess reactivity is small, and would thus favor neither coolant.

3. By choosing Pb-Bi as the coolant, the beginning-of-life fissile loading requirements could be reduced as compared to Na cooled cores for a fixed P/D. If the P/D is optimized for each coolant, TRU loadings would be comparable for both coolants.

4. Thorium based fuels have lower beginning-of-life reactivity, and thus lower burnup potential. However, this may be an advantage by way of lower excess reactivity.

5. It is possible that full core analyses will produce different results based on neutron leakage, but it is highly unlikely if the same parameters (i.e., core geometry, materials, and fuel) are used. Nonetheless,
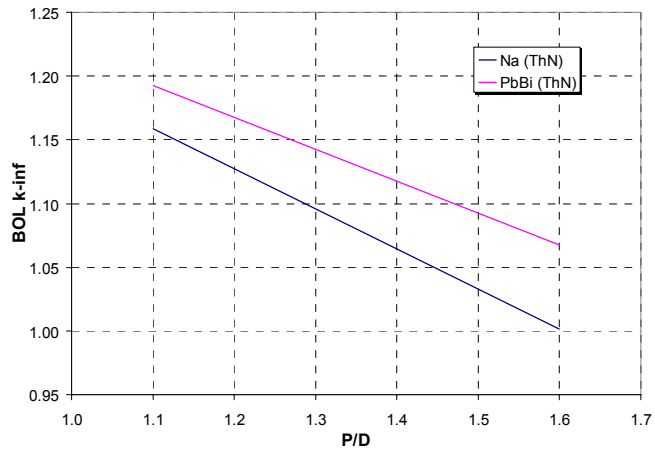
Figure 2.26. K-infinite versus P/D for ThN fuel.
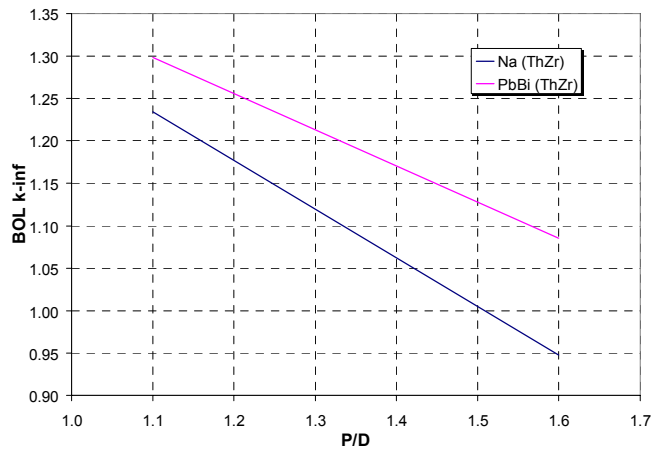
Figure 2.27. K-infinite versus P/D for ThZr fuel.
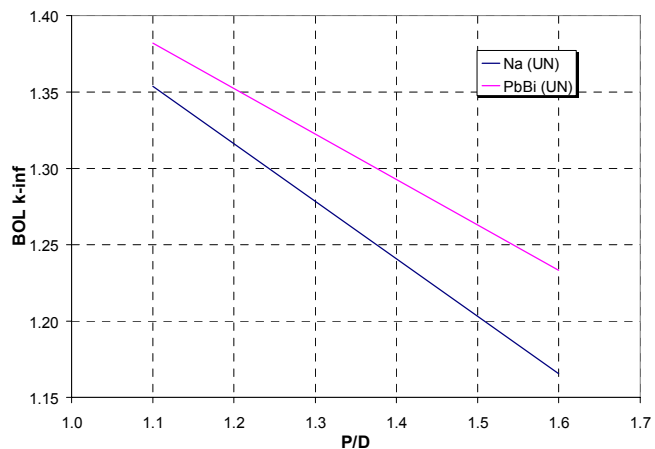
Figure 2.28. K-infinite versus P/D for UN fuel.

54

a few sensitivity studies could confirm this conclusion.

Thus, one can conclude that LBE and sodium-cooled lattices are comparable with respect to TRU destruction rate per MWd, if each lattice is optimized considering neutronics and thermal hydraulic constraints. However, LBE cooled lattices have the potential of achieving higher reactivity-limited burnup, provided that fluence limits on structural materials are not exceeded. The benefit of LBE-cooled systems comes from the smaller coolant void worth, and from better natural circulation capabilities (due to the higher buoyancy force, and the possibility of a more open lattice), thus providing more freedom in the design of a critical TRU burner with passive safety. This claim will have to be proven in future studies.
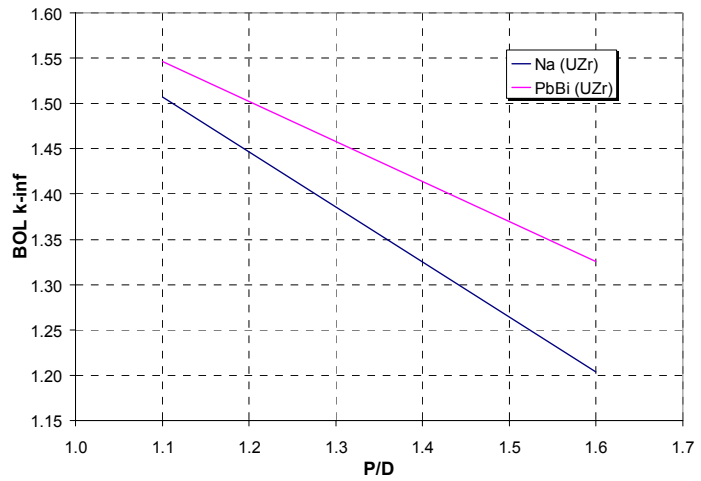
Figure 2.29. K-infinite versus P/D for UZr fuel.

Current and Future Work

Calculations of full core (1/8th reflective geometry) burnup with oxide and nitride fuels are currently being completed. Once the calculations are complete, data on the reactivity limited burnup, discharge isotopics, control rod worth, void reactivity worth, and power profiles (axial and radial) will be extracted and reported.

3. Results of FY-02 Plant Engineering and Economic Studies

3.1. Feasibility of a Gas-Lift Pumping for the Pb-Bi Cooled Reactor (Dr. Jacopo Buongiorno, INEEL)

Forced circulation of the primary coolant in the core of a liquid-metal reactor can be achieved with several different approaches. Traditionally, sodium-cooled reactors have made use of centrifugal pumps similar to those employed in LWRs. More recently, advanced sodium-cooled reactors, like the U.S. IFR, have adopted electromagnetic pumps, which have no rotating parts (Boardman et al. 2000). This is thought to increase the pump reliability, although a substantial penalty is taken on the pump efficiency, i.e., electromagnetic pumps exhibit efficiencies around 40% (GE, 1986) vs. centrifugal pump efficiencies of 85% and higher (Todreas and Kazimi 1990). Centrifugal and electromagnetic pumps are discussed in Section 3.3 of this report.

An alternative way to pump the primary coolant is to artificially lower its density in the region above the core (called the chimney), while maintaining a normal density elsewhere in the primary system (especially in the downcomer). This density imbalance generates a pressure head that drives the coolant flow in the system. For example, this can be achieved by mixing an inert gas with the coolant in the chimney. The low-density mixture rises to the free surface of the reactor pool where the gas separates from the liquid metal. The liquid metal flows back into the downcomer and then to the core, while the gas is compressed and re-injected in the chimney. This pumping approach is known as the gas-lift pump.

In this section the feasibility of a gas-lift pump approach for the Pb-Bi cooled reactor is assessed. The geometry of the primary system assumed for the purpose of this analysis is illustrated in Figure 3.1. The reference lift gas used in the analysis is helium, although analogous results could be obtained with other candidate gases such as argon or nitrogen.

For a 2 m/s velocity in the core the estimated pressure drop around the primary loop is ΔP=715 kPa. With a gas-lift pump approach this head must be provided by the density difference between the chimney and the dowcomer:

$$\Delta P = \alpha \rho g H \qquad (3.1)$$

where α is the void fraction, i.e., the chimney volume occupied by helium, ρ is
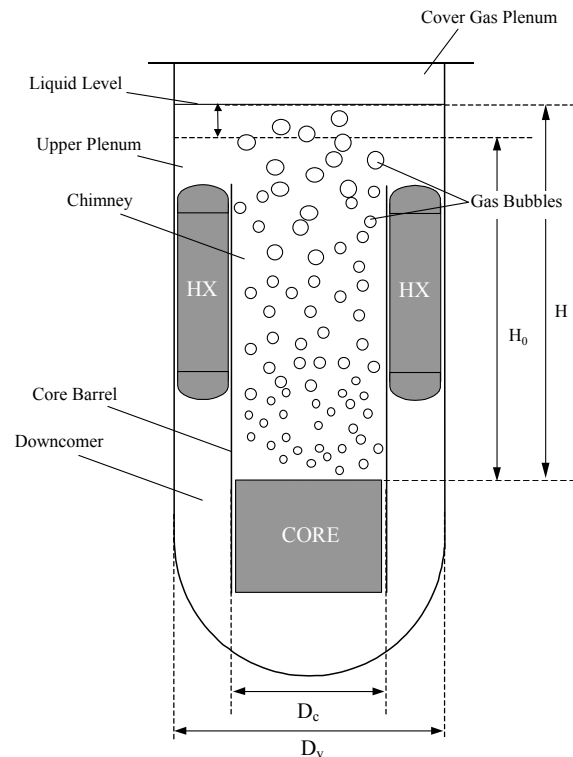
Figure 3.1. Geometry of the primary system.

56

the LBE density, g is the gravity constant, and H is the chimney height measured from the gas-injection point to the free liquid surface of the pool. Note that the free liquid surface swells when gas is injected in the chimney so that the following equations holds:

$$\frac{\pi}{4}D_c^2 H\alpha = \frac{\pi}{4}D_v^2(H - H_0)$$
(3.2)

where D_c and D_v are the chimney and vessel inner diameters, respectively, and H_0 is the chimney height before gas injection. Equations (3.1) and (3.2) constitute a system of two equations with two unknowns, α and H, which can be readily solved to yield:

$$H - H_0 = \frac{\Delta P}{\rho g}\left(\frac{D_c}{D_v}\right)^2$$
(3.3)

$$\alpha = \frac{\Delta P}{\rho g H}$$
(3.4)

For H_0=11.4 m, D_c=3 m and D_v=5.25 m we get H-H_0=2.7 m and α=53%, i.e., gas-lift pumping of the LBE coolant in our case would require generation of a 53% void fraction in the chimney resulting in 2.3 m swelling of the liquid level. Note that such a high value of the void fraction clearly puts the two-phase flow in the chimney outside the domain of a bubbly flow regime. Moreover, such large swelling of the liquid level would require design of a longer vessel, which is in conflict with modularity requirements, increases costs, and makes it more difficult to cope with seismic events.

The gas flow rate required to sustain a 53% void fraction in the chimney was calculated by means of the El-Boher/Lesin correlation developed for void fraction prediction in heavy-liquid-metal/gas two-phase flows (El-Boher et al. 1988). It was found that a helium mass flow rate m=1.6 kg/s is needed. The gas would be injected at the bottom of the chimney at a pressure of about 800 kPa (corresponding to the weight of the LBE column in the chimney) and would rise to the liquid free surface where the pressure is atmospheric, i.e., 100 kPa. From there it is directed to the compressor with a compression ratio equal to 800/100=8, a rather high value, which requires the use of a constant-volume compressor or many axial compressors in series. The compressor power requirements, W, can be calculated by means of the following equation, which assumes ideal gas behavior for helium and an adiabatic compression from P_1=100 kPa to P_2=800 kPa:

$$W = mc_p T\left[\left(\frac{P_2}{P_1}\right)^{\frac{\gamma-1}{\gamma}} - 1\right]$$
(3.5)

where c_p=5.193 kJ/kg·K is the helium specific heat, γ=5/3 is the specific-heat ratio for helium, and T is the compressor inlet temperature. Note that the gas reaches the LBE core outlet temperature because the thermal capacity of the LBE is much larger, thus T=550°C and, from equation (5), W=8.9 MW. However, Equation 3.5 indicates that the compressor power can be lowered if the compression transformation takes place at lower temperature. Obviously, this would require the use of a cooler on the line from the reactor to the compressor. Let's assume that the gas is cooled down to 200°C; in this case T=200°C and Equation (3.5) yields W=5.1 MW. If the coolant were circulated with a mechanical pump, the pumping power, W_p, would be:

$$W_p = m_c \frac{\Delta P}{\rho} \sim 3.8 \text{ MW} \tag{3.6}$$

where m_c is the LBE coolant mass flow rate (54,420 kg/s). It can be seen that the gas-lift pump approach requires significantly more power than the more traditional centrifugal pump.

Finally, the 1.6 kg/s helium mass flow rate corresponds to a 28 m^3/s volumetric flow and to a 3.8 m/s helium superficial velocity at the free liquid surface, enough to entrain considerable amounts of LBE, which would then have to be removed before the compressor inlet.

These results clearly demonstrate that a gas-lift pump approach is not feasible for our reactor. Therefore, this approach will be discarded from further investigation.

3.2. Analyses of Reactor Transients (Cliff Davis, INEEL)

The ATHENA code (Carlson et al. 1986) was used to determine the response of the actinide-burner reactor to a variety of transients, including pump trip, station blackout, reactivity insertion, heat exchanger tube rupture, turbine stop valve closure, steam line break, loss of feedwater preheating, and loss of coolant from the reactor cleanup system. The transients were simulated without reactor scram to demonstrate the safety margins inherent in the reactor design. A summary of results is presented in Section 3.2.10.

The safety margins for the reactor were determined by comparing the maximum calculated temperatures to the transient limits determined by Buongiorno and listed in Section 4.1 of our FY-01 Annual Report (MacDonald and Buongiorno 2001). These transient temperature limits were 725°C for the cladding, 1000°C for the fuel, and 750°C for the guard vessel.

The primary coolant system of the actinide-burner reactor is illustrated in Figures 3.2 and 3.3. Figure 3.3 provides a top view of the vessel showing the core and heat exchanger layout used in the analyses and defines the angles listed in Figure 3.2. (Note that Figure 3.3 shows the FY-01 design and is not the same as Figure 1.2, which shows the current design.) The reactor features a dual-free-level design.
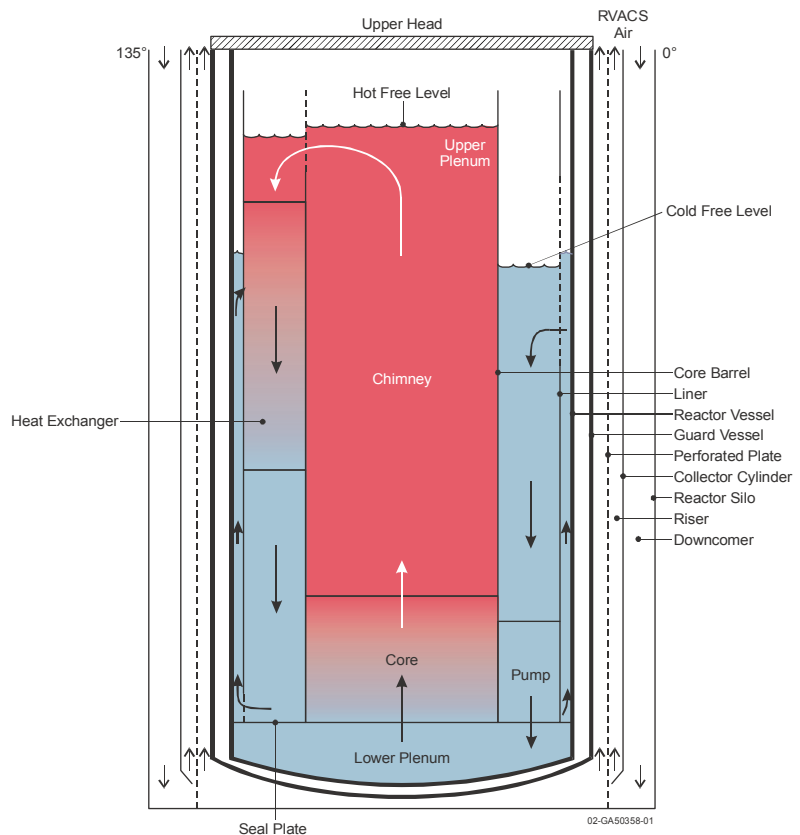
Figure 3.2. Layout of the actinide-burner reactor.

The vessel is separated into different regions by the core barrel, the reactor vessel liner, divider plates, and seal plate. The flow path starts in the lower plenum and extends up through the reactor core and the chimney, which are contained within the core barrel. The upper core barrel contains many large holes that direct the coolant into portions of the annulus between the core barrel and the reactor vessel liner. The upper plenum, which is defined as the region above the first level of holes in the core barrel, below the upper head, and inside the vessel liner, contains the free level of the hot pool. An inert cover gas fills the space between the hot free level and the upper head. The lead-bismuth coolant turns around within the upper plenum, flows through the holes in the upper core barrel, and flows downward through portions of the annulus between the core barrel and reactor vessel liner. This annular region contains four counter-flow heat exchangers. The lead-bismuth flows down on the shell side of the heat exchangers while the secondary coolant flows up on the tube side.
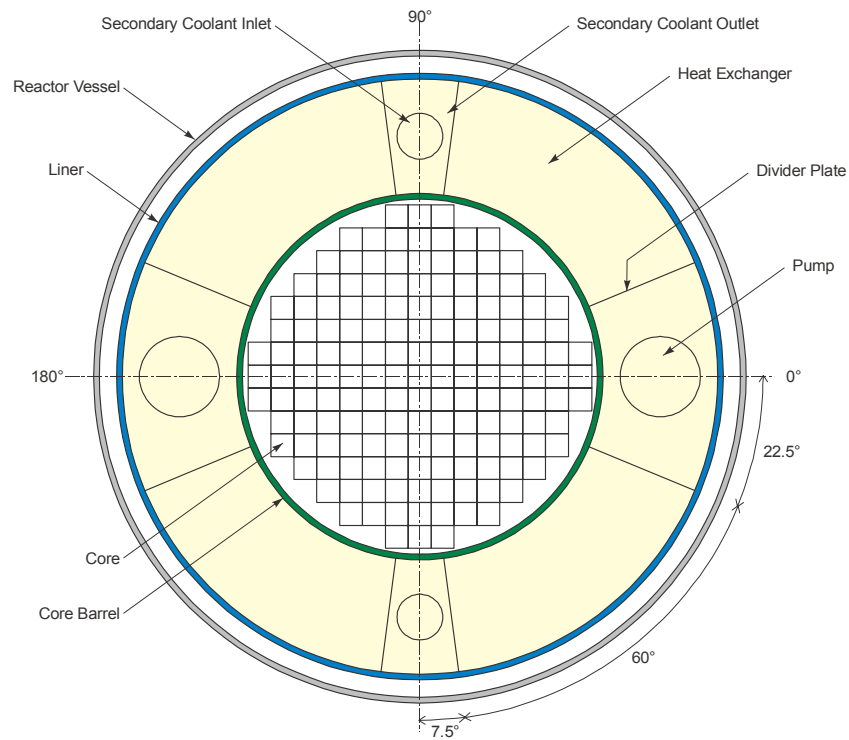
Figure 3.3. Layout of the actinide-burner reactor – top view.

After exiting the bottom of the heat exchangers, the coolant flows down through a downcomer region until reaching holes in the reactor vessel liner located near the elevation of the seal plate. These holes direct the coolant into the annular gap between the liner and the reactor vessel, which is called the vessel riser. The coolant flows upward through the riser until reaching holes located in the upper liner, which direct the fluid into annular regions containing two reactor coolant pumps. The coolant flows down through these annular regions, which are referred to as the pump downcomer, until flowing through the coolant pumps and seal plate into the lower plenum. The upper portions of the vessel riser and the pump downcomer regions are connected to the cover gas in the upper plenum. These connections result in the formation of free levels of relatively cold fluid in the riser and pump downcomer. The levels of these cold pools are considerably lower than the level in the hot pool hot because of the pressure loss across the heat exchangers. The dual-free-level design was utilized so that gas from a ruptured heat exchanger tube does not flow

59

directly past the reactor core. The design limits the positive reactivity insertion associated with voiding in the core following a tube rupture regardless of the flow direction.

The Reactor Vessel Auxiliary Cooling System (RVACS), which is designed to passively remove decay heat, is also illustrated in Figure 3.2. The RVACS design is similar to that used in S-PRISM (Boardman et al. 2000). The RVACS consists of the reactor vessel, a guard vessel, a perforated plate, a collector cylinder, and a reactor silo. Atmospheric air is drawn into the gap between the guard vessel and collector cylinder to provide the ultimate heat sink. The design includes several features to enhance the decay heat removal. These features include using lead-bismuth in the gap between the reactor and guard vessels, a perforated plate in the gap between the guard vessel and the collector cylinder to increase the heat transfer area, and fins or boundary layer trips on the surface of the guard vessel and collector cylinder.

3.2.1. ATHENA Model Description

The ATHENA model of the actinide-burner reactor is illustrated in Figures 3.4 and 3.5. The model represents the primary coolant system, the secondary coolant system, and the RVACS. The primary coolant system is represented by Components 500 through 597 as shown in Figure 3.4.   The reactor core is represented by two parallel flow channels, one (Component 516) representing four high-powered fuel assemblies and the other (Component 510) representing the remaining 153 assemblies. The peaking factor of the four high-powered bundles is 1.16 and the maximum axial peaking factor is 1.155 (determined by Hejzlar and reported in Section 3.4 of MacDonald and Buongiorno 2001). The chimney and upper plenum are represented by Components 520 and 540, respectively. The downcomer, vessel riser, pump downcomers, and pumps are represented by Components 570, 580, 590, and 595, respectively. The heat exchanger, Component

Figure 3.4. ATHENA model of the primary coolant system and RVACS.

560, is based on the design of Dostal et al. (2002) utilizing water as the secondary coolant. Each control volume is approximately 1 m long except in the active core and steam generator, where smaller control volumes are used. The mixture level tracking model is used in the vessel riser and pump downcomer. The average-power and high-power fuel rods, core barrel, reactor vessel liner,

and heat exchanger tubes are represented with heat structures. A 10-micron thick oxide film was modeled on the outside surface of the fuel rods and the heat exchanger tubes to represent fouling.

The secondary coolant system is represented by Components 600 through 620 as shown in Figure 3.5. The feedwater flow is supplied with a time-dependent junction, Component 605. The pressure in the secondary coolant system is set with a time-dependent volume, Component 620. Lead-bismuth flows through the shell side of the heat exchanger and water flows inside the tubes.

The RVACS is represented by Components 800 through 830 as shown in Figure 3.4. The air supply and exhaust are represented with two time-dependent volumes, Components 800 and 830, that are set at atmospheric pressure. The RVACS downcomer and riser are represented by Components 810 and 820, respectively. The model represents all the major heat structures associated with the RVACS, including the reactor and guard vessels, the perforated plate, and the collector cylinder. The lead bismuth in the gap between the reactor and guard vessels was modeled as a heat conducting material rather than as a fluid. The thermal conductivity of the lead bismuth was increased to account for natural convection. Radiation enclosure models were

02-GA50358-04

Figure 3.5. ATHENA model of the secondary coolant system.

used to represent the radiation heat transfer between the guard vessel, perforated plate, and the collector cylinder. The emissivity of these surfaces was set to 0.75, which is representative of the average measured value during the PRISM test program (Hunsbedt and Magee 1988). The surface area of the perforated plate includes a 40% reduction to account for holes. The heat transfer coefficients at the surfaces of the guard vessel, perforated plate, and collector cylinder were doubled to account for the effects of fins or ribs. The factor of two increase is consistent with the heat transfer enhancement that can be achieved by the use of ribs to trip the boundary layer, such as used in S-PRISM (Boardman et al. 2000), due to the thermal entry effect. An insulating material is attached to the outside surface of the collector cylinder to protect the concrete silo from excessive temperature and to prevent heating of the air in the RVACS downcomer, which would reduce the air flow rate.

The model is believed to be conservative because the Dittus-Boelter correlation used by ATHENA predicts heat transfer coefficients that are, on average, about 20% lower than the lower bound of the data reported by Hunsbedt and Magee (1988) for an RVACS without a perforated plate and ribs. Furthermore, the RVACS heat transfer area is based on an active height for heat transfer that is reduced compared to that of the reactor vessel. For example, the primary coolant level during a station blackout is about 3% higher than the height assumed for RVACS heat transfer. No credit is given for heat transfer from the cover gas. Although the heat transfer coefficient from the cover gas to the reactor vessel would be small, natural convection currents in the gap between the reactor and guard vessels would result in relatively effective heat transfer, at least up to the level of the lead-bismuth in that gap.

The geometry of the actinide-burner reactor is summarized in Table 3.1. The outer diameter of the reactor vessel (5.70 m) and height (18.8 m) fit within the rail transportable limits of 6.1 and 19 m identified in Section 2.2 of our FY-01 Annual Report (MacDonald and Buongiorno 2001). The outer diameter of the guard vessel (6.30 m) slightly exceeds the rail transportation limit. The inner diameters of the reactor vessel and liner were increased so that the velocity of the lead-bismuth coolant in the vessel riser and pump downcomer (Components 580 and 590 in Figure 3.4) during normal operation would not exceed the 2 m/s flow velocity limit suggested by the Russians to control corrosion. As an alternative, cutting the system flow rate by 10% would allow the guard vessel to meet the rail transportation limit. Although the guard vessel does not currently meet the rail transportation limit, it is small enough to meet modularity requirements. For example, S-PRISM (Boardman et al. 2000) is considered to be modular and its guard vessel is 10 m in diameter.

Table 3.1. Key parameters for the ATHENA model of the actinide-burner reactor.

Parameter	Value
Core:	
Fuel outer diameter, mm	5.48
Cladding inner diameter, mm	6.32
Cladding outer diameter, mm	7.52
Fuel rod pitch-to-diameter ratio	1.3
Heated length, m	1.3
Gas plenum length, m	2.47
Number of fuel assemblies	157
Steam Generator:	
Lattice	Triangular
Number of tubes	13,316
Tube pitch-to-diameter ratio	1.2
Tube inner diameter, mm	13.9
Tube thickness, mm	4.05
Tube length, m	6.9
Miscellaneous:	
Chimney length, m	10.5
Core barrel inner diameter, m	3.16
Core barrel thickness, m	0.02
Vessel liner inner diameter, m	5.26
Vessel liner thickness, m	0.01
Gap between liner and reactor vessel, m	0.16
Cover gas volume, m^3	59
Pump diameter, m	0.65
Reactor vessel:	
Inner diameter, m	5.60
Thickness, m	0.05
Vessel length, m	18.8
RVACS:	
Gap between reactor and guard vessels, m	0.05
Guard vessel thickness, m	0.25
Gap between guard vessel and perforated plate, m	0.197
Perforated plate thickness, m	0.009525
Gap between perforated plate and collector cylinder, m	0.1716
Collector cylinder thickness, m	0.0254
Collector cylinder insulation thickness, m	0.0508
Downcomer gap thickness, m	0.5842
Active heat transfer length, m	16.3

The ATHENA model shown in Figures 3.4 and 3.5 was used to obtain a steady state for the actinide-burner reactor at normal operating power. The results of the steady-state calculation are

summarized in Table 3.2. The results of the steady-state calculations performed by Dostal et al. (2002) are presented for comparison where available. The feedwater flow rate used in ATHENA was 4.6% higher than Dostal's value, causing a lower steam superheat. Preliminary calculations in which Dostal's results were applied to the ATHENA steam generator model as boundary conditions yielded a total heat removal rate that was in reasonable agreement with, but 2.5% lower than, Dostal's value. The feedwater flow was adjusted so that initial conditions predicted by ATHENA were consistent with Dostal's values. As a result, the primary coolant temperatures calculated by ATHENA were in good agreement with those calculated by Dostal. The maximum cladding temperature predicted by ATHENA was 2.1°C below the 600°C steady-state limit identified by Buongiorno in Section 4.1 of our FY-01 Annual Report (MacDonald and Buongiorno 2002). The dual-free-level design results in relatively cold lead bismuth contacting the reactor vessel wall during normal operation. The temperature of the guard vessel is lower than that of the reactor vessel because of cooling by the RVACS and easily meets the 430°C limit for steady-state operation identified by Buongiorno in our FY-01 Annual Report (MacDonald and Buongiorno 2002).

Table 3.2. Initial conditions for the actinide-burner reactor at rated power.

Parameter	ATHENA	Dostal et al. (2002)
Primary coolant system:		
Core power, MW	700	700
Mass flow rate, kg/s	54,420	54,420
Core inlet temperature, °C	465.9	467
Core outlet temperature, °C	554.3	554.9
Maximum cladding temperature, °C	597.9	600
Maximum fuel temperature, °C	701.2	682.8
Pumping power, MW	3.8	3.1
Cover gas pressure, MPa	0.1	NA[1]
Elevation of the hot pool level, m	15.8[2]	NA
Elevation of the cold pool level, m	11.8[2]	NA
Secondary coolant system:		
Pressure, MPa	15.0	15.0
Feedwater flow rate, kg/s	333.3	316.7
Feedwater temperature, °C	280	280
Steam superheat, °C	178	206
RVACS:		
Power removed, MW	2.5	NA
Air flow rate, kg/s	39.9	NA
Air inlet temperature, °C	38.0	NA
Air exit temperature, °C	100.1	NA
Maximum guard vessel temperature, °C	363.2	NA

1. Not applicable.
2. Elevation is relative to the elevation of the seal plate, which is assumed to be 1.5 m above the bottom of the lower head of the reactor vessel.

The preferred design for the actinide-burner reactor currently utilizes carbon dioxide as the secondary coolant, but water is still being considered (MacDonald and Buongiorno 2001). The steady-state results shown in Table 3.2 were obtained with water as the secondary coolant because carbon dioxide properties are not yet available in ATHENA. The primary coolant parameters presented in Table 3.2 are not affected by the change in secondary fluids because Dostal et al. (2002) varied the heat exchanger design to compensate for fluid differences.

Because the initial conditions of the primary coolant are the same regardless of the choice of secondary coolant, the transient results obtained with carbon dioxide should generally be similar to those presented here with water.

Transient reactor power was calculated using a best-estimate point reactor kinetics model that is based on the calculations of Hejzlar and reported in Section 3.4 of our FY-01 Annual Report (MacDonald and Buongiorno 2001). The point kinetics model used a delayed neutron fraction of 0.0028 and prompt neutron generation lifetime of 2.71×10^{-5} s. The reactivity feedback model was used to simulate the effects of changes in fuel temperature, coolant temperature, and coolant density. The fuel temperature feedback coefficient was -0.0013$/K, which represented the combined effects of Doppler (-0.0007$/K) and fuel thermal expansion (-0.0006$/K). The coolant temperature feedback coefficient, which represented the effects of radial expansion of the lower and upper core plates, was -0.0023$/K. Table 3.3 shows the reactivity feedback due to changes in coolant density. The fuel assembly design results in a slightly positive coolant void worth over the range of interest. Power-squared averaging was used to determine the weighting factors in the feedback model. The decay heat for the station blackout transient was conservatively based on 7.5 effective full-power years, corresponding to 126 and 104 MWd/kgHM burnup in the inner and outer core regions, respectively. For those cases run with reactor scram, the total control rod worth was assumed to be -8.4$. The control rods began moving 1 s after the scram signal was generated and were fully inserted within 3 s.

3.2.2. Primary Coolant Pump Trip

The ATHENA model described in Section 3.2.1 was used to simulate a simultaneous trip of both primary coolant pumps combined with a failure to scram. The initial conditions for the calculation are presented in Table 3.2. The accident was initiated at 10 s. The feedwater flow was held constant until 60 s, when it was reduced to zero over a 10-s period. Continued feedwater flow would overfill the steam generators and result in excessive entrainment of liquid to the steam lines. The turbine header pressure was held constant.

The effect of the pump trip on the normalized coolant flow rate is shown in Figure 3.6. The flow rate decreased smoothly following the pump trip at 10.0

Table 3.3. Coolant density feedback table.

Density, kg/m^3	Reactivity, $
0.0	-8.366
4,000	0.527
6,000	0.879
8,000	0.703
10,250	0.0
10,575	-0.102[1]

1. Obtained by extrapolation.
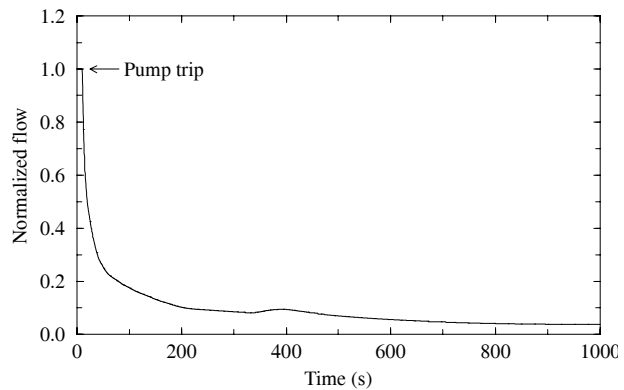
Figure 3.6. Normalized coolant flow rate following the primary coolant pump trip.

s. Natural circulation was fully established at 86 s, when the head produced by the pumps became negative. The rate of the pump coast down was controlled by the pump inertia, which was set to 4930 kg-m^2. With this inertia, the pump speed decreased to half of its initial value in 11.4 s. This rate of coast down is consistent with the 12-s value assumed by Sekimoto et al. (2002) in their analysis of a small, fast reactor cooled by lead bismuth.

The effect of the pump trip on the fluid temperatures at the inlet and outlet of the core is shown in Figure 3.7. The pump trip caused the core outlet temperature to increase rapidly. The cooling by the feedwater resulted in colder water reaching the core near 50 s. The feedwater was terminated 60 s after the pump trip. The termination of feedwater caused the core inlet temperature to begin to increase near 270 s. By the end of the calculation, the core inlet and outlet temperatures exceeded their initial values by about 100°C on average. The reactivity feedback associated with the increase in primary coolant and fuel temperatures caused the core power to decrease as shown in Figure 3.8. The reactor was essentially shutdown by 700 s, when the decay power exceeded the fission power.

The effect of the pump trip on the maximum cladding temperature is also shown in Figure 3.7. The cladding temperature increased following the pump trip until reaching a peak value of 709°C at 58 s. The peak cladding temperature was below the transient temperature limit of 725°C.

The reactivity feedback associated with cooling by the feedwater
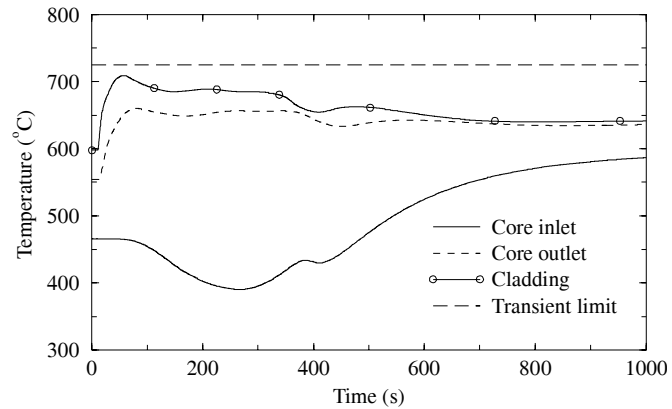
Figure 3.7. Primary coolant and cladding temperatures following the primary coolant pump trip.
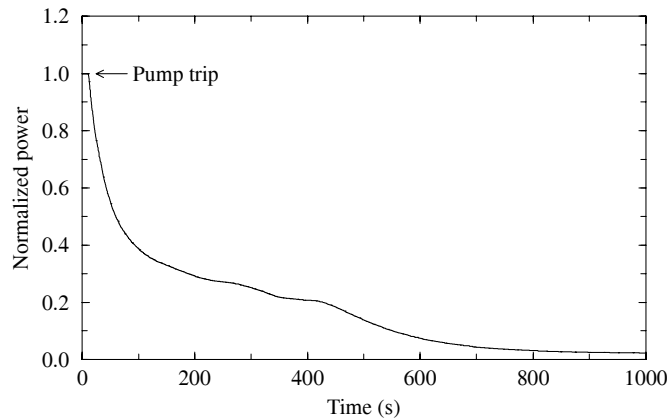
Figure 3.8. Normalized core power following the primary coolant pump trip.

significantly affected the calculated results. For example, a sensitivity calculation showed that if the feedwater flow were not terminated, the cladding temperature would begin to increase at 160s and would slightly exceed the transient limit of 725°C after 430 s. The continued cooling by the feedwater reduced the fluid temperatures in the core compared to the values shown in Figure 3.7. The associated reactivity feedback caused the reactor power to increase to nearly 80% of its initial value and resulted in a maximum cladding temperature of 732°C. A second sensitivity calculation showed that terminating the feedwater at 140 s resulted in a second temperature peak that exceeded the first, but was still below the transient limit. These calculations indicate that there is an ample amount of time to terminate feedwater flow or shut down the reactor via a redundant reactivity control system following a primary coolant pump trip without scram. The response of the actinide-burner reactor with carbon dioxide as the secondary coolant would probably be better than that described above for water. The secondary inlet temperature is more than 100°C higher with carbon dioxide than with water (Dostel in Section 4.3 of MacDonald and Buongiorno 2001). Consequently, the temperature of the lead bismuth exiting the heat exchanger would decrease less with carbon dioxide than with water, which would limit the reactivity feedback.

The relatively low coefficient of thermal expansion for lead bismuth results in a modest pressure increase during this event. The maximum cover gas pressure was 0.12 MPa, representing a 20% increase from the initial value.

Loss-of-flow events do not cause serious consequences in the actinide-burner reactor. The design meets the identified temperature limits following the trip of the reactor coolant pumps combined with a failure to scram when the pumps coasts down to half of their initial speed in 11.4 s. The feedwater needs to be tripped within a few minutes of the initiating event or a redundant reactivity control system is required to provide long-term protection for the failure to scram.

3.2.3. Station Blackout

The performance of the actinide-burner reactor during a station blackout was evaluated using the ATHENA model described in Section 3.2.1. The station blackout was assumed to cause a total loss of feedwater and a reactor pump trip. A failure to scram was also assumed. The initial conditions for the calculation are presented in Table 3.2. The accident was initiated at 0 s.

Figure 3.9 shows the calculated maximum cladding temperature during the station blackout. Although it cannot be seen in the figure, an early temperature peak was calculated to occur at 60s. This temperature peak was similar to that shown in Section 3.2.2 and was caused by the power-to-flow mismatch following the pump trip. The peak value was 721°C, 12°C higher than in the pump trip transient described in Section 3.2.2 because the feedwater was lost instantly in the current calculation. The maximum cladding temperature then decreased as reactivity feedback shut down the reactor similar to that described previously. However, the core's decay heat exceeded the power that was removed by the RVACS as shown in Figure 3.10. The imbalance in heat generation and removal caused the primary coolant system to heat up gradually until the cladding reached a maximum temperature near 18 hours. After this time, the RVACS removed more power than the core generated and the temperature decreased slowly. The peak cladding temperature was 725°C, equaling the transient limit.

Figure 3.9. Maximum cladding temperature during a station blackout.

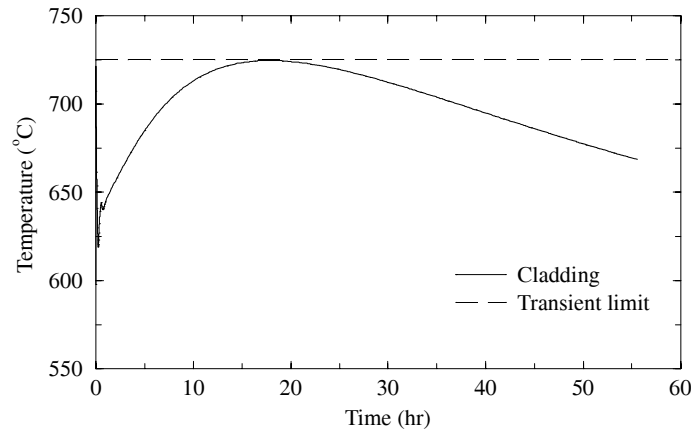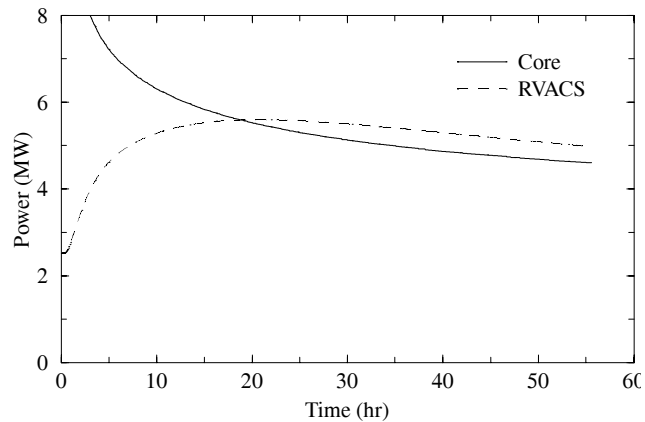**Figure 3.10. A comparison of core decay power and RVACS heat removal during a station blackout.**

66

The relatively low coefficient of thermal expansion of lead bismuth results in a modest pressure increase during this event. The maximum cover gas pressure was 0.14 MPa.

The actinide-burner reactor meets the identified temperature limits following a station blackout even with a failure to scram. The reactor coolant pumps must coast down to half of their initial speed in 11.4 s or more to provide protection during the early power-to-flow mismatch following the pump trip. The RVACS provides adequate long-term cooling considering the conservative assumptions described in Section 3.2.1.

3.2.4. Step Reactivity Insertion

The performance of the actinide-burner reactor following the insertion of a 0.2$ reactivity step was evaluated using the ATHENA model described in Section 3.2.1. A failure to scram was assumed for this transient. The feedwater flow, turbine header pressure, and speed of the primary coolant pumps were assumed to remain constant during the transient. The 0.2$ value represents the maximum worth of a single control rod. The maximum withdrawal speed of a control rod has not been determined, but is clearly bounded by a step insertion of reactivity. The initial conditions for the calculation are presented in Table 3.2. The accident was initiated at 10s.

The withdrawal of a control rod could cause the power peaking near the affected fuel element to increase above the values assumed in Section 3.2.1. However, the point kinetics model cannot simulate the localized neutronic effects of the control rod withdrawal. Thus, this analysis will concentrate on the neutronic and thermal-hydraulic response of the system.

Figure 3.11. Normalized core power following a 0.2$ step reactivity insertion.

Figure 3.11 shows the effect of the step reactivity insertion on the normalized reactor power. The reactor was operating at steady state prior to 10 s, when 0.2$ of reactivity was instantly added to the core. The step reactivity insertion caused the reactor power to increase rapidly. The power increase caused negative reactivity feedback due to the increase in fuel and coolant temperature. The reactivity feedback increased near 60 s when hotter coolant first reached the inlet to the core (see Figure 3.12) and the power reached its maximum value. The core

Figure 3.12. Primary coolant and maximum cladding temperatures following a 0.2$ step reactivity insertion.

power was nearly in equilibrium with the power removed by the heat exchangers when the calculation was terminated at 400 s.

The effects of the step insertion on the maximum cladding and fuel temperatures are shown in Figures 3.12 and 3.13. The increasing temperature of the fluid at the core inlet caused the peak cladding and fuel temperatures to occur about 50 s after the peak power occurred. The peak cladding and fuel temperatures remained below their respective limits.
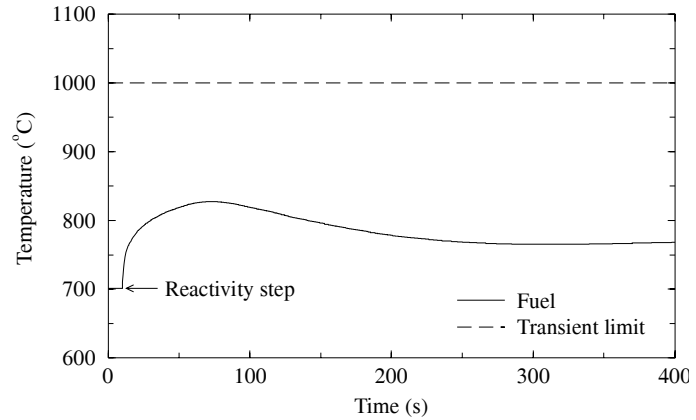
Figure 3.13. Maximum fuel temperature following a 0.2$ step reactivity insertion.

The increase in coolant temperature during the transient caused the coolant to expand, resulting in a small increase in pool level and cover gas pressure. The maximum pressure was 0.11 MPa.

The actinide-burner reactor meets the identified temperature limits following a 0.2$ step reactivity insertion. The point kinetics model indicates that a scram is not required to provide protection for this accident.
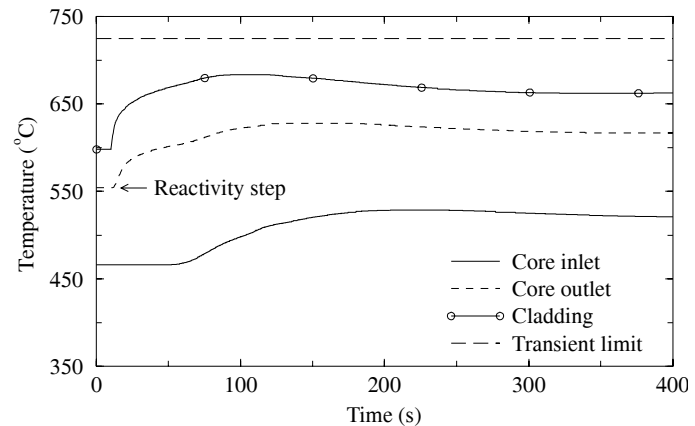
3.2.5. Heat Exchanger Tube Rupture

The performance of the actinide-burner reactor following the rupture of a heat exchanger tube was evaluated using the ATHENA model described in Section 3.2.1. A failure to scram was assumed for this transient. The primary coolant pump speed, feedwater flow, and turbine header pressure were assumed to remain constant during the transient. The initial conditions for the calculation are presented in Table 3.2. The accident was initiated at 0.0 s by a double-ended rupture of a single heat exchanger tube at the lower tube sheet.

A tube rupture event in the actinide-burner reactor will result in flow from the high-pressure secondary side to the low-pressure primary side. This inflow of secondary coolant will pressurize the primary coolant system. A relief valve is required to protect the reactor vessel from excessive pressure. The relief valve will have to discharge into a suppression pool or condenser to prevent release of radioactive polonium from the lead-bismuth to the atmosphere. The relief valve in the calculation was assumed to open when the cover gas pressure reached 0.2 MPa. The valve area was set to 0.1 m^2. The actinide-burner reactor contains over 13,000 heat exchanger tubes as shown in Table 3.1. The pressurization of the primary coolant caused by the rupture of a single tube is small compared to that possible due to a rupture of the feedwater or steam lines. Very thick or double-walled pipes will probably be required to protect the reactor vessel from ruptures of the feedwater or steam lines.

An analytical complication arises for this transient because ATHENA solves continuity, energy, and momentum equations for two phases of a single working fluid, which is lead-bismuth for the actinide-burner reactor. If water enters the system, four phases will be present: liquid lead bismuth, a tiny amount of lead-bismuth vapor, liquid water, and steam. The code cannot model this situation mechanistically as it simulates only two fluid fields, one for a liquid and one for a

gas. A major revision to the code would be required to model all four phases and the interactions between them. However, since the liquid water will quickly boil to steam, approximate quantitative results were obtained using the following three steps. First, the mass flow rate from the secondary side of the heat exchanger to the primary coolant system was calculated. The break flow was discharged into a time-dependent volume whose pressure was set to that of the primary coolant. Second, the flow of water into the primary coolant system was simulated using time-dependent junctions to inject an equivalent amount of non-condensable gas that was a mixture of air and helium. The mixture, which was 90.3% air by mass, had the same gas constant as steam and represented steam density to within one percent over the range of conditions encountered during the tube rupture. The mass flow rate of the injected non-condensable gas was thus equal to the water flow rate calculated during the first step. The volumetric flow rate of the injected gas was approximately equal to that of the water after it had boiled into steam. Finally, the ATHENA control system was used to perform a steady-state energy balance on the lead-bismuth/water mixture. The amount of energy required to bring the water up to the lead-bismuth temperature was then removed from the lead bismuth using a heat structure.

The flow from the ruptured heat exchanger tube is shown in Figure 3.14. The flow rate was limited by choking at both ends of the break. About 90% of the total flow went through the lower tube sheet and into the reactor vessel downcomer (Component 570 in Figure 3). Less flow passed through the other side of the break because wall friction in the tube reduced the stagnation pressure at the choking plane. The mass flow remained nearly constant throughout the calculation because the feedwater flow and header pressure remained constant.
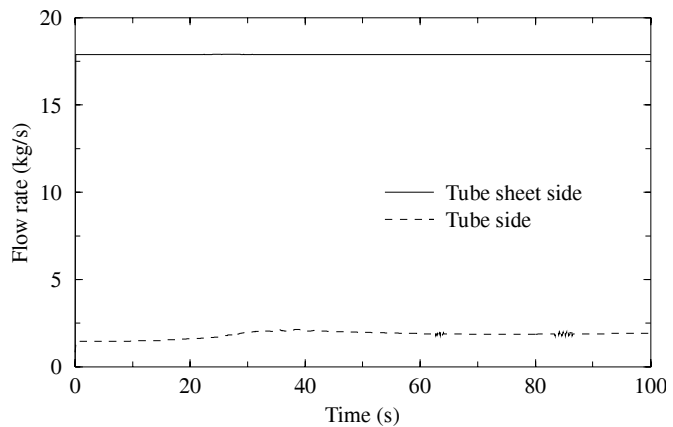
Figure 3.14. Mass flow from the ruptured heat exchanger tube.

The flow pattern in the vessel is illustrated by Figure 3.15, which shows calculated flow rates in the chimney and vessel downcomer. The head produced by the operating primary coolant pumps caused the flow through the chimney to remain upward throughout the transient. The flow downward through the downcomer initially increased as the gas from the ruptured tube displaced liquid from the downcomer. However, the dowcomer flow then reversed as the head reduction due to voiding in the downcomer was sufficient to overcome

Figure 3.15. Flow rates in the reactor vessel following the rupture of a heat exchanger tube.

the initial difference in levels between the downcomer and riser. The voiding caused the mixture level in the hot pool to swell until it reached the top of the core barrel. The lead-bismuth coolant then flowed down through the pump downcomer, entraining a small amount of gas that was carried along to the core. The equilibrium gas flow through the core was about 10% of that from

69

the tube rupture. Thus, the dual-free-level design was effective in limiting the voiding in the core.

Figure 3.15 shows that the downcomer flow oscillated with a period of about 3 s after the flow reversal. The flow oscillations are related to a manometer oscillation between the downcomer and riser liquid levels. The calculated period is about half of that expected for a simple, frictionless manometer.

The flow in the core was similar to that shown for the chimney in Figure 3.15. The magnitudes of the flows in the pump downcomer and riser were similar to those shown for the chimney and downcomer, respectively, but were in the opposite direction.

The flow pattern within the reactor vessel is affected by the drift flux correlations used in ATHENA. The calculated results shown in Figure 3.15 were obtained with the code's default drift flux correlations, which were primarily developed for two-phase mixtures of air and water or steam and water. The application of these water-based correlations to a system containing lead-bismuth and steam represents a significant extrapolation (Davis 2001). A sensitivity calculation was performed in which the El-Boher and Lesin (1988) correlation was used. Although the El-Boher and Lesin correlation was developed to predict the void fraction for cocurrent upflow of several mixtures, including lead-bismuth and steam, the transient conditions were far beyond the range of its database. For example, the calculated fluid temperature was up to 450°C higher than the maximum value in the database of the El-Boher and Lesin correlation. The predicted flow pattern in the sensitivity calculation was similar to that illustrated in Figure 3.15. Nonetheless, experiments will eventually be required to reduce the uncertainty associated with extrapolating correlations beyond the range of their database.

The reactor power was relatively unaffected by the tube rupture as shown in Figure 3.16. The continued operation of the primary coolant pumps and the constant boundary conditions applied to the secondary side of the steam generator resulted in relatively small changes in the power compared to the transients described previously.

The effects of the tube rupture on the primary fluid and cladding temperatures are shown in Figure 3.17. Because of the flow reversal in the downcomer, gas from the tube rupture carried hot lead-bismuth up into the gas space, where it spilled over into the pump downcomer and was supplied to the core. Consequently, the fluid temperature at
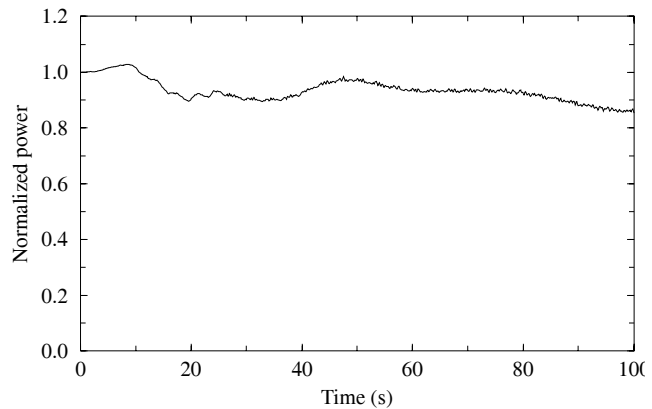
Figure 3.16. Normalized core power following the rupture of a heat exchanger tube.
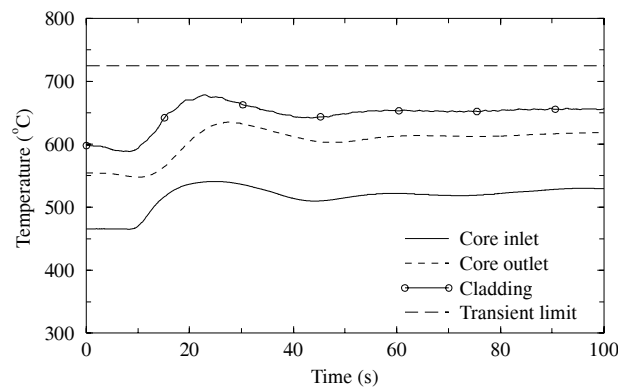
Figure 3.17. Primary coolant and cladding temperatures following the rupture of a heat exchanger tube.

the inlet to the core increased. A similar increase occurred at the exit of the core and in the cladding. The temperatures then stabilized consistent with the new flow pattern in the vessel and the nearly constant core power. The maximum cladding temperature remained below the transient limit.

The pressurization of the reactor vessel due to a ruptured heat exchanger tube is governed by the size and opening pressure of the relief valve, which in the calculation was sized to limit the pressure to 0.2 MPa. The gas flow out of the relief valve will entrain a small amount of lead-bismuth coolant. Using the deposition-controlled correlation of Kataoka and Ishii (1984), the expected rate of entrainment is about 0.003 kg/s.

Although the results are somewhat uncertain because of the required extrapolation of the drift flux correlations, the calculations indicate that the actinide-burner reactor will meet the identified temperature limits following the double-ended rupture of a single heat exchanger tube. The dual-free-level design successfully limits the voiding in the core. A scram is not required to provide protection for this accident. A relief valve is required to protect the reactor vessel from excessive pressure.

3.2.6. Turbine Stop Valve Closure

The performance of the actinide-burner reactor following a rapid closure of the turbine stop valve was evaluated using the ATHENA model described in Section 3.2.1. A failure to scram was assumed for this transient. The accident was initiated at 10 s when the turbine stop valve began to close. The stop valve was fully closed at 10.5 s. A turbine bypass valve was modeled to protect the secondary coolant system from excessive pressure. The valve was sized to relieve 20% of the steam flow at normal operating conditions. The valve began opening when the steam pressure exceeded 16.0 MPa and was fully open at 16.5 MPa. The feedwater flow was assumed to be a function of pressure and decreased from 10% of full flow at 15.5 MPa to 0% at 16.5 MPa. The reactor coolant pumps continued running during the transient. The initial conditions for the calculation are presented in Table 3.2.

The closure of the turbine stop valve caused the secondary coolant pressure to increase rapidly as shown in Figure 3.18. The bypass valve opened at 10.8 s, but could relieve only about 20% of the normal steam flow. The pressure continued to rise until reaching a maximum value of 19.4 MPa at 14.8 s. The pressure then decreased and the valve was throttled to maintain the pressure near 16.1 MPa for the remainder of the transient. A sensitivity calculation with the turbine bypass valve closed indicated that the secondary coolant

Figure 3.18. Secondary coolant pressure following the closure of the turbine stop valve.

pressure would exceed the critical pressure of 22.1 MPa. Thus, some relief capacity will probably be required to protect the secondary coolant system from excessive pressure.

The effects of closing the turbine stop valve on coolant and cladding temperatures are shown in Figure 3.19. The temperatures remained near their initial value until approximately 30 s, when hotter coolant from the heat exchanger first reached the inlet to the core. The temperatures then began to increase, which reduced the core power due to reactivity feedback. The magnitude of the temperature increase was smaller at the exit of the core and in the cladding than at the inlet to the core because of the reduction in core power shown in Figure 3.20. The rate of temperature increase at the inlet to the core slowed near 60 s as the temperature approached an equilibrium value based on the original outlet temperature and the reduced heat removal by the heat exchangers. The continued reduction of core power, coupled with the nearly constant inlet temperature caused the cladding and core outlet temperatures to decrease. However, the core inlet temperature began to increase faster near 80 s again as the initial increase in core exit temperature reached the core inlet. The increase in core inlet temperature caused a similar, but smaller, increase in the core outlet and cladding temperatures. The smaller increase was caused by the

Figure 3.19. Primary coolant and cladding temperatures following the closure of the turbine stop valve.
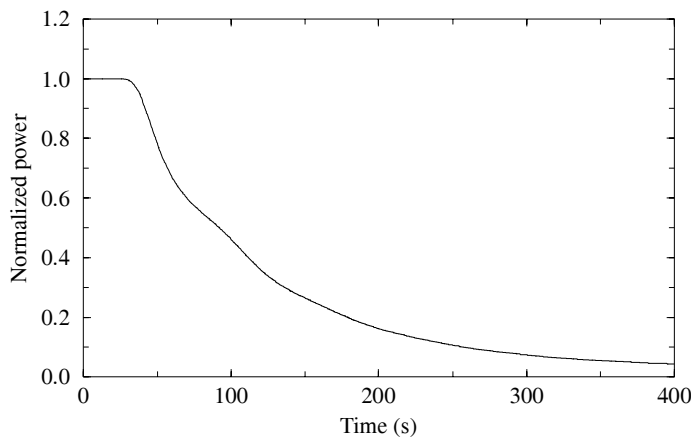
Figure 3.20. Normalized core power following the closure of the turbine stop valve.

continuing reduction in core power. This cycle of increasing and decreasing temperatures continued until sufficient time had elapsed to allow a fluid particle to flow around the primary coolant loop several times. Nearly steady conditions were achieved at the end of the calculation. The final core power was about 4% of the initial value.

The increase in coolant temperature during the transient caused the coolant to expand, resulting in a small increase in pool level and cover gas pressure. The maximum cover gas pressure was 0.12 MPa.

The actinide-burner reactor meets the identified temperature limits following a rapid closure of the turbine stop valve. The maximum cladding temperature was 632°C. A scram is not required to provide protection for this accident. A turbine bypass or relief valve is probably required to protect the secondary coolant system from excessive pressure.

72

3.2.7. Rupture of the Steam Line Piping without Scram

The performance of the actinide-burner reactor following a small rupture in the steam line was evaluated using the ATHENA mo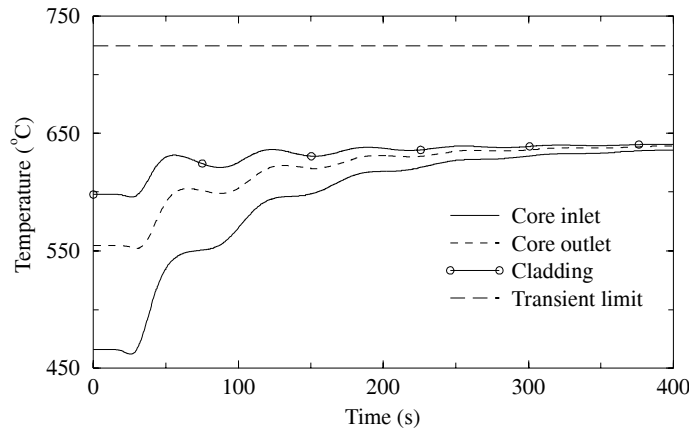del described in Section 3.2.1. The break area was assumed to be 0.05 m^2. This area resulted in insignificant liquid entrainment out the break and thus maximized the potential for overcooling. The actinide-burner reactor contains four heat exchangers, which were combined into a single, equivalent heat exchanger in the ATHENA model as shown in Figure 3.4. Consequently, the rupture simulated by the code was equivalent to the simultaneous blowdown of all four heat exchangers, thus significantly increasing the potential overcooling during this accident. The accident was initiated at 0 s by an instantaneous 0.05-m^2 rupture in the steam outlet piping outside of the reactor vessel. The feedwater flow was held constant for 5 s and then was ramped to zero at 10 s to simulate the isolation of the feedwater system. A failure to scram was assumed for this accident. The reactor coolant pumps were assumed to continue running. The initial conditions for the calculation are presented in Table 3.2.

Figure 3.21 shows the mass flow rates into and out of the heat exchanger during the early portion of the transient. The rupture in the steam line caused the flow out the break to accelerate until reaching a maximum value that was about three times the initial value. The break flow then decreased until reaching zero near 15 s, when the blowdown of the secondary coolant system was completed.
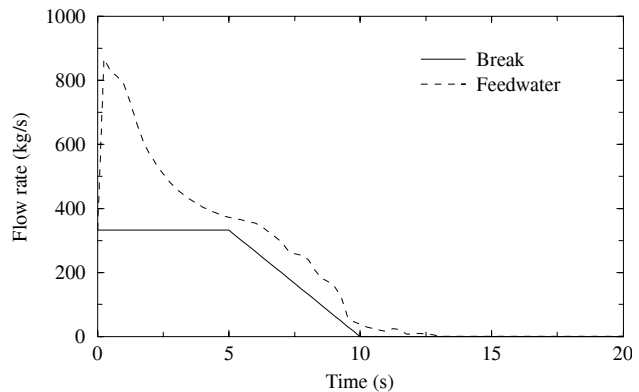
Figure 3.21. Break and feedwater flow rates following a rupture in the steam line.

The rupture in the steam line caused insignificant overcooling of the primary coolant system as shown in Figure 3.22. The rupture caused a small reduction in the core coolant and cladding temperatures beginning near 20 s. However, the amount of cooling was limited by the small initial liquid inventory in the heat exchangers, coupled with the termination of the feedwater flow. The core inlet temperature began increasing near 26 s due to the dryout of the heat exchangers. The subsequent increases and decreases in temperatures were related to the loop transport time as described in Section 3.2.6.
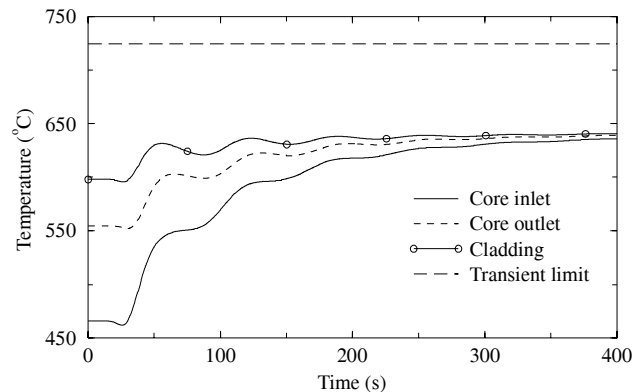
Figure 3.22. Primary coolant and cladding temperatures following a rupture in the steam line.

The effect of the rupture on the reactor power is shown in Figure 3.23. The initial overcooling caused by the break resulted in a slight increase in reactor power. The power then decreased in response to the increase in coolant temperatures following the dryout of the heat exchangers.

73
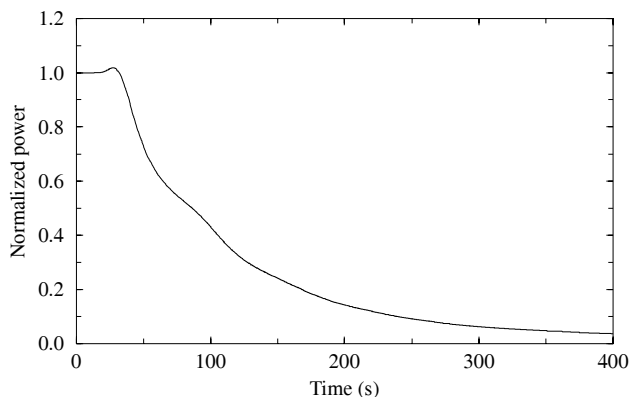
Figure 3.23. Normalized core power following a rupture in the steam line.

A steam line break does not result in significant overcooling in the actinide-burner reactor. The overcooling potential is limited by the small water inventory in the heat exchangers compared to the heat capacity of the lead-bismuth coolant. The state at the end of the calculation was similar to that described previously in Section 3.2.3 for the station blackout except that the reactor coolant pumps were still running. These pumps should be tripped to minimize the heat load placed on the RVACS unless cooling could be established to one of the heat exchangers unaffected by the ruptured steam line.

3.2.8. Loss of Preheating Without Scram

The performance of the actinide-burner reactor following a loss of feedwater preheating was evaluated using the ATHENA model described in Section 3.2.1. The accident was initiated at 10 s by an instantaneous decrease in feedwater temperature to 5°C. A failure to scram was assumed. The feedwater flow, steam line pressure, and pump speed were held constant. The initial conditions for the calculation are presented in Table 3.2.

The effects of the decrease in feedwater temperature on primary coolant and cladding temperatures are shown in Figure 3.24. The decrease in feedwater temperature occurred at 10 s. Colder fluid began to reach the core after a delay due to the time required for the fluid to flow between the outlet of the heat exchanger and inlet to the core. The core outlet and cladding temperatures initially decreased with the inlet temperature. The resulting decrease in primary coolant temperatures caused the reactor power to increase due to reactivity feedback as shown in Figure 3.25. The increase in core power caused the cladding temperature to begin to increase near 60 s when the rate of temperature decrease at the inlet to the

Figure 3.24.   Primary coolant and cladding temperatures following a loss of feedwater preheating.

core slowed. The maximum cladding temperature remained far below the transient limit.

74

The calculated decrease in core inlet temperature was much smaller than the decrease in feedwater temperature. For example, the decrease in feedwater temperature was 275°C whereas the core inlet temperature decreased by at most 56°C during the transient. The smaller decrease in core inlet temperature was caused by the constant pressure and saturation temperature on the secondary side of the heat exchangers and the increase in reactor power.
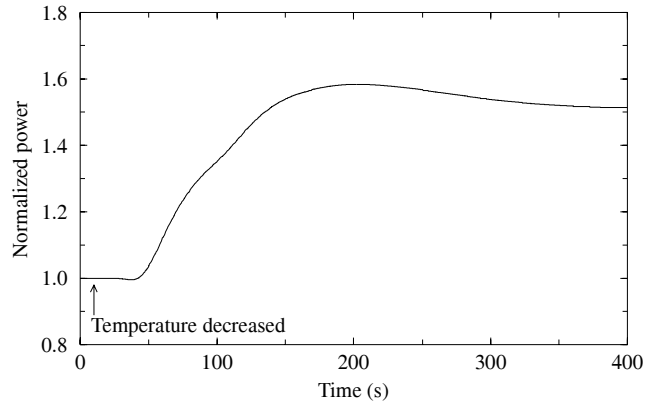
Figure 3.25. Normalized reactor power following a loss of preheating of the secondary coolant.

The actinide-burner reactor is not susceptible to overcooling accidents initiated by a loss of feedwater preheating. All temperatures remained below their respective transient limits. The cladding temperature also remained well above 125°C, the freezing point of lead-bismuth. Thus, the reactor is not susceptible to freezing following a loss of preheating.

3.2.9. Cleanup System LOCA Without Scram

Figure 3.2 shows that the principal flow paths of the actinide-burner reactor are contained within the reactor vessel. Since there are no external loops containing lead-bismuth, the design is not susceptible to large loss-of-coolant accidents (LOCAs). However, the reactor will probably use a small cleanup system to reduce the polonium concentration and control chemistry in the primary coolant. Consequently, the possibility of accidents initiated by ruptures in the cleanup system was considered.

A conceptual design of the cleanup system was developed so that the response of the actinide-burner reactor to ruptures in the cleanup system could be evaluated. As shown in Figure 3.26, the cleanup system draws suction from the hot pool, routes the fluid through the upper head at the top of the reactor vessel, through a mass exchanger, and then back through the upper head to the cold pool. A pump is not required during normal operation because the difference

Figure 3.26. Schematic of the cleanup system for the actinide-burner reactor.

between the hot and cold pool levels provides the motive force for flow through the cleanup system. The normal mass flow rate of the system, 60 kg/s, was selected by Buongiorno to reduce

75

the polonium concentration of the primary coolant by two orders of magnitude compared so the case without cleanup (Section 6.5 in MacDonald and Buongiorno 2001). The cleanup piping was chosen to be 4-inch Schedule 10s. This pipe schedule yields a low fluid velocity (0.6 m/s) that results in minor head losses within the piping during normal operation. An orifice downstream of the mass exchanger limits the flow through the cleanup system.

The ATHENA model of the cleanup system and the connections to the reactor vessel are shown in Figure 3.27. The type and design of the mass exchanger have not been finalized, but it was assumed to operate at 0.13 MPa and that five velocity heads, based on the piping area, were lost across the mass exchanger. Valve 740 represents the orifice. Its area was adjusted to obtain the desired flow rate of 60 kg/s. The resulting orifice caused a loss of 170 velocity heads based on the piping area during normal operation. Although not currently modeled, a heat exchanger may be required to reduce the lead-bismuth temperature to the correct operating temperature for the mass exchanger. If the heat exchanger were designed to operate passively, it would provide cooling in addition to that provided by the RVACS and hence would increase safety margins following a station blackout.

The ATHENA model was revised slightly from that described in Section 3.2.1 to represent the cleanup system. The nodalization of Component 540 was increased to more accurately represent the elevation of the inlet to the cleanup system. In addition, the cover gas pressure was raised from 0.1 to 0.3 MPa, the hot pool liquid level was raised 0.17 m, and the elevation of the bottom of the upper vessel head was reduced by 0.75 m. These latter changes prevented the

Figure 3.27. ATHENA model of the cleanup system.

drawing of a severe vacuum in the mass exchanger due to the loss in hydrostatic head associated with raising the lead-bismuth coolant. The analysis assumed that that the elevation of the mass exchanger was 1.0 m above the bottom of the upper head and 1.58 m above the normal hot pool level. If the cover gas were at atmospheric pressure, raising the coolant 1.0 m would reduce the pressure in the mass exchanger to approximately zero and would cause flashing of the lead-bismuth. The net effect of these changes was to reduce the initial gas volume from 59 m^3 to 36 m^3. The reduction in gas volume would cause pressure changes during transients to exceed those reported previously, but would still result in acceptably low maximum pressures.

The selected design prevents the hot pool level from dropping below the elevation of the holes in the core barrel, which would prevent natural circulation of the primary coolant and interfere with

heat removal by the RVACS, following a rupture in the cleanup system and a subsequent pump trip. The calculations described in Section 3.2.2 showed that the hot pool level decreased about 0.8 m when the pumps were tripped. Consequently, the inlet to the cleanup system, which represents the minimum possible level following a rupture in the cleanup system, was placed 1 m above the lowest holes in the core barrel. The initial hot pool level was selected so that the hot level would not expand to the top of the vessel liner until the average coolant temperature reached 750°C, which would require that the cladding temperature far exceed its transient limit of 725°C. Such an expansion would allow liquid from the hot pool to spill over into the cold pool, which would have the deleterious effect of allowing flow to bypass the heat exchangers in reactivity insertion events with the primary coolant pumps operating.

The performance of the actinide-burner reactor following a double-ended guillotine rupture in the piping of the cleanup system was evaluated using the ATHENA model illustrated in Figures 3.4, 3.5, and 3.27. The LOCA was initiated at 10 s by closing Valve 720 and opening Valves 750 and 755 (see Figure 3.27) over a 1 s period. A failure to scram was assumed. The feedwater flow, steam line pressure, and pump speed were held constant. The time-dependent volumes downstream of the break junctions were set at atmospheric pressure. The initial conditions for the calculation were nearly identical to those presented in Table 3.2, except that the cover gas pressure and pool levels were increased as described previously. The flow through the cleanup system had a negligible effect on the fluid and cladding temperatures shown in Table 3.2.

The primary flow path from the actinide-burner reactor to the confinement atmosphere was from the hot pool. Figure 3.28 shows that the flow from the hot side of the break reached a maximum value shortly after the breaks opened and then declined gradually. The flow of lead-bismuth through the break caused the pool level and cover gas pressure to decrease as shown in Figures 3.29 and 3.30. The decreases in cover gas pressure and, to a lesser extent, the hot pool level reduced the pressure upstream of the break and caused the gradual decline in the flow rate. The break flow from the hot pool terminated naturally at 430 s when the control volume upstream of the break reached atmospheric pressure. The effective isolation of the break flow at 430 s caused the liquid level and cover gas pressure to stop decreasing. The inlet to the cleanup system remained below the surface of the hot pool throughout the transient.
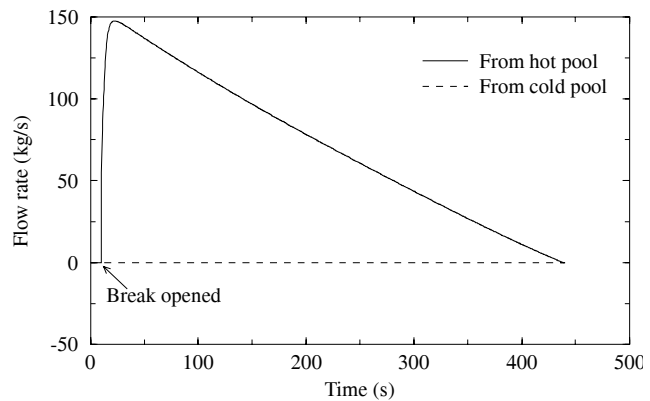
Figure 3.28. Break flow rates following a LOCA in the cleanup system.
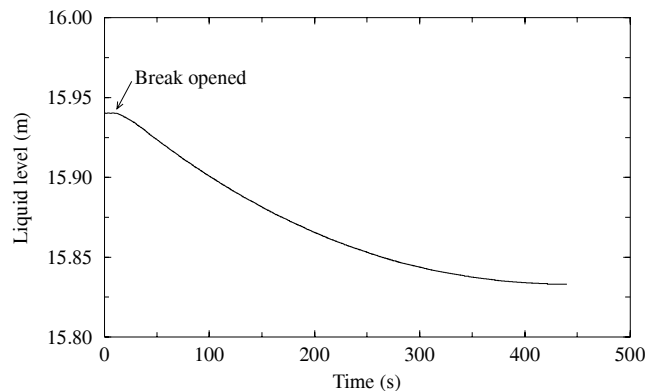
Figure 3.29. Hot pool level following a LOCA in the cleanup system.

Figure 3.28 shows that the flow from the cold pool was negligible compared to that from the hot pool. In fact, air from the confinement atmosphere was drawn into the discharge side of the cleanup system and a liquid level was formed. The cover gas pressure raised the liquid level above that in the cold pool, but was unable to push the lead-bismuth up to the elevation of the break.

The LOCA did not significantly affect reactor operation. Figure 3.31 shows that the primary coolant and cladding temperatures remained nearly constant during the transient. The reactor power did not vary appreciably because there was insignificant reactivity feedback and scram was not simulated.

Although not finalized, a cleanup system can be designed that reduces the polonium concentration in the primary coolant while passively limiting the amount of coolant lost during a LOCA. The conceptual design described here used the difference in levels between the hot and cold pools to provide the motive force for flow during normal operation, although a pump will probably be required to initially fill the cleanup system with lead-bismuth.
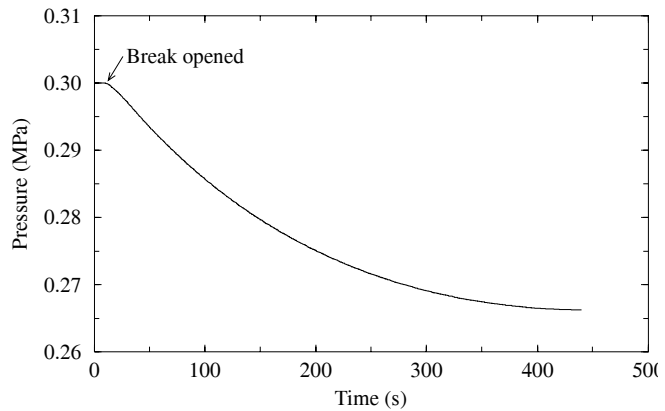
Figure 3.30. Cover gas pressure following a LOCA in the cleanup system.
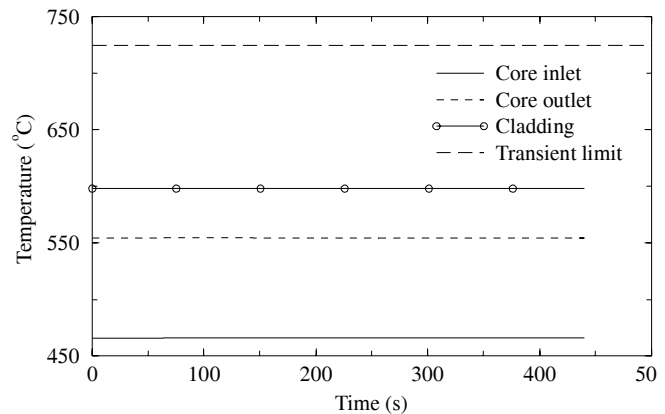
Figure 3.31. Primary coolant and cladding temperatures following a LOCA in the cleanup system.

3.2.10. Summary of Transient Results

The ATHENA code was used to determine the response of the actinide-burner reactor to a variety of transients, including pump trip, station blackout, reactivity insertion, heat exchanger tube rupture, turbine stop valve closure, steam line break, loss of feedwater preheating, and loss of coolant from the reactor cleanup system. The transients were simulated without reactor scram to demonstrate the safety margins inherent in the reactor design. The results are summarized in Table 3.4. The table identifies the initiating event, the calculated peak temperatures for the cladding, fuel, and guard vessel, and the corresponding temperature limits identified by Buongiorno and reported in Section 4.1 of our FY-01 Annual Report (MacDonald and Buongiorno 2002). Although not discussed previously, the table also shows the effect of reactor scram on three transients, including the pump trip, blackout, and tube rupture events.

Table 4 shows that the cladding temperature was always closer to its limit than the fuel and guard vessel temperatures. Thus, the cladding temperature is the most limiting parameter for the actinide-burner reactor. The most limiting transient is initiated by a station blackout. The station blackout coupled with a failure to scram produced a peak cladding temperature that was equal to

78

the transient limit. The margin to the temperature limit increased to a more comfortable 24°C when a reactor scram was simulated.

Table 3.4. Summary of transient results.

	Peak temperature (°C)		
	Cladding	**Fuel**	**Guard vessel**
Limit	**725**	**1000**	**750**
Transient			
Primary coolant pump trip without scram	709	753	382
Primary coolant pump trip with scram	600	701	363
Blackout without scram	725	759	532
Blackout with scram	701	701	516
0.2$ step reactivity insertion without scram	684	828	369
Heat exchanger tube rupture without scram	679	766	364
Heat exchanger tube rupture with scram	598	701	363
Turbine stop valve closure without scram	632	704	379
Steam line break without scram	641	707	381
Loss of feedwater preheating without scram	621	779	363
LOCA in the cleanup system without scram	598	701	363

The minimum margin between the peak fuel temperature and its transient limit was 172°C, which was large compared to the cladding. The transients initiated by a step reactivity insertion and a loss of feedwater preheating were the most limiting relative to fuel temperature because they caused significant increases in reactor power.

The minimum margin between the peak guard vessel temperature and its transient limit was 218°C. The station blackout, which was the only transient causing a significant increase from its initial value, was the most limiting event relative to guard vessel temperature. Although the guard vessel temperature had not yet reached steady state when the calculations of the other transients were terminated, the eventual steady results were bounded by the station blackout, in which maximum values were obtained.

The station blackout without scram results in two cladding temperature peaks. The first temperature peak occurs about one minute after the start of the event and is caused by the power-to-flow mismatch following the trip of the primary coolant pumps. The pumps must coast down to half of their initial speed in 11.4 s or more in order to meet the cladding thermal limit. The second temperature peak occurs about 18 hours after the start of the event and is associated with the balance between the power generated by the core and that removed by the RVACS.

A steam line break does not result in significant overcooling in the actinide-burner reactor. The overcooling potential is limited by the small water inventory in the heat exchangers compared to the heat capacity of the lead-bismuth coolant.

A cleanup system can be designed that reduces the polonium concentration in the primary coolant while passively limiting the amount of coolant lost during a LOCA.

The transient initiated by a heat exchanger tube rupture resulted in the highest cover gas pressure of the cases evaluated. Because of the high pressure on the secondary side of the heat exchangers, a relief valve will be required to protect the reactor vessel. The maximum pressure is governed by the relief valve, which was set to open at 0.2 MPa in this analysis. The next most limiting transient was the station blackout, which produced a peak cover gas pressure of 0.14

MPa. If the design changes associated with the cleanup system as described in Section 3.2.9 are implemented, the peak pressures would be somewhat larger than stated above because of the higher initial cover gas pressure and the reduced gas volume.

The actinide-burner reactor exhibits excellent safety characteristics. The reactor met the identified temperature limits for all the transients evaluated. Reactor scram was not required for any of the cases considered. Overall, the ABR is far more passively safe than any currently operating nuclear power plant.

3.3. Improvement and Benchmark of the Metal-Fuel Performance Model (Dr. Jacopo Buongiorno, INEEL)

During FY-01 a simple one-dimensional thermal-mechanical model for prediction of the irradiation performance of metal fuel was developed by this author. This enabled calculation of the expected lifetime for the fuel of the LBE-cooled reactor. A detailed description of the model and justification of its assumptions were provided by Buongiorno in Appendix B of our FY-01 Annual Report (MacDonald and Buongiorno 2001). The model largely builds on the sodium-cooled Integral Fast Reactor (IFR) fuel development experience, and can predict the temperature, stress and strain history of a metal fuel pin of known operating conditions. The model takes into account elastic, thermal-expansion, thermal-creep, irradiation-creep, and swelling effects. Plastic strains are neglected because, at the temperatures of interest, the stresses in the cladding remain well below the yield strength of typical cladding materials (e.g., HT-9). The model assumes that the fuel/clad gap closes at about 2 at% burnup and that by then 80% of the fission-gas inventory is released in the fission-gas plenum, independent on the fuel composition. While the cladding deformation is calculated, the fuel deformation is specified by specifying the fuel outer radius and axial expansion as a function of burnup. The stresses, strains and displacements in the cladding are determined by establishing the three sets of equations typical of static structural mechanics analysis (i) the displacement/strain relations, (ii) the equilibrium equations, and (iii) the stress/strain relations. The cladding is represented by a single axial node, where either the peak temperature, or the peak burnup or both can be applied.

During FY-02 two major improvements took place. First, better constitutive equations for irradiation creep and thermal creep of the cladding material, HT-9, were obtained from the metallic-fuels handbook of the IFR program. These equations correlate the creep strain of HT-9 with fast-neutron dose and temperature for the irradiation-creep term, and with temperature and time for the thermal-creep term. All regimes of thermal creep are modeled, i.e., primary, secondary and tertiary, while the old model only accounted for secondary creep. The second improvement consisted in allowing for non-constant temperature, dose, and linear heat generation rate during irradiation. The new version of the model can simulate the behavior of a metal fuel pin with arbitrarily-changing operating conditions.

The model was benchmarked with actual metal-fuel irradiation data from the IFR development program. The data from subassembly X430 of the Experimental Breeder Reactor II (EBR-II) were used to this purpose. The HT-9 clad advanced driver fuel test consisted of a 37-pin subassembly containing four fuel alloys: U-10Zr, U-19Pu-10Zr, U-22Pu-10Zr and U-26Pu-10Zr. The geometry of the fuel pins is reported in Table 3.5.

Nine representative pins were selected for the benchmark exercise (Table3.6). For each pin the irradiation time, linear power, and cladding temperature histories were input to the model. Note that the fuel pins with higher Pu content (pins 5 through 9) were irradiated for shorter times, which resulted in lower discharge burnup.

Table 3.5. Geometry of the X430 Fuel Pins (from Crawford et al. 1994).

Parameter	Value
Cladding OD	7.37 mm
Cladding ID	6.55 mm
Cladding Thickness	0.41 mm
Fuel Slug Diameter	5.71 mm
Pin Length	71.43 cm
Fuel Slug Length	34.29 cm
Fission Gas Plenum Length	36.51 cm
Fuel Smeared Density	76%

Table 3.6. Comparison of model predictions with actual irradiation data.

Fuel Composition	Pin #	Burnup, at. %	EOL[*] Cladding Radial Strain, % (meas.)	EOL[*] Cladding Radial Strain, % (calc.)
U-10Zr	1	11.8	0.76±0.10	0.76
	2	11.8	0.62±0.10	0.72
U-19Pu-10Zr	3	11.6	0.52±0.10	0.74
	4	11.7	1.17±0.10	0.81
U-22Pu-10Zr	5	6.4	0.45±0.10	0.20
	6	6.6	0.38±0.10	0.22
U-26Pu-10Zr	7	6.6	0.28±0.10	0.21
	8	6.4	0.41±0.10	0.20
	9	4.1	0.38±0.10	0.08

* EOL: End Of Life

It can be seen that the accuracy of the model in reproducing the experimental data is acceptable at high burnup (±20% average error for Pins 1, 2, 3 and 4). On the other hand the model appears to systematically under-predict the end-of-life cladding strain at lower burnup (Pins 5, 6, 7, 8 and 9). Given the simplicity of the model, the uncertainties on the constitutive equations, and our interest in predicting cladding strains and failure at high burnup, we conclude that the model performs quite satisfactorily and will be further used for analysis in this project.

3.4. Pump Selection (R. Herron, MIT)

3.4.1. Introduction

The purpose of this section is to select and size the reactor coolant pumps for the ABR. For each potential pump type, we evaluate whether it can provide the necessary flow, head, and efficiency, whether it fits the dimensions of the reactor, and whether it can operate under the ABR temperature conditions. The options for the coolant pumps for the lead-bismuth eutectic (LBE) cooled reactor do not present a clear choice. The starting point will be a comparison of coolant pumps specified for use in other similarly sized liquid metal cooled reactors. Due to the nature of the LBE coolant and the lack of development in technology for its circulation, the best option may not be the most advantageous, but the one that is least disadvantageous.

3.4.2. Current Pumping Requirements of the LBE Reactor

The thermal power of the reactor, $\dot{Q}$, and the temperature rise across the core, ΔT, determine the mass flow rate for the current LBE reactor design. Equation (3.7) determines the mass flow rate for a specific heat at constant pressure, $\overline{c}_P$, averaged over the temperature range of ΔT.

$$\dot{m} = \frac{\dot{Q}}{\overline{c}_P \Delta T} \tag{3.7}$$

For the temperature range of interest, 400°C to 600°C, the average specific heat of LBE, $\overline{c}_P$, is 146.37 J/kg/K [Lyon 1952]. With the current thermal power of 700 MWth and a core temperature rise of 87.9°C, the LBE reactor requires a coolant mass flow rate of approximately 54,420 kg/sec [Dostal et al. 2002]. The average density over the LBE reactor's temperature range, $\overline{\rho}$, is 10,080 kg/m³, which yields a volumetric flow rate of 5.40 m³/sec [Lyon 1952]. The required pumping power is the product of the volumetric flow rate and pressure drop around the reactor loop, ΔP. The current design requires a pressure head of 0.441 MPa to overcome the core pressure losses [Dostal et al. 2002]. For the simple analysis performed here, the pressure drop in the heat exchangers will be neglected. This core pressure drop value is based upon the current core velocity limit of 2 m/sec. The velocity limit of 2 m/sec preserves the cladding's protective oxide layer. Circulating the LBE coolant through the core thus requires 2.38 MWe of pumping power.

The two possible pump selections for circulating the LBE coolant are a centrifugal pump or an electromagnetic (EM) pump. Both have met with success in nuclear power plants of varying sizes and coolants, but are very different in design and fundamental theory of operation. A third approach, the gas-lift pump, is discussed in Section 3.1 above and has been discarded.

Centrifugal pumps are commonly used in light water reactors. The theory of centrifugal pump operation is well understood and their use is well documented. In a centrifugal pump a spinning impeller accelerates the fluid, creating a velocity head. The diffuser, which surrounds the rotating impeller, converts the velocity head into a pressure head. There are three basic categories of centrifugal pumps: radial, mixed, and axial. All operate on the basis of converting velocity head to pressure head [Tuzson 2000]. Centrifugal pumps have been adapted to work with both water and denser fluids, such as liquid metals.

An EM pump circulates fluid by exerting a force on the liquid by the reaction between a current passing through the fluid and a surrounding magnetic field. Because a current must pass through the fluid that is pumped, EM pumps are limited to liquid metal applications, such as sodium and LBE. A unique trait of an EM pump is that no moving parts are placed in the fluid [Baker and Tessier 1987].

Since very little research has been published on LBE reactors, sodium-cooled reactors will be used for comparison. Although sodium and LBE are both liquid metals, it must be remembered that the two have different density and viscosities that affect how the fluid is pumped and the power required. Some simple calculations regarding the work to circulate each coolant through equivalently powered reactors make these differences apparent. Using the data in Table 3.7 with Equation (3.7) the relative pumping power required for an LBE reactor versus a sodium-cooled reactor is approximately 7.06 [Spencer 2000]. It is important to note that the numbers provided by Spencer are for a 300 MWth LBE-cooled reactor and a 250 MWth sodium-cooled reactor.

This discrepancy (17%) is small relative to the pumping power ratio. The ratio of 7.06 can still be used as a rough estimate of the relative pumping power of LBE to sodium.

Table 3.7. Parameters to calculate the relative work for circulating LBE (versus sodium) around a similarly sized nuclear reactor with the same pitch-to-diameter ratio [Spencer 2000]

	LBE	Na
Power, $\dot{Q}$ (MWth)	302	251
Core Inlet Temperature (ºC)	350	350
Temperature Rise, ΔT (ºC)	150	150
Average Temperature (ºC)	425	425
Core Pressure Drop, ΔP (MPa)	0.248	0.031
Density, $\bar{\rho}$ (kg/m^3)	10,190	854
Specific Heat, $\bar{c}_P$ (J/kg/K)	146.4	1278.2
Volumetric Flow Rate, Q_C (m^3/sec)	1.35	1.53
Pump Work, $\dot{W}_{PUMP}$ (W)	334,800	47,430
Pump Work Ratio (LBE/Na)		7.06

3.4.3. Similar Liquid Metal Cooled Reactors

The reference LBE reactor has a thermal power rating of 700 MWth [Table 1.3]. There are several other proposed liquid metal reactors of similar power rating throughout the world. The S-PRISM reactor is a modular reactor designed with many of the same goals as the LBE reactor. Current designs are for a thermal power of 1000 MWth and four EM pumps [Boardman 2000]. The Brest 300 is a similarly sized liquid metal cooled reactor that uses centrifugal pumps for circulation. Instead of lead-bismuth eutectic, the Brest 300 concept uses pure lead as the coolant [Adamov 1994]. Table 3.8 presents a summary of key parameters for each of these three reactors.

Table 3.8. Comparison between the current LBE reactor design and similar proposed designs.

	ABR	S-PRISM[*]	Brest 300[**]
Power, $\dot{Q}$ (MWth)	700	1000	700
Coolant	Lead-Bismuth	Sodium	Lead
Core Inlet Temperature (ºC)	467	370	420
Core Outlet Temperature (ºC)	555	510	540
Temperature Rise, ΔT (ºC)	92	139	120
Reactor Configuration	Pool	Pool	Pool
Number of Pumps	*TBD*	4	4
Pump Design	*TBD*	EM	Centrifugal
Design Pump Flow Rate (m^3/sec)	*TBD*	1.37	1.00
Total Flow Rate, Q_C (m^3/sec)	5.40	5.49	4.00
Pump Head, ΔP (kPa)	441.0 (core)	758.0	252.6
Pump Power (MWe)	*TBD*	1.04	0.25
Total Pump Power, $\dot{W}_{PUMP}$ (MWe)	2.38	4.16	1.01

TBD – To be determined,   *Boardman 2000,   **Adamov 1994

3.4.3.1. Electromagnetic (EM) Pumps

Electromagnetic pumps can circulate metallic fluids without the use of moving parts in the fluid. An induced current and a magnetic field create a force in the fluid that produces a pressure head. The force acting on the fluid is the Lorentz Force [Baker and Tessier 1987].

$$\vec{F} = I\vec{L} \times \vec{B} \tag{3.8}$$

As shown by the cross product in Equation (3.8), the created force is mutually perpendicular to the current and magnetic field lines. There are several variations of EM pumps. Conduction pumps are the simplest EM pumps and create currents in the fluid by conduction. In induction pumps the current is induced in the fluid and there are several different methods of achieving the pumping force. The most common of these is the annular linear induction pump (ALIP).

There are several advantages to using EM pumps with metallic working fluids. The first of these is that the use of EM pumps permits a sealed system. The fluid flow section of an EM pump is simply an annular section of pipe and because the pump is sealed into the system, there is no need for cover gas cleanup systems on each pump. Also, since the EM pump is sealed, like any other section of pipe, there is no need to extend the primary boundary to include the coolant pumps [Boardman 2001].

Another significant advantage of the EM pump is that it is less susceptible to corrosion and erosion than its centrifugal pump counterparts. This is due to the lack of moving parts in the fluid. Conventional pumps create pressure differentials by converting velocity head into pressure head. High velocities are required to create large pumping heads. These high velocities increase erosion and corrosion at the impeller blade tips and in the volute casing. Electromagnetic pumps create the pumping force within the fluid, greatly reducing the fluid velocity relative to pump components. For this reason an EM pump is also less likely to be cavitation limited than a conventional pump [Baker and Tessier 1987].

Although EM pumps have several key advantages that make them especially attractive for use with corrosive liquid metal coolants, they also have some inherent shortcomings. The first of these is an overall efficiency much lower than that of a centrifugal pump. Efficiencies in the range of 40% to 50% are generally expected from a well-designed EM pump. Given that the power required to circulate the coolant in an LBE-cooled reactor is about seven times greater than that of a sodium-cooled reactor, this may result in a large consumption of power and lower cycle efficiency [Lefevre 2001]. Recall however that this ratio was determined using the pitch-to-diameter ratios provided by Spencer [2000].

In addition to low efficiency, an EM pump has temperature limitations due to material limitations of the insulation used in the stator windings. Although advances have raised the maximum operating temperature of the insulation to 538°C (1000°F), this increase may not be enough to allow for the use of an EM pump with the LBE reactor. Also, since the EM pump is submersed in the coolant, heat produced in the pump must be rejected to the coolant. To ensure efficient and reliable heat transfer to the coolant pool a temperature differential of 167°C (300°F) is required between the internal components of the pump and the pool or core inlet temperature [Boardman 2001].

Another disadvantage of the EM pump is its dependence on the electrical resistance of the fluid. An EM pump creates pumping forces by passing a current through the fluid. This current

interacts with a magnetic field to create a pumping force proportional to the current and the field strength. Ohm's Law, Equation (3.9), governs the relationship between voltage and current.

$$V = IR \qquad (3.9)$$

In an EM pump, the fluid provides some electrical resistance to the applied voltage. For a given fluid electrical resistance, doubling the current requires the voltage across the fluid to be doubled. As the electrical resistance of the fluid increases, the applied voltage must increase proportionally to maintain the same current, and thus pumping force, in the liquid.

An increase in the fluid's electrical resistance is also a concern due to electrical power losses. Equation (3.10) relates the power lost to the electrical resistance and applied current.

$$P = I^2 R \qquad (3.10)$$

The lost power is directly proportional to the electrical resistance of the fluid. The amount of power lost is a concern because an increase in self-consumed power lowers net power plant efficiency. At the same thermal power, if less power is consumed in pumping the coolant, more net electrical power can be produced. Also, any heat generated in the pumps must be dissipated to the surrounding coolant. This further limits the core inlet temperature and, as a result, the core outlet temperature.

3.4.3.2. Centrifugal Pumps

The category of centrifugal pumps includes a variety of different style pumps. Three general variations of the centrifugal pump are the radial, mixed, and axial flow pumps. Radial flow centrifugal pumps create the pump head completely with centrifugal forces. In an axial flow pump, the propelling or lifting action of the impeller vanes on the liquid develops pressure. And, as the name suggests, mixed flow pumps develop a pressure head using a combination of the centrifugal and axial lift forces. Current centrifugal pump designs for water service have efficiencies of approximately 85% [Tuzson 2000].

Like EM pumps, centrifugal pumps have various advantages and disadvantages. One of the biggest advantages of selecting a centrifugal pump is the large base of knowledge and experience. Centrifugal pumps have long been used and a large body of knowledge has been accumulated. These experiences include use in nuclear reactors and in pumping both water and heavy liquid metals. Experience with pumping lead bismuth eutectic coolant is available from Mitenkov (1999) and Li (2001).

Temperature limitations are not a serious concern with centrifugal pumps. In most pump designs the motor assembly can be mounted out of the coolant. With this configuration there are no sensitive electrical components that must dissipate heat to the coolant. The only temperature concern would be for the actual metal components of the pump, which would be a concern in any pump design.

The main disadvantage of centrifugal pumps is the significant one of erosion and corrosion within the pump housing. High velocity at the impeller blade tips and on the inside of the pump housing can lead to corrosion and erosion. This problem can be alleviated in part by the use of mixed or axial flow pumps, which rely more upon propelling or lifting forces to create pressure head. But

the velocity of the fluid relative to the pump components is still significantly higher than in EM pumps [Tuzson 2000].

3.4.4. Pump Selection for the LBE Reactor

Both EM pumps and centrifugal pumps have advantages and disadvantages regarding their adoption for service in a nuclear reactor cooled by LBE. The selection of a centrifugal pump however would leave fewer obstacles to overcome in both design and application. A significant factor in the selection of a centrifugal pump is based upon the inherent material properties of the LBE coolant.

3.4.4.1. EM Pump Limitations

The LBE coolant over the temperature ranges of the current reactor design is not compatible with continued use in an EM pump. One of the most important criteria that dictates the design of the LBE reactor, and also limits the options in pump selection, is the melting, or freezing, temperature of LBE. Lead-bismuth eutectic solidifies at 125°C, and lead solidifies at 327°C, while sodium solidifies at a lower temperature of 97.8°C [Lyon 1952]. These temperatures have an impact on the operating temperatures of the reactors they cool. In order to prevent freezing in the cold leg of the reactor loop the core inlet and outlet temperatures must be set higher than the freezing temperature of the coolant. A safe envelope must be provided to account for transients, such as loss of preheating of the secondary coolant. The freezing temperature may preclude the use of a pure lead coolant. However, the adoption of a supercritical CO_2 power cycle, which has a heat exchanger inlet temperature of 389°C, may minimize the possibility of coolant freezing.

In the loss of preheating of the secondary coolant, the inlet temperature of the secondary coolant can decrease significantly. As a result, the temperature of the LBE coolant at the outlet of the intermediate heat exchanger or steam generator also decreases. Calculations by Davis found that in the forced circulation condition with water as the secondary coolant (i.e. steam cycle) the LBE temperature in the cold leg dropped to approximately 250ºC [MacDonald and Buongiorno 2001]. The loss of secondary preheating can lower the core inlet temperature by approximately 50ºC. This situation is currently the worst-case scenario for freezing in the cold leg. It should be noted that Davis's calculations used a core thermal power of 650 MWth, as opposed to the current power of 700 MWth [MacDonald and Buongiorno 2001]. For the sake of the general calculations provided here, the difference is assumed negligible.

Another material property that dictates the pump selection is the electrical resistance of the LBE coolant. At operating temperatures the electrical resistance, R, of the LBE coolant is approximately 5 to 6 times higher than that of the sodium coolant. The electrical resistance of LBE and sodium versus temperature is shown in Figure 3.32 [Lyon 1952]. The higher electrical resistance requires a higher voltage and leads to greater electrical losses in the coolant. This results in decreased efficiency and additional heat that must be rejected to the coolant. The inability to operate at high temperature is
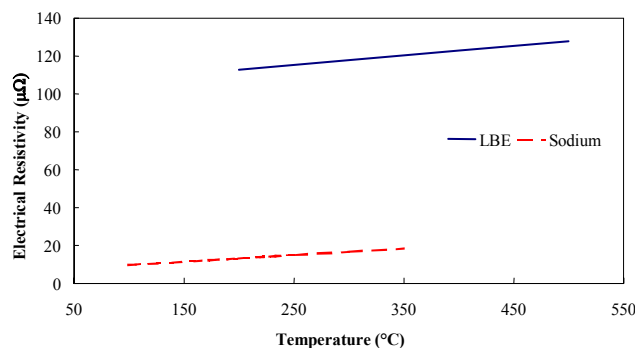
Figure 3.32. Electrical resistivity of sodium and LBE [Lyon 1952].

a weakness of the EM pump's design and the additional heat lowers the probability of success in an LBE reactor.

Table 3.9 shows the temperature ranges of the S-PRISM reactor and the current LBE reactor design. The current LBE reactor design calls for core inlet and outlet temperatures of 467°C and 554.9°C [Dostal et al. 2002]. The temperature rise across the core is a function of core thermal power and coolant mass flow rate and specific heat. Because the coolant mass flow rate is velocity limited, for the same core size and power the temperature rise ΔT cannot be changed.

The current insulation used in EM pumps is rated for an operational temperature of 538°C (1000°F) and requires a temperature differential between the pump and the coolant of at least 167°C (300°F) to

Table 3.9. Comparison of the current temperature parameters of the S-PRISM (sodium-cooled) and LBE (lead-bismuth eutectic cooled) reactors.

		Temperature (°C)
Maximum Insulation Temperature		537.8
Minimum Temperature Differential		166.7
S-PRISM	$T_{Core\ IN}$	371.0
	$T_{Core\ OUT}$	510.0
	$T_{Insulation}$	537.7
LBE	$T_{Core\ IN}$	467.0
	$T_{Core\ OUT}$	554.9
	$T_{Insulation}$	633.7

dissipate the heat produced by the pump. The difference between these two values is 371°C. Therefore, to operate an EM pump for the prerequisite life span of approximately 30 years requires cold leg temperatures that do not exceed 389°C. The current design for the LBE reactor proposes a cold leg temperature of 467°C. This is significantly higher than the 371°C inlet temperature required to preserve the electrical insulation inside an EM pump. Lowering the cold leg temperature by the necessary 96°C to allow EM pump operation would lower the core outlet temperature by the same amount. The S-PRISM design, which makes use of four EM pumps, has a core inlet temperature of 371°C [Boardman 2000]. This is within the envelope for EM pump operation of 371°C. Figure 3.33 graphically represents these temperature relations. The horizontal line represents the maximum operating temperature for sustained EM pump operation. Both plants with lead-based coolants are above this line.

Figure 3.33 shows the current core outlet temperature is 555°C. The current mass flow rate of 54,420 kg/sec, which is determined by the desired power and the LBE coolant, requires a core inlet temperature of 467°C. The criteria set forth above provide a new operating envelope for use with an EM pump. The maximum operating temperature of the EM pump's electrical insulation sets a maximum core inlet temperature of 371°C. If the worst-case scenario of loss of secondary preheating is assumed to create a temperature drop of 50°C, then the lowest operating the core inlet temperature can be set is 175°C to preclude coolant freezing. These two temperature bounds set a new core outlet temperature window of 263°C to 459°C. Core outlet temperatures in

Figure 3.33. Operating temperature range for three liquid metal cooled reactors.

this range would allow the use of an EM pump without either melting the insulation in the EM pump or freezing the LBE coolant in the cold leg during transients. Dostal's calculations showed a temperature drop approximately of 10ºC across the steam generator and a drop of 20ºC across the intermediate heat exchanger for the supercritical-CO_2 cycle [Dostal et al. 2001].

These criteria provide an even lower operating temperature window of 257ºC to 471°C for the steam cycle, and 247ºC to 461ºC for the supercritical-CO_2 cycle. It should also be noted that this window does not provide for a factor of safety; a realistic operating window would be much smaller. These numbers are considerably less than the current maximum temperatures of 540ºC and 538ºC in the steam and supercritical-CO_2 cycles

Figure 3.34 shows the relation between core outlet temperature and the efficiency of each cycle [Dostal 2001]. The result is that with decreasing core outlet temperature, the efficiency of the power cycles drop considerably. Both the steam and supercritical-CO_2 cycles were created with the goal of maximum efficiency centered on a core outlet temperature of 555ºC. To achieve maximum cycle efficiency at a lower temperature would require redesigning the current power cycles. Even with redesigned power cycles with maximum efficiency at the new operating temperature, the overall efficiency would be significantly lower due to the large drop in maximum operating temperature.
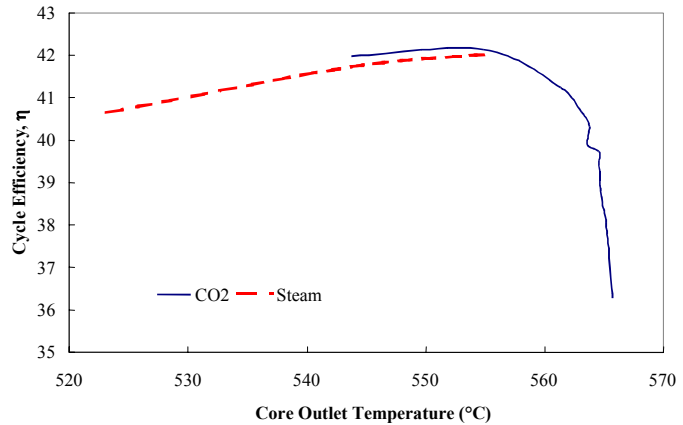
Figure 3.34. Efficiencies of power cycles with current configurations as a function of core outlet temperature.

The maximum operating temperature for each cycle would drop approximately 100ºC, which is not acceptable given the goals of cycle efficiency and cost-effectiveness.

Consequently, despite the advantages and convenience of selecting an EM pump for use in the LBE reactor, it is not an option due to the material properties of LBE and the EM pump temperature limitations. The use of an EM pump would require lowering the core inlet and outlet temperatures to the point where cycle efficiency would be too low to make the reactor profitable.

3.4.4.2. Centrifugal Pump Selection

Designing a centrifugal pump is a highly empirical process. This procedure becomes even more empirical for a liquid metal pump because of higher viscosities and densities. Higher viscosities translate into lower Reynolds numbers, which indicate a larger boundary layer on the impeller blade. Losses will be greater than those experienced in water applications.

The pump design process involves building a small model geometrically similar to the planned prototype pump. Data collected from tests on the model provide an indication of how the larger prototype pump will perform. The affinity laws scale the results of the model up to the larger size of the prototype. The relationship between the model and prototype provides two means of evaluating the performance of a pump for the LBE reactor. Either the pump for an existing LBE-cooled reactor can be scaled or a pump used in pressurized water reactors can be scaled and modified using viscosity correction factors.

Affinity Laws

The affinity laws provide a means of predicting the performance of a pump using data from an existing geometrically similar model. The basis for the affinity laws is the principle of specific speed, n_S, a dimensionless quantity. Dimensions may vary depending on the units chosen, but the specific speed is the speed necessary with a given impeller to produce one unit of volumetric flow per unit time at one unit of head [Stepanoff 1957]. Equation (3.11) is the formula for specific speed. The n term is the rotational speed of the impeller in revolutions per second (RPS). The head term, H, is the pump head in meters and Q is the volumetric flow in meters cubed per second. The gravitational constant, g, is included to provide proper units for n_S.

$$n_S = \frac{n\sqrt{Q_C}}{(gH)^{3/4}}$$ (3.11)

Geometrically similar impellers have a constant specific speed. In general, the model pump's performance is evaluated at its best efficiency point, BEP. These data define the specific speed of the pump. The specific speed sets the performance of the pump at a variety of sizes. If two of the three variables in the specific speed equation are known, then the third can be determined. Two of these three parameters are usually determined by system conditions. For a constant specific speed the ratio of prototype impeller diameter to model impeller diameter is determined by Equation (3.12) [Karrasik et al. 2001].

$$\frac{D_2}{D_1} = \frac{n_1}{n_2}\left(\frac{H_2}{H_1}\right)^{1/2}$$ (3.12)

This process may also be worked in reverse. If the ratio of impeller diameters is known, either the head or pump speed can be set to determine the remaining parameters.

While the specific speed relationship and affinity are true for all centrifugal pumps and fluids, they are derived for water. As a result, there may be some error introduced when applied to other more viscous and dense liquids, but these errors will be minimal [Karassik et al. 2001].

Scaling a Lead-Bismuth Pump

Very little research has been done in the U. S. on the design of centrifugal pumps for use in a nuclear reactor cooled by heavy metal whereas considerable work has been done on the design of sodium pumps, but relative to lead-bismuth, sodium is more similar to water in density and viscosity. The majority of the work on lead-bismuth pumps has been done in Russia and, as such, the SVBR-75 design is the most likely candidate for scaling an existing lead-bismuth coolant pump for use in the LBE reactor.

The SVBR-75 is a 300 MWth nuclear reactor cooled by lead-bismuth eutectic circulated by two centrifugal pumps [Zrodnikov 2000]. Limited information is available regarding these pumps, but the literature provides enough information to apply the affinity laws to obtain a general estimation of the performance in the LBE reactor of a geometrically similar pump. Table 3.10 presents a summary of the important parameters for both the SVBR-75 and LBE reactors. The head term is expressed in meters of lead-bismuth and is an estimate for the LBE reactor. The current design has a core pressure drop of approximately 0.5 MPa, which corresponds to 5.0

meters of lead-bismuth. This value was doubled to provide an initial estimate of total head required. The pump head for the SVBR-75 is also approximate and was estimated based on the core pressure drop.

Table 3.10. Important parameters for the SVBR-75 and LBE reactors

	SVBR-75	LBE
Total Core Mass Flow Rate, $\dot{m}$ (kg/sec)	11,180	52,258
Total Core Volumetric Flow Rate, Q_C (m³/sec)	1.10	5.16
Number of Pumps	2	*TBD*
Pump Diameter (m)	0.5	*TBD*
Pump Head (m)	~ 5.0	~ 10.0

TBD – To be determined

These values are used in the specific speed and affinity law formula presented above. The scaling results using this formula are in Table 3.11.

Table 3.11. Results of the scaling of the SVBR-75 to meet the requirements of the LBE reactor

	2 Pumps	3 Pumps	4 Pumps
n_2/n_1	0.77	0.95	1.09
Impeller Diameter (m)	0.91	0.75	0.65

The term n_2/n_1 represents the ratio of the rotational speeds of the proposed LBE pump and the SVBR-75 pump, respectively. The columns indicate the pump speed ratio and diameter requirements for meeting the LBE reactor's pumping needs with two, three, or four pumps. Because the LBE reactor has a pool configuration and the circulation pumps operate in parallel, each pump provides the same head and a portion of the overall volumetric flow rate. The current reactor design has a volumetric flow rate of 5.40 m³/sec based on the film limit of 2 m/sec flow velocity and a thermal power of 700 MWth.

These calculations only provide an estimate of what is possible with a similar pump. In general pumps become more hydraulically efficient as the impeller diameter increases. Table 3.11 indicates that the LBE reactor's pumping requirements are met by two pumps geometrically similar to the SVBR-75's pumps, but with an increased impeller diameter of 0.91 meters. The current annular gap between the core chimney and the reactor vessel in the LBE reactor is 1.05 meters. Figure 3.35 illustrates the important dimensions of the LBE reactor. Also, the speed ratio of 0.77 shows that the LBE reactor coolant pump would be run at a lower speed than the SVBR-75 pump. Lower speeds lead to lower hydraulic efficiencies but there will be less erosion of the pump components. These calculations should only serve as a rough indicator of what is possible from a well-designed lead-bismuth eutectic coolant pump.   More fine-tuning of blade configurations is necessary, but two centrifugal pumps can meet current pumping requirements and fit within the current reactor vessel arrangement.
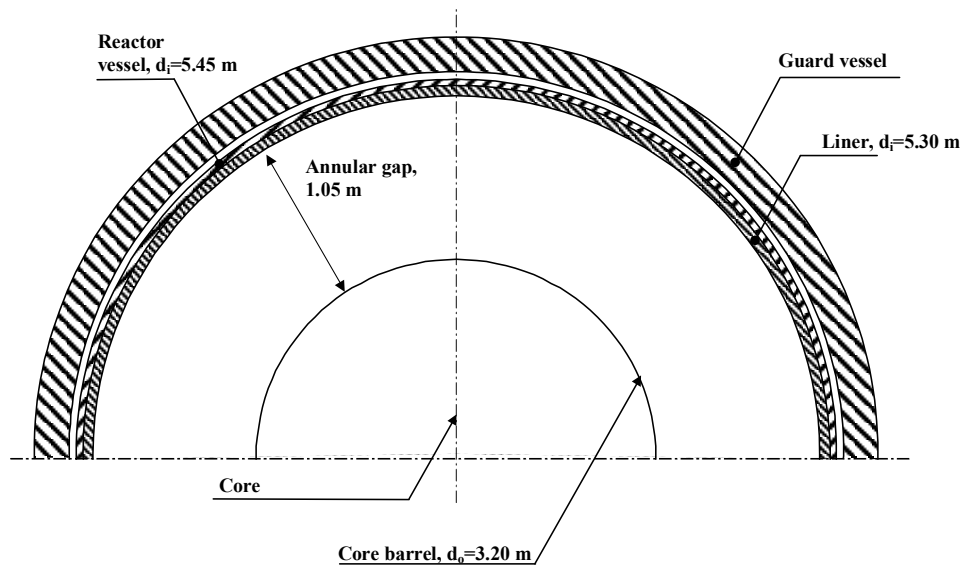
Figure 3.35. Schematic of major reactor internals (note the annular gap of 1.05 meters between the reactor vessel and core barrel) [Dostal, et al, 2002].

Scaling and Correcting a Water Pump

The alternative to scaling an existing lead-bismuth coolant pump is to scale the performance of a well-known water coolant pump. Performance data for water pumps is widely available and correction factors can adjust pump performance for high viscosities and densities. Data for Westinghouse reactor coolant pump model V-11002-A1 were used for scaling. Figure 3.36 is the set of performance curves for this pump [Mach 2001].
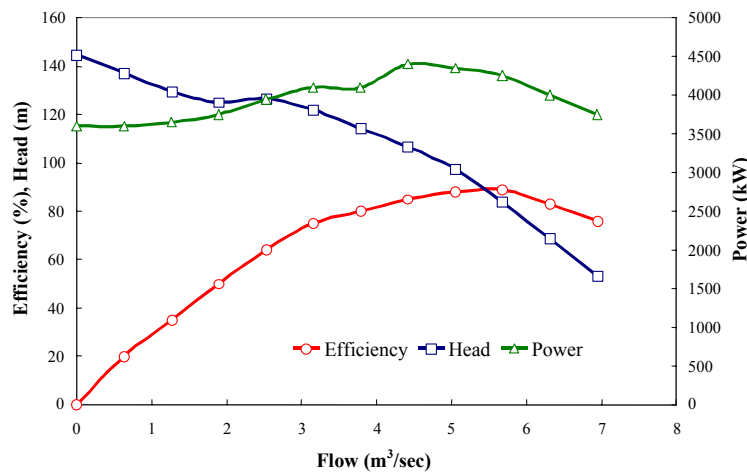
Figure 3.36. Westinghouse reactor coolant pump model V-11002-A1 [Mach, 2001]

The standard procedure for scaling a pump is to use the operating conditions at best efficiency point (BEP). These are the conditions for which the pump was designed to operate. Doing so for the Westinghouse reactor coolant pumps yields a pump speed of 1190 RPM, a head of 83.8 meters of water, and a volumetric flow rate of 5.7 m^3/sec. Using the specific speed relationship and affinity laws the performance of this pump was scaled to meet the requirements of the LBE

reactor. The results were that the LBE pump would have an impeller diameter of 0.28 meters and operate at 2269 RPM, neither of which is reasonable. The impeller may have maximum hydraulic efficiency at these conditions, but the operating speed is much higher than the typical operating window for a centrifugal pump. To obtain a wider range of values, the specific speed and affinity laws were applied over the entire range of operation for the Westinghouse pump and the calculations were performed for every level of efficiency. Figure 3.37 is a plot of these results. Every point on this plot satisfies the LBE reactor's pumping requirements. The efficiency, specific speed, and impeller diameter are given over a range of pump speeds in RPM.
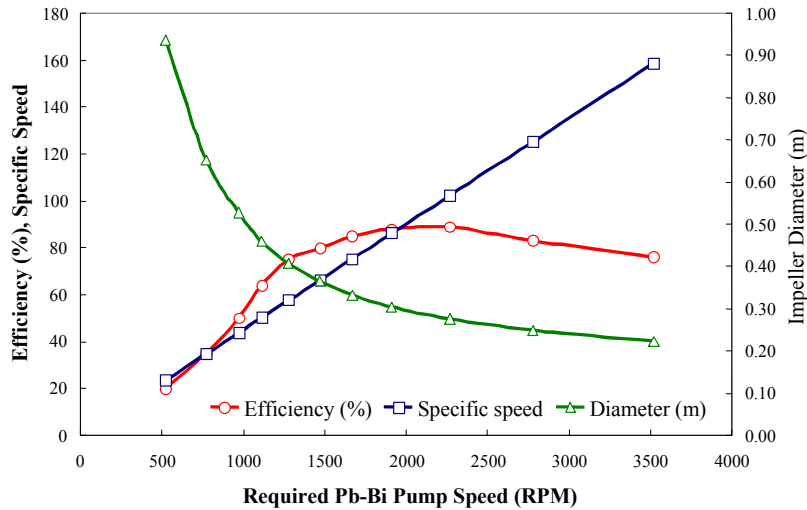
Figure 3.37. Range of performance capable for an LBE pump scaled from a Westinghouse water pump

Once an operating point has been selected, the performance of the water pump with a molten lead-bismuth coolant must be determined. The Hydraulic Institute provides a set of curves for correcting centrifugal pump performance for use with fluids of higher viscosity than water. This chart is presented in Figure 3.38 [Karassik et al. 2001]. To use this correction chart, select a volumetric flow rate from the horizontal axis and proceed vertically upward to the desired pump head. From this point proceed either left or right to the viscosity line for the pumped fluid. Proceeding vertically from this point will intersect the three curves for the head, capacity, and efficiency correction factors. These factors correct for the degraded performance of a water pump used with a more viscous and dense working fluid. Using this chart the performance point of a centrifugal pump can be iteratively found.

Applying the performance of the Westinghouse water pump over its entire range of operation to the lead-bismuth coolant yields interesting results. Due to the high capacity and low head required of the LBE reactor coolant pumps, the intersection with the viscosity line is off the chart to the left. As a result, all three correction-factors are approximately 1.0 (100%), i.e., the hydraulic performance of the Westinghouse pump is not significantly degraded when used with a lead-bismuth coolant.

These relations provide a rough estimation of the performance that can be achieved with an impeller geometrically similar to the Westinghouse pump. Because the pump was designed for use with water, further improvements may be possible. Selecting a realistic point from the scaled curves in Figure 3.36 gives an operating speed of 1275 RPM, an impeller diameter of 0.41 meters, and an efficiency of 75.0%. These numbers are a crude estimation and varying the

impeller blade configuration will likely further improve performance. These calculations only provide an indication that the requirements of the LBE reactor can be met with two centrifugal pumps that will easily fit within the current annular gap of 1.05 meters.
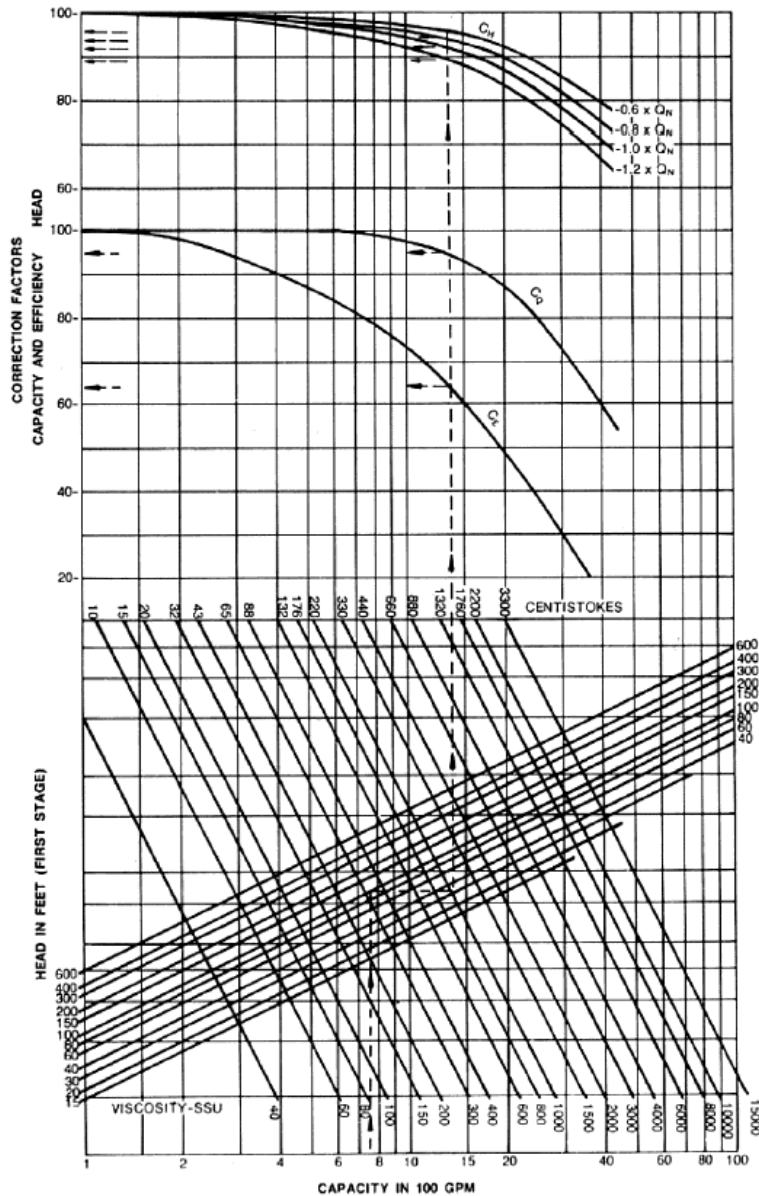
Figure 3.38. Viscosity performance correction chart for use of water tested centrifugal pump data [Karassik 2001]

3.4.5. Pump Cavitation

Cavitation is the condition when cavities of vapor form in the fluid due to a local pressure drop. These cavities collapse when the fluid flow reaches a region of higher pressure within the pump. Cavitation is a major concern because bubble formation can lower pump output and efficiency

and the collapse of these bubbles on pump surfaces can cause significant erosion damage. To begin vapor bubble formation the pressure must correspond to the vapor pressure of the fluid at the local temperature. Because pump performance, and thus cavitation prediction is largely based on experimentally determined parameters, these ideas will be applied to a liquid metal pump with the goal of establishing a method for predicting cavitation and an envelope for cavitation-free operation.

3.4.5.1. Cavitation Theory

Because pump design and evaluation are largely experimental, most theoretical relations are based on coefficients determined from testing on similar pumps. Pump cavitation occurs when Equation (3.13) is satisfied.

$$H_a + h_s = h_l + h_v + \frac{c_1^2}{2g} + \lambda \frac{w_1^2}{2g} \tag{3.13}$$

The various terms of this equation are summarized in Table 3.12. It is important to note that this equation only holds true for centrifugal pumps. Axial flow pumps, which generate a pressure head through propeller motion, do not form an entirely enclosed channel. Thus Equation (3.13), which is derived from Bernoulli's equation, is not applicable to axial flow pumps. In axial flow pumps cavitation is a very localized occurrence

Table 3.12. Definition of terms used in the cavitation equation

Variable	Definition
H_a	System absolute pressure expressed in meters of fluid
h_s	Static head above pump centerline
h_l	Head loss in suction pipe and impeller inlet
h_v	Vapor pressure at coolant temperature
c_1	Average absolute velocity at impeller inlet
λ	Experimental coefficient
w_1	Average relative velocity at impeller inlet
g	Acceleration due to gravity

and does not significantly drop the head produced by the pump.

Cavitation can be predicted by the experimental relationship between the velocity at the impeller inlet and the suction pressure at cut-off capacity [Stepanoff 1957]. The last two terms on the right hand side of Equation (3.13) represent the velocity head of the fluid flow at the pump impeller entrance. The sum of these terms is the dynamic depression, Δh, and states that the dynamic depression can be expressed as a fraction of the total head. This fraction of the total head is the cavitation constant, σ. The term H represents the total head produced by the pump

$$\frac{c_1^2}{2g} + \lambda \frac{w_1^2}{2g} = \Delta h = \sigma H \tag{3.14}$$

If Equation (3.14) is substituted into the original relationship, Equation (3.13), the result is Equation (3.15).

$$H_a + h_s - h_l - h_v = \sigma H \tag{3.15}$$

Solving this equation for σ provides a dimensionless variable that can be used to compare cavitation conditions in two similar pumps.

$$\sigma = \frac{H_a + h_s - h_l - h_v}{H} = \frac{\Delta h}{H} \tag{3.16}$$

Like the pump scaling performed in Section 3.4.4 for similar pumps with constant specific speeds, the cavitation constant σ is also constant. The Δh term can be experimentally determined to be the drop in net positive suction head that produces a 3% drop in pump head. The Δh term is known as the dynamic depression. This relationship is only valid in the region where the affinity laws hold true. If cavitation has already begun, similarity relations are no longer satisfied. Since the data used to predict cavitation is taken from Westinghouse pump performance curves, it is reasonable to believe that the model is not experiencing serious cavitation over the range of data provided. Recall the model is the pump for which performance data is known, while the prototype is the pump for which performance is being predicted.

3.4.5.2. Cavitation Prediction

The pump scaling performed in Section 3.4.4 provides an operating point for both the Westinghouse pump, known as the model, and the scaled prototype pump that fulfills the needs of the LBE reactor. At the chosen operating point on the model pump a given head is produced at a given volumetric flow rate. If the produced head is decreased by 3%, a different flow rate is found. The two different flow rates require different values of NPSHR, which is the net suction pump head required. This is the minimum pump head to prevent the onset of global cavitation in the pump. The difference between these NPSHR values is the term Δh for the model pump. Since both the produced head and the change in NPSHR are known, the dimensionless cavitation term can be calculated. Figure 3.39 illustrates the graphical relation between the decrease in head and dynamic depression.
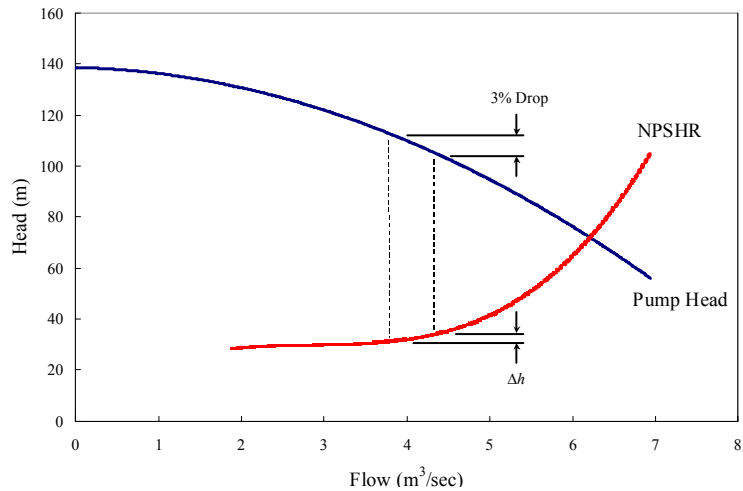
Figure 3.39. The dynamic depression is the change in NPSH that produces a 3% drop in the head generated by the pump

The pump scaling laws determine the parameters for the prototype pump that meets the needs of the LBE reactor. At a constant specific speed, the cavitation number (σ, defined below) will also be constant. Since the head to circulate the primary coolant is also known, the value of Δh for the LBE pump is determined. Equation (3.16) can be expressed as:

$$H_a + h_s - h_l - h_v = \Delta h \tag{3.17}$$

All the terms in Equation (3.17) are in units of meters of LBE coolant. The ambient pressure in the reactor is H_a, and the vapor pressure of the primary coolant is h_v. The vapor pressure of LBE coolant is negligibly small (its value at 467°C is 4.4x10^{-7} Pa, which translates into 4.4x10^{-9} m LBE). The h_l term is the head loss at the impeller inlet. The magnitude of the head loss at the pump inlet cannot accurately be predicted a priori. Instead, it will remain an independent variable in this evaluation of cavitation. This makes it possible to determine an envelope for cavitation-free operation to serve as a design guideline. The dependent variable in this relation is the suction head required, h_s, which is the net positive suction head required to prevent cavitation in the pump. Since h_s is measured in meters of LBE, it can be thought of as the depth of the pump impeller inlet necessary to prevent cavitation. Hence we develop the map for predicting cavitation based on the transformation of Equation (3.17) to Equation (3.18).

$$h_s = h_l + h_v - H_a + \Delta h \tag{3.18}$$

Figure 3.40 is a plot of h_s versus h_l for the base case in which the pump must provide 2.0 MPa (approximately 20 meters of LBE) of head to circulate the primary coolant (a very conservative assumption). Note the relationship is linear between the head loss at the pump inlet and the suction head required, which could be predicted from the form of Equation (3.18).
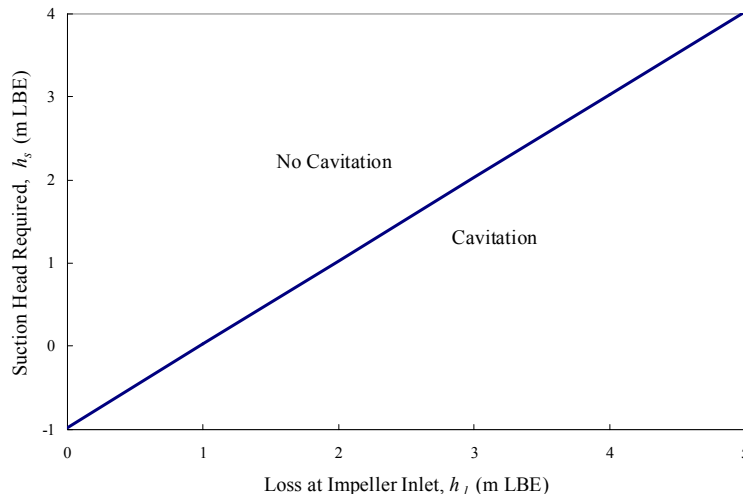
Figure 3.40. Map predicting cavitation for the base case of an LBE pump that generates 2 MPa of pump head, a LBE coolant vapor pressure of 80.9 kPa, and dynamic depression (ΔH) of 0.31 meters.

These results may be interpreted as not conservative due to the small value chosen for the vapor pressure of the LBE coolant. The current analysis uses an LBE vapor pressure of 4.4x10^{-7} Pa, which is evaluated at the cold leg temperature of 467.0°C. The temperature anywhere in the primary system is not expected to exceed 800°C during any transient and this corresponds to an LBE vapor pressure of 14.7 Pa, which corresponds to 0.148 m LBE. Therefore, the pump cavitation is not very sensitive to the value of the LBE vapor pressure, since its value is negligibly small.

Although this evaluation has shown that cavitation is not a serious concern under the conditions in the LBE reactor, it is important to remember the special conditions of this evaluation. These relationships are valid for centrifugal pumps only, and do not include axial flow or propeller type pumps, which generate pump head in a different manner. Nor do these relationships cover very localized cavitation at impeller blade tips. Evaluations such as these would require both well developed models of the pump and considerable experimental work.

Localized cavitation can also be particularly damaging to pump components, and deserves further attention. Worthy of further research is the formation and collapse of gas bubbles within the LBE

coolant. The cover gas, most likely argon, has a finite solubility in LBE. A change in the local pressure could cause the solubility limit to change, which would lead to the formation of cover gas bubbles.   Upon either entering a higher-pressure region or impacting internal pump components, damaging cavitation could occur. Again, research such as this requires a better picture of the actual pump design and flow paths.

3.4.6. Pump Erosion

Another concern is the erosion of centrifugal pump components. Corrosion concerns have created a 2.0 meters per second velocity limit throughout the reactor core and heat exchangers. This limit was set to prevent the erosion of the protective oxide film layer on the internal reactor components. Since a centrifugal pump circulates fluid by converting a velocity head into a pressure, high speeds within the pump are unavoidable. Never the less, it may be helpful to make an estimate of the LBE velocity within the pump. This calculation requires the selection of an example pump and operating point. Section 3.4.4 found that two pumps geometrically similar to the Westinghouse centrifugal pump could meet the pumping needs of the LBE reactor with impellers 0.41 meters in diameter, operating at a speed of 1275 RPM. Since information on the Westinghouse pump is limited, several assumptions will have to be made about the dimensions of the pump.

Fluid velocity calculations in centrifugal pumps are performed with a velocity triangle.   The components of the velocity triangle are the absolute velocity of the impeller tip (u), the absolute coolant velocity at the impeller tip (c), and the velocity of the coolant relative to the blade tip (w). These three velocities can be thought of as vectors (Figure 3.41).   The angle the fluid absolute velocity vector makes with the impeller tip absolute velocity is θ.
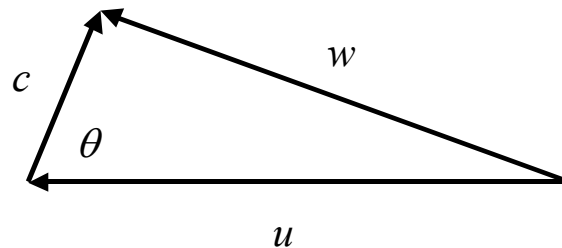
Figure 3.41. Centrifugal pump velocity triangle; relates the coolant absolute velocity (*c*), the impeller absolute velocity (*u*), to the velocity of the coolant relative to the impeller (*w*).

Few specifics are known about the pump at this point. The only known value is the absolute velocity of the impeller tip, u. A well-designed pump will convert the majority of the velocity head it creates into a pressure head, thus the radial velocity will be small. Also, the angle between the coolant and impeller absolute velocities will be small.   An appropriate first approximation of the LBE velocity in the reactor coolant pump is the absolute velocity of the blade tip (i.e., if both c and θ are small then $w \approx u$). Where n is the rotational speed of the pump impeller in revolutions per second, the highest LBE velocity relative to the pump impeller can be approximated by Equation (3.19).

$$u = \pi \cdot D \cdot n \qquad\qquad (3.19)$$

Applying Equation (3.19) calculates a relative LBE velocity of 27.4 meters per second. Given that this is much higher than the coolant limit of 2.0 meters per second elsewhere in the reactor, some special provisions may be required to keep corrosion and erosion in the reactor coolant

pumps to a minimum. This may require special materials, a coating, plating, or easily replaceable pump components and is worthy of future attention.

3.4.7. Pump Selection Conclusions

Either of the two methods, scaling an existing LBE pump or applying viscosity correction-factors to a water pump, can be used to verify that the pumping requirements of the current design for the LBE reactor can be met. Recall from above it was determined that two pumps with impeller diameters of 0.41 meters operating at 1275 RPM could meet the pumping needs of the LBE reactor. Although large uncertainties are associated with each method, their effects on pump performance are negligible. A pump specially designed for the LBE application, as opposed to scaled from another reactor, will likely yield even better results. These improvements will result in higher efficiencies and smaller pump dimensions. Also, a method for determining an envelope for pump cavitation was presented. Again, it is important to recall that this theory is accurate for predicting global pump cavitation. Evaluating cavitation at the impeller blade tips is significantly more difficult. Once a more refined design for the pump impeller is known, the evaluation of both the localized pump cavitation and velocity throughout the pump require further attention. Also, a more refined design will make it possible to determine coolant velocities throughout the pump to provide a better estimation of the effects of erosion.

3.5. Heat Exchanger Design (R. Herron, MIT)

3.5.1. Introduction

The work of Dostal et al. [2002] provides a starting point for the steam generator and heat exchanger designs. His work provides base case values of total surface area and convection coefficients to validate the final steam generator and heat exchanger designs. The objective here is to update the design with the addition of support baffles and improved modularity.

One important concept adopted from Dostal's work was the coolant configuration in the steam generators and CO_2 heat exchanger. For all heat exchanger variants the primary coolant fills the shell side and the secondary coolant is in the tubes. A configuration like this has two advantages. Because the primary coolant (LBE) operates at atmospheric pressure, the shell does not need to serve as a pressure boundary. Instead, the tubes contain the pressure of the secondary coolant, which is approximately 15.0 MPa for the superheated water steam generator and 19.72 MPa for the CO_2 heat exchanger [Dostal et al. 2002]. Because of their small diameter, normal thickness tubes can withstand the high internal pressure. Also, the secondary coolants are more fouling than the LBE coolant, and the tube side is easier to clean [Kakaç and Liu 1998]. In addition to revisions of the superheated steam and supercritical CO_2 heat exchangers, a supercritical steam generator is presented here for a supercritical steam cycle. The pressure for the supercritical cycle is 25.0 MPa.

Important modifications have been made, however, to the earlier iterations of the heat exchanger design. These include the addition of shell side baffles and a shift to a more modular design. The previous design made use of two large kidney-shaped heat exchangers, which filled the annular gap between the core barrel and the reactor vessel. The new modular design uses eight cylindrical heat exchangers, which facilitates the repair and replacement of damaged heat exchangers.

Baffles in a shell and tube heat exchanger serve two very important functions. First, they provide support for the tubes and improve structural rigidity. This prevents tube sagging and decreases the magnitude of tube vibration. Tube natural frequency is a function of tube length and adding support baffles effectively shortens the length of the tube, which raises its natural frequency. Increasing the natural frequency reduces the threat of resonance and damage due to vibration [Kakaç and Liu 1998]. Second, baffles force the shell side coolant into cross flow over the tube bundles. This provides higher heat transfer coefficients than longitudinal flow along the tube bank. Several varieties of baffles are available to the heat exchanger designer, but single segmental baffles were chosen due to simplicity of design.

3.5.2. Shell Side Heat Transfer

All three heat exchanger variants have the primary LBE coolant on the shell side. Thus, the relationships governing shell side heat transfer will be the same for the steam generators and heat exchangers.
A special Nusselt number correlation was chosen because the shell side LBE flows through the tube bundle in cross flow. Hsu's Nusselt number correlation is for a constant heat flux tube bank in liquid metal cross flow [Foust 1976]. Throughout this section a subscript s denotes shell side properties (primary coolant) and the subscript t denotes tube side properties (secondary coolant).

$$Nu_s = 0.958 \left(\frac{\phi}{d_o} \right)^{1/2} \left(\frac{p - d_o}{p} \right)^{1/2} Pe^{1/2}$$

(3.20)

The second term on the right side of the equation is a function of the tube bundle's pitch-to-diameter ratio and is given by a look-up table. For simplicity in the computer calculation routine for calculating the shell side heat transfer coefficient this table was approximated by a third order polynomial:

$$\frac{\phi}{d_o} = 7.4627 \left(\frac{d_o}{p} \right)^3 - 4.9543 \left(\frac{d_o}{p} \right)^2 + 1.5838 \left(\frac{d_o}{p} \right) + 1.9232$$

(3.21)

The heat transfer coefficient is a function of the Nusselt number, the effective diameter of the tube bundle, and the thermal conductivity of the LBE coolant.

$$h_s = \frac{Nu_s \cdot k_{LBE}}{d_e}$$

(3.22)

The effective diameter, d_e, is a function of tube pitch, p, and tube outside diameter, d_o, for a tube bank with a triangular pitch [Kakaç and Liu 1998].

$$d_e = \frac{4 \left(\frac{p^2 \sqrt{3}}{4} - \frac{\pi \cdot d_o^2}{8} \right)}{\pi \cdot d_o / 2}$$

(3.23)

The above set of correlations provides a means of calculating the ideal convection coefficient (h_s) for a liquid metal in cross flow over a bundle of heat exchanger tubes with a triangular pitch. The Bell-Delaware method of heat exchanger design supplies a set of correction factors, J, to adjust for the differences between the ideal and average convection coefficient, $h_{s,avg}$.

$$h_{s,avg} = J_c J_l J_b J_s J_r h_s \qquad (3.24)$$

The series of correction factors factor adjust for different effects introduced by the use of baffles. The product of the five correction factors can be taken as 0.6 for a well-designed and constructed heat exchanger [Kakaç and Liu 1998].

The use of shell side baffles requires special relations to define certain parameters, such as mass flux. With shell side baffles the primary coolant does not fill the diameter of the shell, but instead flows perpendicularly across the tube bundle between a set of baffles. Adjusting the flow area accordingly and carrying this forward in calculating the mass flux, G_s, and Reynolds number, Re_s, compensates for this difference. Equation (3.25) defines the shell side flow area. The independent variables are inside shell diameter, D_s, shell length, L, and total number of baffles, N_b.

$$A_s = \frac{D_s L}{N_b + 1} \qquad (3.25)$$

To fit within the allotted space between the reactor vessel and the core chimney, the heat exchanger inside shell diameter is nominally one meter.

3.5.3. Tube Side Heat Transfer

The procedure for determining the heat transfer coefficient on the tube side is distinctly different, depending on the use of either a single phase (supercritical-CO_2) or two-phase (H_2O) coolant.

3.5.3.1. Superheated Steam Generator

The superheated steam generator is composed of four heat transfer regions. These are the sub-cooled region, the nucleate boiling region, the post critical heat flux region, and the superheated region.

Sub-Cooled Region

The sub-cooled region is the entrance region to the steam generator. The feed water temperature is set by the power cycle and the saturation temperature is a function of the tube side pressure. Sub-cooled nucleate boiling is neglected. This region has only single-phase flow, so the Dittus-Boelter correlation determines the Nusselt number [Todreas and Kazimi 1990].

$$Nu_t = 0.023 \, Re^{0.8} \, Pr^{0.4} \qquad (3.26)$$

The convection coefficient in this region is a function of the Nusselt number, given by Equation (3.26). Water exits the sub-cooled region as a saturated liquid.

Nucleate Boiling Region

The nucleate boiling region extends from saturated liquid to the point of critical quality. In this region the Chen correlation determines the convection heat transfer coefficient. The convection coefficient in this region can be thought of as the superposition of convection and nucleate boiling heat transfer coefficients. Chen uses a suppression factor, S, to suppress the heat transfer by nucleate boiling and calculate an accurate two phase heat transfer coefficient, $h_{2\phi}$.

$$h_{2\phi} = h_c + h_{NB} \tag{3.27}$$

The convection coefficient is given by a correlation similar to the Dittus-Boelter correlation. All fluid properties are evaluated at the saturation point and the F term is an additional correction factor.

$$h_c = 0.023 \left(\frac{G_t d_i (1 - x_{critical})}{\mu_f} \right)^{0.8} Pr_f^{0.4} \frac{k_f}{d_i} F \tag{3.28}$$

The F term is a function of X_{tt}, a constant based on the fluid properties at the saturation point.

$$\frac{1}{X_{tt}} = \left(\frac{x}{1-x} \right)^{0.9} \left(\frac{\rho_f}{\rho_g} \right)^{0.5} \left(\frac{\mu_g}{\mu_f} \right)^{0.1} \tag{3.29}$$

The nucleate boiling component of the Chen correlation likewise uses fluid properties evaluated at the saturation point. In addition, there are factors included for the difference between the wall temperature and the bulk fluid temperature, and the suppression factor S. The suppression factor is a function of the Reynolds number in the region and the correction factor for the convection coefficient, F. The subscript f denotes liquid properties and the subscript g denotes gas properties.

$$h_{NB} = S(0.00122) \left[\frac{\left(k^{0.79} c_p^{0.45} \rho^{0.49} \right)_f}{\sigma^{0.5} \mu_f^{0.29} h_{fg}^{0.24} \rho_g^{0.24}} \right] \Delta T_{sat}^{0.24} \Delta P^{0.75} \tag{3.30}$$

$$S = \frac{1}{1 + 2.53 \cdot 10^{-6} \left(Re_f \, F^{1.25} \right)^{1.17}} \tag{3.31}$$

The Chen correlation determines the heat transfer coefficient at a point in the nucleate boiling region where the local quality is x. This steam generator design uses a value of half the critical quality to determine an average heat transfer coefficient in the nucleate boiling region [Todreas and Kazimi 1990].

Post Critical Heat Flux Region

The post critical heat flux region accounts for heat transfer to the steam from dry-out to saturation. In this region there is a significant deterioration of the heat transfer coefficient from the nucleate boiling region. The Groeneveld correlation is a common method for calculating the heat transfer coefficient in this region:

$$Nu_t = 0.00109 \left\{ Re_g \left[x + \frac{\rho_g}{\rho_f}(1-x) \right] \right\}^{0.989} Pr_g^{1.41} Y \qquad (3.32)$$

$$Y = \left[1 - 0.1 \left(\frac{\rho_f - \rho_g}{\rho_g} \right)^{0.4} (1-x)^{0.4} \right]^{-1.15} \qquad (3.33)$$

Here, again, an average quality provides an average heat transfer coefficient over the region.

Superheated Region

The LBE reactor produces steam superheated nearly 200ºC above the saturation temperature. As a result, the superheated region accounts for the majority of the steam generator's tube length. Because the heat transfer is single phase (the coolant enters this region as saturated steam) the Dittus-Boelter correlation determines the Nusselt number, like in the sub-cooled region. All fluid properties are calculated at the average temperature in the region. This is the average of the saturation and steam generator outlet temperatures.

Critical Quality

We require the critical quality to determine the average heat flux in the nucleate boiling region. Determining the critical quality is an iterative process, which begins with the assumption of a reasonable value for the critical quality (here 0.5 was used). The CISE-4 relationships were used in determining the critical quality. An assumed value of the critical quality makes it possible to determine a shell side coolant temperature change over the nucleate boiling region. The h_{fg} term is the latent heat of vaporization of water at the local conditions and c_s is the specific heat of the shell side coolant.

$$\Delta T_s = \frac{\dot{m}_t h_{fg} x_{critical}}{\dot{m}_s c_s} \qquad (3.34)$$

Given the shell side coolant temperature at the inlet, it is now possible to determine the shell side coolant temperature at the outlet to the region. Using these parameters and the NTU method, which will be fully explained in Section 3.5.5.2, the critical length is determined.

$$l_{critical} = \frac{NTU \cdot \dot{m}_s c}{U_{total} \pi d_o N_t} \qquad (3.35)$$

The critical length, $l_{critical}$, provides the critical quality according to Equation (3.36).

$$x_{critical} = \frac{a_{CISE4} l_{critical}}{l_{critical} + b_{CISE4}}$$ (3.36)

The CISE-4 constants, a_{CISE4} and b_{CISE4}, are found according to Equations (3.37) through (3.39) [Todreas and Kazimi 1990].

$$a_{CISE4} = \frac{1}{1 + 1.481 \cdot 10^{-4} \left(1 - \frac{p}{p_c}\right)^{-3} G_t} \quad \text{if } G \leq G^*$$ (3.37)

$$a_{CISE4} = \frac{1 - \frac{p}{p_c}}{\left(\frac{G_t}{1000}\right)^{1/3}} \quad \text{if } G > G^*$$ (3.38)

$$b_{CISE4} = 0.199 \left(\frac{p_c}{p} - 1\right)^{0.4} G \cdot d_i^{0.4}$$ (3.39)

The p_c term is the critical pressure for water. Equation (3.40) determines the mass flux G^* [Todreas and Kazimi 1990].

$$G^* = 3375 \left(1 - \frac{p_c}{p}\right)^3$$ (3.40)

An iterative process is required between the critical quality and the convection coefficient in the nucleate boiling region. Initial guesses for each can be refined until the difference between successive iterations minimized.

3.5.3.2. Supercritical Steam Generator

The possibility of a supercritical steam cycle was investigated as a power conversion cycle for the lead-bismuth-cooled reactor. Supercritical steam generators heat water from sub-cooled to supercritical without a distinct phase change. This is achieved by maintaining the pressure on the tube side, where the secondary water coolant flows, above the critical pressure. The critical pressure for water is 22.09 MPa and the critical point is at a temperature of 374.2°C.

Because no distinct phase change occurs, the above correlations are not appropriate for calculating the convection coefficients for a supercritical steam generator. Cho, Chou, and Cox [1976] provide the following correlation for the Nusselt number for supercritical steam:

$$Nu_t = 0.00459 \left(\frac{G d_i}{\mu_b}\right)^{0.923} \left(\frac{h_w - h_b}{T_w - T_b} \cdot \frac{\mu_w}{k_i}\right)^{0.613} \left(\frac{v_b}{v_w}\right)^{0.231}$$ (3.41)

The same subscript conventions apply here. The subscript w indicates the water property evaluated at the local wall temperature and the subscript b indicates the water property evaluated

at the bulk coolant temperature. The v terms are the specific volume of the coolant, which is the inverse of the coolant's density. Another property unique to the supercritical steam generator is the fouling factor. A fouling factor of 0.000026 m^2K/W is appropriate for the tube side of a supercritical steam generator [Cho, Chou, and Cox 1976]. The Nusselt number is converted to a convection coefficient by the conventional means. The thermal conductivity of the coolant is evaluated at the wall temperature.

$$h_t = \frac{Nu_t \cdot k_w}{d_i}$$

(3.42)

3.5.3.3. CO₂ Heat Exchanger

The procedure for determining the tube side heat transfer coefficient is significantly simpler for the supercritical-CO_2 heat exchanger. Since this heat exchanger is single phase an averaged heat transfer coefficient can be used. The starting point is calculating the tube side Nusselt number. Barnes and Jackson developed a correlation for the turbulent forced convection of CO_2 [Kakaç and Yener 1995].

$$Nu_t = 0.023\,\mathrm{Re}^{0.8}\,\mathrm{Pr}^{0.4}\left(\frac{T_w}{T_b}\right)^{-0.27}$$

(3.43)

The temperature correction term, $\left(T_w/T_b\right)^{-0.27}$, is unnecessary for wall to bulk temperature ratios of less than 1.2, where the temperatures are expressed in absolute units. A conservative estimate of this temperature ratio can be made at the gas inlet to the CO_2 heat exchanger, where the LBE temperature is 467ºC and the CO_2 temperature is 389ºC, which is a temperature ratio of 1.1. Thus, the temperature ratio term can be set to 1.0, which reduces Equation (3.43) to the Dittus-Boelter correlation. The Nusselt number then provides a means of calculating the average tube side convection coefficient based on the inside diameter and CO_2 thermal conductivity.

$$h_t = \frac{Nu_t \cdot k_{CO_2}}{d_i}$$

(3.44)

All the properties for the CO_2 were calculated based on the average of the tube inlet and outlet temperatures.

3.5.4. Overall Heat Transfer

After the heat transfer coefficients for both the tube side and shell side are known, it is necessary to compute an overall heat transfer coefficient, U. The overall heat transfer coefficient simplifies the heat exchanger design process and allows calculation of the heat flux as a function of the primary and secondary coolant temperatures. Equation (3.45) is the overall heat transfer coefficient for a heat exchanger with clean surfaces. This provides the overall heat transfer coefficient based on the tube outside surface area.

$$\frac{1}{U_c} = \frac{1}{h_s} + \frac{d_o}{2k_{tube}}ln\left(\frac{d_o}{d_i}\right) + \frac{d_o}{h_t d_i}$$

(3.45)

Unfortunately, heat exchangers rarely have clean heat transfer surfaces. As a result, fouling factors must be introduced to compensate for the fouling of surfaces and decreased heat transfer. Fouling factors are determined for both shell side and tube side surfaces.

$$\frac{1}{U} = \frac{1}{h_s} + R_{f,s}d_o + \frac{d_o}{2k_{tube}}ln\left(\frac{d_o}{d_i}\right) + R_{f,t}d_o + \frac{d_o}{h_t d_i} \tag{3.45}$$

On the LBE shell side region the fouling factor is due to the presence of a thin oxide layer, which prevents further corrosion. This oxide layer is approximately 0.0001 meters thick, which is relatively thin compared to the tube's radius of curvature. Thus, the oxide layer can be modeled as a plane without introducing any significant error. The fouling factor of the oxide layer is the ratio of the layer thickness to its thermal conductivity.

$$R_{f,s} = \frac{t_{oxide}}{k_{oxide}} \tag{3.46}$$

The determination of the water/CO_2 tube side fouling factors is considerably more complex. As a result, fouling factors provided by TEMA were used in calculations. The steam generator (superheated and supercritical) and heat exchanger the tube side fouling factors were selected as 0.000176, 0.000026, and 0.000088 m^2K/W, respectively [Kakaç and Liu 1997].

3.5.5. Heat Exchanger Sizing

If an overall heat transfer coefficient, U, is known, the $\varepsilon - NTU$ method provides a simple means of sizing a heat exchanger.

3.5.5.1. Energy Balance

The first step is to perform an energy balance to determine the coolant mass flow rates and the inlet and outlet temperatures. All energy transferred to the primary coolant by the reactor core must be transferred to the secondary coolant. This determines the total energy, Q. The core inlet and outlet temperatures also set the heat exchanger outlet and inlet temperatures, respectively. The secondary coolant inlet temperature is set by the analysis of the power cycle, as is the primary coolant mass flow rate. Equation (3.48) is the heat exchanger energy balance. The h terms represent the coolant enthalpy at the inlets and outlets of the heat exchanger. Specific heat and the inlet and outlet temperatures may also be used, but here the enthalpy convention is used to be broadly applicable to single and two-phase heat exchangers.

$$Q = \dot{m}_s\left(h_{in} - h_{out}\right)_s = \dot{m}_t\left(h_{out} - h_{in}\right)_t \tag{3.48}$$

Since the secondary coolant's enthalpy at the outlet is a function of temperature, Equation (3.48) determines the secondary coolant mass flow rate and maximum temperature as a function of other system parameters.

3.5.5.2. The *ε-NTU* Method

The $\varepsilon - NTU$ method provides a non-iterative means of calculating unknown heat exchanger parameters. This method is based on the fact that the inlet and outlet temperatures of a coolant are functions of the overall heat transfer coefficient, total surface area, and the heat capacities of the two coolants. Equation (3.49) is the basic governing relationship of the $\varepsilon - NTU$ method [Kakaç and Liu 1998].

$$NTU = \frac{UA}{C_{min}} \qquad (3.49)$$

In the $\varepsilon - NTU$ terminology, C represents the heat capacity of a coolant stream, which is the product of the specific heat and mass flow rate. The subscripts *min* and *max* represent the smaller and larger heat capacities of the two streams. The left side of Equation (3.49), NTU, is a function of ε, the ratio of coolant stream heat capacities (C_r), and the geometry of the heat exchanger. The geometry of the heat exchanger is a shell and tube geometry with multiple passes and cross-flow with an overall counter flow orientation. The method for determining NTU depends on the arrangement of the fluid streams. There are two basic cases: (1) the fluid stream of minimum heat capacity (C_{min}) is mixed, or (2) the fluid stream of maximum heat capacity (C_{max}) is mixed. The first case is true for the boiling regions of the superheated steam generator, while the second is true for all other regions and heat exchangers.

The ε term is often referred to as the "effectiveness" of a heat exchanger and is the ratio of the actual heat transfer to the maximum possible heat transfer.

$$\varepsilon = \frac{Q}{Q_{max}} = \frac{C_s\left(T_{in} - T_{out}\right)_s}{C_{min}\left(T_{s,in} - T_{t,in}\right)} = \frac{C_t\left(T_{out} - T_{in}\right)_t}{C_{min}\left(T_{s,in} - T_{t,in}\right)} \qquad (3.50)$$

Depending on the arrangement of the fluid streams, a series of equations determines the NTU value for the region. For either case the basic relation is the same. In Equation (3.51) ε is the overall effectiveness of the heat transfer region and ε_p is the effectiveness of a single cross flow pass. The term n is the number of passes per heat transfer region and is not required to be an integer [Kays and London 1964].

$$\varepsilon = \frac{\left(\dfrac{1 - \varepsilon_p\, C_{min}/C_{max}}{1 - \varepsilon_p}\right)^n - 1}{\left(\dfrac{1 - \varepsilon_p\, C_{min}/C_{max}}{1 - \varepsilon_p}\right)^n - \dfrac{C_{min}}{C_{max}}} \qquad (3.51)$$

When the fluid stream of maximum heat capacity is mixed (case (2)) the following series of equations are used. The cross flow pass effectiveness (ε_p) is determined by Equation (3.52). This determines Γ, which then determines NTU [Kays and London 1964].

$$\varepsilon_p = 1 - \exp\left(-\Gamma\, C_{max}/C_{min}\right) \qquad (3.52)$$

$$\Gamma = 1 - \exp\left(-NTU \cdot C_{min}/C_{max}\right) \tag{2.53}$$

For the case when the stream of maximum heat capacity is unmixed (case (1)), a different relation is use to calculate NTU for the ε_p given by Equation (3.51). In the boiling regions the ratio of heat capacities is taken to be zero, since the temperature of the boiling fluid is a constant. Thus, NTU can be determined directly from ε_p with Equation (3.54) [Kays and London, 1964].

$$\varepsilon_p = 1 - \exp\left(-NTU\right) \tag{3.54}$$

Now that NTU is known, the only remaining unknown is the total surface area per heat exchanger, A. Equation (3.49) defines the total surface area in terms of known heat transfer and coolant parameters.

This procedure is used for all heat exchanger calculations. The steam generators introduce two unique requirements, though. Because the tube side heat transfer coefficients vary significantly over the length of the heat exchanger, the $\varepsilon - NTU$ method must be performed stepwise. This requires the length of the superheated steam generator to be divided into four heat transfer regions. For the supercritical steam generator the heat transfer coefficient is highly dependent on the wall temperature so the length must be subdivided into many more regions.

3.5.5.3. Heat Transfer Area

The overall heat exchanger length is dependent on the required overall heat transfer surface. Equation (3.55) is the total surface area per heat exchanger.

$$A = \pi \cdot d_o N_t L \tag{3.55}$$

N_t is the total number of tubes per heat exchanger and is given by a packing formula, Equation (3.56) [Kakaç and Liu 1997].

$$N_t = 0.785 \left(\frac{CTP}{CL}\right)\frac{D_s^2}{p^2} \tag{3.56}$$

Kakaç and Liu calculated values for CTP and CL of 0.93 and 0.87 for a single pass shell and tube heat exchanger with a triangular pitch. These two equations determine the overall length of the heat exchanger tubes. Now all heat exchanger parameters can be determined.

3.5.5.4. Axial Variation in the Shell Side Convection Coefficient

An averaged shell side convection coefficient was used in computing the overall convection coefficient. Recall Equation (3.46) from above. This is the formula for the overall convection coefficient. The shell side convection coefficient will vary slightly over the length of the heat exchanger, but not significantly enough to introduce noticeable error. The CO_2 heat exchanger will be used to evaluate the effects of this axial variation. The averaged shell side convection coefficient used is 44,577 W/m²K. The shell side convection coefficient really varies from 45,494 to 43,687 W/m²K from the inlet to the outlet, respectively. Although this is a significant change of nearly 2,000 W/m²K, due to the tube wall resistance and the small values for the tube

side convection coefficients in all three heat exchanger variants, the effect on the overall convection coefficient is negligible. For the CO_2 heat exchanger the overall convection coefficient as a function of the shell side convection coefficient is plotted below, in Figure 3.42.
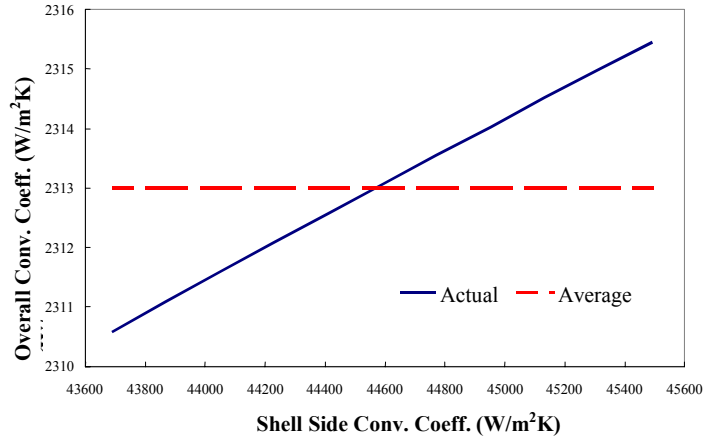
Figure 3.42. Variation of the overall convection coefficient over the range of shell side convection coefficient values.

Note that the overall convection coefficient varies approximately 5 W/m^{2}K over the whole rage of shell side convection coefficients. Thus it seems reasonable to use an averaged shell side convection coefficient in determining the overall heat transfer properties of the heat exchanger designs.

3.5.6. Shell Side Pressure Drop

Due the high pumping power required to circulate the LBE primary coolant, the shell side pressure drop is a major concern. Minimizing the shell side pressure drop minimizes self-power consumption and maximizes the net plant efficiency. The heat exchanger is of a multiple pass, cross flow, shell and tube design. This complex configuration makes the formula for the shell side pressure drop equally complex. Equation (3.57) is Kakaç and Liu's formula for the shell side pressure drop, where N_b is the number of baffles per heat exchanger.

$$\Delta P_T = [(N_b - 1)\Delta P_{bi} R_b + N_b \Delta P_{wi}]R_l + 2\Delta P_{bi}\left(1 + \frac{N_{cw}}{N_c}\right)R_b R_s \tag{3.57}$$

This equation uses several terms that are further defined below. ΔP_{bi} and ΔP_{wi} are the pressure drop components between adjacent baffles and in the baffle window, respectively.

$$\Delta P_{bi} = 4f\frac{G_s^2}{2\rho_s}\left(\frac{\mu_{s,w}}{\mu_s}\right)^{0.14} N_c \tag{3.58}$$

$$\Delta P_{wi} = \frac{\dot{m}_s^2(2 + 0.6N_{cw})}{2\rho_s A_s A_w} \tag{3.59}$$

The terms N_c and N_{cw} indicate the number of tube rows the primary coolant passes between adjacent baffles and in the baffle windows, respectively. The term p_p is the tube bank pitch in the direction of coolant flow.

$$N_c = \frac{D_s\left(1 - 2\dfrac{L_c}{D_s}\right)}{p_p} \tag{3.60}$$

$$N_{cw} = \frac{0.8L_c}{p_p} \tag{3.61}$$

If the reasonable assumption is made that the primary coolant viscosity ratio, raised to the 0.14 power, is approximately unity, then some simplifications can be made. If the constant coefficients for each term (ΔP_{bi} and ΔP_{wi}) are lumped together, then the following simplifications can be made.

$$\Delta P_{bi} = 4f\frac{G_s^2}{2\rho_s}\left(\frac{\mu_{s,w}}{\mu_s}\right)^{0.14}N_c \approx \left(4\cdot 0.184\cdot\frac{1}{2}N_c\right)\frac{V_s^{1.8}\mu_s^{0.2}}{d_e^{0.2}\rho_s^{0.2}} = C_1\frac{\rho_s^{0.8}V_s^{1.8}\mu_s^{0.2}}{d_e^{0.2}} \tag{3.62}$$

$$\Delta P_{wi} = \frac{\dot{m}_s^2\left(2 + 0.6N_{cw}\right)}{2\rho_s A_s A_w} = \frac{2 + 0.6N_{cw}}{A_s A_w}\frac{\dot{m}_s^2}{2\rho_s} = C_2\frac{\dot{m}_s^2}{\rho_s} \tag{3.63}$$

Equation (3.64) is the formula for the shell side pressure drop with these simplifications.

$$\Delta P_T = \left[(N_b - 1)R_b R_l + 2\left(1 + \frac{N_{cw}}{N_c}\right)R_b R_s\right]\Delta P_{bi} + \left[N_b R_l\right]\Delta P_{wi} \tag{3.64}$$

Again, further simplification is possible by lumping the constants associated with each term into one constant. The result is Equation (3.65).

$$\Delta P_T = \left[C_3(N_b - 1) + C_4\right]\frac{\rho_s^{0.8}V_s^{1.8}\mu_s^{0.2}}{d_e^{0.2}} + C_5 N_b\frac{\dot{m}_s^2}{\rho_s} \tag{3.65}$$

For our application the primary coolant mass flow rate, $\dot{m}$, is constant because the thermal power of the reactor core is 700 MW. The second term in Equation (3.65) can be replaced with a new constant, C_6.

$$\Delta P_T = \left[C_3(N_b - 1) + C_4\right]\frac{\rho_s^{0.8}V_s^{1.8}\mu_s^{0.2}}{d_e^{0.2}} + C_6 N_b \tag{3.66}$$

Since the temperature drop of the primary coolant across the heat exchanger is constant, assuming that the viscosity and density terms in Equation (3.66) are constant is not unrealistic. This assumption yields the final version of the simplified shell side pressure drop equation.

$$\Delta P_T = \left[C_7 \left(N_b - 1 \right) + C_8 \right] \frac{V_s^{1.8}}{d_e^{0.2}} + C_6 \tag{3.67}$$

This simplified pressure drop equation intuitively shows the relationship between the number of baffles, coolant velocity, and tube bank geometry (expressed by the equivalent diameter, d_e). This nature of this equation supports the results found later in Section 0. The definitions of the constants that appear in Equations (3.62) to (3.67) are summarized in Table 3.13.

Table 3.13. Constants used in pressure drop simplification presented in Equations (3.62) to (3.67).

Constant	Definition
C_1	$0.368 N_C$
C_2	$\dfrac{2 + 0.6 N_{cw}}{2 A_s A_w}$
C_3	$R_b R_l C_1$
C_4	$2 \left(1 + \dfrac{N_{cw}}{N_c} \right) R_b R_s C_1$
C_5	$R_l C_2$
C_6	$\dfrac{\dot{m}_s^2}{\rho_s} C_5$
C_7	$\dfrac{\rho_s^{0.8}}{d_e^{0.2}} C_3$
C_8	$\dfrac{\rho_s^{0.8}}{d_e^{0.2}} C_4$

3.5.7. Design Constraints

There are three major constraints on the LBE heat exchangers. These are vibrations, primary coolant velocity, and structural analysis. These criteria must be satisfied for the heat exchangers to operate properly over the expected life of the plant. The sections below provide methods for compensating for these aspects.

3.5.7.1. Tube Bank Vibrations

The flow of the primary coolant over heat exchanger tubes can induce tube bank vibrations. This mechanism can be a major source of damage to heat transfer equipment. While these vibrations cannot be eliminated, it is important to incorporate them into the design to minimize the probability of resonance and the damage it can create. While there are a wide variety of flow induced vibration mechanisms, the focus here will be on the three with the most potential for causing damage to the heat exchanger tube bundle. These are fluid-elastic instability, turbulent buffeting, and vortex shedding.

Fluid-Elastic Instability

Fluid-elastic instability is also known as "whirling" instability. Fluid-elastic instability cannot occur with a single, isolated tube. The source of fluid-elastic instability is fluid flow past a vibrating body with an asymmetric cross section. An isolated cylindrical tube has a symmetric cross section and thus there is no force due to lift. However, bundles of tubes exert forces on one another, which can create momentary asymmetric cross sections for each tube. The drag force, F_D, acts in the direction of relative fluid flow velocity and the angle between the drag force and the direction of fluid flow is defined as α'. The angle α' is also known as the "angle of attack."

110

The force perpendicular to the drag force is the lift force, F_L. Connors proposed the following equation as the limiting criteria for fluid-elastic instability [Singh and Soler 1984]:

$$\frac{V_s}{f_{fei}d_o} = K\sqrt{\frac{m\delta}{\rho \cdot d_o}}$$

(3.68)

The term K is a constant and has been determined to be 3.3 by Pettigrew. Other terms represent the tube mass per unit length (m), the logarithmic decrement (δ), and the fluid density (ρ). A simple method of analysis is to determine the critical velocity for resonance due to fluid-elastic instability and compare it with the known coolant velocity. For fluid-elastic instability, this critical coolant velocity is found using Equation (3.69).

$$\frac{V_s}{f_n d_o} = 3.3\sqrt{\frac{m\delta}{\rho \cdot d_o^2}}$$

(3.69)

Vortex Shedding

Vortex shedding is well characterized for a single tube in uniform cross flow. At low Reynolds numbers ($Re < 5$) the flow is un-separated, but as the flow velocity increases, the pressure gradient forces the boundary layer around both sides of the tube. As the boundary layer is pushed back, it curls into a vortex and separates from the tube's surface, creating a localized pressure drop. This process alternates on either side of the tube, which creates an alternating force perpendicular to the direction of flow. The frequency of this alternating force, or lift, can be related to the free stream velocity (V), tube outer diameter (d_o), and the Strouhal number [Singh and Soler 1984]:

$$S = \frac{f_{vs}d_o}{V_s}$$

(3.70)

The Strouhal number, S, is a dimensionless term that is the ratio of the frequency of vibration to the characteristic frequency [Todreas and Kazimi 1990]. For sub-critical flow ($Re \leq 2 \times 10^5$) and trans-critical flow ($Re \geq 3.5 \times 10^6$) the expected Strouhal numbers are 0.2 and 0.3, respectively.

In the intermediate flow regime, the Strouhal number for vortex shedding varies and can be as high as 0.45. The effect of this is that the frequency of vortex shedding is not a distinct value, but can be a broad band of frequencies [Singh and Soler 1984]. Since the Strouhal number varies, a broad band of fluid flow velocities will satisfy Equation (3.70) for a given natural frequency. The vertical spacing between the lines in Figure 3.43 illustrates that for the intermediate flow regime ($2 \times 10^5 \leq Re \leq 3.5 \times 10^6$) there is a broad band of Strouhal numbers.
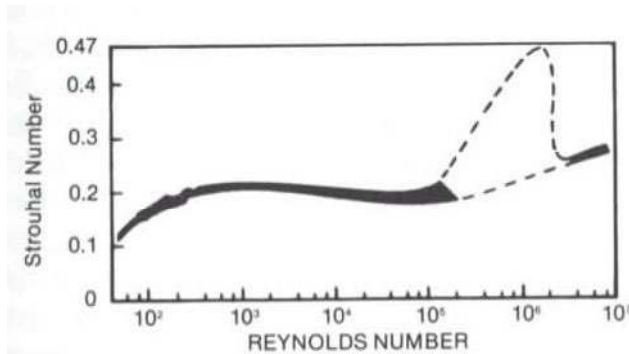
Figure 3.43. Strouhal number versus the Reynolds number [Singh and Soler 1984].

111

The variability of the Strouhal number makes it difficult to derive a critical velocity to minimize vibrations due to vortex shedding. As in turbulent buffeting correlations, the critical velocity for periodic wake shedding is a function of the tube displacement due to the flow. If a value of the lift coefficient is assumed, Pettigrew used $C_L = 0.07$, and the tube deflection is kept to within 2% of the tube diameter, a critical velocity correlation can be derived. This correlation can be used to derive Equation (3.71) [Singh and Soler 1984].

$$V_s = \frac{1}{C_L \rho} \pi \sqrt{0.04 C_L \rho \cdot \delta \cdot m} f_n$$ (3.71)

Turbulent Buffeting

Turbulent buffeting occurs at all flow velocities and possesses a much larger frequency spectrum than vortex shedding. The amplitude of vibrations due to turbulent buffeting is small, though, and roughly proportional to V_s^2. The nature of turbulent buffeting for an isolated tube is well understood, but larger tube banks complicate analysis. Tubes upstream affect those downstream, adding to the turbulent effect. At some point deep enough in the bank a steady state is reached. Owen proposed the following equation to determine the frequency induced by turbulent buffeting [Singh and Soler 1984]:

$$f_{tb} = \frac{V_s}{d_o x_l x_t} \left[3.05 \left(1 - \frac{1}{x_t} \right)^2 + 0.28 \right]$$ (3.72)

The terms x_l and x_t represent the longitudinal and transverse pitch-to-diameter ratios, respectively.

$$x_l = \frac{p_l}{d_o} ; \ x_t = \frac{p_t}{d_o}$$ (3.73)

Equation (3.74) is the critical velocity correlation for turbulent buffeting.

$$V_s = f_n d_o x_t x_l \left[3.05 \left(1 - \frac{1}{x_t} \right)^2 + 0.28 \right]^{-1}$$ (3.74)

3.5.7.2. Velocity Limit

To correct for increased fluid flow velocity through the gap the mass flux, G_s, must be a function of the pitch-to-diameter ratio. Equation (3.75) provides a corrected mass flux term.

$$G_s = \frac{\dot{m}_s}{A_s} \left(\frac{d_o}{p - d_o} \right)$$ (3.75)

Recall from above that the flow area is $A_s = D_s L/(N_b + 1)$. In calculating the mean gap fluid velocity an approximation was used for A_s. The distance between neighboring baffles was assumed to be 1.0 meter. Because the baffle spacing is nominally 1.0 meter, this approximation introduces an error of less than ten percent. For example, if the length of the heat exchanger is 9.5 meters, there will be 8 baffles. This translates to a spacing of 1.06 meters, which is 6% greater than the assumed value. This approximation also adds conservatism to the velocity calculations by decreasing the primary coolant flow area, which slightly increases the fluid flow velocity.

Maintaining the protective oxide film layer on the structural components of the LBE reactor requires a maximum coolant velocity to be set throughout the primary coolant system. The heat exchangers are not immune to this velocity limit. While circulating the primary coolant on the shell side of the heat exchangers in cross flow has several advantages, including increased heat transfer, it results in an increased fluid flow velocity. This increased fluid flow velocity is further aggravated by the pitch and outside diameter of the tube bundle. The mean gap velocity, not the mean coolant velocity across the bundle, sets the velocity limit. The mean gap velocity is the coolant velocity through the gap created by two neighboring heat exchanger tubes. Equation (3.76) determines the mean gap velocity.

$$V_{gap} = J_b J_l \frac{G_s}{\bar{\rho}_{LBE}}$$

(3.76)

The J factors account for coolant flow that does not flow over the bundle in cross flow. The J_b term adjusts for leakage between the tube bundle and the shell. The J_l term adjusts for both tube-to-baffle leakage and shell-to-baffle leakage. All variants of the LBE heat exchangers will have removable tube bundles, which provides larger clearances. A realistic value for both of the J terms is 0.7 [Kakaç and Liu 1998].

3.5.7.3. Tube Structural Analysis

Due to the high pressures in the heat exchanger tubes a structural analysis is necessary. The tube internal pressures are 15.0, 25.0, and 19.72 MPa for the superheated steam, supercritical steam, and supercritical CO_2 heat exchangers, respectively. The shell side pressure is negligible relative to the internal pressures. Because the tubes have thick walls (i.e., $t_{tube}/R_{mean} \geq 0.1$), the ASME (American Society of Mechanical Engineers) formula for a thick cylinder can be used to calculate the primary membrane stress intensity. Here P_m is the primary membrane stress while P is the net pressure acting on the internal wall of the tube (the internal pressure minus the external pressure). The thickness of the tube is t_{tube} [ASME 2001].

$$P_m = \frac{P\left(\frac{d_o}{2} - t_{tube}\right)}{t_{tube}} + \frac{P}{2}$$

(3.77)

The first term of Equation (3.77) is the average tangential or hoop stress due to the internal pressure and the second term is the average radial stress due to the internal pressure.

113

The ASME refers to the term P_m as the primary membrane stress intensity. At operating temperatures this stress intensity must be less than the allowable stress intensity, S. Knowing this value makes the tube wall thickness a function of both the internal pressure and outer tube diameter.

$$t_{tube} = \frac{d_o}{\frac{2S}{P} + 1} \qquad (3.78)$$

This formula determines the tube thickness given the tube diameter and internal pressure.

3.5.8. Application of Design Principles

Both the principles of heat transfer and damage mechanisms are presented above. In order to design a robust heat exchanger these two areas must be combined. The two main goals of the heat exchanger design, to minimize the overall length and shell side pressure drop, are related. The shell side pressure drop is a function of the number of times the primary coolant must cross the tube bundle, which is determined by the number of baffles. In turn, the overall length of the heat exchanger and the need to minimize tube vibrations can set the necessary number of baffles.

Since there are several variables involved in the heat exchanger design (outer tube diameter, pitch, and number of baffles) the initial evaluation assumed there is approximately one baffle per meter of overall heat exchanger tube length. This should provide a reasonable heat exchanger design, which limits both tube vibration and fluid flow velocity. Setting the fluid flow velocity makes it possible to solve the heat exchanger design problem in terms of one variable, the pitch-to-diameter ratio. Initial estimates limit the fluid flow velocity to 2.0 meters per second, but higher velocities were also evaluated, since they may be achievable and provide more favorable designs. All three variants, steam, supercritical steam, and supercritical CO_2, are evaluated by this method.

3.5.8.1. Pitch-to-Diameter Ratio

A general relationship can be found between fluid flow velocity and the pitch-to-diameter ratio, regardless of the secondary coolant in the tubes. This will provide several pitch-to-diameter ratios to be further investigated for each heat exchanger variant (superheated steam, supercritical steam, and supercritical CO_2). The baffle spacing is 1.0 meter, which provides a good balance between heat exchanger tube stability and pressure drop. These pitch-to-diameter ratios serve as design points for evaluating the three heat exchanger variants. In the heat exchanger calculations pitch-to-diameter ratios to the hundredths place are used. Table 3.14 is a summary of the relationship between the pitch-to-diameter ratio and coolant velocity.

Table 3.14. Primary coolant velocities and corresponding pitch-to-diameter ratios

Nominal Coolant Velocity (m/sec)	Actual Coolant Velocity (m/sec)	Pitch-to-Diameter Ratio
2.0	1.995	$1.198 \approx 1.20$
2.5	2.500	$1.152 \approx 1.15$
3.0	2.989	$1.124 \approx 1.12$

3.5.8.2. Superheated Steam Generator

The steam cycle proposed by Dostal et al. [2002] serves as the basis for this steam generator design. The steam generator parameters are a feed water temperature of 280ºC and an outlet temperature of 540ºC, which require a secondary coolant mass flow rate of 322 kg/sec at 15.0 MPa.

Figure 3.44 is a plot of the required heat exchanger tube length for each coolant velocity as a function of heat transfer tube outer diameter. The coolant velocities plotted are the same as in Table 3.14: 2.0, 2.5, and 3.0 meters per second. Because the overall heat transfer coefficient is limited by the heat transfer through the tube wall and on the inside tube surface, the primary coolant velocity has little effect on the necessary length of the heat exchanger.

The shell side pressure drop is a strong function of the coolant velocity (Figure 3.45). Since a low shell side pressure drop is desirable, the 2.0 meters per second coolant velocity was chosen, which corresponds to a pitch-to-diameter ratio of 1.20. Since the shell side pressure drop is essentially constant over the range of tube diameters at the pitch-to-diameter ratio of 1.20 (Figure 3.45), the tube length

Figure 3.44. Required superheated steam generator length
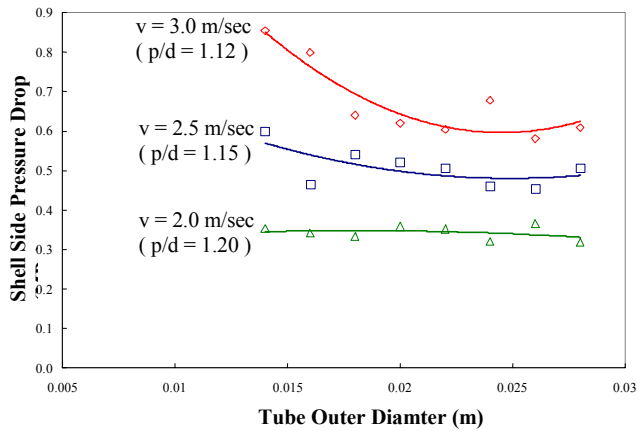
Figure 3.45. Resultant shell side pressure drop of the superheated steam generator

will determine the tube diameter used. Because the reactor vessel is approximately twenty meters high, the vessel dimensions do not impose a limit on the length of the heat exchanger. To determine the tube outer diameter for the chosen pitch-to-diameter ratio an overall heat exchanger length must be chosen. Knowing the tube outer diameter determines the pressure drop across the heat exchanger.

In sizing a heat exchanger it is normal practice to oversize the heat transfer surface area to account for fouling. Typically the surface area is oversized by 20-40% [Kuppan 2000]. The overall heat transfer coefficient determined above in Section 3.5.4 included fouling factors for both inside and outside surfaces. As a result, there is no need to oversize the heat exchanger surface area in this design to account for fouling.

For the superheated steam generator a nominal tube length of 9.0 meters with a pitch-to-diameter ratio of 1.20 was chosen. Iterating over one tenth of a millimeter increments of outer tube diameter results in a tube length of 9.00 meters and an outer tube diameter of 18.8 millimeters.

The resultant shell side pressure drop is 382.4 kPa. These and all other heat exchanger results are summarized in Section 3.5.9.

3.5.8.3. Supercritical Steam Generator

Previous work did not address the possibility of a supercritical steam cycle. The supercritical cycle for the LBE reactor is presented in Section 3.7. This power cycle has a secondary mass flow rate of 337.5 kg/sec, a feed water temperature of 280.0ºC, and an outlet temperature of 39.9ºC. The pressure for this cycle is 25.0 MPa. Figure 3.46 is a plot of tube lengths versus outer tube diameters for various coolant velocities, while Figure 3.47 is a plot of pressure drop versus tube outer diameter. Using the same methodology presented in Section 3.5.8.2 and a nominal length of 9.0 meters and a pitch-to-diameter ratio of 1.20 the actual supercritical steam generator parameters were determined. The actual length is 9.02 meters and the tube outer diameter of 21.5 millimeters. The shell side pressure drop is 332.7 kPa.
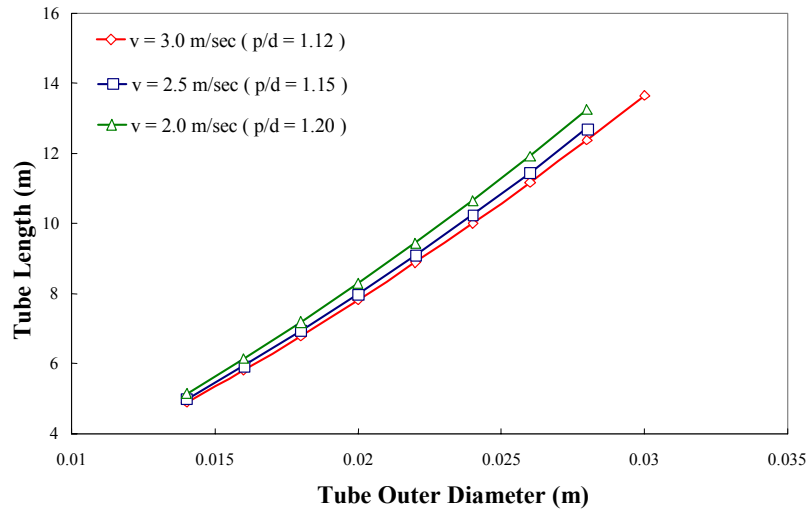
Figure 3.46. Required supercritical steam generator length.
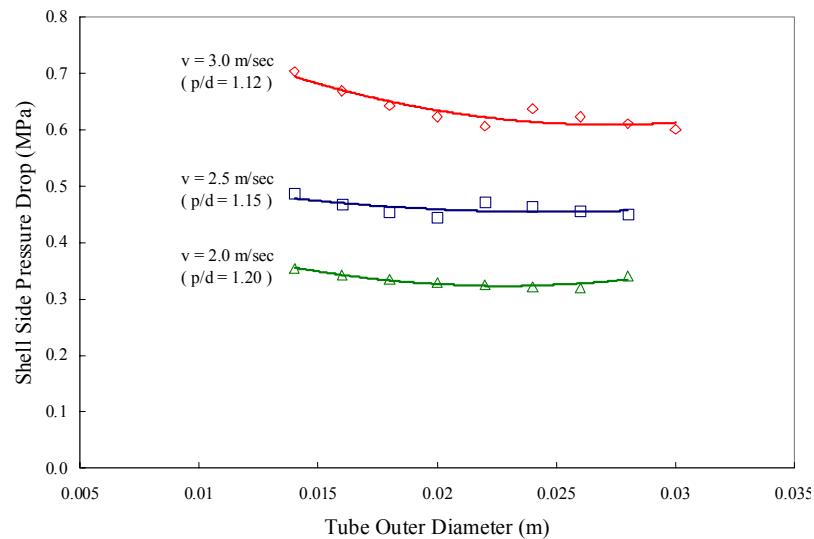
Figure 3.47. Resultant shell side pressure drop of the supercritical steam generator.

116

3.5.8.4. Supercritical CO$_2$ Heat Exchanger

The supercritical CO$_2$ cycle with recompression requires a heat exchanger that operates at inlet and outlet temperatures of 389.8ºC and 538.1ºC, and a secondary mass flow rate of 3,831.9 kg/sec. The pressure for the supercritical cycle is 19.72 MPa. Figure 3.48 is the plot of required tube length versus tube outer diameter for each primary coolant velocity. Figure 3.49 is a plot of shell side pressure drop versus tube outer diameter for each primary coolant velocity. Again, a nominal tube length of 9.0 meters and a pitch-to-diameter ratio of 1.20 were chosen. Iteration of the tube outer diameters in millimeter increments found the necessary tube length to be 9.04 meters with an outer tube diameter of 16.9 millimeters. The shell side pressure drop was 428.3 kPa.

3.5.9. Summary of Heat Exchanger Design Results
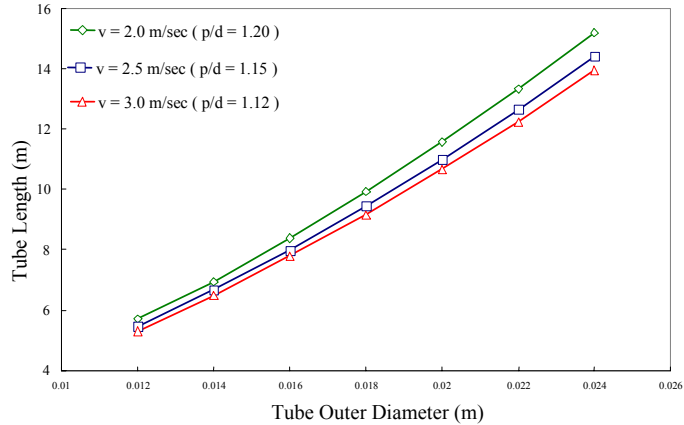
Figure 3.48. Required supercritical CO$_2$ heat exchanger length.
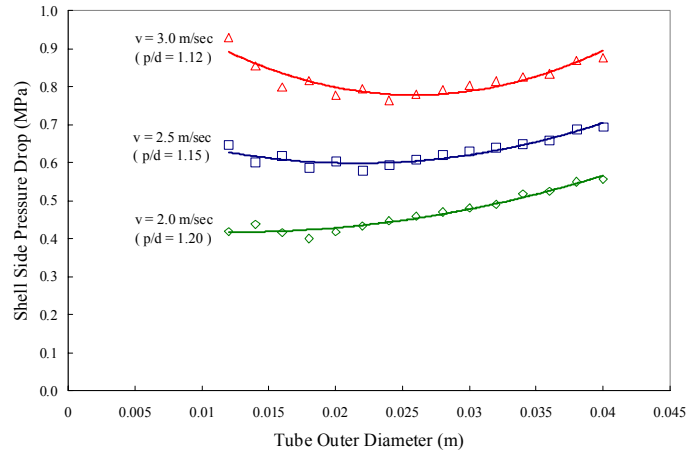
Figure 3.49. Resultant shell side pressure drop of the supercritical CO$_2$ heat exchanger.

Although the target nominal length for all three heat exchanger variants was nine meters, the actual lengths were slightly longer. This was due to the steep slope of the length versus diameter curve. Selecting realistic tube outer diameters precluded matching the goal and actual heat exchanger tube lengths. The results of each of the three heat exchanger variants are summarized below in Table 3.15. These designs meet all the constraints imposed on vibration and structural mechanics. Table 3.16 shows that the actual LBE gap velocities in the shell are much lower than the critical velocities for resonance by the three major mechanisms. Figure 3.50 is a side view schematic of one of the modular cylindrical heat exchangers. Figure 3.51 shows the placement of the heat exchangers within the reactor vessel and the flow path of the LBE coolant. Figure 1.2 shows a top view of the vessel with the core and heat exchanger layout shown. The heat exchangers thermal design was performed with a 3cm allowance for the heat exchanger vessel wall thickness. More recent analysis has shown that the stresses within the heat exchanger vessel violate the ASME limits for 316 stainless steel. Therefore, it will be necessary in the next design iteration in FY-03 to increase this wall thickness. However, it is anticipated that this can be readily accommodated by increasing the length of the heat exchangers and reducing their diameter or by rearrangement of core assemblies within a suitable reduced core barrel diameter.

Table 3.15. Summary of heat exchanger final design parameters.

	Parameter	Superheated Steam	Supercritical Steam	CO_2
INPUT	Power Transmitted (MWth)	700	700	700
	Primary Mass Flow Rate (kg/sec)	54,420.0	54,420.0	54,420.0
	Primary Inlet Temperature (ºC)	554.9	554.9	554.9
	Primary Outlet Temperature (ºC)	467.0	467.0	467.0
	Secondary Inlet Temperature (ºC)	280.0	280.0	389.8
	Secondary Coolant Pressure (MPa)	15.0	25.0	19.72
GEOMETRY	Shell Inside Diameter (m)	1.0	1.0	1.0
	Tube Length (m)	9.00	9.02	9.04
	Tube Outer Diameter (mm)	18.8	21.5	16.9
	Tube Thickness (mm)	3.01	4.97	3.39
	Pitch-to-Diameter Ratio	1.20	1.20	1.20
	Baffle Cut (%)	65	65	65
	Number of Baffles	8	8	8
	Tubes per Heat Exchanger	1,649	1,261	2,040
	Heat Transfer Surface Area per Heat Exchanger (m^2)	876.4	768.0	979.6
OUTPUT	Secondary Mass Flow Rate (kg/sec)	322.0	337.5	3,831.9
	Secondary Outlet Temperature (ºC)	530.0	539.9	538.7
	Primary Coolant Velocity (m/sec)	1.98	1.98	1.98
	Shell Side Pressure Drop (kPa)	382.4	332.7	428.3
	Shell Side Heat Transfer Coefficient (W/m^2K)	42,514.1	40,097.0	44,840.3
	Tube Side Heat Transfer Coefficient (W/m^2K)	3,394.9 / 44,853.1 / 3,301.9 / 1,353.0	3,459.0	6,357.4
	Overall Heat Transfer Coefficient (W/m^2K)	1,711.8 / 5,440 6 / 1,676.8 / 807.8	1,186.5	2,325.8
	Secondary Coolant Outlet Velocity (m/sec)	4.21	4.37	23.17

Table 3.16. Summary of critical velocities for preventing resonance due to flow-induced vibrations.

	Superheated Steam	Supercritical Steam	CO_2
Fluid-elastic instability critical velocity (m/sec)	69.2	97.3	14.6
Vortex shedding critical velocity (m/sec)	44.4	62.4	9.3
Turbulent buffeting critical velocity (m/sec)	3,892	4,162	835.5
Actual gap velocity (m/sec)	1.98	1.98	1.98

Figure 3.50. Schematic of cylindrical heat exchanger (nominal length of nine meters and shell diameter of one meter).

Figure 3.51. Schematic of heat exchanger placement within the vessel and LBE flow-path.
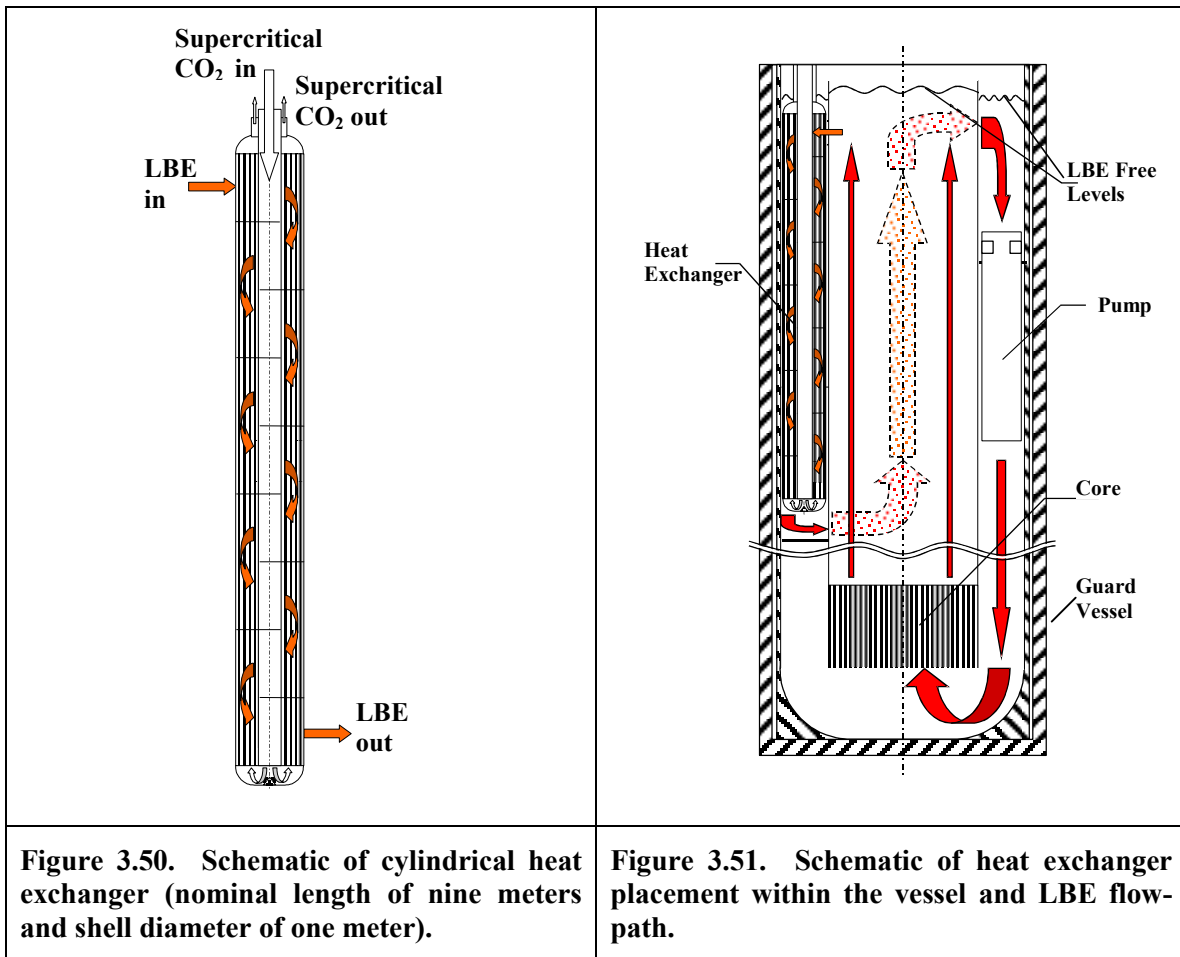
3.6. Heat Exchanger Accident Analysis (MIT)

3.6.1. Introduction

One of the design basis accident scenarios in a nuclear reactor is that of a steam generator tube rupture (SGTR). In water-cooled and liquid metal-cooled reactors this accident manifests itself in different ways. The hypothesized accident scenario in an LBE reactor is significantly different and deserves attention. The objective here is to provide an initial evaluation of the consequences of a heat exchanger tube rupture in the LBE reactor along with the procedure and systems necessary to respond to and mitigate the consequences of this transient.

3.6.2. Standard Scenario

The steam generator tube rupture accident in the BR is modeled here as a double-guillotine break of a single steam generator tube. The initial break flow rate instantaneously accelerates to choked flow. The choked flow dictates that the secondary coolant is flowing through the orifices at the speed of sound in the secondary coolant at the local temperature. Propagation of the single tube failure to adjacent tubes is not considered credible based on the very low probability of this event. Ongoing work at ANL to investigate single-followed by propagation to adjacent tube-ruptures in

PWR steam generators indicate that such an event sequence is extremely unlikely. Further investigation of the potential failure propagation for the tighter pitch steam generator in this case to confirm this assumption will be necessary. When water is the secondary coolant the flow into the primary will be two-phase. The calculation of two-phase critical flow will be addressed below.

Two consequences of the addition of H_2O or CO_2 to the lead bismuth eutectic in the primary loop need to be evaluated: 1. for the H_2O injection the possibility of a steam explosion needs to be addressed; and 2. for both H_2O and CO_2 injection the production of lead oxide which has a melting temperature above the maximum temperatures in the primary loop must be addressed. If the concentration of lead oxide is allowed to reach appreciable values, then solid lead oxidant particles, or slag, could form throughout the loop. This slag could alter flow paths, affecting circulation throughout the primary loop. In addition there is also the threat of pressurizing the reactor vessel due to high partial pressures of water vapor, CO_2 or gaseous reaction products.

3.6.3. Steam Explosion

The following discussion is taken from Buongiorno et al, 2001. An issue associated with the evolution of subcooled water droplets in molten heavy metal is that of steam explosion. Under certain conditions (typically low operating pressure and high subcooling of the water droplets) the vapor film blanketing the liquid droplet is not stable and a violent expansion of the droplet can occur, which causes a shock wave that can damage the reactor structural materials. There seems to be a general agreement that a steam explosion can occur only if:

a) The interface temperature T_i is above the temperature for homogeneous nucleation of the dispersed phase [Henry 1974, Reid 1983, Furuya 1996],

b) T_i is below the critical temperature of the dispersed phase [Henry 1975, Furuya 1996],

c) The operating pressure is below a threshold value [Henry 1978, Branover 1992, Furuya 1996, Kinoshita 2000].

Several fluid pairs have been found to satisfy these conditions, ranging from liquefied natural gas/water to refrigerant/oil to water/Pb-Bi. Condition a) expressed the fact that no vapor bubble nucleation can occur if the liquid at the interface is not sufficiently superheated. On the other hand, if homogenous nucleation occurs, a vapor film quickly forms at the interface. This film may be unstable resulting in oscillations of the interface, which eventually lead to film collapse and consequent violent vaporization [Matsumura 1996]. If the interface temperature is above the critical temperature of the dispersed phase, the film is relatively thick and does not collapse [Henry 1975]. Finally, if the system pressure is large, the vapor embryos generated at the interface by homogenous nuclear cannot grow rapidly. This is due to the large density of vapor at high pressure. Consequently, the generated vapor can be easily accommodated by a moderate volume increase of the vapor embryos and the phase change is not explosive. The value of the pressure above which no steam explosion occurs was found to be ~0.2 MPa for R-22/water and R-22/oil [Henry 1977], 0.5 MPa for water/molten NaCl [Henry 1978], 0.15 to 0.5 MPa for water/Pb-Bi [Corradini 2002, Furuya 1996], and ~0.2 MPa for butane/ethylene [Branover 1992].

At lead bismuth/water mixing conditions relevant to the SG-tube rupture accident in the ABR, the interface temperature is about 450°C while the critical temperature of water is 374°C. Therefore, condition a) for steam explosion is met, but condition b) is not because the interface temperature

120

is below the critical temperature of water. Moreover because the vessel lead-bismuth free level can be set at least 0.5m above the top of the heat exchanger tubes, (0.5m of Pb-Bi is equivalent to 0.05 MPa) the design can insure that condition c) is not met either. Therefore it can be concluded that the design features can provide ample safety margin to steam explosion under steam generator tube failure.

3.6.4. Lead Oxide Formation

3.6.4.2. Possible Reactions

Lead and/or Bismuth oxide can be produced from several alternate, and often coupled, reactions as follows, assuming only gas phase reactions with liquid metal(s):

$$Pb + H_2O(g) \rightarrow PbO + H_2(g) \qquad\qquad 3.79$$

$$Pb + 2H_2O(g) \rightarrow PbO_2 + 2H_2(g) \qquad\qquad 3.80$$

$$2Pb + O_2(g) \rightarrow 2PbO \qquad\qquad 3.81$$

$$2PbO + O_2(g) \rightarrow 2PbO_2 \qquad\qquad 3.82$$

$$2Bi + 3H_2O(g) \rightarrow Bi_2O_3 + 3H_2(g) \qquad\qquad 3.83$$

$$4Bi + 3O_2 \rightarrow 2Bi_2O_3 \qquad\qquad 3.84$$

$$2H_2O(g) \rightarrow 2H_2(g) + O_2(g) \qquad\qquad 3.85$$

$$Pb + CO_2(g) \rightarrow PbO + CO \qquad\qquad 3.86$$

$$Pb + CO(g) \rightarrow PbO + C \qquad\qquad 3.87$$

$$Pb + 2CO_2(g) \rightarrow PbO_2 + 2CO(g) \qquad\qquad 3.88$$

$$Pb + 2CO(g) \rightarrow PbO_2 + 2C \qquad\qquad 3.89$$

$$2Bi + 3CO_2(g) \rightarrow Bi_2O_3 + 3CO(g) \qquad\qquad 3.90$$

$$2Bi + 3CO(g) \rightarrow Bi_2O_3 + 3C \qquad\qquad 3.91$$

$$2CO_2(g) \rightarrow 2CO(g) + O_2(g) \qquad\qquad 3.92$$

Determining which of these products would actually form in a heat exchanger accident requires a complete analysis of the coupled system of reactions, which includes the decomposition of water in one case and the coupled CO/CO_2 system in the case of CO_2. Both thermodynamics, which

determines if a given reaction is possible and kinetics, which determines rates of reactions must be considered. Given that a reaction is possible, as defined by a negative free energy, one must then look at the kinetics for each step in a process to determine the rate-limiting step to establish overall rates. Additionally, while most, as will be seen below, of the above reactions are not thermodynamically favored, the presence of radiolysis of CO_2 or H_2O will also need to be considered in a detailed analysis (although the reactor will be scrammed after any heat exchanger or steam generator tube rupture).

3.6.4.2. Gibbs Free Energy

Energy is associated with any chemical reaction. When energy is released by the reaction, it is said to be spontaneous. A common predictor of the spontaneity of a chemical reaction is the Gibbs free energy of the system. The Gibbs free energy of a system at a moment in time is defined as the enthalpy of the system minus the product of the temperature and entropy of the system [Dean 1999].

$$G = H - T \cdot S \qquad (3.93)$$

The change in the Gibbs free energy during a reaction predicts the spontaneity of the reaction. From Equation (3.93) the change is the Gibbs free energy of the system is:

$$\Delta G = \Delta H - T \cdot \Delta S \qquad (3.94)$$

If the change in the Gibbs free energy, ΔG, is greater than zero, energy is absorbed in the reaction. Thus the reaction will not be spontaneous. However, if the change in the Gibbs free energy is negative, the reaction will be spontaneous. For purposes of this analysis all reactions will be will be evaluated at the hot leg temperature (555°C). For equations set 3.79-3.92 at 555°C (828K) the Gibbs Free Energy Change is positive for all but reactions 3.81, 3.82, and 3.84.

For equation set 3.81, 3.82, and 3.84 at 555°C (828K) Table 3.17 presents the calculations for the change in Gibbs free energy [Dean 1999]. All equations are normalized so that the coefficient of the O_2 term is unity. A more spontaneous reaction is indicated by a more negative change in free energy. Thus the most spontaneous and energetic reaction is of lead and oxygen to form lead oxide. Next is the formation of bismuth oxide (Bi_2O_3). The least likely of the three reactions is the formation of lead dioxide (PbO_2). Since the Gibbs free energy change is greatest for the production of PbO, lead oxide is the most likely product of the reaction of either coolant with the LBE coolant.

Table 3.17. Summary of Gibbs free energy calculations [Dean, 1999]

Normalized Reaction	Enthalpy Change (kJ/mol)	Entropy Change (kJ/mol/K)	Temperature (K)	Gibbs Free Energy Change (kJ/mol O_2)
$2Pb + O_2 \longrightarrow 2PbO$	-438.0	-0.202	740.0	-288.5
$Pb + O_2 \longrightarrow PbO_2$	-277.4	-0.201	740.0	-128
$\frac{4}{3}Bi + O_2 \longrightarrow \frac{2}{3}Bi_2O_3$	-382.7	-0.180	740.0	-249.5

While the reactions of equation set 3.81, 3.82 and 3.84 are spontaneous, they require the presence of free O_2. Free O_2 is only available in this tube failure event from the decomposition of H_2O or

CO_2 either thermally or due to radiolysis. The thermal decomposition reactions will be very slow or essentially zero at the lead-bismuth temperature of about 500°C. Radiolysis of CO_2 is very unlikely based on gas reactor CO_2 experience. Radiolysis of H_2O is well documented for LWR systems and is thus a possibility that must be addressed in a more complete analysis of the accident. However, such a scenario is considered unlikely to produce significant oxide formation during the accident because the reactor will be quickly scrammed. Thus we conclude that significant amounts of lead oxide will not form.

3.6.5. Calculating Choked Flow

For completeness, if we wish to evaluate the effects of this small rate of lead oxide formation, we need to estimate the rate of addition of the secondary coolant (H_2O or CO_2) to the primary system during the accident. The total addition of secondary coolant to the primary loop can be determined if several parameters are known. These include the temperature and pressure of the secondary coolant, the geometry of the orifices created by the tube break, and the total time elapsed between tube rupture and isolation of the heat exchanger. The secondary coolant properties will be evaluated at the local temperature in the secondary (tube) side of the heat exchanger, as opposed to the local temperature in the primary (shell) side of the heat exchanger. This is a reasonable assumption given that the transient should be relatively short. It also adds conservatism to the evaluation since a colder liquid has a greater density. The relations for the determining the critical mass flux differ depending on whether the critical flow is single-phase or two-phase. The CO_2 power cycle has single-phase critical flow and the steam cycles have two-phase critical flow.

3.6.5.1. Single Phase Critical Flow (CO_2)

The mass flux, G, at choked flow for a single-phase fluid is given by Equation (3.95). Here γ is the specific heat ratio (i.e., the ratio of the specific heat at constant pressure to that at constant volume) and R is the ideal gas constant (0.1889 kJ/kg/K for CO_2), P is the pressure and T is the absolute temperature. To add conservatism to this estimation the temperature and pressure will be evaluated at the heat exchanger inlet conditions, which are 389ºC and 19.72 MPa, respectively.

$$G = P\sqrt{\frac{\gamma}{R \cdot T}\left(\frac{2}{\gamma+1}\right)^{\left[\frac{\gamma+1}{2(\gamma-1)}\right]}} \qquad (3.95)$$

3.6.5.2. Two-Phase Critical Flow (H_2O)

For H_2O the calculation of the choked or critical flow rate is more difficult because upon leaving the heat exchanger the water will flash to steam due to the drop in pressure to below the saturation point. The CO_2 model requires only the assumption of the orifice diameter, but the H_2O model requires some assumptions about the length of the heat exchanger tube, also. To simplify the model, the assumption will be made that the tube ruptures at its midpoint. This situation creates two ruptured tubes that are 4.5 meters in length with an orifice equal to the inside diameter of the tube. Figure 3.52 illustrates the dimensions of the model.

Figure 3.52: Schematic of a ruptured heat exchanger tube; for this analysis L is 4.5 meters and d_i is the tube inside diameter
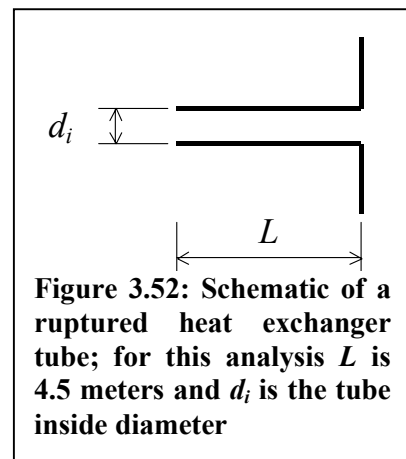
Because the length of the ruptured tube is greater than 0.1 meters, Equation (3.96) can be used to determine the critical flow [Todreas and Kazimi, 1990].

$$G \approx \sqrt{2[p - p_{sat}]\rho_f + G_{ERM}^2} \qquad (3.96)$$

The term p represents the actual pressure in the tube and the p_{sat} term represents the saturation pressure at the feedwater temperature. The difference of these terms accounts for the increased mass flux through the ruptured tube due to the subcooling of the feedwater. The G_{ERM} term is the mass flux determined by the equilibrium rate model. Equation (3.97) is the formula for the equilibrium rate model, which is valid for a tube length of greater than 0.1 meters and a length to diameter ratio of greater than 40.

$$G_{ERM} = \frac{h_{fg}}{v_{fg}} \sqrt{\frac{1}{Tc_p}} \qquad (3.97)$$

The v_{fg} term is the change in specific volume during vaporization and the temperature must be in absolute units [Todreas and Kazimi, 1990].

The accident scenario calls for the double guillotine rupture of one tube. The total mass flow rate of secondary coolant into the primary loop as a function of time (t) can be calculated using Equation (3.98).

$$\acute{m}_{TOTAL}(t) = G \frac{\pi \cdot d_i^2}{4}(2) \qquad (3.98)$$

where G is the mass flux and d_i is the inside tube diameter. Application of the above analysis for the three heat exchanger variants allows a determination of the mass of secondary coolant deposited in the primary loop as a function of time. The results of this analysis are shown graphically in Figure 3.53. The total mass deposited is a linear relation with time. The CO_2 heat exchanger accident deposits the least mass of coolant due to its low density. The superheated steam generator deposits slightly more than the supercritical steam generator because the effect of subcooling is greater than that of the higher pressure. It is important to emphasis the two conservative assumptions made for this analysis.

1. The pressure in the secondary side of the heat exchanger is constant (thus the mass flow rate is also constant after
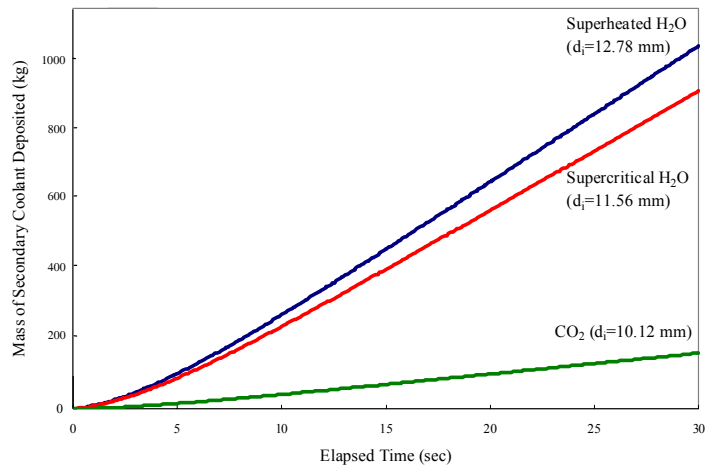
Figure 3.53. Mass of secondary coolant that enters the primary loop during heat exchanger accidents

reaching critical flow.)

2. The inventory of the secondary loop is large enough to supply secondary coolant for the length of the transients plotted in Figure 3.53.

3.7. Supercritical Steam Cycle (R. Herron, MIT)

3.7.1. Introduction

Both Rankine and Brayton power cycles have been investigated as power cycles for the LBE reactor [Dostal et al. 2002]. Due to high primary coolant outlet temperature available with the LBE reactor (approximately 550ºC) a supercritical steam power cycle may be possible. The objective here is to perform an initial investigation of a supercritical steam cycle to evaluate if it is desirable alternative to either the superheated steam or supercritical CO_2 power cycles.

3.7.2. Supercritical Steam Generator

An important component in the success of a supercritical steam cycle is the heat exchanger. The work in Section 3.5 provides a design for a supercritical steam generator. Although the tubes must be significantly thicker due the increased internal pressure compared to the superheated steam cycle, the improved average heat transfer and lower mass flow rate make it possible to design a steam generator within the same design envelope of a cylinder one meter in diameter and nine meters in length. The details of the supercritical steam generator design are given in Section 3.5.3. Table 3.18 provides a summary of the basic parameters with which the supercritical steam generator was designed.

Table 3.18. Basic operating parameters for the supercritical steam cycle

Parameter	
Total Power (MWth)	700.0
Total Water Mass Flow Rate (kg/sec)	337.5
Maximum Pressure (MPa)	25.0
Feedwater Temperature (ºC)	280.0
Maximum Temperature (ºC)	539.9

3.7.3. Power Cycle

In a supercritical steam cycle the working fluid, water, does not cross the saturation curve during the addition of heat (state 2 to state 3). This is accomplished by maintaining the pressure above the saturation pressure for the given temperature. The temperature-entropy diagram for a simple supercritical steam cycle is given in Figure 3.54. States 1 through 4 represent the pump inlet, pump outlet, turbine inlet and turbine outlet, respectively.

The critical pressure for water is 22.09 MPa and the critical temperature is 374.2ºC. Thus to
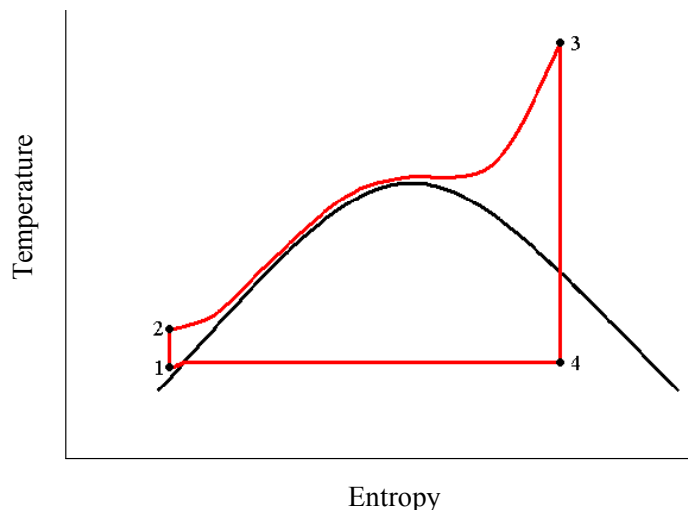
Figure 3.54. Temperature-entropy diagram of a simple, supercritical steam cycle.

125

prevent the working fluid from crossing the saturation curve the pressure from state 2 to state 3 must be maintained above 22.09 MPa. The current range of operating pressures for supercritical steam cycles is 24.0 to 38.0 MPa.

3.7.4. Existing Supercritical Steam Power Cycles

Oka and Koshizuka [2000] have proposed a nuclear reactor cooled by light water above the critical pressure. With an outlet temperature of 508ºC at 25.0 MPa their supercritical steam power cycle achieves a net efficiency of 44.0%. As shown in Section 3.5 the supercritical heat exchanger for the LBE reactor can produce supercritical steam at 25.0 MPa and 539.9ºC. The cycle presented by Oka and Koshizuka is too complex to optimize here for the LBE reactor but demonstrates that it is possible to achieve high efficiencies without a second pass of through the reactor's heat exchangers. Figure 3.55 is a schematic of the Oka and Koshizuka cycle.
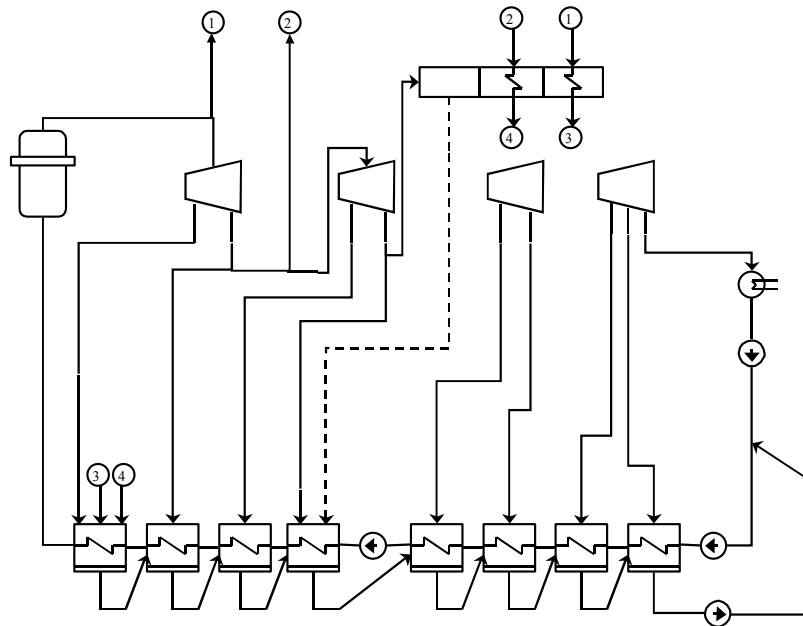
Figure 3.55. Schematic of supercritical steam cycle for the SCLWR [Oka and Koshizuka 2000].

Oka and Koshizuka also provide a plot of cycle efficiency versus core outlet temperature, which is equivalent to the steam generator outlet temperature in the LBE reactor. At a steam temperature of 540ºC and 25.0 MPa the power cycle is capable of achieving a thermal efficiency of approximately 44.6%. Figure 3.56 is a plot of gross thermal efficiency versus steam temperature.
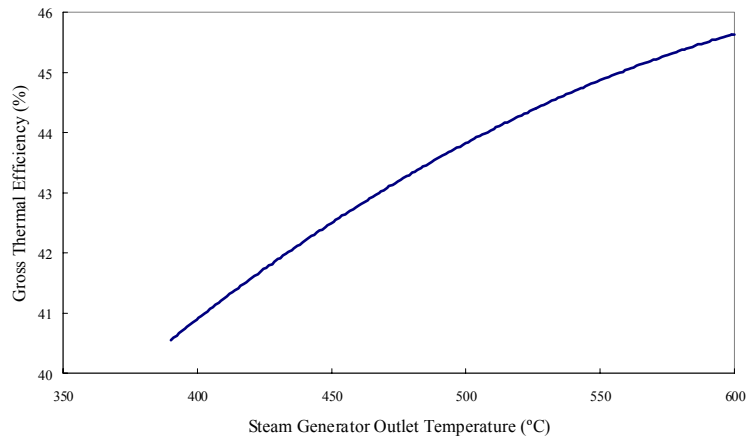
Figure 3.56. With a steam generator outlet temperature of 540ºC, the LBE reactor with a supercritical steam cycle can achieve thermal efficiencies of approximately 44%.

126

The supercritical steam cycle presented by Oka and Koshizuka is able to achieve high efficiencies through the use of moisture separation and reheat stages. The moisture separation after the second turbine stage raises the enthalpy of the steam entering the third and fourth turbines. The final reheat with live steam makes it possible to achieve a high inlet temperature into the third and fourth turbines. Also, the pressure of this stream is lowered significantly to increase the entropy, which produces a higher exit quality in the turbines. In the Oka and Koshizuka cycle, steam at 502ºC and 23.6 MPa is used to reheat steam at a much lower pressure of 1.2 MPa. This makes it possible to reach a temperature of 485ºC at the inlet to the low-pressure turbines. Because the outlet temperature of the LBE reactor's supercritical steam generators is approximately 40ºC higher it is possible to reach even higher temperatures after the reheat stage.

3.7.5. Supercritical Steam Cycle Conclusions

The net efficiencies obtainable with the supercritical steam cycle are competitive with those of the supercritical CO_2 power cycle. The current CO_2 power cycle has a net efficiency of 44.6% and a thermal efficiency of 45.8%. However, the balance of plant design with the CO_2 power cycle is much simpler. Also, since Oka and Koshizuka [2000] achieve an efficiency of 44.6% at an outlet temperature of 540ºC it may be possible to achieve high efficiencies with this cycle at lower temperatures (which could lower the maximum temperature in the primary or decrease the size of the heat exchangers). Although the cycle shown here will need optimization for the thermal power and temperatures of the LBE reactor, it demonstrates that a high thermal efficiency is possible without additional steam passes through the reactor's heat exchangers.

3.8. Under-LBE Viewer (R. Herron, MIT)

3.8.1. Introduction

The opaqueness of liquid metal coolants, including LBE, presents some difficulties in the maintenance of a fast reactor. Several scenarios can be hypothesized where it would be necessary to "see" inside the reactor vessel. The coolant cannot be removed from the vessel because, in addition to being extremely difficult to accomplish, it provides radiation shielding and heat removal. Significant progress has been made towards the development of an under-coolant viewer for the sodium-cooled reactor, but no such work has been completed for an LBE coolant. The objective here is to illustrate how a similar system could be successful in providing three-dimensional ultrasonic viewing under a LBE coolant.

Throughout the 1990's researchers at Toshiba worked on the development of an under-sodium three-dimensional visual inspection technique. This research is still ongoing with the ultimate goal of achieving the same resolution that is possible with an optical fiberscope in air, which is a resolution of 0.8 millimeters. In the latest published report the project has achieved a resolution of less than 2.0 millimeters, which is significant progress towards the ultimate goal [Karasawa et al. 2000]. The Toshiba system has also been successful in identifying complex, blind targets in sodium at distances between 0.4 and 1.0 meters.

To create images, the under-coolant viewer uses an array of ultrasonic transducers. The current variant is a 36 by 36 matrix array of transducers. These transducers compose a phased array, in which each transducer can both transmit and receive ultrasonic signals [Karasawa et al. 2000].

3.8.2. Operating Conditions

There are two limiting conditions for an under-coolant, ultrasonic viewer associated with the coolant. These are the coolant temperature and the radiation environment. While there may also be other potentially limiting factors, such as corrosion, these will be assumed negligible in comparison to temperature and radiation. These effects can also be neglected due to the relatively short periods of usage for the under-LBE viewer.

3.8.2.1. Radiation Conditions

The interior of a reactor vessel is a highly radioactive environment. In the case of sodium coolants, for which the under-coolant viewer was initially designed, both the fuel and the coolant itself are radiation sources. Irradiated sodium has the isotope ^{24}Na, which is an energetic gamma emitter with a half-life of 14.8 hours. The LBE coolant provides a much more favorable radiation environment than the sodium coolant. Although irradiated LBE contains the ^{210}Po isotope, which is a long-lived alpha emitter ($t_{1/2}$ = 138.4 days), the properties of LBE make it "self-shielding." The high atomic mass number of LBE makes it an effective attenuator of charged radiation. As a result, the under-coolant viewer is less susceptible to harm from ionizing irradiation in the LBE reactor. Since the viewer would only be used during periods of reactor shut down, neutron damage should be eliminated.

3.8.2.2. Temperature Conditions

Due to the sensitivity of the electronic components involved in the 3-D viewer and the fact that the viewer must be submerged in the coolant to operate, the operating temperature is potentially limiting. The Toshiba viewer operates at approximately 200ºC, which was dictated by the trace heating in the Japanese demonstration fast breeder reactor [Karasawa et al. 2000]. Recall from earlier that the melting point of sodium is 97.8ºC while that of LBE is 125.0ºC. Thus there is no reason to believe that the coolant temperature in the LBE reactor could not be lowered safely to 200ºC. Also, the temperature limit for the sodium viewer was set with the additional heat deposited by radiation in mind. Since the LBE coolant is self-shielding, the decrease in energy deposition from radiation may provide a larger operating envelope for the under-LBE viewer.

3.8.3. Sound Transmission Properties

Since the physical properties of sodium and LBE are distinctly different, there exists the possibility that these differences could affect the performance of the under-coolant viewer in the LBE reactor. The under-coolant viewer operates in the ultrasonic spectrum. Although this means the operating frequency is above the audible range (f >20 kHz), the same basic principles of sound transmission and acoustics apply. The two fundamental properties that determine the effectiveness of the under-coolant viewer in the LBE reactor are the speed and attenuation of sound in the coolant.

3.8.3.1. Speed of Sound in Coolant

The more significant of the two properties is the speed of sound in the coolant. The wavelength of the transmitted ultrasonic wave directly affects the achievable resolution in the coolant. A shorter transmitted wavelength, in general, provides better resolution. Toshiba bases the achievable axial resolution on the wavelength of the ultrasonic wave [Karasawa et al. 2000]. For

example, if the transmitted wavelength is one meter, then the maximum axial resolution will be one meter.

The speed of sound in the medium (c), frequency, and wavelength, are related by Equation (3.99).

$$\lambda = \frac{c}{f} \qquad (3.99)$$

For a fixed frequency, as the speed of sound in the coolant increases, so does the wavelength. Since the achievable resolution worsens with increasing wavelengths, a medium with a slower speed of sound will produce better resolution. In this case resolution is the ability to discern between neighboring topographic features. A lower value for resolution is more desirable. Abramov [1994] provided the liquid metal properties in listed Table 3.19.

Table 3.19. Liquid metal coolant properties [Abramov 1994].

Coolant	Temperature (ºC)	Density (kg/m³)	Speed of Sound (m/sec)	Thermal Conductivity Coefficient (m/sec grad)
Sodium (Na)	100	946	2395 ± 25	0.3
Lead (Pb)	335	10,950	1790 ± 15	0.5
Bismuth (Bi)	280	10,164	1635 ± 5	0.5

Although no properties are provided for the eutectic mixture of lead and bismuth, the speed of sound in LBE can be expected to be similar to the speed of sound in each of its components. Since the speed of sound in the heavy metal coolant is slower than in sodium, the resolution will be better. This hypothesis has also been validated through communication with Toshiba [Komai 2002] Although Table 3.20 lists the speed of sound in sodium as approximately 2400 meters per second, the value used by Toshiba in their calculations was 2500 meters per second [Karasawa et al. 2000]. This is presumably due to the elevated temperature of 200ºC used by Toshiba. The ultrasonic frequency used by the under-sodium viewer is 5.0 MHz (10^6 seconds^{-1}). Applying Equation (3.90) yields a wavelength of 0.5 millimeters. This is the same as the axial resolution actually achieved in tests. If the speed of sound in LBE is assumed to be approximately 1800 meters per second, then the same calculation produces a wavelength of 0.36 millimeters at the same 5 MHz frequency. Regardless of particular values used in the calculations, the axial resolution of an ultrasonic viewer in LBE will at least as good, and most likely better, than a similar viewer in sodium. For example, resolution was improved in the Toshiba tests in water, which has a speed of sound of approximately similar to that in LBE [Karasawa et al. 2000].

3.8.3.2. Attenuation Losses

The under-sodium viewer was designed to operate at a range of distances, from 0.4 to 1.0 meters. One coolant property that will determine the effective range of the viewer is the loss by attenuation. The attenuation losses in a fluid are gauged by the attenuation coefficient, α. The attenuation of an ultrasonic wave depends on losses caused by viscosity and those caused by thermal conductivity. Kočiš and Figura [1996] stated that the total attenuation coefficient is the sum of the viscosity and temperature coefficients. The α_V term accounts for the attenuation in

liquids caused by viscosity and the α_T accounts for attenuation caused by thermal conductivity. For ultrasound in liquid metals the value of α_T is several times greater than the value of α_V [Kočiš and Figura 1996].

$$\alpha = \alpha_V + \alpha_T = \frac{2\pi^2}{\rho c^3}\left[\frac{4}{3}\mu + k\left(\frac{1}{c_v} - \frac{1}{c_p}\right)\right]f^2 \tag{3.100}$$

The right side of Equation (3.100) indicates that the attenuation coefficient is a function of several fluid properties and the frequency of the transmitted wave. Since these detailed fluid properties of LBE are unknown, the assumption will be made that both sodium and LBE are incompressible fluids. This is a reasonable assumption given that liquid metals are both within approximately 100ºC of their melting temperatures. As a result, the specific heat at constant volume equals the specific heat at constant pressure ($c_v = c_p$). Equation (3.100) now simplifies to Equation (3.101).

$$\alpha = \frac{2\pi^2}{\rho c^3}\left(\frac{4}{3}\mu\right)f^2 \tag{3.101}$$

Recall from above that the wavelength is a function of the speed of sound in the medium and the frequency, $\lambda = c/f$. The following further simplification can be made.

$$\alpha = \frac{8}{3}\frac{\mu\pi^2}{\rho c \lambda^2} \tag{3.102}$$

Now given the viscosity, density, speed of sound, and wavelength, a close approximation of the attenuation coefficient can be made (based on the assumption of the incompressibility of liquid metal coolants). Using Equation (3.102) the attenuation coefficients of sodium and LBE are 0.0213 and 0.0272 meters[-1], respectively. The relative magnitude of these values agrees with the thermal conductivity attenuation coefficients (α_T) of those in Table 3.19. Table 3.20 is a summary of the values used to calculate the attenuation coefficients. These values are based on fluid properties at 200ºC and sodium and LBE speeds of sound of 2500 and 1800 meters per second, respectively.

The attenuation of sound in a liquid is exponential. Equation (3.103) is the governing relationship for the wave intensity a distance x from the source [Abramov 1994].

Table 3.20. Summary of attenuation coefficient calculations calculated with Equation (3.102) [Lyon 1952, Abramov 1998].

Property	LBE	Sodium
Viscosity (Pa sec)	0.00253	0.000456
Density (kg/m^3)	10,484	903.3
Wavelength (m)	0.00036	0.0005
Frequency (MHz)	5.0	5.0
Speed of Sound (m/sec)	1800	2500
Attenuation Coefficient (m^{-1})	0.0272	0.0213

$$I_x = I_o e^{-2\alpha x} \tag{3.103}$$

This is graphically illustrated in Figure 3.57. At any given distance from the source, the intensity of the same wave is less in the LBE coolant than in the sodium coolant. Figure 3.57 is normalized and indicates that there will be a slight decrease in the range of the under-coolant viewer in LBE, but not so much as to preclude its use, especially given the success the original sodium coolant version has had at ranges up to one meter.

3.8.4. Conclusions Regarding Under-LBE Viewing

Research so far has shown that an ultrasonic, 3-D viewer for "seeing" under
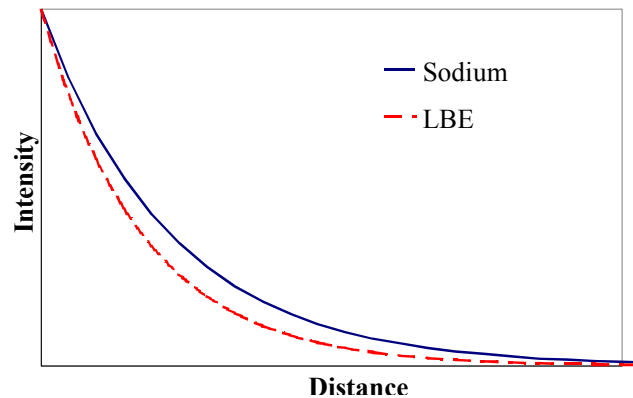
Figure 3.57. Normalized ultrasonic wave intensity versus distance for a 5.0 MHz signal in both sodium and LBE coolants

the opaque sodium coolant in a fast breeder reactor is functional. Based on the relative properties of sodium and the lead-bismuth eutectic coolant proposed for the LBE reactor, such a viewer will have similar success in an LBE coolant. Because the speed of sound in LBE is slower than that in sodium, the resolution in the LBE viewer will be as good or better than the sodium version. With slightly higher attenuation losses, the range in LBE will be shorter than in sodium coolant, but will not be large enough to significantly affect operation.

3.9. Supercritical Recompression CO_2 Brayton Cycle (V. Dostel, MIT)

Last year the supercritical CO_2 recompression Brayton cycle was identified as the most promising option for the current LBE cooled reactor design. The basic features and reference design were described by this author in Section 4.3 of our FY-01 Annual Report (MacDonald and Buongiorno 2002). This year the work on the supercritical-CO_2 recompression cycle has continued with funding from the INEEL Gas-Cooled Fast Reactor LDRD project and is documented in Dostal et al. [2002b]. However, all the results are applicable to the LBE cooled reactor as well. The investigation focused on identifying the cycle optimum operating conditions and preliminary design of the components. The preliminary component design was focused on identification the component dimensions. This section summarizes the basic findings as described in Dostal et al. [2002b], where the reader should refer for further information.

3.9.1. Recompression Cycle

The recompression cycle is shown in Figure 3.58. The advantage over the simple Brayton cycle is in the reduction of the heat rejection from the cycle by introducing another compressor (a recompressing compressor) before the precooler. The flow is split before entering the precooler and heat is rejected only from part of the fluid flow. The outlet of the recompressing compressor is connected between the high and low temperature recuperator. This is another difference from the simple Brayton cycle where only one recuperator is used. Otherwise, the cycle is the same.
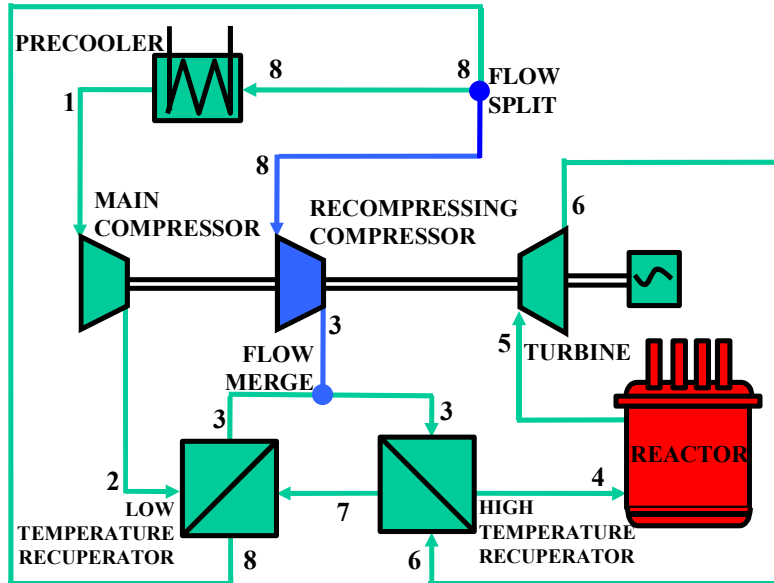
Figure 3.58. Scheme of recompression Brayton cycle.

In the main compressor (points $1 - 2$) a fraction of the fluid flow is compressed to high pressure. In the low temperature recuperator it is preheated to the recompressing compressor outlet temperature (points $2 - 3$). Then the fluid is merged with the rest of the fluid flow from the recompressing compressor (point 3). The entire fluid flow is then preheated in the high temperature recuperator to the reactor inlet temperature (points $3 - 4$). The heat addition into the cycle takes place in the reactor (points $4 - 5$). The fluid leaves the reactor at the highest cycle temperature. At this temperature it enters the turbine, where fluid expansion (points $5 - 6$) generates rotational energy, which is converted into electricity in the generator. After leaving the turbine the high temperature fluid is cooled in the high (points $6 - 7$) and low (points $7 - 8$) temperature recuperators, where the available heat is transferred to the cooler high-pressure side fluid flow. Before entering the precooler the fluid flow is split (point 8). One part is recompressed to high pressure (points $8 - 3$), the other is cooled in the precooler to the main compressor inlet temperature (points $8 - 1$).

Table 3.21 contains the component characteristics that were used in the analyses of the supercritical-CO_2 recompression Brayton cycle. The cycle was analyzed at a turbine inlet temperature of 550°C and a compressor inlet temperature of 32 C. The cycle efficiency was evaluated over a range of recompressed fractions.

Table 3.21. Recompression cycle component characteristics.

Compressor polytropic efficiency (%)	89.0
Turbine polytropic efficiency (%)	90.0
Recuperator effectiveness (%)	98.0
Pressure drop across precooler (%)	0.4
Pressure drop across recuperator (%) (hot side, high temperature)	0.4
Pressure drop across recuperator (%) (hot side, low temperature)	1.5
Pressure drop across recuperator (%) (cold side, high temperature)	0.4
Pressure drop across recuperator (%) (cold side, low temperature)	1.5
Pressure drop across reactor (%)	2.0
Generator efficiency (%)	98.0
Mechanical losses (%)	1.0

Some results of this analysis are shown in Figure 3.59. These were obtained for a recompressed fraction of 0.45. The region of the highest efficiency is very close to the "cliff edge" after which the efficiency drops significantly. This edge corresponds to the location of compressors in the best region, where their work is the lowest. This corresponds to a main compressor inlet pressure slightly above the critical pressure. The edge shows, where the compressor inlet pressure drops below this pressure. In the region of the lower pressure ratios the cycle efficiency is fairly steady. Hence during operation one should maintain the compressor

Figure 3.59. Efficiency of recompression Brayton cycle.

inlet pressure and vary the compressor outlet pressure. This is an important finding for the cycle control scheme.

Another interesting finding is that an optimum compressor outlet pressure exists. One can observe the location of the peak efficiency between 20 and 25 MPa. It was observed that with decreasing recompressed fraction the optimum pressure shifts to higher pressures. However, this optimum is merely thermodynamic, since the analysis was performed with fixed fractional pressure drops. In reality, the fractional component pressure drops will be reduced as the pressure increases, which will turn into an efficiency improvement.

3.9.2. Design Case Studies of the Recompression Brayton Cycle

In order to correctly evaluate the potential of the cycle and identify the optimum operating conditions a code that iterates on the recuperator pressure drops was developed. The parametric studies were carried out for a range of high temperature effectiveness and recompressed fractions (note that the recompressed fraction determines the low temperature recuperator effectiveness, since once the recompressed fraction is known, the low temperature recuperator effectiveness is fixed). This analysis yielded values of the size of the recuperators (in specific means of m^3/MW_e) and cycle efficiency for a certain recompressed fraction and high temperature recuperator effectiveness. This helped to optimize the value of high temperature recuperator effectiveness and recompressed fraction. The reason why an optimum value of high temperature recuperator effectiveness and recompressed fraction exist arise from the different contributions of high and low temperature recuperators to the cycle efficiency. Increasing the high temperature recuperator effectiveness past the value at which its contribution to efficiency increase is miniscule is not reasonable, because, for a fixed total volume of recuperators, the low temperature recuperator effectiveness will drop and overall the cycle efficiency will decrease.

The scheme to optimize the split of the recuperator volumes is the following. First, calculate the cycle efficiency for different high temperature effective nesses and recompressed fractions. Design the recuperators, i.e. evaluate the size and the pressure drops. On the 3-dimensional plot of cycle efficiency versus the high temperature recuperator effectiveness and recompressed fraction (see Figure 3.60 and Figure 3.61) plot the lines of constant recuperator sizes. Inspecting the efficiency dependence on the high temperature recuperator effectiveness and recompressed fraction

Figure 3.60. Cycle efficiency and recuperator sizes for the recompression Brayton cycle.

yields their optimum values at which the cycle achieves the highest efficiency. It can be clearly seen that optimum values of high temperature recuperator and recompressed fraction exist. These values are different for different recuperator sizes.
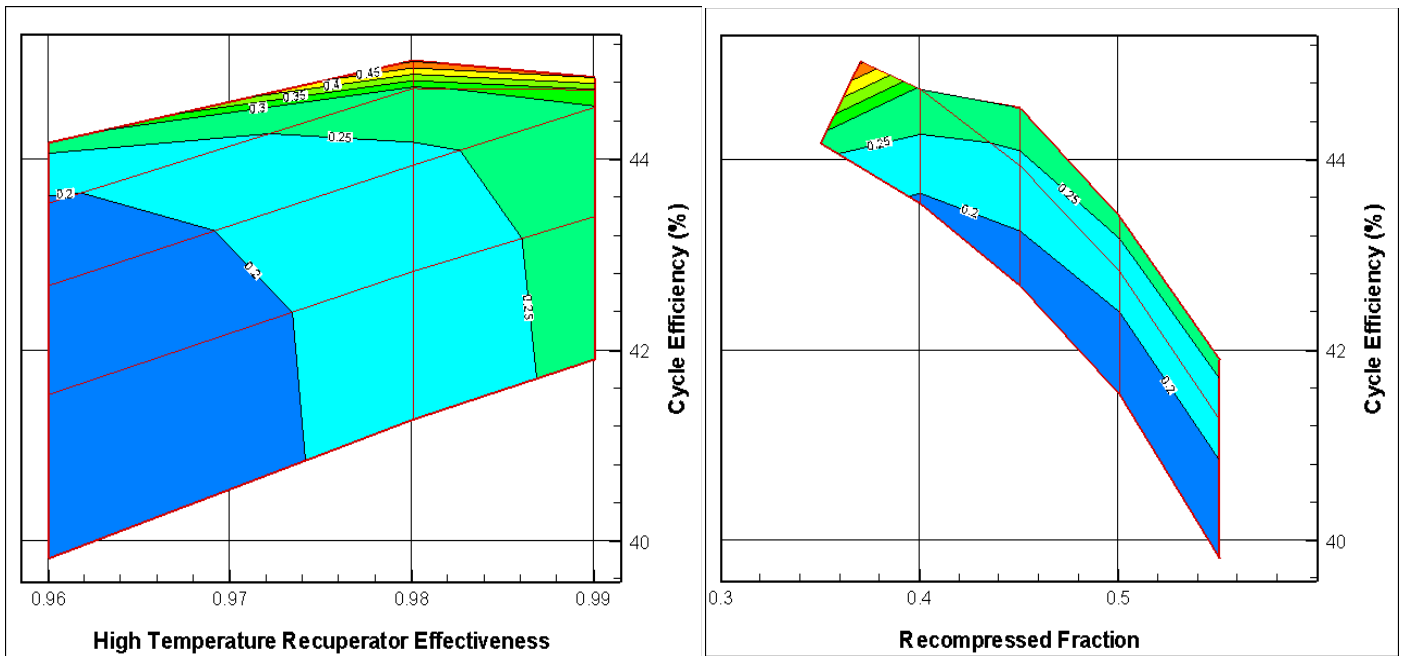
Figure 3.61. Projections of cycle efficiency surface plot for the recompression Brayton cycle.

134

If the optimum value of the high temperature recuperator volume at lower recuperator volumes is exceeded, the cycle efficiency drops significantly. The recompressed fraction also has an optimum value. However, exceeding this value is not accompanied by a significant reduction of the cycle efficiency. The reduction becomes more significant at high recuperator volumes, which are not intended for cycle use. In performing the design one should first optimize the recompressed fraction and then, based on the recompressed fraction, select the optimum value of the high temperature recuperator effectiveness. It was found that the last year reference design operates very close to the optimum values. Therefore, there is no need to redesign the cycle.

3.9.3. Component Design

This section describes the current state of the supercritical CO_2 recompression Brayton cycle component design effort. At present, detailed component designs have not been fully completed. However, most of the design issues have been addressed and sufficient knowledge is now available regarding the component dimensions and performance.

3.9.3.1. Supercritical CO_2 Recompression Brayton Cycle Heat Exchanger Design

The heat exchangers are by far the largest supercritical CO_2 recompression Brayton cycle components. One of the main goals is to keep the cycle compact. Therefore it is necessary to survey current heat exchanger technology and select a heat exchanger type that is compact and has a small pressure drop. Classical shell and tube heat exchangers are not suitable. In order to achieve a high degree of compactness the tube diameters would have to be very small. This would introduce difficulties in manufacturing. Furthermore, the pressure differential in the recuperator is large, so the tube wall would have to be thick to withstand the difference between the high and low cycle pressures. Due to these reasons different types of compact heat exchangers were surveyed.

Compact heat exchangers have been used for several decades and the operating experience with them is satisfactory. They were developed mainly for gas applications since gases have, in general, poor heat transfer capabilities. In order to improve the heat transfer, extended surfaces are used. Compact heat exchangers can be divided into several types based on their means for heat transfer augmentation: fins, plates, matrices etc.

Two different compact heat exchanger types were investigated. The first choice, plate and fin compact heat exchangers performed well and their size was reasonable. However, when the high-pressure differential was taken into account and a basic structural analysis was performed, the required material thickness (mainly that of the parting plates) was too high. This increased the size of the heat exchangers beyond acceptable values and hence use of these heat exchangers had to be abandoned.

The second possibility investigated was use of printed circuit heat exchangers manufactured by HEATRIC. These heat exchangers are not sensitive to high pressures and high-pressure differentials since they consist of many plates into which the channels are chemically etched. These channels have the shape of a semicircle with diameters about 1 to 2 mm. The channels can be straight or wavy. Figure 3.62 shows a cut through a printed circuit heat exchanger showing the shape of the channels [HEATRIC 2002, Hesselgreaves 2001]. In our case, the recuperators achieve the best thermal performance when the channel diameters on the hot and the cold side are the same, even though the pressure drop on the cold side is about three times more than on the hot side.
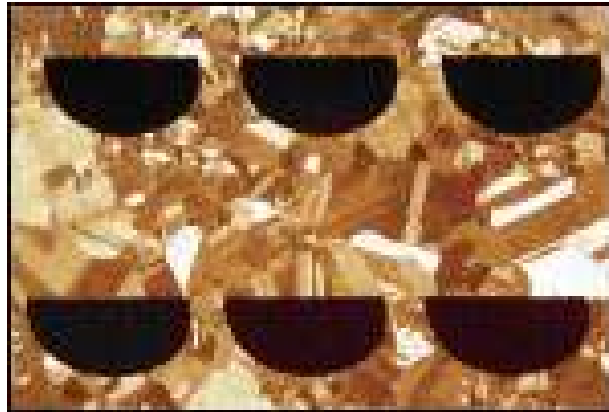
Figure 3.62. Channel shape of the printed circuit heat exchangers [HEATRIC 2002].

A simplification was made by treating the heat exchanger as having counter-current flow. The heat exchanger configuration as manufactured by HEATRIC is counter-current with one flow path having a Z shape as shown in Figure 3.63. This simplification is not conservative and the results will underpredict the real size. A better model will be developed in the future that will be capable of evaluating the Z-flow path more precisely.
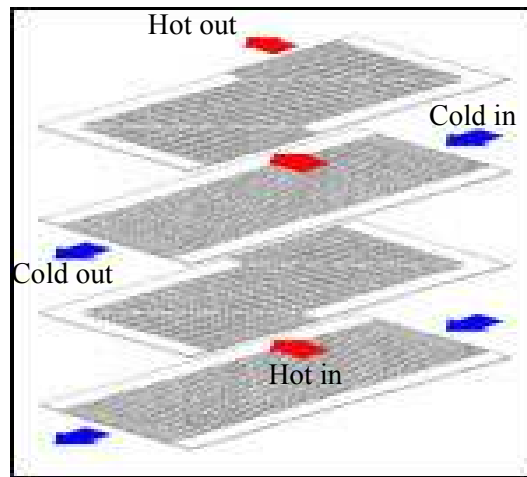
Figure 3.63. Z shape countercurrent flow of the recuperator [HEATRIC 2002].

Decreasing the recompressed fraction to the minimum possible value, where the cycle achieves the highest efficiency, is not reasonable, as the improvement of the cycle efficiency decreases whereas the recuperator size increases rapidly. The diameter of the semicircular channel is a very important parameter. Decreasing the channel diameter reduces the pressure drop across the recuperator. This is because the plate thickness is reduced as the channel diameter is reduced, which, together with more channels per plate, increases the heat transfer area per cubic meter. This reduces the overall length of the recuperators and thus their total volume and the pressure drop. Because of this behavior the only limitation on the channel diameter is given by manufacturing technology. The channel diameter should be as small as possible. Since a 1 mm channel diameter is the lowest quoted value [Hesselegreaves 2001], it was used for further design efforts.

Table 3.22 shows five case studies of recuperators. The importance of the channel diameter can be clearly seen in the first row. Recuperators with channel diameter of 0.5 mm are the smallest among the others presented in the table. The cycle efficiency is very high. The cycle loses only 0.08 % in the efficiency due to the pressure drop. If manufacturing of printed circuit heat exchangers with 0.5 mm channel diameters were possible, it would be of great help to cycle deployment. However, even with a channel diameter of 1 mm the cycle achieves a high

efficiency and the recuperators are still of acceptable size. In the high-pressure drop case (the last row) the cycle efficiency drops by 0.4% due to the pressure drop and the volume of the heat exchangers is reasonable. Note that the heat exchanger volumes cover only the printed circuit heat exchanger active heat transfer volume. Additional volume will be introduced by plena and piping.

Table 3.22. Case studies of recuperator sizes.

Width (m)	Height (m)	Channel Diameter (m)	Length HTR (m)	Length LTR (m)	dP HTR-HS	dP HTR-CS	dP LTR-HS	dP LTR-CS	Cycle Efficiency[*] .(%)	Volume (m^3/MW$_e$)
1.5	3	0.0005	0.4323	0.4303	0.0002	0.0016	0.0001	0.0009	45.19	0.2329
1.5	3	0.001	0.9385	0.9072	0.0002	0.0015	0.0001	0.0008	45.2	0.4984
1.2	3	0.001	0.9831	0.9463	0.0003	0.0023	0.0002	0.0013	45.15	0.4168
1.1	3	0.001	1.0029	0.964	0.0004	0.0027	0.0002	0.0015	45.13	0.3579
1	2	0.001	1.1439	1.0959	0.001	0.0074	0.0005	0.0043	44.87	0.2688

[*] Cycle efficiency with 0 pressure drops across the recuperators is 45.27%
Legend: HTR – high temperature recuperator, LTR – low temperature recuperator, dP – fractional pressure drop, HS – hot side, LS – cold side

The design of the precooler is not as difficult as the design of the recuperators. Since the precooler acts only as a heat sink it affects the cycle efficiency only through its pressure drop. By varying the face area it is possible to design a heat exchanger such that it will have the desired pressure drop. The question is the optimization for size vs. cost. The other consideration in the case of the precooler is the value of pumping power on the water side. This reduces the net efficiency of the cycle. The final optimization can be done only if the exact cost of the printed circuit heat exchanger is known and one can quantify the cost benefits. Otherwise, the same considerations as in the case of the recuperators apply.

3.9.3.2. Turbo-Machinery Design

For both component types (turbine and compressors) axial flow machines were selected. The main reason for this was the requirement of multiple stages and the fact that the efficiency of radial flow machines drops significantly when multiple stages are used. In general, axial flow machines dominate large power applications whereas centrifugal machines are restricted to low powers, where the flow is too small and efficient use of axial blades is not possible. Another important aspect of turbo-machinery design is synchronization with the grid. This sets the rotational speed of the turbo-machinery. It is not intended to use frequency converters in the present applications since their efficiencies and power rating do not achieve the required level of performance needed here.

Compressor Design

In this work only a 2-dimensional simplified analysis is performed in order to assess the necessary number of stages and their hub and tip diameters. Using the 2-dimensional theory, only two components of velocity, axial and tangential, are considered. This analysis is usually sufficient for the later compressor stages, which have short blades. However, due to the high pressure of the CO_2 in the cycle the inlet blade lengths are very small so the 2-dimensional analysis should be sufficient for preliminary assessment. The design is usually performed in such a way that the axial velocity is kept constant. The blade speed, axial velocity, and fluid deflection in the rotor blades should be kept high to obtain high stage pressure ratio.

Blade speed is a function of the rotational speed and diameter. It affects the centrifugal stress in the rotor blades. The maximum centrifugal tensile stress occurs at the blade root and can be calculated from:

$$\sigma = \frac{\rho_s}{2} u_t^2 \left[1 - \left(\frac{r_r}{r_t} \right)^2 \right]$$ (3.104)

The ratio r_r/r_t is called the hub-tip ratio and is one of the input parameters for compressor calculations. ρ_s is the density of the material and u_t is the tip speed. To minimize the stress the tip speed should be kept low and high hub-tip ratios should be used. In our case the tip speed is set by the tip diameter, since the compressor rotational speed is synchronized with the grid. The importance of the selection of the hub-tip ratios will be discussed later as it affects more than just blade stresses. However, for the hub-tip ratios that will be used, the stresses are low.

Axial velocity is limited due to aerodynamic reasons. The maximum relative velocity will occur at the tip of the first stage. Current technology enables Mach numbers up to about 1.1 without excessive losses. However, for our case, since the main effort is to design a highly efficient compressor, the limiting value of axial velocity is set such that the speed of sound is not exceeded at the tip of the first stage.

High fluid deflections in the rotor blades result in a high rate of diffusion. The currently used criterion for allowable diffusion is called the diffusion factor and was developed by NASA. Application of the diffusion factor is not simple, so an earlier simple criterion, the so-called de Haller number, was used instead. The de Haller number is defined as the ratio of the relative velocity at stator inlet v_2 to the relative velocity at rotor inlet v_1. The de Haller number should be at least 0.72 in order to avoid excessive losses.

Another important aspect of design is assessment of blockage in the compressor annulus. Due to the adverse pressure gradient in the compressor, the boundary layers along the annulus walls become thicker as the fluid passes through the compressor. This reduces the effective area of the annulus and the axial velocity through the compressor. The result of this is that the work capacity is reduced. In order to account for this effect, the work done factor λ is introduced. This factor is less than unity and expresses the fraction of work that is done compared to the work that would be done if the blockage in the compressor annulus would not occur. Another way to account for this phenomenon is to assign blockage factors to reduce the effective annulus area. Both approaches represent empirical corrections developed by compressor manufacturers. In this work the work done factors were used.

Using the above design criteria, parametric studies were performed and possible values of the main design parameters were selected. The number of stages and the hub and the tip diameters were evaluated. The calculation followed the procedure described in [Cohen et al. 1991]. The calculations were performed over a wide range of hub-tip ratios and axial velocities. For each value of hub-tip ratio and axial velocity, the de Haller number and speed of sound were checked to see if they satisfy the design limits. The number of stages and the tip diameter were then estimated to evaluate the compressor size.

To select the design values those points that satisfied the velocity and diffusion limits were considered. Since one of the requirements is compactness those cases with a low number of stages and tip diameters were of primary interest. Once the efficiency calculations are done the selected cases should be reconsidered based on the values of efficiency. Currently, the cases in Table 3.23 are considered as the reference design:

Table 3.23. Compressor characteristics.

	Max Tip Diameter (m)	Number of stages	Axial velocity (m/s)	Maximum velocity (m/s)
Main Compressor	0.94	2	130	197
Recompressing Compressor	1.09	3	120	234

Turbine Design

Design of a turbine is in general simpler than compressor design, since the pressure gradient has the same direction as the fluid flow. In this analysis the simple mean-diameter treatment was used. Since CO_2 turbines are not commonly manufactured parametric studies were carried out in order to identify optimum values of turbine parameters. An important requirement on the hub diameter is imposed by the high-pressure differential across each stage. When the hub diameter is reduced, the number of blades is also reduced. This means that the bending stress within the blade increases. Blade bending stress is not limiting in the case of steam turbines, where due to the large diameters the centrifugal stress is much more important. However, in such a high power density machine as the CO_2 turbine the bending stress is very important for the profile selection and overall turbine design. Therefore, the hub diameter selection must be confirmed in the future by structural analysis.

The reference turbine parameters are listed in Table 3.24. The following design guidelines were developed for the turbine design based on the parametric studies. The hub diameter should be kept as small as possible. The optimum number of stages is 4 to 7. Increasing the rotational speed will hurt the turbine efficiency. Reducing the rotational speed on the other hand increases the number of stages that have to be used. The standard 60 or 50 rps are well-suited rotational speeds at which the turbine achieves high efficiency with a reasonable number of stages. The currently estimated turbine efficiency is 91%, however this number was obtained using the steam turbine correlations. In the future the gas turbine approach will be used in order to further improve this estimation.

Table 3.24. Reference turbine parameters

Reaction	0.5
Profile angle	72°
Mass flow rate	3644.3 kg/s
u/c	0.9
Rotational speed	60 rps
Inlet pressure	19.4 MPa
Outlet pressure	7.7 MPa
Inlet temperature	550 $^{\circ}$C
Hub diameter	0.5 m

Comparison with other turbines

For the same rotor diameter and u/c a helium turbine has about 10 times more stages and the polytropic turbine efficiency is better than for a CO_2 turbine. However, use of such a large number of stages is not reasonable. The usual rotor dimension for a helium turbine at synchronized rotational speed is about 1.5 m [Yan and Lidsky 1993]. For this rotor diameter the helium turbine efficiency is lower than for CO_2 and the turbine still has more stages than a CO_2 turbine. The helium turbine is about 4-5 times longer. Figure 3.64 compares a steam turbine and a helium turbine to the CO_2 turbine. In addition to the size reduction, the big advantage of the CO_2 turbine is that it can be a single body design, whereas both steam and helium turbines usually employ more turbine bodies (high, medium and low-pressure in the case of steam, a high-pressure unit to power compressors and a low-pressure unit to power the generator in the case of helium). This further increases the difference in size as additional plena and piping are necessary.

Steam turbine: 55 stages / 250 MW
Mitsubishi Heavy Industries Ltd, Japan (with casing)

5 m

Helium turbine: 17 stages / 333 MW (167 MW$_e$)
X.L.Yan, L.M. Lidsky (MIT) (without casing)

Supercritical CO$_2$ turbine: 4 stages / 450 MW (300 MW$_e$)
(without casing)
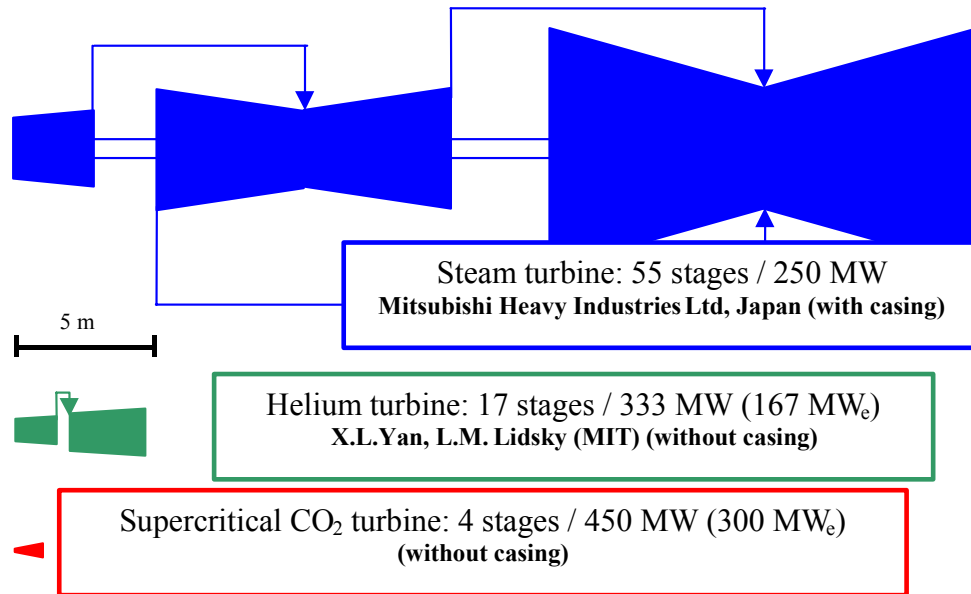
Figure 3.64. Comparison of turbine sizes for steam, helium and CO$_2$.

3.9.4. Summary

This chapter described the approach toward optimization of the recuperator sizes and preliminary design of the main components used in the supercritical-CO$_2$ Brayton cycle. For any given total volume of recuperators an optimum of recuperator size with respect to the efficiency exists. This optimum is described by the optimum values of high-temperature recuperator effectiveness and recompressed fraction.

The necessity for effective recuperators led to the consideration of compact heat exchangers. In order to accommodate the high-pressure differential, the printed circuit heat exchangers manufactured by HEATRIC were selected. The most important factor for the performance evaluation is the heat exchanger geometry and flow arrangement. Due to the lack of literature on this type of heat exchanger some simplifying assumptions were made. The heat exchangers were treated as counter-flow even though in reality they are counter-flow combined with crossed flow in the headers. This assumption is not conservative, and a better model that represents the real flow arrangement will be developed in the future. The diameter of the semicircular channel was selected as 1 mm as this is the lowest dimension referenced [Hesselgreaves 2001]. Reducing the diameter further would significantly improve the heat exchanger performance. A conservative assumption was to select the heat conduction characteristic length equal to the plate thickness, even though it is likely to be smaller in reality. The recuperators are of acceptable size.

Designing the precooler is significantly simpler than designing the recuperators. The same type of heat exchanger as for the recuperators is used. The precooler is designed to minimize the pumping power of the cooling water and pressure drop on the gas side and still have an acceptable size.

A preliminary design of the turbo-machinery was also completed. The very encouraging finding is that the turbo-machinery size is miniscule compare to any other currently used fluid. It is about 30 times smaller than conventional steam turbines and about 5 times smaller than helium turbo-machinery.   The preliminary efficiency calculation results are close to 92% efficiency (accounting for kinetic energy losses). The size of a 300 MW$_e$ turbine is about 1 m long and 0.8

m in diameter with approximately 5 stages. A similar evaluation was performed for the compressors giving on the order of 2 and 3 stages for the main and recompressing compressors respectively. The maximum diameter is about 1.1 m. The efficiency calculations have not yet been completed, but the design satisfies the de Haller condition for allowable diffusion between stages. The detailed analysis and estimation of off-design performance will be carried out in the future.

Overall, the cycle components are compact and their design should not impose significant requirements on research and development. The main unanswered question is the stability and off-design performance of the compressor.

3.9.5. Future Work

The future work will focus on the refining the component designs, plant dynamic and transient behavior, and development of a control scheme and off design point performance assessment. The component refinements will focus on the development of a better model for the performance estimation of printed circuit heat exchangers, thus improving the accuracy of the size estimation of the recuperators and precooler. On the turbo-machinery side, the current design will be finalized. The off design point efficiency maps will be generated. These maps will be used for the control analysis. A plant layout and overall footprint will be developed. The development of the control scheme will strive for high efficiency over a wide range of operating conditions.

3.10. Capital Cost Analysis (R. Herron, MIT)

3.10.1. Introduction

In the previous years of this project, Kim et al. [2000] and Driscoll and Kim [2001] focused on the selection of various parameters for a LBE-cooled reactor with natural circulation. The lifetime levelized capital cost was used as a means of evaluating the optimum thermal power, reactor configuration, and balance of plant parameters. The goal of this economic analysis is to evaluate the total capital cost of the current LBE plant design. This analysis differs from the work of Kim in that it focuses on the capital cost of the LBE plant as a whole in different configurations as opposed to the effect individual parameters have on the lifetime levelized capital cost. Delene and Hudson [1993] presented a standard method for capital cost analyses in their report "Cost Estimate Guidelines for Advanced Nuclear Power Technologies". The report provides a summary of the techniques for both a complete, ground-up cost analysis and a method for adjusting and scaling an existing capital cost analysis. The later was done for this LBE reactor. The terminology and cost account structure for this work are presented in Appendix B.

3.10.2. Capital Cost Analysis Methods

The techniques involved in the scaling of an existing capital cost analysis are based on several simple relationships. These are the scaling of costs based on electrical output, accounting for interest accrued during construction, calculating contingencies, and converting between constant and current dollars. These relationships, which are presented below, are basic mathematical relations, but can become complex when performed repeatedly for all cost accounts.

3.10.2.1. Scaling Relationships

Because a ground up capital cost analysis was beyond the scope of this report, the ALMR cost analysis was scaled to the size of the LBE plant. Capital costs are scaled according to the simple relationship provided by Equation (3.105) [Delene et al. 1988].

$$Cost_{new} = Cost_{base} \left(\frac{Power_{new}}{Power_{base}} \right)^a \qquad (3.105)$$

The *Power* terms represent the electrical output of each power plant. The term a is the "scaling factor," which is a property of the component being scaled. Components that are less dependent on the size of the power plant (electrical output) will have values of a that approach zero. Components that are very dependent on the size of the power plant will have scaling factors that are close to unity. Table 3.25 is a summary of the scaling factors provided by the NECDB. Note that the scaling factor for land and land rights is zero, which indicates that the property size for a nuclear reactor is not dependent on electrical output. The opposite is true of the turbine plant equipment, which is heavily dependent on reactor size.

Table 3.25. Scaling factors from the NECDB [Delene et al. 1988]

Account	Nuclear CONCEPT	Nuclear Derived	Coal
Direct Costs			
Land and Land Rights	0.00	0.00	0.00
Structures and Improvements	0.50	0.59	0.45
Reactor/Boiler Plant Equipment	0.60	0.80	0.40
Turbine Plant Equipment	0.80	0.83	0.70
Electric Plant Equipment	0.40	0.39	0.30
Miscellaneous Plant Equipment	0.30	0.59	0.20
Main Condenser Heat Rejection System	0.80	1.06	0.80
Indirect Costs			
Construction Services	0.45	0.69	0.50
Home Office Engineering and Services	0.20	0.60	0.60
Field Office Engineering and Services	0.40	0.69	0.50
Owner's Costs	0.50	0.64	0.55
Cost-Weighted Average	0.50	0.64	0.55

Table 3.25 has three columns of scaling factors. The third column is for coal plants and is included only as a point of reference. The column entitled CONCEPT contains scaling factors used by the CONCEPT computer code for cost analysis. These scaling factors are appropriate for small changes in reactor size (i.e. 10% to 20%). The Derived column indicates the average scaling factors derived from data collected on a wide variety of actual reactors. These factors are more appropriate for very large changes in power. The cost-weighted average factor is the weighted average of all scaling factors for a power plant [Delene et al. 1988].

3.10.2.2. Interest During Construction

Cash Flow
Because it is important to consider the time value of money in a capital cost analysis, when funds are spent affects the cost of the power plant. The flow of cash can be split into two distinct regions. These are the periods before and after construction begins. Cash flows may differ from project to project, but Figure 3.65 is an example of a commonly accepted cash flow diagram. The vertical axis represents the cumulative expenditure of cash versus time, the horizontal axis. Before construction begins the general assumption is that the flow of cash is constant. A constant cash flow produces a constantly rising cumulative cash flow line, which is indicated in the left

side of Figure 3.65. After construction begins the cumulative cash flow is sinusoidal. The actual cash flow follows a cosine function of time, which produces a cumulative cash flow line that is a sine function of time. The right side of Figure 3.65 is the cumulative cash flow line in this time period. It is standard practice to have a cumulative expenditure of 10% of the total overnight cost at the time construction begins.
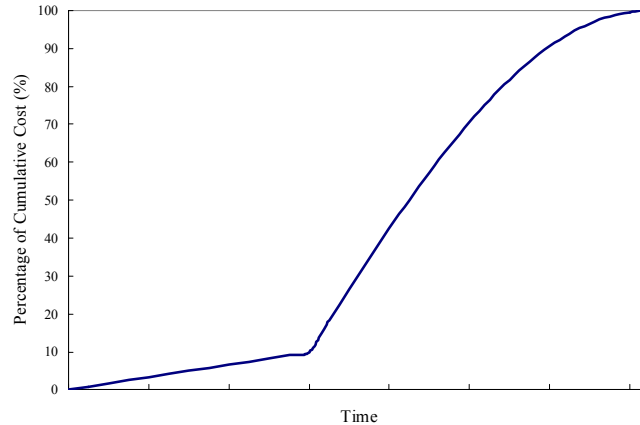
Figure 3.65. Cash flow diagram with 10% of funds spent before construction begins.

The LBE reactor capital cost analysis used the same cash flow schedule as the ALMR standard. Although the LBE rector design eliminates the need for an intermediate heat transport system, this component is not in the critical path for the construction of ALMR. In other words, the addition or subtraction of the intermediate heat transport system does not affect the construction time of the ALMR plant. Due to the number of blocks per plant and the construction learning curve, the construction times differ for each of the four basic plant types. Table 3.26 is a summary of the construction schedules for the ALMR and LBE plants. The letter (F or N) distinguishes between FOAK and NOAK power plants, while the number (1 or 3) distinguishes between power plants with one or three power blocks.

To simplify calculations, an inflation free cost of money can be introduced (X_0). An inflation free cost of money allows constant dollars to be used throughout the capital cost analysis. The last step of the capital cost analysis is to convert from constant dollars to nominal dollars of the year of plant completion. For a given inflation rate (f) and a nominal dollar average cost of money (X), an inflation free cost of money can be calculated according to Equation (3.106) [Park and Sharp-Bette 1990]. Since the ALMR cost analysis was performed in constant dollars, this is the most straightforward method for calculating the interest during construction. Equation (3.107) calculates the interest during construction, where C_i is the funds spent in the ith quarter. The terms t_i and t_{op} represent the time of the ith quarter and the time of construction completion, respectively [Delene and Hudson 1993].

Table 3.26. Cash flow schedules for ALMR and LBE plants [Gokcek et al. 1995].

Plant Type	Time Before Construction Begins (months)	Time After Construction Begins (months)
F1	36	51
F3	36	69
N1	30	39
N3	30	51

$$X_0 = \frac{1+X}{1+f} - 1 \tag{3.106}$$

$$IDC = \sum_i C_i \left(1 + X_0\right)^{t_{op} - t_i} \tag{3.107}$$

3.10.2.3. Contingency Calculations

As defined above, the allowance for contingency adjusts for uncertainties in the capital cost analysis. The base construction cost is the most likely cost of plant construction and the addition of the contingency allowance provides an upper bound for the total construction cost. The contingency for each cost account is expressed as a percentage of the estimated cost. A larger contingency percentage indicates a greater uncertainty as to the actual cost of the account. For example, well-established technology will have smaller contingency percentages than new technology because cost estimates for well-established technology have lower uncertainty. Sample contingency values are provided in Table 3.27.

Table 3.27. General Electric's contingency values [Gokcek et al. 1995]

Nuclear Island		Balance of Plant	
NSSS (safety-grade)	25%	Turbine Generator	5%
NSSS (non-safety)	15%		
Other Factory Equipment	10%	Other Factory Equipment	7%
Site Materials	10%	Site Materials	10%
Direct Labor	20%	Direct Labor	15%
Construction Services	15%	Construction Services	12%
Engineering and Home Office Services	15%	Engineering and Home Office Services	12%
Field Office Services	15%	Field Office Services	12%
Owners Costs	20%	Owners Costs	15%
		Land	10%

The contingency values provided in Table 3.27 are based on General Electric's own experience and are the values used in the 1994 ALMR capital cost analysis. The Department of Energy established a standard set of contingency values in the NECDB, which are slightly more conservative than the ones presented by General Electric, but GE feels their contingency values are accurate given their own experience with balance of plant components. Note that, given the relatively new technology of commercial liquid metal reactors, the contingency value for the nuclear steam supply system is 15% or 25%, but for the well-known technology of turbine generators the value is significantly smaller at 5%.

3.10.2.4. Constant to Current Dollar Conversion

Because the ALMR capital cost analysis was completed in constant 1994 dollars, the LBE plant capital cost analysis was likewise completed in constant 1994 dollars. While having both values in 1994 dollars is illustrative for comparing the economic competitiveness of the LBE to the ALMR, the overall economic competitiveness of the LBE plant is best expressed in 2002 dollars. This will provide the total cost of the LBE power plant if it were finished and ready for operation this year. Doing so requires an average inflation rate (f_{AVG}) and the number of years between

the reference date and the current date (n). Now the total cost in constant dollars can be converted to current dollars using Equation (3.108) [Park and Sharp-Bette 1990].

$$Cost_{CURRENT} = Cost_{CONSTANT} \cdot (1 + f_{AVG})^n \qquad (3.108)$$

The Gross Domestic Product Implicit Price Deflator is a measure of the average inflation rate. In 1994 the index was 0.960, but by 2002 it had risen to 1.107 (the scale is centered on 1996, where the index is 1.000) [www.eia.doe.gov, 2002]. The index value in 1994 is the constant dollar value and the index value in 2002 is the current dollar value. Applying Equation (3.98) yields an average inflation rate between 1994 and 2002 of 1.80%. This average inflation rate will be used later to convert the cost analysis results from constant 1994 dollars to current 2002 dollars.

3.10.3. Application of Scaling Relationships

The ALMR concept was designed to be completely modular. As opposed to a single monolithic plant, the ALMR was composed of multiple, smaller reactors. The standard unit was a power block, which consisted of two reactors and two steam generators coupled to a single turbine generator. The thermal power of each reactor was 840 MWth for a combined power of 1680 MWth per block. With ALMR's steam cycle net efficiency of 37.9%, one power block provided 622 MWe. Complete ALMR power plants could have been composed of one, two, or three power blocks, for electrical power outputs of 622, 1244, or 1866 MWe, respectively.

The ALMR capital cost analysis presents four separate cases, which are labeled F1, F3, N1, and N3. The letter, N or F, describes whether the plant is FOAK or NOAK versions, while the number represents the number of power blocks per plant. In addition, the F1 capital cost analysis (FOAK plant with one power block) includes the costs associated with large common facilities. Large common facilities allow for the expansion of a one-block plant to two or three blocks. This concept would have allowed the electrical output of existing power plants to grow with the power needs of the area.

In order to minimize errors, the LBE plant was organized the same as the ALMR plant. Using the relationships presented above each of the four cases (F1, F3, N1, and N3) was scaled from the power of the ALMR to that of the LBE plant. Although for most cost accounts the scaling was performed according the electrical output (as per the standards presented by Delene and Hudson) several adjustments were made to account for the distinct differences between a lead-bismuth and sodium-cooled reactor.

3.10.3.1. Nuclear Steam Supply System (NSSS)

The nuclear steam supply system is the cost account that includes the majority of the reactor components: reactor vessels, intermediate heat exchangers, and main coolant pumps. While the majority of the common cost accounts between the ALMR and the LBE reactors were scaled according to electrical output, these components were scaled differently. This is due to the differences between the sodium and LBE coolants.

Vessels

Because of the differences in the properties of the two liquid metal coolants, the reactor vessels for the ALMR and LBE reactors differ by more than size. First, because of the corrosive nature of the LBE coolant, a different material was chosen for the reactor vessels. Second, because LBE is approximately ten times denser than sodium the vessels for the LBE reactor must be

significantly more robust to support the mass of the coolant. This translates to thicker vessel walls and thus a greater mass. Due to these two major differences the reactor vessels were scaled by factors that account for the cost of materials and the fabrication cost instead of the electrical outputs of each plant.

Scaling based on the cost of the materials was performed according to Equation (3.109).

$$Cost_{new} = f_{MATERIAL} \cdot f_{FABRICATION} \cdot Cost_{base} \tag{3.109}$$

The two factors, $f_{MATERIAL}$ and $f_{FABRICATION}$ adjust the base cost due to the differences between materials costs and fabrication costs for the two reactors. Each of these factors is the ratio of the materials and fabrication costs of the two reactors. The product of these two ratios provides the ratio of the new component cost to the old component cost based on the mass of material involved. However, the material factor is actually composed of two ratios. These are the ratio of the masses of the new and base components and the ratio of the cost per kilogram ($Price$) for the material used in each component. The product of these two ratios provides the definition of $f_{MATERIAL}$ given in Equation (3.110).

$$f_{MATERIAL} = \frac{Mass_{new}}{Mass_{base}} \frac{Price_{new}}{Price_{base}} \tag{3.110}$$

The prices of materials were found from Carpenter Technology, a supplier of large amounts of raw materials. The material used for the majority of the components in the ALMR design was SS316. Work is ongoing on the material selection for the LBE plant, but the material with the most promise currently is 400-series ferritic steel [Ballinger 2002]. Prices were obtained for 316 and 440c (which represents the price of a material for the LBE reactor). These prices, quoted for a 1000-pound purchase, are given in Table 3.28. Table 3.29 presents the mass ratios of the vessels and heat exchangers used in the LBE capital cost analysis.

In addition to the cost of the raw materials involved in making a component, there is the cost of fabrication. Since the components in the nuclear steam supply system must be made in compliance with Section III of the ASME pressure vessel code, fabrication costs were assumed to be a linear relationship with mass. The original cost estimate for the ALMR report included the cost of fabrication, so the scaling due to mass in Equation (3.109) also factors for the differences in fabrication costs. Thus the scaling factor for fabrication costs is equal to unity ($f_{FABRICATION} = 1$). Thus Equation (3.110) can be simplified to yield Equation (3.111).

Table 3.28. Materials prices for ALMR and LBE reactor components

Reactor	Material	Price ($ per pound)
ALMR	316	2.49
LBE	440c	2.05

Table 3.29. Mass ratios of LBE to ALMR reactor components

Component	Mass Ratio (LBE/ALMR)
Heat Exchangers	14.97
Reactor Vessels	2.62

$$Cost_{new} = \frac{Mass_{new}}{Mass_{base}} \frac{Price_{new}}{Price_{base}} Cost_{base} \tag{3.111}$$

146

Heat Exchangers and Main Coolant Pumps

The ALMR concept used a sodium coolant and had two heat transport loops: a primary and an intermediate. The primary heat transport system cost account was a lumped account that included the capital costs of both the intermediate heat exchangers and main coolant pumps. The intermediate heat exchangers were similar to the LBE heat exchangers (see Section 3.5) in that they are of a straight tube design. The straight tubes make it possible to determine the total mass of the heat exchangers for each reactor to scale according to the method discussed in the previous section. Unfortunately it's difficult to determine the percentage of the primary heat transport system cost attributed to the heat exchangers and the percentage attributed to the main coolant pumps. The ALMR coolant pumps are also electromagnetic, as opposed to centrifugal pumps as in the LBE design.

If the estimated cost of the ALMR intermediate heat exchangers is assumed to be a fraction F of the total estimated cost of the primary heat transport system cost account, then $1-F$ represents the fraction of the primary heat transport system cost attributable to the ALMR main coolant pumps. This allows the following relationship to be drawn between the capital costs of the primary heat transport system for the ALMR and LBE reactor.

$$Cost_{new} = Cost_{base}\left[F\left(\frac{Mass_{new}}{Mass_{base}}\right)\left(\frac{Material_{new}}{Material_{base}}\right)+\left(1-F\right)\left(E\right)\right] \qquad (3.112)$$

The E term accounts for the differences between the costs of the ALMR and LBE main coolant pumps. This ratio is very difficult to gauge for two reasons. First, the ALMR used electromagnetic main coolant pumps while the LBE plant uses centrifugal pumps. These two pumps can differ significantly in cost. Second, the scale of each of these pumps also differs significantly. The ALMR plant uses four pumps to circulate the primary coolant, while the LBE plant uses only two. This is further complicated by the differences in density and specific heat between the two liquid metal coolants. As a result, it is very difficult to estimate the cost ratio of the two primary coolant circulation systems. The most straightforward and reasonable approach is to scale the pump component of the primary heat transport system cost account in the same manner that has been used throughout the rest of the plant. This will be done by the electrical output with the scaling factor used for reactor plant equipment (a=0.6). Equation (3.112) can now be rewritten to produce the following equation:

$$Cost_{new} = Cost_{base}\left[F\left(\frac{Mass_{new}}{Mass_{base}}\right)\left(\frac{Material_{new}}{Material_{base}}\right)+\left(1-F\right)\left(\frac{Power_{new}}{Power_{base}}\right)^{a}\right] \qquad (3.113)$$

Intermediate Heat Transport System and Steam Generators

Like most sodium-cooled reactors the ALMR plant made use of an intermediate heat transport system (IHTS), which transferred energy from the primary loop to the steam generators. In the LBE plant neither the IHTS or steam generators are necessary because LBE is an inert coolant and does not violently react with water or air. As described above, the cost of the avoided LBE steam generators is represented by the scaled cost of the intermediate heat exchangers in the ALMR. As a result the cost accounts that include the IHTS and the steam generators for the ALMR, 220A.222 and 220A.223, are not included in the LBE plant capital cost analysis.

3.10.4. Sensitivity Analysis

Applying the relationships above makes it possible to make an estimate of the capital cost of the LBE plant based on the capital cost analysis of the ALMR plant performed in 1994. Unfortunately one significant value is unknown. This unknown is the value of F to be used in Equation (3.113). This value F determines the fraction of the primary heat transport system cost account that is attributable to the intermediate heat exchangers. Since this value is not accurately known, the first step is to perform a sensitivity analysis. This will provide total cost values for the LBE plant for a given value of this factor F, which is varied over the range from 0 to 1. The capital cost of the LBE plant is also dependent on net efficiency. The current steam power cycle has an efficiency of 42.0%, but a sensitivity analysis will be performed over a wider range. Table 3.30 provides key data used throughout the capital cost analysis. Table 3.31 provides the capital cost of the ALMR plant, on a dollars per kilowatt-electric basis, in both 1994 and 2002 dollars [Gokcek et al. 1995].

Table 3.30. Constants used in LBE capital cost analysis.

| Variable	Value Used
Inflation-Free Average Cost of Money, X_0, (yrs^{-1})	6.19%
1994 GDP Implicit Price Deflator	0.960
2002 GDP Implicit Price Deflator	1.170
LBE Plant Net Efficiency	42.0%
LBE Thermal Power (MWth)	700

Table 3.31. Results of 1994 ALMR capital cost analysis [Gokcek, et al. 1995].

ALMR Plant Type	1994 $/kWe	2002 $/kWe
F1 (622 MWe)	2,394	2,761
F3 (1866 MWe)	1,838	2,120
N1 (622 MWe)	1,904	2,196
N3 (1866 MWe)	1,562	1,801

3.10.4.1. Variation of heat exchanger to EM Pump Cost Ratio, *F*

The only unknown in the capital cost analysis of the LBE reactor is the fraction of the primary heat transport system cost account attributable to the IHXs in the ALMR. Evaluating the capital cost, on a dollars per kilowatt-electric basis, will illustrate the overall dependence of the cost of the LBE reactor on this ratio, F. Figure 3.66 is a plot of the cost, in 2002 dollars per kilowatt-electric, for each of the four cases over a wide range of values for F. For this evaluation the net cycle efficiency was set at 42.0%, which is a conservative estimate, given the 3.5ºC decrease in maximum operating temperature due to the redesign of the steam generators.

Figure 3.66. LBE reactor cost as a function of the primary heat transport system cost ratio, *F*.
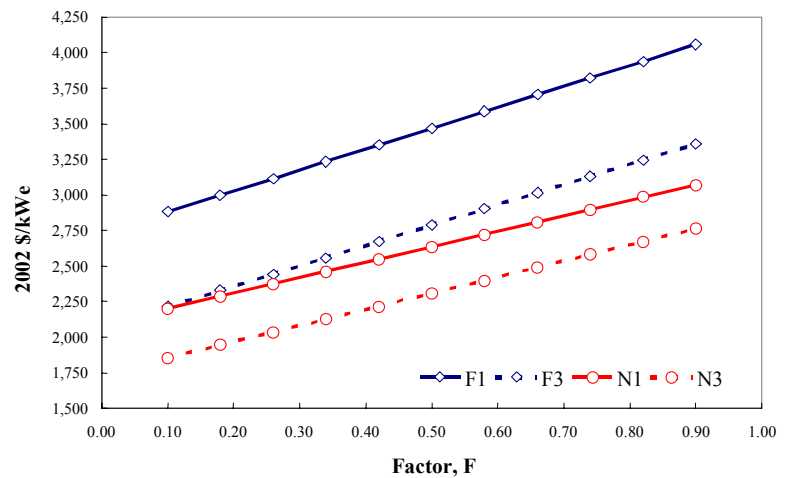
Unfortunately, the primary heat transport system is a larger portion of the capital cost for the LBE plant than for the ALMR plant. This is because the heat exchangers in the LBE reactor must be

significantly more robust than the intermediate heat exchangers in the ALMR. The intermediate heat exchangers the ALMR are sodium-to-sodium, and have less surface area as a result of the excellent heat transfer properties of sodium. They also have thinner tubes due to the small pressure differential between the primary and intermediate loops. Recall from Table 3.27 the steam generators in the LBE reactor have a mass approximately fifteen times greater than the intermediate heat exchangers in the ALMR. The heat exchangers for the LBE reactor are more massive, and thus more expensive.

3.10.4.2. Variation of Net Cycle Efficiency

The current superheated steam cycle has a net cycle efficiency of 42.0%. Since the capital cost analysis is a function of the electric output of the power plant, changes in net efficiency will affect both the overall capital cost for the LBE reactor and on a per kilowatt-electric basis. Figure 3.67 is a plot of the cost per kilowatt-electric (in 2002 dollars) as a function of the net cycle efficiency. In this plot the primary heat transport system ratio (F) is held constant at 0.25.
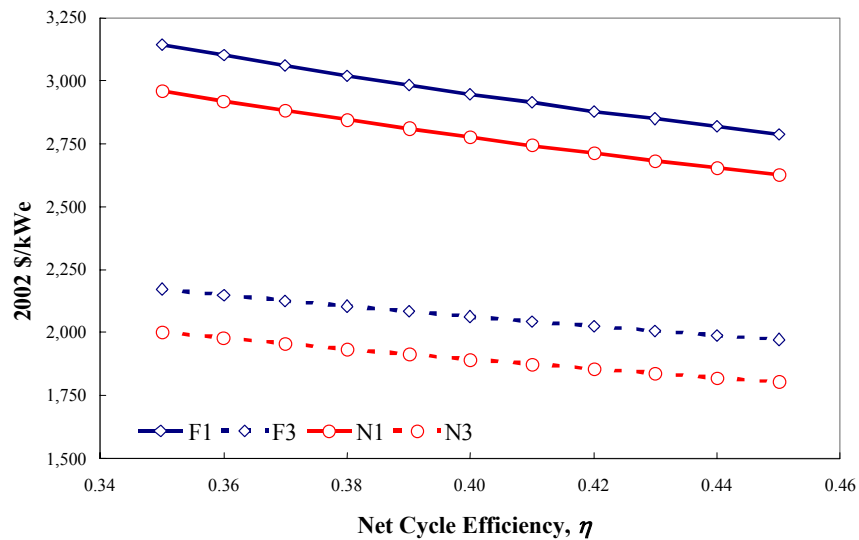

Figure 3.67. LBE reactor cost versus net power cycle efficiency (constant $F = 0.25$).

The cost per kilowatt-electric for the LBE reactor is a weak function of the net cycle efficiency, as evidenced by the shallow slope of the lines in Figure 3.68. As would be expected, the LBE reactor is more economical at higher efficiencies. Also note the big cost savings for the NOAK reactors as opposed to the FOAK reactors.

3.10.5. Summary of the Capital Cost Analysis

As shown above, the overall cost of the LBE plant is highly dependent on the fraction of the total primary heat transport system cost attributed to the intermediate heat exchangers. This is because the steam generators in the LBE reactor are significantly more robust than the IHXs in the ALMR plant. If this fraction is relatively small, on the order of one-quarter ($F = 0.25$), then the LBE plant is very competitive with the ALMR plant. Table 3.32 is a summary of the capital cost analysis, given in 2002 dollars per kWe, if the intermediate heat exchangers make up 25% of the primary heat transport system cost in the original capital cost analysis.

Figure 3.66 suggests that there is some break-even primary heat transport system ratio that makes the ALMR and LBE cost per kWe equivalent. By iterating over F this value can be found. Table 3.33 provides the primary heat transport system cost ratio where the costs per kilowatt-electric for the ALMR and LBE plants are the same.

All the break-even primary heat transport system ratios given in Table 3.33 are reasonable given that the primary heat transport system cost account for the ALMR plant consists of the cost of two intermediate heat exchangers and four EM pumps. This work indicates that the LBE reactor is economically competitive on a capital cost per kilowatt-electric basis with the ALMR. Although the LBE plant requires more robust reactor vessels and significantly larger in-vessel heat exchangers, the elimination of the intermediate heat transport system and the associated intermediate loop heat exchangers (i.e., the steam generators) and associated facilities give it an economic edge. It should be noted that the current guideline for the Generation IV nuclear power plants is 1000 dollars per kilowatt-electric. The LBE cost estimates exceed this in part because they are based on an approximately ten-year-old cost analysis. Future work should focus on the cost analysis of the supercritical CO_2 power cycle, which has a higher efficiency and a lower capital cost.

Table 3.32. Comparison of ALMR and LBE capital cost (constant $F = 0.25$).

Plant Type	ALMR Total Cost (2002 $/kWe)	LBE Total Cost (2002 $/kWe)
F1	2,761	2,542
F3	2,120	1,991
N1	2,196	1,938
N3	1,801	1,661

Table 3.33. Break-even primary heat transport system cost ratios for LBE competitiveness with ALMR.

Plant Type	PHTS Ratio, F
F1	0.43
F3	0.36
N1	0.54
N3	0.40

4. Results of FY-02 Material Studies

In collaboration with the Massachusetts Institute of Technology (MIT), the INEEL is investigating the dissolution and corrosion characteristics of typical structural metals exposed to lead or lead-bismuth coolant. This section reports the results of the FY-02 dissolution and corrosion experiments. Section 4.1 details the research completed at the INEEL, whereas Section 4.2 provides the research results from the collaborative work performed at MIT. Section 4.1 is broken down as follows: 4.1.1 presents information on our experimental apparatus and experimental procedures. Sections 4.1.2 and 4.1.3 present the inductively coupled plasma (ICP) and scanning electron microscope (SEM) results. Discussions of the coolant chemistry control, the effects of zirconium in the LBE coolant, and the relative reaction rates of the various commercial alloys are presented in Section 4.1.4.

The MIT results are presented in Section 4.2. The experimental apparatus and overall test matrix is discussed in Section 4.2.2. The experimental results for refractory metals tested in Pb are presented in Section 4.2.3. Results for Fe-Si alloys tested in both Pb and Pb-Bi are presented in Section 4.2.4. Issues related to the development of advanced Fe-based alloys are discussed in Section 4.2.5.

4.1. INEEL FY-02 Material Studies (Dr. Eric Loewen and Philip MacDonald, INEEL)

The overall objective of the current program is to further explore the effects of temperature, time, and oxygen potential on the corrosion behavior of selected potential fuel cladding and core structural materials and to make use of this understanding to suggest the composition of more resistant advanced alloys. Four lead-bismuth eutectic (LBE) corrosion test campaigns, exposing several commercially available U.S. steels were performed during FY-02. However only the detailed results for the first two tests are presented in this Annual Report. Funding limitations prevented the analysis of the last two campaigns. Measurements were taken of the sample interaction layers with respect to time, temperature, and alloy type to quantify the damage rates. Corrosion coupons of HT9 steel, 410 and 316L stainless steel, F22 low alloy steel, and iron with three different level of silicon (1, 2 and 3wt.%) were tested at 550 to 700°C for times of 100, 300, 600, 700, and 1,000 hours inside corrosion cells made from hafnium stabilized zirconium alloy and 410 stainless steels during the four tests. Various zirconium alloys were also tested for 100 to 1000 hours at 550 to 700°C. The results of this study show that at low temperatures (<550°C) zirconium has good corrosion resistance to LBE due to the presence of an adherent oxide layer. At higher temperatures (650°C and above), the zirconium alloys are easily dissolved by the LBE. The oxygen potential was controlled within a range of about 10^{-27} and 10^{-40} atm using solid carbon to remove excess oxygen as carbon dioxide and reduce any PbO formed. SEM, energy dispersive X-ray (EDX) analysis, and ICP analyses were all performed on the samples to determine the depth of the interaction (corrosion) layer, and the composition of the LBE and interaction layer. Our FY-02 testing program also included tensile testing of these materials to quantify any embrittlement effects of the LBE exposure. Tensile bars were exposed to LBE at 550, 650, and 700°C for 1,000 hours.

Table 4.1 presents an overview of the experiments performed to date at the INEEL and the key variables in each of those experiments. Experiments 1 through 7Y were conduced in FY-00 and FY-01 and are discussed by Loewen and MacDonald in our FY-01 Annual Report (MacDonald

and Buongiorno 2001). Experiments 10 through 13 were conducted in FY-02, but analysis of the experimental data from Experiments 12 and 13 is not yet complete, so only the results from Experiments 10 and 11 are presented. Oxygen was injected at a level of 10 ppm in an Argon carrier gas for the experiments at high oxygen potential in prior years. Hydrogen was injected in the highly reducing experiments. The results reported here for FY-02 were obtained using INEEL's solid carbon buffer system ($C/O_2/CO/CO_2$) to control the O_2 potential. This INEEL-developed buffer system uses solid and gaseous carbon to control the O_2 level in the LBE to the desired value. The oxygen potential control system is discussed in more detail in Section 4.1.1 below.

Table 4.1. Overview of INEEL lead corrosion experiment runs.

Run No.	PO$_2$	Temp (°C)	Cell Material	Time (hr)	Melt	Metal Samples	Comments
1	Oxidation	600	316 SS	3	Pb, As, Sb[a]	316, 410,F-22, Zr	Initial run to validate safety systems and overall operability.
2	Oxidation	650	316 SS	7	Pb, As, Sb[a]	316, 410,F-22, Zr	Two-day run to validate re-melting lead after freezing.
3	Oxidation	500	316 SS	100	Pb, As, Sb[a]	316, 410,F-22, Zr	Used industrial gasses to establish oxidation conditions.
5	Highly Reducing	500	316 SS	100	Pb, As, Sb[a]	316, 410,F-22, Zr	Used new mass spectrometer to establish reducing conditions with H$_2$ injection.
7	Highly Reducing	500	316 SS	100	Pb[b]	316, 410,F-22, Zr, HT9	Replicate of Experiment 5, with pure lead, but some carbon in the melt.
7X	Oxidation	500	316 SS	100	Pb[b]	316, 410,F-22, Zr, HT9	Replicate of Experiment 3, with pure lead, but some carbon in the melt.
7Y	Oxidation	500	316 SS	100	Pb[b]	316, 410,F-22, Zr, HT9	Replicate of Experiment 7.
10	Carbon Control	550	Zr, 1%Hf	100, 300, 1000	Pb-Bi	316, 410,F-22, Zr, HT9	First long-duration run.
11	Carbon Control	650	Zr, 1%Hf[c]	100, 300, 1000	Pb-Bi	316, 410,F-22, Zr, HT9	Conducted with Experiment 10.
12	Carbon Control	650	410 SS	100, 300, 1000	Pb-Bi	316, 410,F-22, Zr, HT9, Fe + 1, 2, and 3% Si	Second long-duration Run.
13	Carbon Control	700	410 SS	100, 300, 700[d]	Pb-Bi	316, 410,F-22, Zr, HT9, Fe + 1, 2, and 3% Si	Conducted with Experiment 12.

a. Approximately 2.54wt% Sb, 0.53wt% As, and balance Pb.

b. Pure lead (99.99wt%), however, Experiments 7 and 7X contained a small but unknown amount of carbon, the lead for Experiment 7Y was carefully cleaned prior to the test.

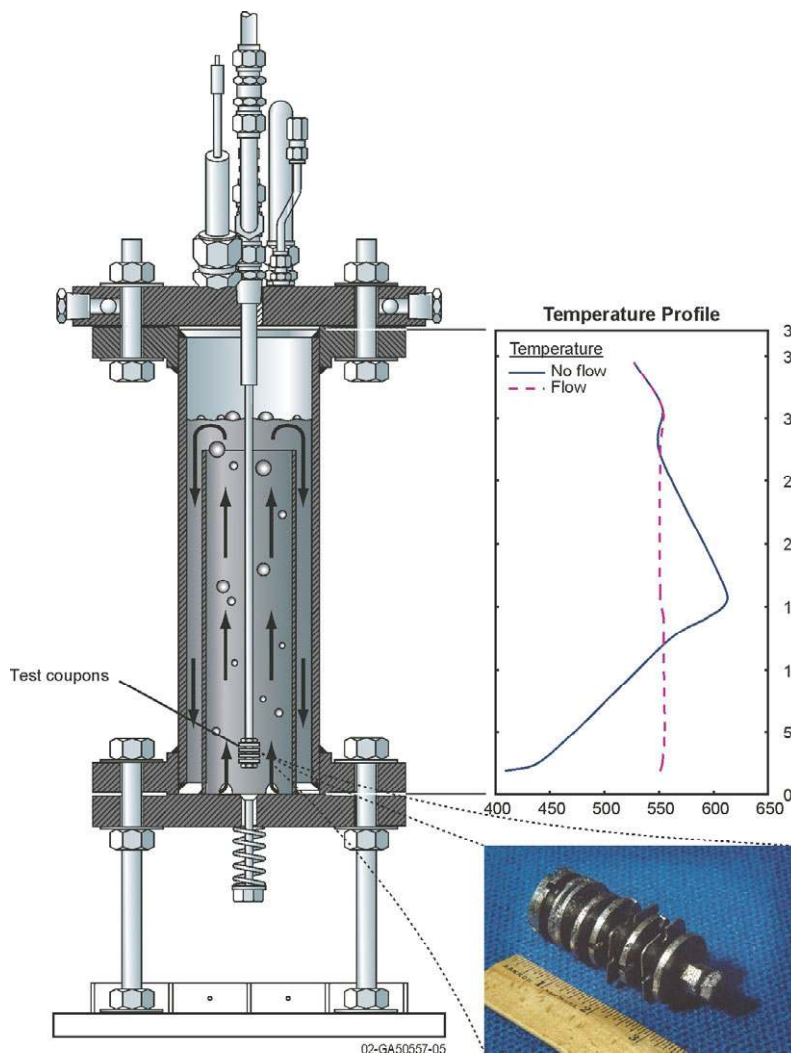c. Severe degradation of the zirconium corrosion cell due to exterior oxidation.

d. Experiment stopped early due to LBE leak that shorted out the heaters.

4.1.1. Description of the Experimental Apparatus

The INEEL forced-convection corrosion cell consists of a heated vessel with a shroud and gas flow system, which is shown in Figure 4.1. The gas composition and flow rates, heat input, and shroud and vessel dimensions are adjusted such that a controlled LBE coolant flow rate, temperature, and oxygen potential are created within the vessel. Various coupons are placed on a lance at the center of the vessel for testing, as shown in the lower right of Figure 4.1. The test coupons were separated from each other and from the lance by alumina spacers. Tensile specimens were also placed on the outside of the shroud in the down-comer region. The lance is made of low alloy steel and is also used for the gas injection. The detailed modeling and measurement of the liquid flow is explained in our previous publications [MacDonald and Buongiorno 2001, Loewen and MacDonald 2001a and 2001b].

A resistance furnace is used to heat the experimental apparatus to isothermal conditions. A typical temperature profile for the rig under static and flowing conditions is shown in Figure 4.1. The corrosion cells for Experiments 10 and 11 were fabricated from hafnium-stabilized zirconium alloy pipe (1wt.% Hf balance Zr). The zirconium alloy cells

Figure 4.1. Corrosion cell, test specimens, and temperature profile at an average temperature of 650°C.

were pre-oxidized using steam at 540°C for 6 hours, producing a tightly adhering, black oxide layer. The corrosion cells for Experiments 12 and 13 fabricated from 410-stainless steel.

A mass spectrometer and O_2-meter measured the gas composition entering and exiting the corrosion cell. The mass spectrometer is an AERO VAC 2900 sampling system. This is a turnkey system consisting of a computer-controlled residual gas analyzer system that includes a heated oven-enclosure that houses the system and a Model 1600 Mass Spectrometer/Residual Gas Analyzer, with a two-stage fractionation-free manifold system. This mass spectrometer can accurately measure the O_2 level down to about 10 ppm.

The O_2 meter is a Thermox II, which is a self-contained portable analyzer using an electrochemical cell made of ZrO_2 heated to 760°C, with a lower detection level of 0.1 ppm O_2. Unfortunately, the presence of CO (generated in the corrosion cell by the reduction of the PbO) caused the Thermox meter to read off-scale low during startup of the experiment (as would any other combustible gas), however, accurate measurements were obtained on the inlet gas stream. Also, the period during which the Thermox II meter read off scale low was a good indicator for when the cell contained lead-oxide that was being reduced by the carbon buffer material.

By continuously analyzing the gas phase during the experiment, we could determine the O_2 potential in each corrosion cell using both meters. With the submerged gas injection and isothermal conditions, it is probable that there was equilibrium between the gas phase and LBE O_2 partial pressure. The use of the carbon buffer system probably controlled the O_2 partial pressure to within the range of 10^{-27} to 10^{-40} atm. But, we cannot be entirely sure of the O_2 partial pressure in the LBE because of the presence of the zirconium, also competing for the O_2 (as mentioned above, hafnium stabilized zirconium corrosion cells were used for Experiments 10 and 11, and Zircaloy test coupons were placed in all four FY-02 experiments). The oxygen potential in the LBE may have been below 10^{-40} during the higher temperature experiments (Experiments 11, 12, and 13) because of the significant quantities of zirconium in solution in the LBE.

Data collection was performed to relate the corrosion rate to the interaction layer thickness, as a function of temperature, time, and alloy composition. Four steel or stainless steel alloys (HT9, 410, 316L, and F22) and Zr4 were tested at the temperatures and times listed in Table 4.1. Metal Samples, Inc., supplied the metallic specimens stamped from rolled sheets and machined into the proper dimensions (3.175 cm O.D. and 0.32 cm thick). The chemical composition of each steel is listed in Table 4.2. The 410-stainless steel was cold rolled. The F22 alloy was annealed at 1650º and then 1380ºF. The 316L stainless steel was heat treated at 820ºC and cooled in air. The precise thermal history of the HT-9 alloy is not known because it was cut from a nonirradiated fuel channel box from Argonne National Laboratory West.

Each sample was polished on one side to a 0.3-mm mirror finish (except HT9 due to a nominal thickness of 1.07 mm), thereby producing a uniform surface finish to quantify the corrosion rate between time and temperature steps. The specimens were fixed onto a lance separated by alumina spacers and inserted, polished side down, into the corrosion cell. Figure 4.1 shows a set of specimens at the end of a lance after 1,000 hours of exposure in LBE. Tensile specimens were placed on the outside of the inner shroud (LBE down flow area) for the duration of the experiment.

Table 4.2. Composition of test specimens as specified by the manufacturer.

Element	HT9	410	316L	F22
C	0.2		0.011	0.093
Nb				0.002
Cr	12.0	12.54	16.340	2.139
Cu			0.340	0.120
Mn		0.68	1.490	0.404
Mo	0.1		2.070	0.925
Ni	0.55		10.120	0.122
P			0.028	0.006
S			0.015	0.0013
Si		0.83	0.570	0.130
Sn				0.006
V	0.3			
W	0.5			
Fe	Balance	Balance	Balance	Balance

Upon removal from the molten LBE, the specimens were shaken to remove excess liquid LBE. Then, the samples were cross-sectioned, mounted in epoxy, and mechanically polished inward to a 0.3-mm mirror finish, using alumina and silicon carbide. Detailed corrosion and interaction morphologies were obtained with a Philips XL, 20-keV electron beam, scanning electron-

microscope (SEM). For purposes of this analysis the interaction layer was defined as the narrow band between the alloy substrate and the LBE solidified on the surface. The entire sample cross-section was scanned, and detailed measurements were taken at three separate locations to accurately portray the characteristics of that sample. Energy dispersive X-ray (EDX) analysis was used to analyze the chemical composition of the interaction layers. The X-ray spectrum M-line was used for both the lead and bismuth; the K-line was used for all remaining materials.

Muller et al. [2002], recommend that the O_2 level in LBE be bounded as follows:

$$2\Delta_f G_{PbO}^0 > RT \ln p_{O_2} > 0.5 \Delta_r G_{Fe_3O_4}^0 \qquad (4.1)$$

Further, Li [2002] and Lefhalm [2001] have examined the use of active control of O_2 in an LBE system using an H_2 and H_2O mixture to control the O_2 partial pressure. They assume that the oxygen partial pressure in the gas phase above the molten metal is in equilibrium with the oxygen partial pressure in the LBE. However, the exchange of O_2 between the gas phase and liquid metal is limited by diffusion. Therefore, the kinetics of this equilibrium is unique for each geometry and must be measured for each LBE system.

The results reported herein were obtained using INEEL's solid carbon buffer system $(C/O_2/CO/CO_2)$ to keep the O_2 between the bounds established in Equation (4.1). This INEEL-developed buffer system (with a provisional patent) uses solid and gaseous C to control the O_2 level in the LBE. The calculated standard free energy of formation of oxides are presented in Figure 4.2, as a function of temperature and normalized for one-gram atom of O_2. From visual inspection and ICP analysis, we suspect very little breakdown of the ZrO_2 layer on the cell surfaces in the zirconium corrosion cell operated at 550ºC. Therefore, in this temperature range the O_2 control was probably due to the carbon buffer, as expected. However, when the cell was operated at 650ºC, some ZrO_2 spalled off the inside surface, resulting in above saturation zirconium levels in the LBE. Since the
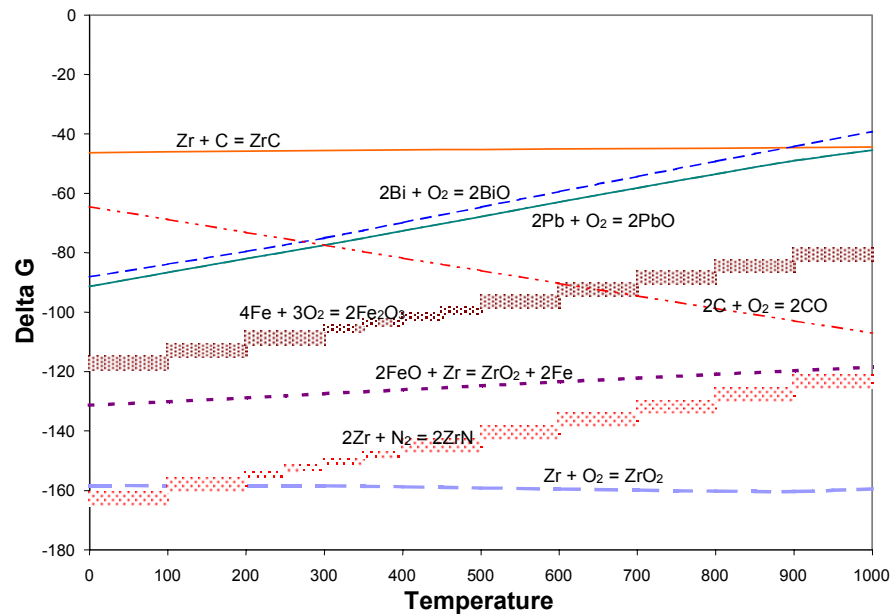
Figure 4.2. Gibbs free-energy of formation of metal oxides as a function of temperature.

freshly exposed zirconium consumed O_2, our O_2 partial pressure was not under carbon control, but probably below 10^{-40}. The zirconium apparently acted as a passive inhibitor to metal dissolution and corrosion. Based on data from Figure 4.2, calculations, and oxide layer measurements, we indirectly infer that the O_2 potential was approximately 10^{-23} at 550°C during Experiment 10, 10^{-22} at 650°C during Experiments 11 and 12, and 10^{-21} at 700°C during Experiment 13.

4.1.2. Inductively Coupled Plasma (ICP) Results

Mass transfer of elements from structural and/or cladding materials to the LBE coolant can affect the coolant chemistry and, in some cases, govern the molten LBE attack of materials. If the concentration of the structural material in the LBE is at saturation, further dissolution is limited, mitigating corrosion if temperature and O_2 partial pressure remain constant (He et al. 2001). The solubility for metallic elements in LBE and/or Pb ranges from the percent level for nickel to a few ppm for iron. Thus, even with our large LBE mass relative to the corrosion sample weight (27.7 kg LBE/1.8 kg sample), saturation conditions were still reached with several elements during the test periods.

The composition of the LBE from the four experiments was analyzed each time the cell was opened at 100, 300, and 1000 hours. Samples were taken of the LBE that was drained out in the tray, and from the dust. We believe that most of the dust was metal oxide. The dust was generally the composition of fine talcum powder, gray to dark gray in color. Each of the LBE samples was dissolved in an acid for ICP analysis. An Inductively Coupled Plasma-Atomic Emission Model Y device was used to make the measurements. The ICP heated the samples into a plasma state and measured the wavelengths emitted from the samples to find the amount of material in each sample. Tests were performed for the following metals: As, Cr, Fe, Ni, Sb, and Zr.

When the LBE is saturated with these metals, further dissolution is unlikely to occur. In order to minimize this possibility, a large mass of LBE was used in comparison to the corrosion and tensile specimen mass. For example, the mass of the LBE in Experiments 10 and 11 was 24.5 kg whereas the mass of all the samples (and the lance on which they were placed) was 540 grams. Therefore, the metal corrosion coupons made up only about 1% of the molten LBE bath.

The solubility of metals in the LBE is a function of temperature. There have been several investigations of this phenomenon and a few general conclusions can be made from these investigations: (1) Iron solubility decreases linearly with increasing Pb concentration [Weeks 1969]. (2) Not much is known about the Zr/Pb/Bi system, and there is no data on the system [Hansen 1958]. (3) Corrosion in LBE systems is caused chiefly by the relatively high solubility of the several of the significant components in steels and stainless steels such as nickel and Cr. If there is a temperature gradient in the system, non-uniform mass transfer will occur due to the temperature dependent solubility, unless there is some form of protective layer [He et al. 2001]. (4) Due to the high affinity for O_2 of the steel components at these high temperatures of interest, a protective oxide layer will form on the steel if sufficient oxygen is present, reducing corrosion [Li 2002].

For example, the solubility of Fe in LBE as a function of temperature is shown by He et al. [2001] to be:

$$\text{Log}(c_{Fe}) = 6.01 - 4380/T \qquad\qquad (4.2)$$

where T is in degrees Kelvin. For an operating temperature of 550 C (as existed in Experiment 10) the solubility level is 5 ppm whereas at a temperature of 650°C (as existed in Experiment 11) the saturation concentration increases to 18 ppm. Similar relationships have been developed for Ni, Cr, Zr, and are shown in Equations 4.3, 4.4, and 4.5 respectively [He et al. 2002, Weeks 1969].

$$\text{Log}(c_{Ni}) = 5.53 - 843/T \qquad\qquad (4.3)$$

$$\text{Log}(c_{\text{Cr}}) = 3.98\text{-}2280/\text{T} \tag{4.4}$$
$$\text{Log}(c_{\text{Zr}}) = 6.15\text{-}3172/\text{T} \tag{4.5}$$

Table 4.3 provides the calculated solubility-limited concentration of each of these elements as a function of temperature for Experiments 10 and 11 as well as the measured concentrations. The first four columns in Table 4.3 are the calculated solubility limits of the various elements of interest in ppm and grams for each experiment. The next two columns show the fraction of the available material in the cell for a particular experiment, that would have to dissolve in order to reach the solubility limits, in percent. The average of the ICP measured values in the LBE over the life of the experiment in ppm are provided in the right-hand two columns. Notice that only a small amount of the available iron must be dissolved to reach the solubility limits, and the ICP measured concentrations are well above the calculated solubility limits. Also, only a small amount of the available chrome need be dissolved to reach the solubility limits and the ICP measured concentrations at the two experiment temperatures are approximately consistent with the calculated solubility limits. Also, the solubility of nickel in LBE is very high, but very little nickel was available in the experimental apparatus and therefore the measured nickel concentrations are relatively low. Finally, sufficient zirconium was available and it appears that the zirconium solubility in both experiments reached or exceeded the solubility limits. The ICP measurements as a function of time and temperature are discussed in more detail below.

Table 4.3. Calculated amounts of various elements in solution in the LBE at the solubility limits (in ppm and grams) and percent of the available material that could be dissolved versus the ICP measured concentrations at the end of the experiment.

Element	Cal. Solubility Limit at 550°C (ppm)	Cal. Solubility Limit at 650°C (ppm)	Cal. Solubility Limit at 550°C (g)	Cal. Solubility Limit at 650°C (g)	Available Material Dissolved at 550 °C (%)*	Available Material Dissolved at 650 °C (%)*	ICP Measured Concentration at 550°C ** (Average ppm)	ICP Measured Concentration at 650°C ** (Average ppm)
Fe	4.9	18.4	0.12	0.45	0.05%	0.20%	66.4	166.4
Cr	16.2	32.4	0.40	0.79	1.3%	2.6%	8.2	14.7
Ni	32,000	41,400	784	1,014	14,500%	19,900%	51.4	32.0
Zr	198	518	4.9	13	3.0%	7.9%	116.1	1,576.0
* Percentage of the material in the cell required to dissolve in order to reach the solubility limit								
** Average amount of material in solution as measured by ICP (ppm)								

The amount of each material present in the cell also changes over time with removal of the samples. At each time interval some of the sample trains (lances) were taken out of the system, resulting in a decreased amount of material as shown in Table 4.4. The masses of Fe, Cr, and Ni were determined, as they were the only steel components measured by ICP in these tests. The mass of zirconium can be considered infinite because the cells

Table 4.4. Mass of corrosion coupons per alloy (grams).

Alloy	Experiment 10 (550 °C)			Experiment 11 (650°C)		
	100h	300h	1000h	100h	300h	1000h
316	48.9	32.7	16.3	45.1	30.0	14.8
410	136.0	104.1	72.0	132.2	101.7	70.7
CS	36.7	36.7	36.7	36.6	36.6	36.6
HT9	56.4	44.4	32.5	56.6	44.3	32.0
F22	95.0	77.0	58.7	95.9	77.5	59.1
Zr702	46.6	31.0	15.5	46.0	30.9	15.4
Zr4	80.9	65.0	49.2	80.9	65.0	49.2
Zr705	40.9	27.3	14.1	41.6	27.8	14.1
Total Mass	541.2	418.1	294.9	534.8	413.8	291.9

themselves were constructed of zirconium. Table 4.5 provides the estimated mass of Fe, Ni, and Cr exposed at each time interval in the LBE during the experiment.

Table 4.5. Mass of the various steel elements in the samples versus time (grams)

Element	Experiment 10 (550°C)			Experiment 11 (650°C)		
	100h	300h	1000h	100h	300h	1000h
Fe	236.5	187.4	138.0	230.7	183.3	135.4
Ni	5.4	3.7	1.9	5.1	3.4	1.
Cr	31.0	23.1	15.1	30.0	22.3	14.7

The following paragraphs discuss the ICP measurements of the LBE metal and the dust as a function of time and temperature. Figures 4.3-4.9 show the results of the ICP measurements. The figures provide concentrations of, Zr, Fe, Cr, and Ni, as well as As and Sb. Each Figure contains plots of the data from both runs for: 1) bulk coolant concentration vs. time, 2) bulk coolant concentration vs. temperature, and 3) dust concentration vs. time. The concentration of each metal was expected to approach the solubility limit gradually over time; however, this was not the case. Several explanations can be formed as to why the metal concentration behaved as it did.

Figure 4.3 shows the Fe concentration data for the two test campaigns. The iron concentration levels were far above the solubility limits during both runs, and were much higher at 100 hours than any of the other time intervals. The large surface area and mass of the Fe, compared to the rest of the alloying elements in the samples, will
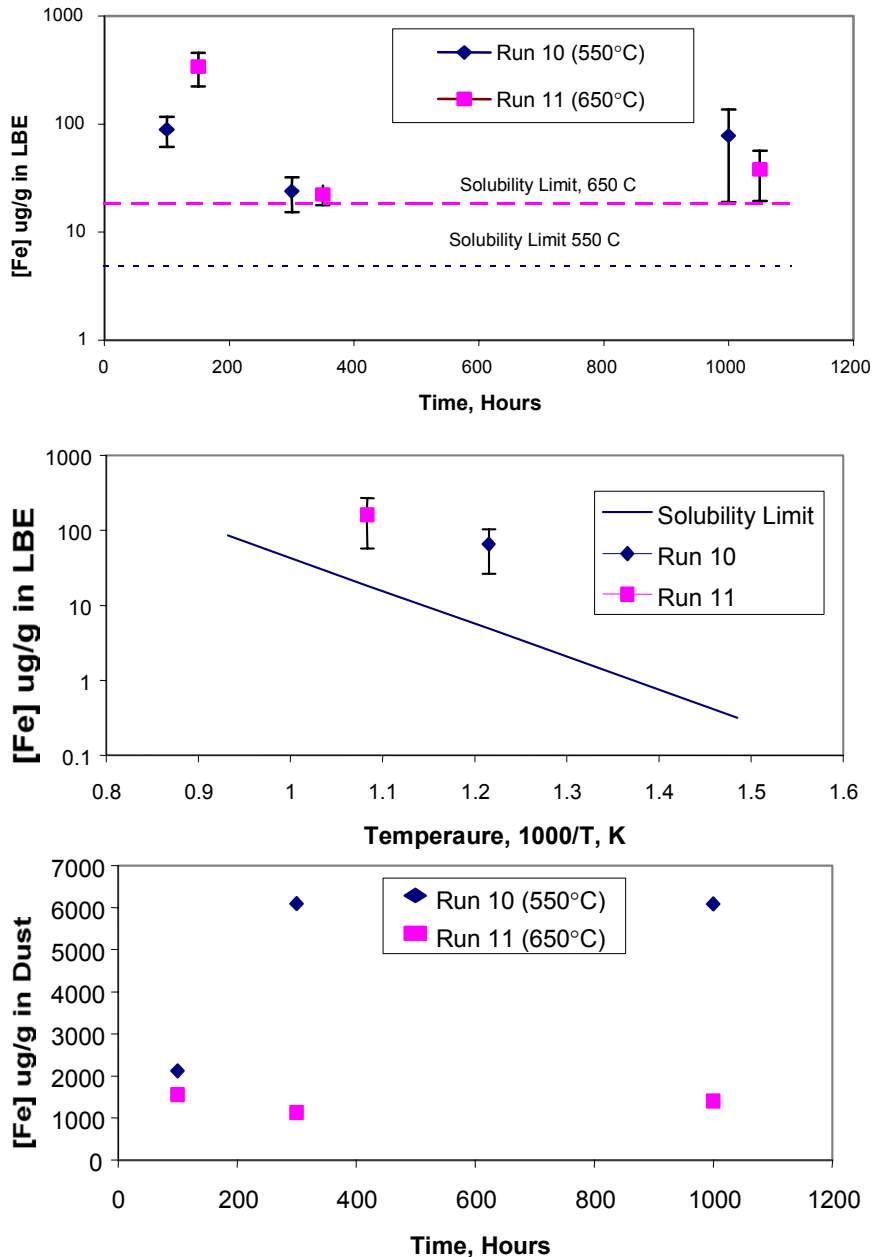
Figure 4.3. Iron solubility curves.

158

increase the likelihood of the Fe going into solution. As shown in Table 4.5, the Fe represents about 87 to 89% of the sample material (excluding the Zircaloy samples). Also, the concentration of the Fe in the LBE bulk coolant above the saturation limit may be due, in part, to the reduction of the Fe_3O_4 protective films by the zirconium via the following reaction:

$$Fe_3O_2 + Zr = 3Fe + ZrO_2$$
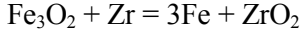
Also, it is possible that iron oxide spalled off some of the thermocouple or lance surfaces and was entrained in the molten LBE.

The nickel concentration levels were far below the solubility limits for both runs as shown in Figure 4.4. We believe these low concentration levels can be attributed to the very small amount of nickel present in the corrosion cell during each experiment. As listed in Table 4.5, there was only about 5g of nickel in the cell at the beginning of each experiment. This value was reduced to about 3.5g at 300 hours. The maximum nickel concentration possible due to the available material is also shown in the top figure of Figure 4.4. The measured nickel concentrations are near the maximum possible value.

The nickel dust concentrations shown in Figure 4.4 followed the same pattern as the Fe dust concentrations shown in Figure 4.3. The high dust concentrations at 300 hours during Experiment 10 might explain the dip in the bulk coolant concentration level

Figure 4.4. Nickel solubility curves.

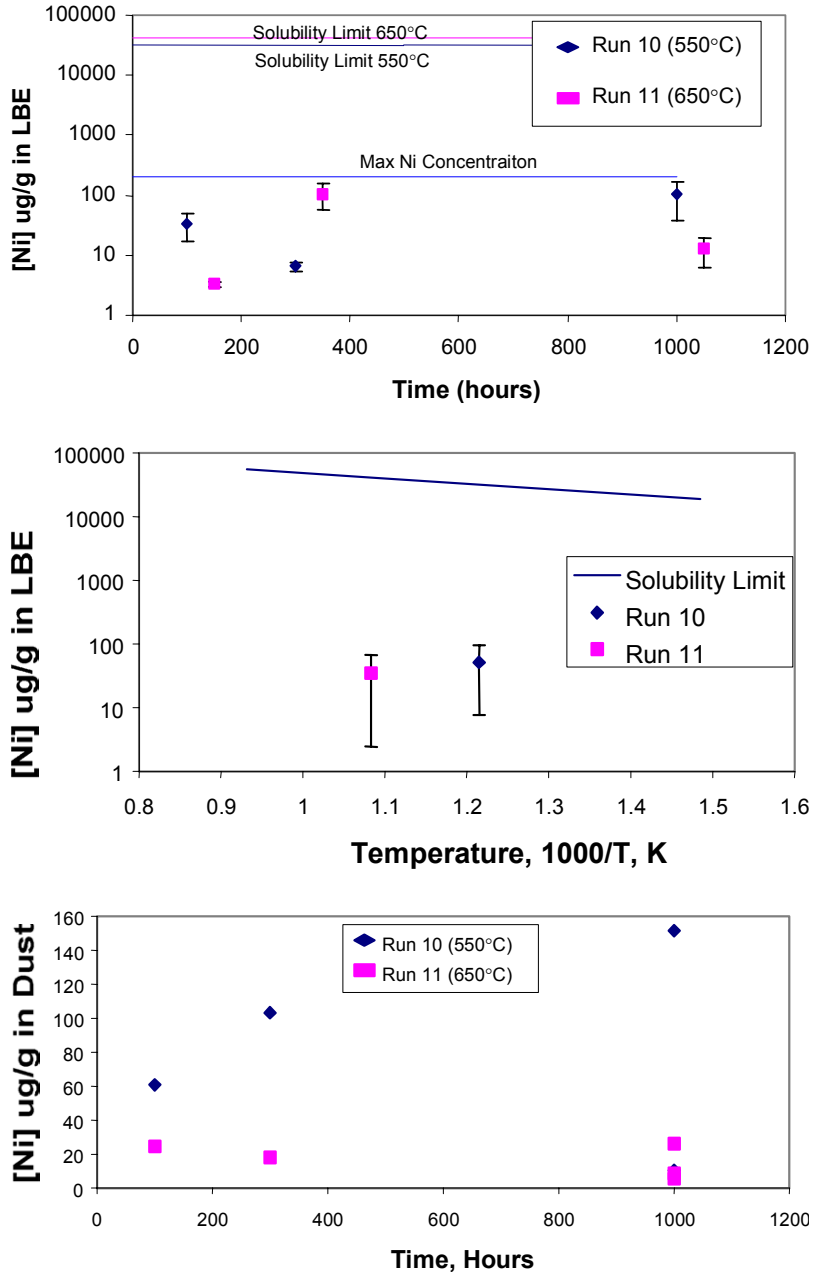at 300 hours. The mass of nickel steadily decreases over time, and may also account for the fluctuating data.

159

The chrome concentration in the LBE as measured by the ICP is shown in Figure 4.5. The measured concentrations agreed with the calculated solubility-limited amount especially during Experiment 11 when the concentration increased over time and approached the solubility limit. An influx of O_2 may have occurred when the cell was opened at 100 hours during Experiment 10, causing oxidization of the Cr, and therefore showing a decrease in Cr concentration at the 300-hour mark. Chrome readily oxidizes (as compared to Fe and Pb); only zirconium will oxidize before Cr.
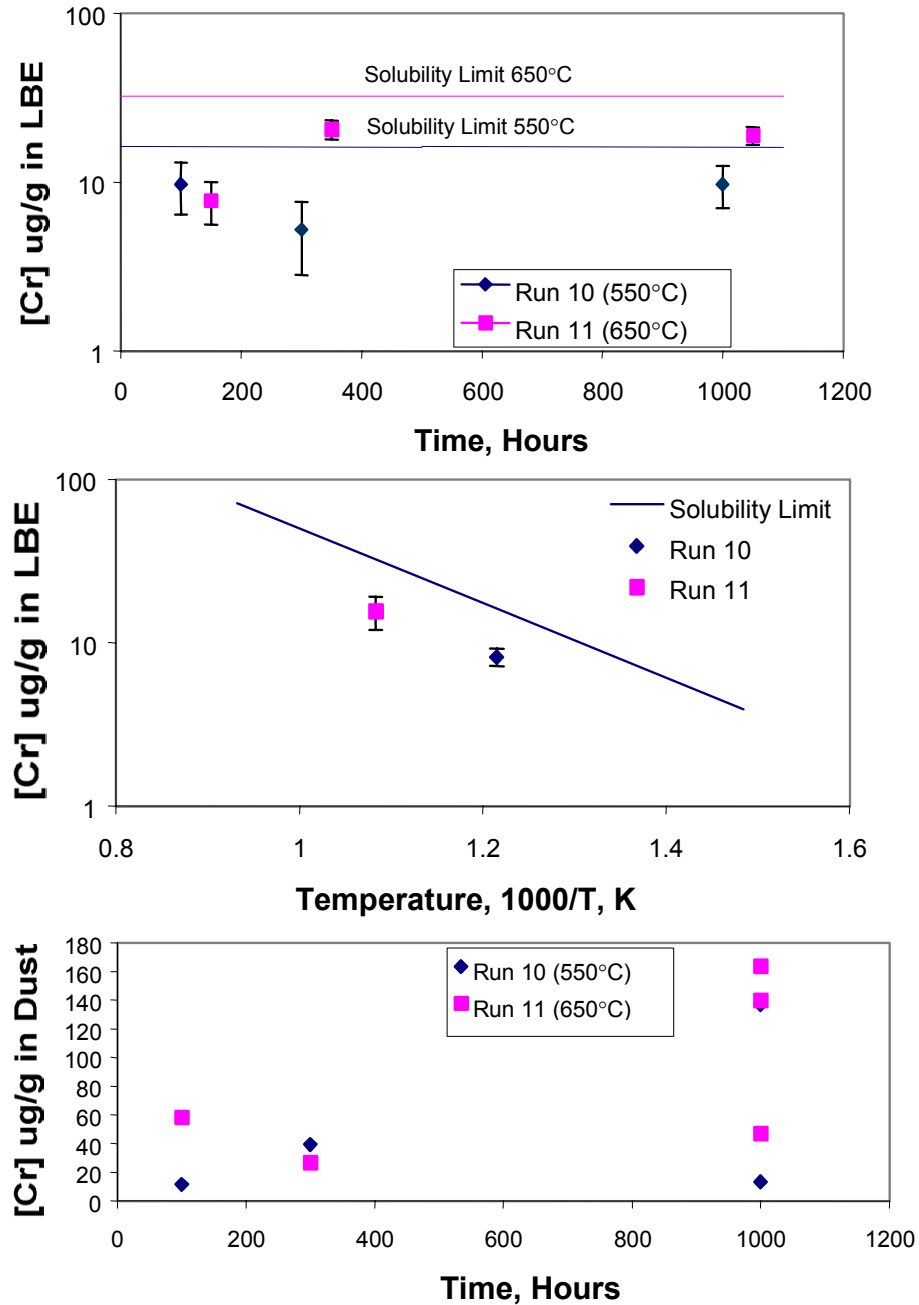

Figure 4.5. Chrome solubility curves.

The zirconium concentrations for Experiment 10 were about 144 ppm at 100 hours and then decreased significantly to about 11 ppm at 300 and 1000 hours as shown in Figure 4.6. The 100-hour zirconium concentration in the LBE that is above the solubility limit may have been due to initial wetting of the pre-oxidized surface or due to zirconium oxide falling off the inside of the cell and becoming entrained in the molten LBE. (The corrosion cells were initially passivated by holding them at a temperature of 600°C while injecting water for 4 hours.) The zirconium concentration levels were also above the solubility limits for all of Experiment 11. The reduction in the zirconium concentration in Experiment 10 after 100 hours may have been due to the fact that zirconium oxide was then taken out of the system in the form of dust. During Experiment 11, however, the oxide layer on the inside of the cell continuously fell off. The reason the zirconium concentration level remained constant and well above the solubility limit during Experiment 11 may have been that the dust was removed from the cell at about the same rate as the zirconium oxide entered the cell.
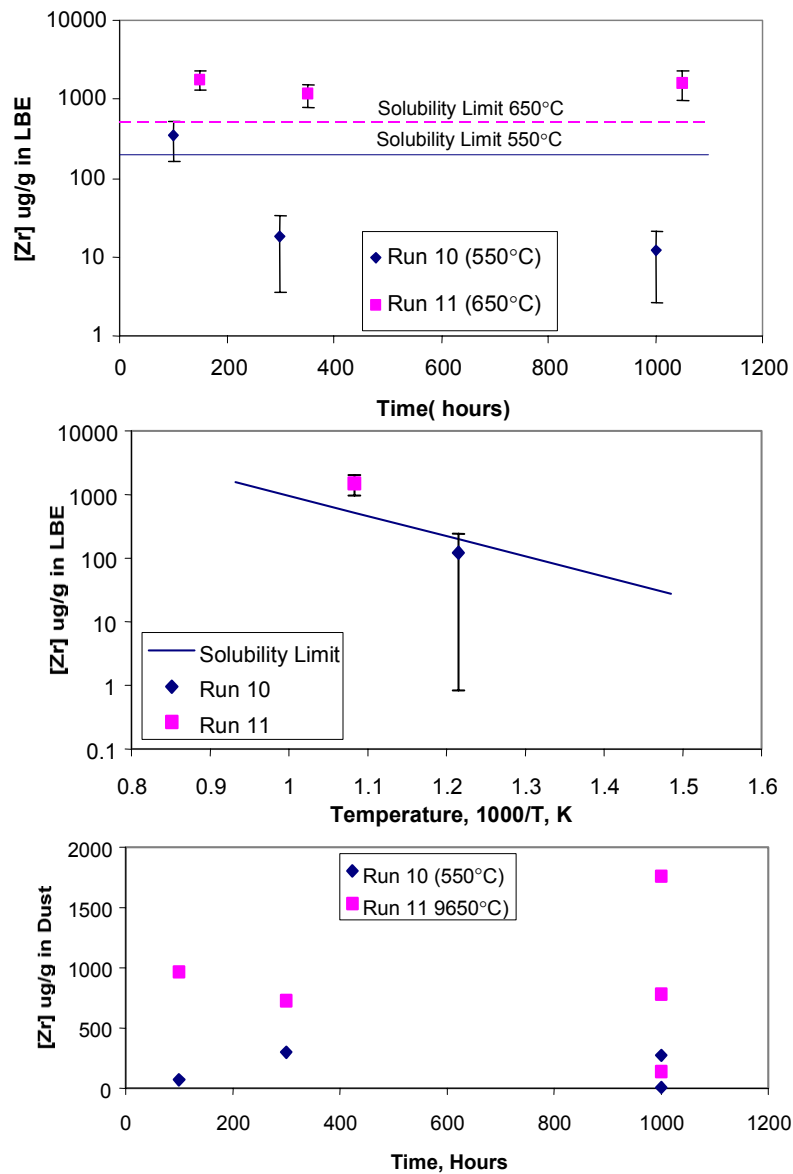

Figure 4.6. Zirconium solubility curves.

Arsenic (As) and antimony (Sn) are common impurities found in lead and are completely miscible in LBE [Anderko 1958]. Figures 4.7 and 4.8 show the concentrations of these impurities in the LBE bulk coolant and dust vs. time.

Since the As was not present in any of the materials used in the cell or in the samples, it likely came from impurities in the original lead placed in the cell, even though the lead had an initial purity of 99.9% (this is the purist lead we are able to obtain in large quantities at a reasonable price). A detectable level was found in Experiment 10 at 100 hours, but it was apparently quickly oxidized out of the system, as indicated by the dust measurements shown in Figure 4.7. A small amount of As was observed in Experiment 11 and it was also apparently removed from the melt by oxidation. One would expect the dust values to approach the lower detection limit over an extended period of time for each of the runs.

The Sb concentrations in the LBE bulk coolant shown in Figure 4.8 were somewhat erratic during Experiment 10 and rose gradually during Experiment 11. The high numbers at the beginning of Experiment 10 suggest there was some Sb present in the Pb before it was placed in the cell, again due to slight impurities in the lead used. The dust concentrations steadily decreased, showing that the Sb was being removed by oxidation. Since no Sb was being introduced into the system, we would expect these numbers to have gone below the detection limit over time.

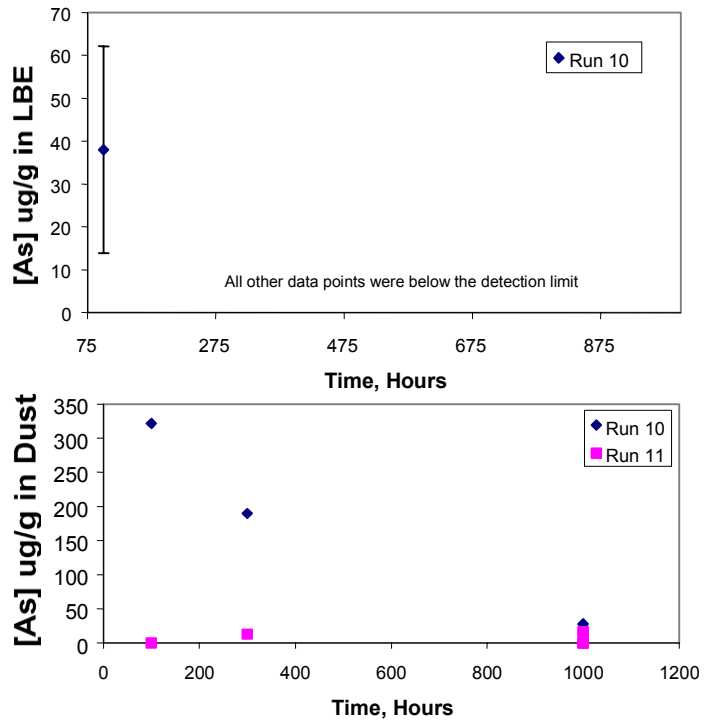The trends of the concentrations of the Fe, Ni, and Cr in the LBE bulk
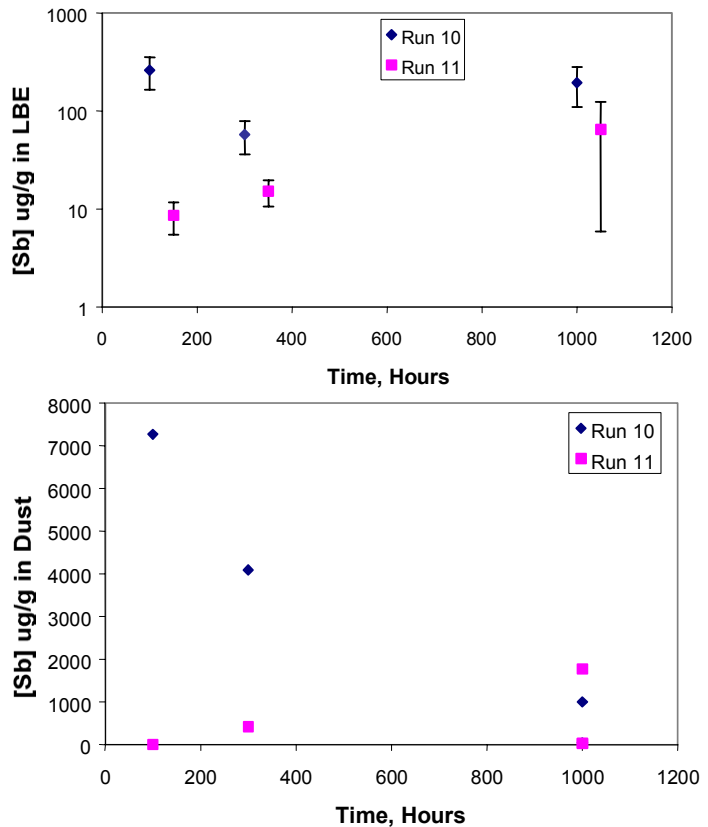

Figure 4.7. Arsenic ICP data.

Figure 4.8. Antimony ICP data.

162

coolant were nearly identical during Experiment 10. They were all relatively high at 100 hours, lower at 300 hours, and then high again at 1000 hours. We believe there was a large influx of O_2 into the system when the Experiment 10 cell was opened to remove the samples at 100 hours, causing much more of the material to be oxidized and taken out of the system than when the cell was opened at 300 hours.

The Fe, Ni, and Cr concentration data from Experiment 11 is not as consistent, but it is probable that many of the discrepancies between the concentration trends with the different metals can be attributed to the competing reactions for O_2 between the Fe, Cr, Zr, and C. Also, some of the metal in the LBE bulk coolant may have come from the samples being oxidized directly, and was not a function of the solubility of that element in the LBE. The oxidation of zirconium and Cr is very favorable at 650°C, and that can explain the higher levels of those elements in the dust compared to the others. This may also explain why the concentrations of the Fe, Ni, and Cr in the LBE bulk coolant did not increase significantly between Experiments 10 and 11.

The time average ICP measured element concentrations are compared with the respective solubility limits as a function of temperature in Figure 4.9. As mentioned in the introduction to this section, the iron values are considerably above their solubility limits, the nickel values are well below their solubility limits, and the chrome and zirconium values are more consistent with their solubility limits (however, the zirconium value at 650°C is much higher than the solubility limit). Except for the nickel, the effect of temperature on the element concentration appears to be as expected.
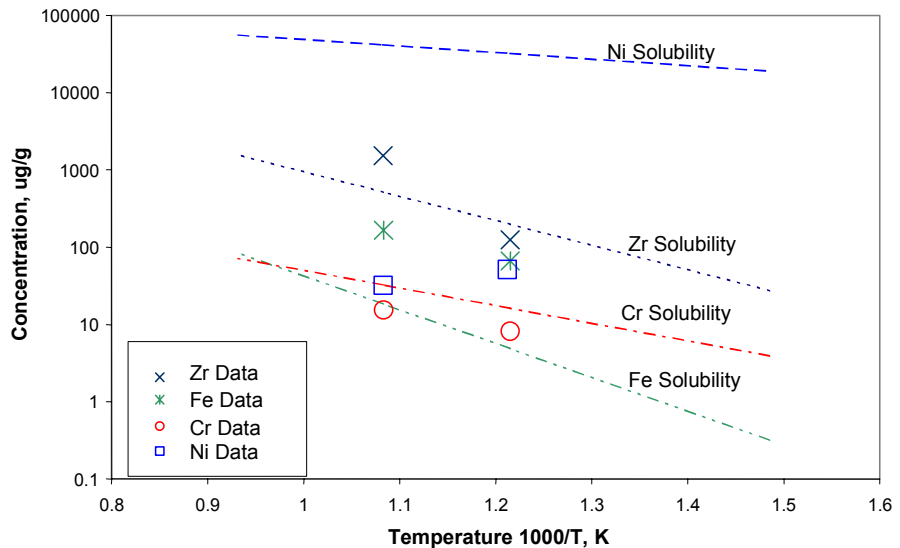

Figure 4.9. Comparisons of the time average ICP data for the concentrations of Fe, Cr, Ni, and Zr in the LBE bulk coolant (pints) versus the calculated solubility limits (lines).

4.1.3. SEM Results

Figures 4.10 to 4.13 show the SEM micrographs of the interaction layers on the surfaces of the HT-9, 410 stainless steel, 316L stainless steel, and F22 samples with respect to time and temperature. Unfortunately the magnification is not the same for all the photomicrographs, however, it is as consistent as the SEM would allow. The left-hand vertical column contains the photomicrographs from Experiment 10 and the right-hand vertical column contains the photomicrographs from Experiment 11. The horizontal rows represent each time step: 100, 300, and 1,000 hours. This allows easy comparisons of the interaction layers as a function of time and temperature.
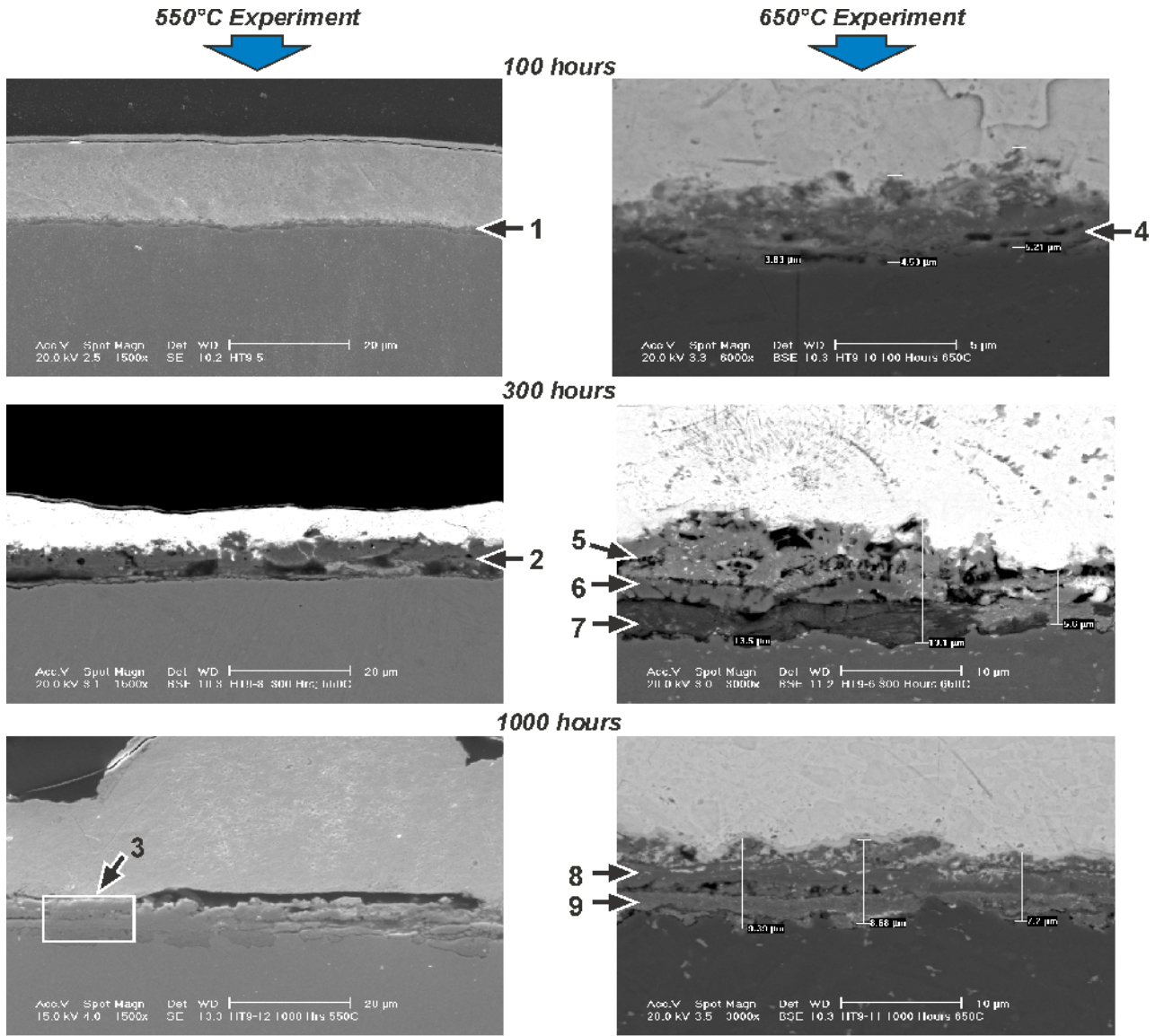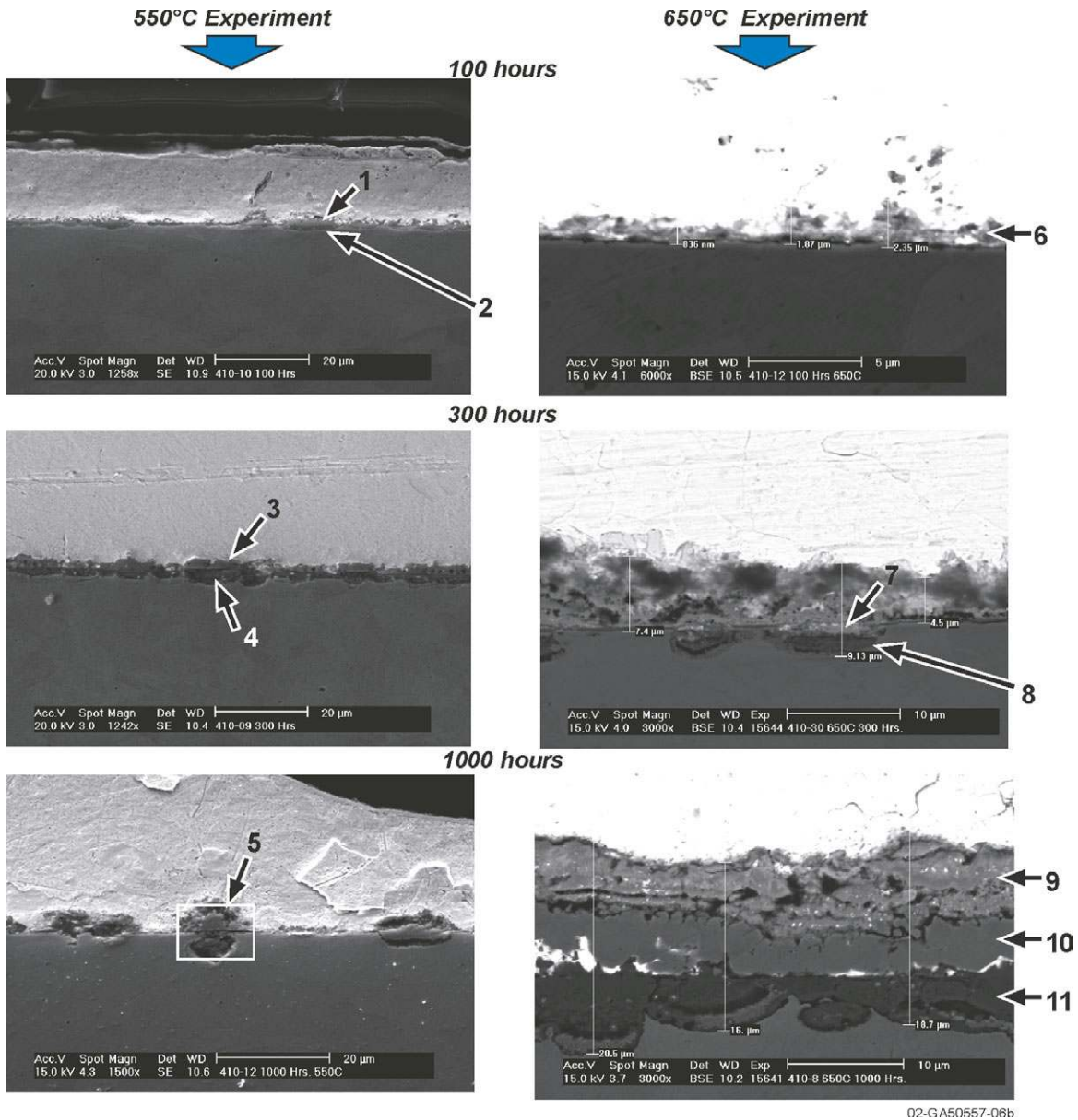
Concentration of elements in the interaction layers in %:

Layer	Temp.	Time	Fe	Cr	W	Pb	Bi	Al	C	Zr	Sr	Ca	Hf	O
1	550°C	100	60.0	5.9	0.9	18.7	13.7	0.5	0.2					
2	550°C	300	63.1	7.7	0.9	2.1	2.6	0.4	0.2					23.2*
3	550°C	1000	66.2	7.4	0.6	1.4	1.1		0.1					23.2*
4	650°C	100	34.9	4.5		22.7	24.3	0.3	0.5	12.0	0.8			
4	650°C	100	28.1	2.0		28.4	29.7	0.2	0.3	10.6	0.8			
5	650°C	300							1.3	73.4			25.3	
6	650°C	300	98.5	1.1					0.1	0.25				
7	650°C	300	79.4	18.0	1.2	0.6			0.1			0.6		
8	650°C	1000	8.2	0.4		28.0	16.0	0.7		36.8			9.9	
9	650°C	1000	29.0	2.2		8.7	20.3	1.5		28.8			8.6	
Base			86.4	12.0	0.5									

* An oxygen peak was measured at this location, the values are estimated based on stoichiometry.

Figure 4.10. Photomicrographs of the cross-sections of the HT-9 samples from Experiments 10 (550°C) and 11 (650°C) at 100, 300, and 1,000 hours.
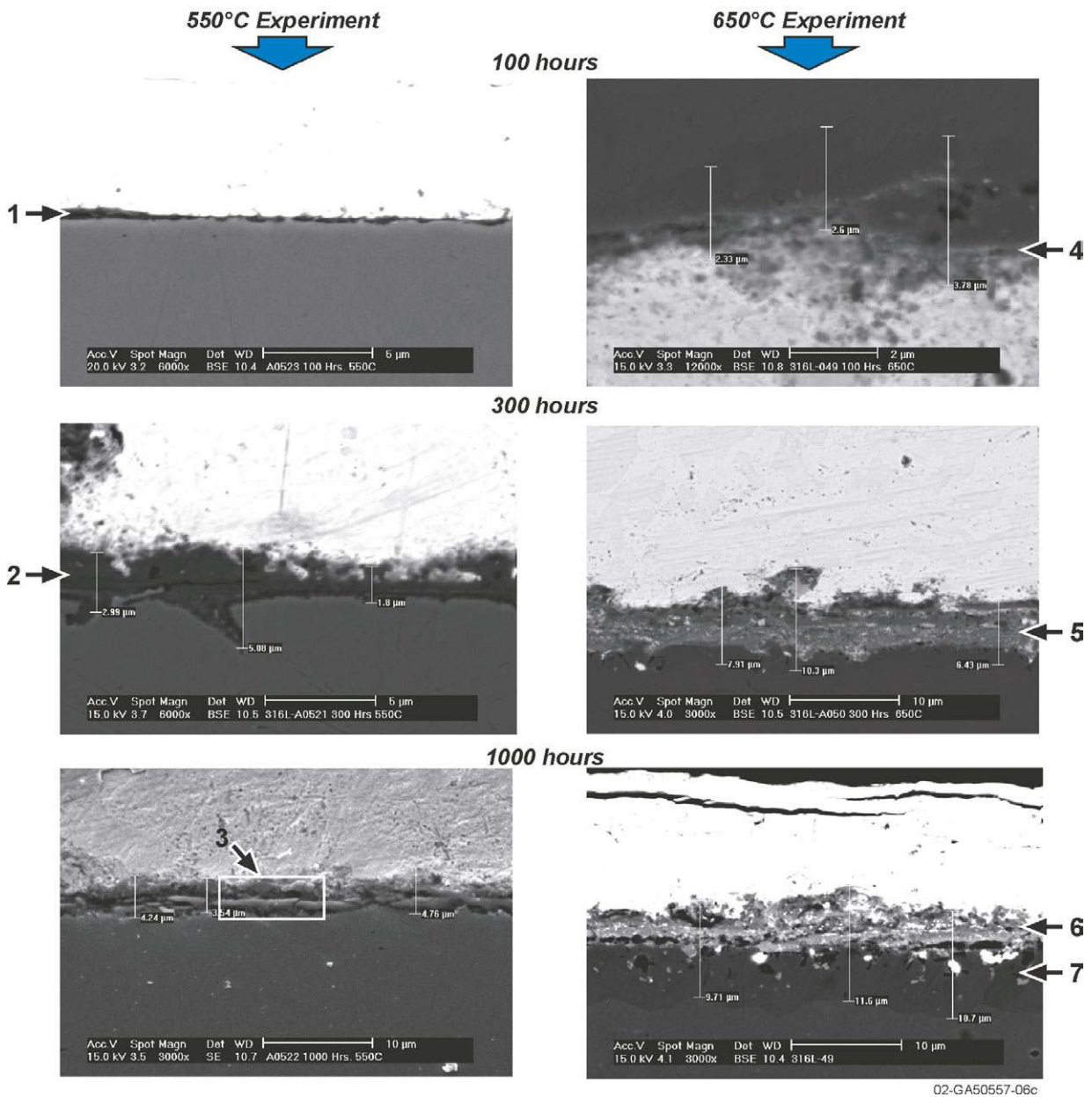
Concentration of elements in the interaction layers in %:

Layer	Temp.	Time	Fe	Cr	Si	Bi	Pb	Mn	O	Al	Na/Ca/Sr	Hf	Zr
1	550°C	100	45.6	0.7	0.9		31.5	0.04	18.9*	2.3			
2	550°C	100	59.2	12.4	0.4	3.4	0.13	0.51	24.0*				
3	550°C	300	53.3	13.1	0.8		4.5	0.51	25.1*	2.7			
4	550°C	300	49.3	18.8	0.6	3.4	1.6	0.53	25.0*	0.7			
5	550°C	1000	47.7	12.2		6.6	7.5		23.2*	1.9	0.96 (Na)		
6	650°C	100	41.1	12.1	0.5	18.6	23.5			2.2	2.0(Re)		
7	650°C	300	14.8			10.0	7.8					14.0	53.4
8	650°C	300	29.9	59.2	0.3	1.0	0.3	5.6			3.6 (Ca)		
9	650°C	1000	2.7			8.7	7.8		21.8*	1.5	0.14 (Sr)	15.5	41.9
10	650°C	1000	92.3	0.90		2.3	3.2						1.3
11	650°C	1000	45.7	24.2	0.6	0.03	1.4	2.4	25.7*				
Base			86.0	12.5	0.8			0.7					

* An oxygen peak was measured at this location, the values are estimated based on stoichiometry.

Figure 4.11. Photomicrographs of the cross sections of the 410 stainless steel samples from Experiments 10 (550°C) and 11 (650°C) at 100, 300, and 1,000 hours.
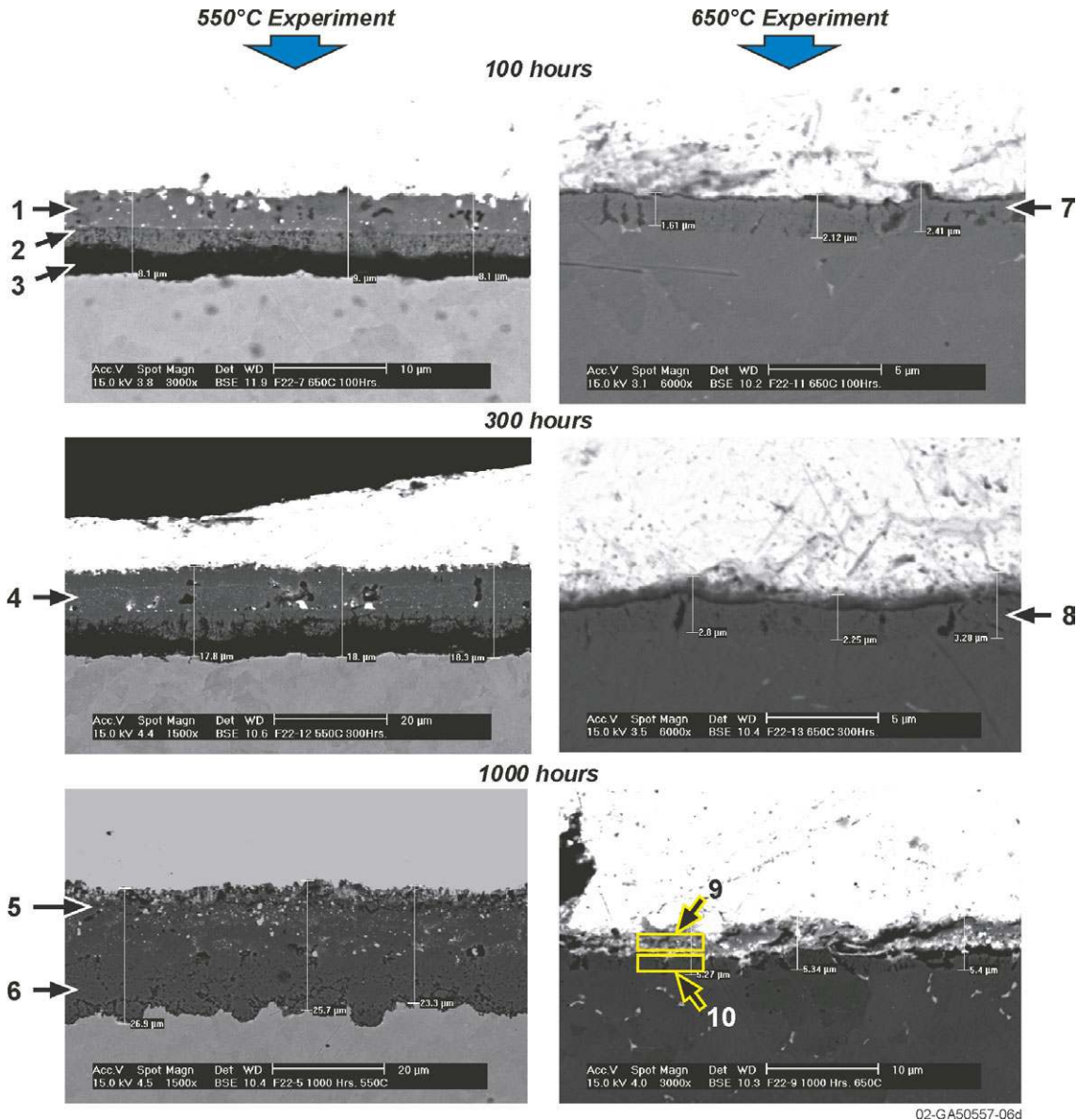
Concentration of elements in the interaction layers in %:

Layer	Temp	Time	Fe	Cr	Ni	Al	O	Si	Pb	Bi	Zr	Sr	Hf	Mo
1	550°C	100	1.8	0.56		0.5			43.6	53.5				
2	550°C	300	64.9	7.6	1.0	1.3	24.4*	0.84						
3	550°C	1000	46.6	18.3	7.4	1.7		10.2	15.7					
4	650°C	100	82.2	8.1					3.35	1.5	4.7	0.19		
5	650°C	300	10.7	1.4		1.4	20.1*	0.17	11.5	22.7	24.0	0.17	8.2	
6	650°C	1000	6.3	0.5		1.2	19.8*		16.3	16.7	30.3		8.8	
7	650°C	1000	61.0	33.3	1.4	0.3		0.24						3.7
Base			69.0	16.3	10.1			0.6						2.1

* An oxygen peak was measured at this location, the values are estimated based on stoichiometry.

Figure 4.12. Photomicrographs of the cross sections of the 316L stainless steel samples from Experiments 10 (550°C) and Experiment 11 (650°C) at 100, 300, and 1,000 hours.

Concentration of elements in the interaction layers in %:

Layer	Temp	Time	Fe	Cr	Pb	Bi	Al	O	Sr	Si	Zr	Mn	Mo	Hf
1	550°C	100	72.5	0.5	2.6	2.1	0.19	21.8*	0.33					
2	550°C	100	66.3	3.6	5.8	1.7	0.29	22.0*		0.3				
3	550°C	100	32.0	1.1	4.4	2.3	25.6	34.0		0.6				
4	550°C	300	73.0	1.6	2.0	0.2	0.27	22.3*	0.44					
5	550°C	1000	76.5			1.3		22.2*			0.10			
6	550°C	1000	73.5	2.7	0.1			22.8*		0.1		0.16	0.64	
7	650°C	100	95.7	2.8	1.6									
8	650°C	300	88.3	3.8	3.3	1.5	0.97				2.2			
9	650°C	1000	36.7	1.4	18.7	13.4	1.41		0.70		21.6			6.0
10	650°C	1000	97.5	1.5			0.35		0.03		0.64			
Base			96.1	2.1						0.1		0.4	0.9	

* An oxygen peak was measured at this location, the values are estimated based on stoichiometry.

Figure 4.13. Photomicrographs of the cross-sections of the F22 samples from Experiments 10 (550°C) and Experiment 11 (650°C) at 100, 300, and 1,000 hours.

Figure 4.10 shows six different SEM cross-section photomicrographs of the HT-9 samples from Experiments 10 and 11. The top layer (light in color) is the LBE solidified on the coupon. This layer is followed by one or more measurable interaction layers, and then the metal substrate at the bottom. The table at the bottom of the figure shows the composition of the different layers. The reaction layers generally contain somewhat less Fe than in the original alloy along with some Cr, Pb, and Bi. At 550°C, the Cr content is about ½ that of the original composition, but the Cr concentration in the interaction layers is significantly less than ½ at 650°C. Small amounts of N, Al, and carbon are also present in most of the layers (the Al and carbon probably came from the polishing compound). In Experiment 11 there was also a significant amount of zirconium and hafnium from the corrosion cell deposited in some of the surface layers (the surface layers with the zirconium and hafnium are shaded on the table). Notice that the overall thickness of the interaction layers increases with respect to time and temperature.

Figure 4.11 shows the SEM cross-section photomicrographs of the 410 stainless steel samples from Experiments 10 and 11. The 410-stainless steel exhibited local pitting after both experiments. In general, the interaction layers again contained somewhat less Fe than in the original alloy; some Cr, Pb, and Bi; and relatively small amounts of Si and Al (from the polishing compound). Significant amounts of oxygen were also measured at 7 locations. Also observable at 650°C is spalling of the corrosion layer, which was Cr rich, whereas the topmost layer again had significant quantities of zirconium and hafnium from the corrosion cell.

Figure 4.12 shows the SEM cross-section photomicrographs of the 316L stainless steel samples. These photomicrographs show the interaction layers generally increasing with respect to time and temperature. However, pitting can be observed at 300 hours and 550°C. Again the outer layers on the Experiment 11 samples (650°C) contain significant zirconium and hafnium.

Figure 4.13 shows the SEM cross-section photomicrographs of the F22 low alloy steel samples from Experiments 10 and 11. These photomicrographs show a large increase in the interaction layers with respect to time in Experiment 10 at 550°C, but at 650°C there were relatively small interaction layers. At 550°C, the interaction layers have somewhat less iron than in the original alloy, the Cr is near its compositional amount, and there are modest amounts of Pb and Bi present. At 650°C, the Fe fraction in the interaction layers is noticeably higher than at 550°C.
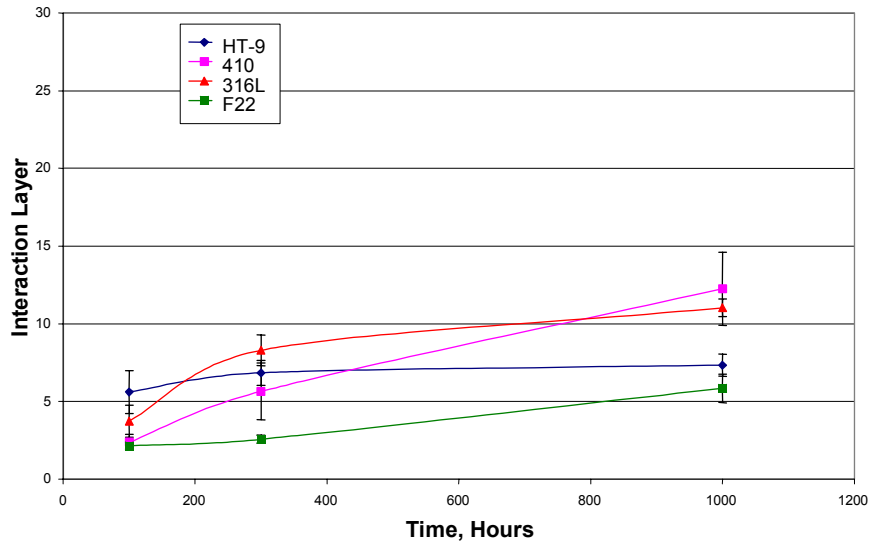
The change in the total interaction layer thickness of all four alloys during Experiment 10 (550°C) is plotted in Figure 4.14 as a function of time. (The measurements of the thickness of all the
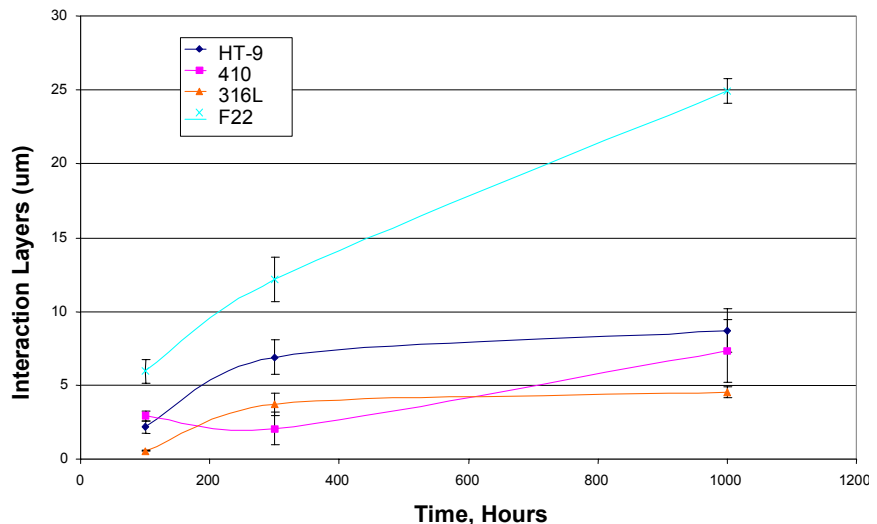
Figure 4.14. Total interaction layer thickness as a function of time for the HT-9, 410 stainless steel, 316L stainless steel, and F22 low alloy steel samples in Experiment 10 (550°C).

168

interaction layer(s) of each coupon were averaged together and plotted with respect to time.) The average deviation of the measurements is shown on the figure and provides a general indication of the variation in total layer thickness of the specimen. Notice that the F22 low alloy steel has the highest interaction layer formation rate and the 316L and 410 stainless steels appear to have the lowest interaction layer formation rates.

Figure 4.15 shows that the opposite trend occurred during Experiment 11 at 650°C where the F22 low alloy steel had the lowest interaction layer formation rates, while the 316L and 410 stainless steels appear to have the highest interaction layer formation rates. Remember that the zirconium was present only in the interaction layers of the 650°C coupons.

Figure 4.15. Total interaction layer thickness as a function of time for the HT-9, 410 stainless steel, 316L stainless steel, and F22 low alloy steel samples in Experiment 11 (650°C).

Based on the data shown in Figures 4.14 and 4.15 and using Equation (4.5), Experiment 10 at 550°C was at 63% of saturation for zirconium, while Experiment 11 at 650°C was at 295% of saturation (some of the zirconium detected in the LBE from Experiment 11 may have been ZrO_2 that sluffed off the surface of the corrosion cell). The measured corrosion rates generally decreased or remained about the same from 550°C to 650°C. Therefore, we conclude that the higher zirconium and hafnium concentrations in the LBE bulk coolant in Experiment 11 (as compared to the zirconium and hafnium concentrations in the LBE bulk coolant during Experiment 10) were more effective in suppressing the interaction layer formation rates in Experiment 11.

4.1.4. Discussion of the Coolant Chemistry Control, Effects of Zirconium Addition, and Relative Reaction Rates of Commercial Alloys

The interaction layer formation rates of four metal alloys (F-22, 410, 316, and HT9) exposed to molten LBE were measured, as discussed above. The results of this analysis lead to the conclusion that the pre-oxidized hafnium stabilized zirconium corrosion cells resulted in a liquid phase chemistry that affected the sample corrosion/dissolution in the cell. The gas phase measurement data showed complete removal (below the instrument detection level) of the O_2 and a reduction in the nitrogen (N_2) concentration. The inert argon gas used to induce LBE flow in the cell contained trace amounts of N_2 (100 to 200 ppm), O_2 (70 to 100 ppm), and H_2 (1 to 10 ppm). In the 550°C run, the preformed ZrO layer on the inside surface of the corrosion cell remained intact, as evidenced by the zirconium concentration in the LBE being 37% below the saturation level, however, in the higher temperature run, the ZrO layer on the inside surface of the

corrosion cell was sluffing off into the bath, resulting in a zirconium concentration in the LBE bulk coolant of 295% of saturation. This resulted in the thermodynamically favorable reactions of the zirconium with the N_2 C, and O_2. Thus, the zirconium in solution in the LBE slows down the corrosion of some of the alloys by forming a layer of zirconium compounds (we suspect both nitrides and carbides of zirconium) on the sample surfaces (Ilincev 2002), and by consuming excess O_2. Similar behavior was reported by Horsley and Maskrey (1958) in bismuth only. Therefore, the solid carbon was not totally consumed in our system because most of the O_2 was being scavenged by the zirconium.

With the present experimental evidence, it is informative to look at the four alloys in two subgroups differentiated by nickel content: The interaction layer formation rates of the Ni-containing metals HT9 and 316L at 550 and 650°C are best represented by a logarithmic fit to the data previously presented in Figures 4.14 and 4.15, as follows:

$$\text{At 550 C, } R_{HT9} = 0.7463 Ln(t) + 2.3154 \quad R_{316L} = 1.7137 Ln(t) - 6.9022 \qquad (4.6)$$
$$\text{At 650°C, } R_{HT9} = 2.822 Ln(t) - 10.2710 \quad R_{316L} = 3.1560 Ln(t) + 10.430 \qquad (4.7)$$

where t is time in hours and R is the corrosion rate in units of μm/hr. HT-9 was also susceptible to a limited amount of pitting, which may have been due to not polishing the HT-9 coupons for these experiments.

The 316L stainless steel interaction layer formation rates were predictable, increasing with both time and temperature, as other investigators have shown [Lefhalam et al. 2001, Li 2002]. The 316L stainless steel interaction layer formation rates at 550°C were relatively low, however, the 316L stainless steel had relatively large interaction layers after exposure to 650 C LBE. This degradation of the 316L stainless steel seems to be connected to the mass transfer of the Ni, as indicated by the ICP results in Figure 4.4. Because nickel is very soluble in Pb, as seen in Figure 4.2, it contributed to the interaction layer formation rate. Once the nickel went into solution, it precipitated out in cooler regions and created dust that was taken out of the system. Although highly soluble in the LBE bulk coolant [Equation (4.3)], the saturation level was never reached because of the small mass in the system. The higher the concentration of nickel in the LBE, the slower the rate of dissolution into the LBE, thus explaining the logarithmic behavior.

As shown in Figure 4.16, LANL's tests of 316L in the corrosion loop at Obninsk revealed an interaction layer formation slightly smaller than ours, while their HT-9 coupon had a substantially larger interaction layer formation than did ours [Li 2002]. This could be due to saturation of the nickel in the LBE
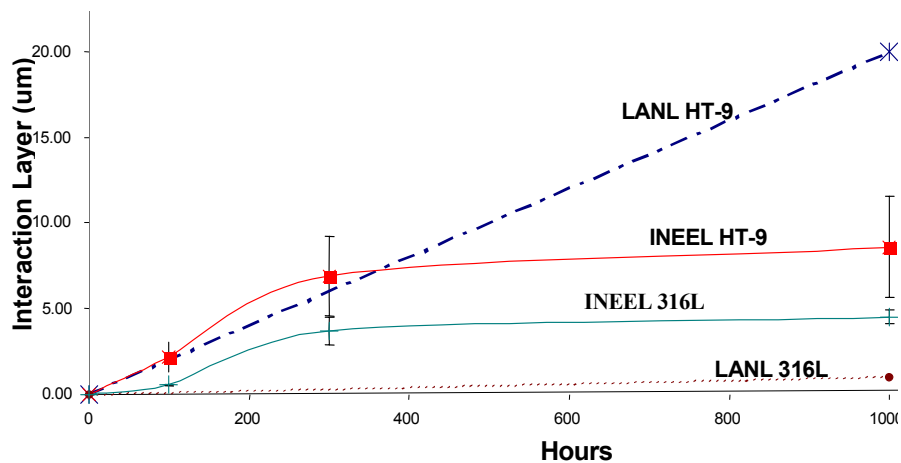
Figure 4.16. Interaction layer thickness in microns versus time for the HT9 and 316L stainless steel samples tested at 550°C at INEEL and LANL.

170

bulk coolant in the loop they tested in. Their data over 3000 hours appear to agree with our findings that the 316L stainless steel degrades logarithmically.

The interaction layer formation rates of the group of alloys without nickel (F-22 and 410) at both temperatures is approximately linear, as given in the following equations:

At 550°C, $R_{F22} = 0.0204t + 4.8$ $R_{410} = 0.0056t + 1.4$ (4.8)
At 650°C, $R_{F22} = 0.0043t + 1.5$ $R_{410} = 0.0106t + 1.8$ (4.9)

Recall that the F22 low alloy steel exhibited the highest interaction layer formation rate at 550°C but the lowest rate at 650°C. Some areas were virtually free of an interaction layer, while other areas had holes and crevices. The high interaction layer formation rate at 550°C may be due to the fact that the F22 is a low alloy (2 wt% Cr) steel compared to the other steels, therefore, the Fe is not protected as much from mass transfer. The low interaction layer formation rate at 650°C may have been due to the presence in the LBE bulk coolant of excess zirconium. Ilincev (2002) has stated that "Ti or Zr inhibition is most effective on steels with relatively high C and N activity, i.e. carbon and refractory steels with low contents of Cr, Mo, V and other carbide and nitride-forming elements………..Stainless chrome, chrome-nickel and low alloy steels stabilized with strong carbide- and nitride-forming elements do not form protective (ZrN and ZrC) films and thus corrode as fast as if no inhibitor were present".

Finally, we note that the structural material interaction layer formation due to contact with molten LBE may be occurring in two ways. The first is the mass transfer of the nickel and Fe, which go into solution and either precipitate out in a cooler region of the cell, or oxidize out of the system in the form of dust. The second way is the oxidation of materials on the coupon, which then changes the composition of the layer between the Pb and the metal substrate. Note that all the data we have presented is reaction layer data. If we had removed the reaction layers and made weight loss measurements we might know more about the exact overall corrosion/dissolution rate, but we would not have learned anything about the reaction layer compositions.

4.2. FY-02 MIT Materials Studies (J. Lim and Professor R. Ballinger)

4.2.1. Introduction

While liquid metals, in particular Pb and Pb-Bi alloys, are very attractive from a neutronics and thermal hydraulic point of view, there are a significant number of materials issues which, if not addressed, will negate the other advantages. Key materials issues are related to the fact that most metals have a finite solubility in Pb and Pb-Bi alloys. Moreover, the solubility will be a strong function of temperature. Thus, if the metal surfaces are not protected in some way, there will be a continuous removal of material from hot regions of the system and the deposition of material in the colder regions. The key technical challenges to the successful use of Pb-Bi coolant are to find ways to eliminate or at least mitigate this effect. Possible alternatives include: (1) use of a material which has a very low solubility in Pb-Bi, (2) use a coating of some kind, (3) operate in an environment in which a self protecting film forms, or (4) reduce the operating temperature such that the dissolution rate is acceptably low.

The economic viability of Pb and Pb-Bi alloy cooled power systems requires that the operating temperature be as high as possible. Thus, reducing operating temperature is an unsatisfactory

solution. Coatings, while an attractive alternative at first look, are difficult to apply, difficult to maintain, and their effectiveness difficult to monitor.

Figure 4.17 shows a schematic that illustrates the effect of the key variables on the operating "window" for a potential Pb-Bi system. Current iron based alloys are limited to temperatures below 550°C due to corrosion restrictions. At temperatures above 550°C metal dissolution kinetics becomes limiting for low oxygen potential environments. For systems that rely on film stability to limit degradation, a quantitative knowledge of the controlling variables is lacking in the 550-650°C range. An increase in the operating temperature for iron-based alloys is possible but only with a better understanding of the fundamental processes involved.

With respect to the use of active oxygen control as a means of limiting dissolution, Figure 4.18 shows the effect of increasing temperature on the viability of active oxygen control in general. At low oxygen concentrations film formation is not possible and the system is controlled by metal dissolution. As the oxygen potential is increased a region of oxide film stability is reached. As the temperature is further increased the kinetics are such that the region of film stability constricts until a point is reached where the film is unstable for any oxygen potential.

If we combine the effects of velocity and temperature on materials requirements for Pb and Pb-Bi alloy systems we can identify R&D needs for increased temperature operation. Figure 4.19 represents an attempt to do this.
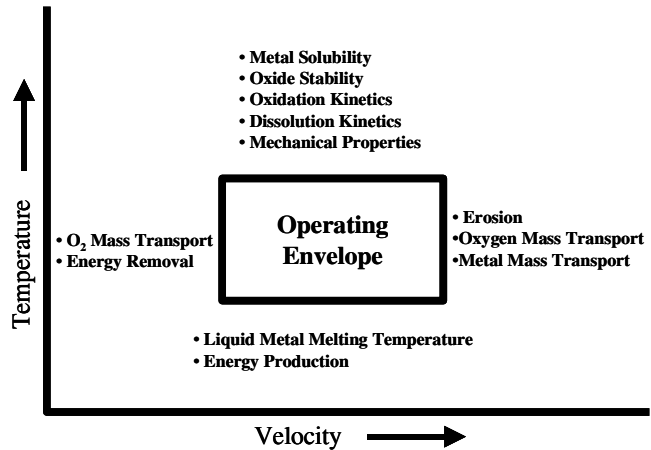

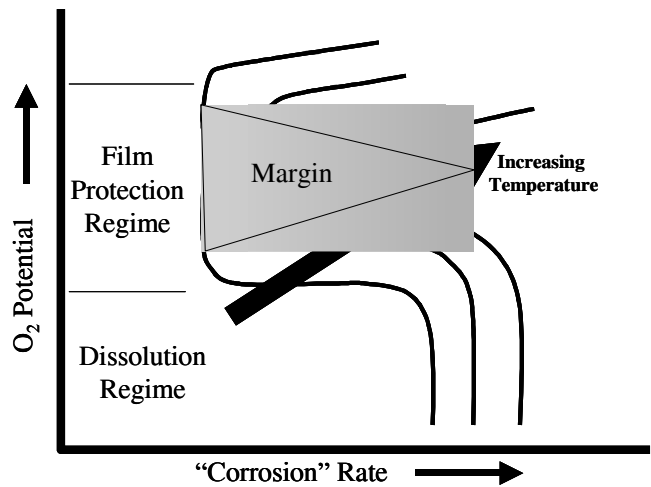**Figure 4.17. Schematic of operating restrictions for Pb-Bi.**

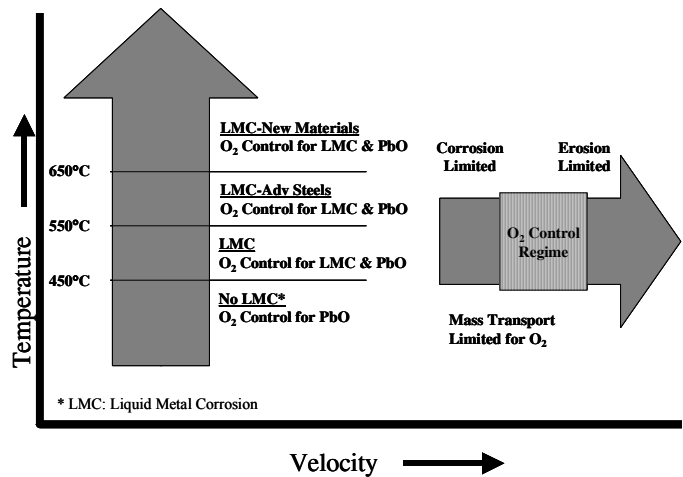**Figure 4.18. Relationship between corrosion rate and oxygen potential.**

Figure 4.19. Relationship between temperature and velocity and materials requirements for Pb-Bi operation.

172

For applications where the temperature is below 450°C liquid metal corrosion (LMC) is not an issue and the preferred material is steel or stainless steel. An active oxygen control system to promote film formation is not required. The upper bound on the oxygen potential is that at which PbO forms. This upper limit insures against the formation of "sludge" which would foul the system. In the temperature range 450-550°C LMC becomes an issue and active oxygen control is required. In this temperature range iron-based alloys are acceptable. At temperatures above 550°C our lack of a fundamental knowledge for the iron alloy system becomes an issue. While it is felt, based on Russian experience, that the iron-based alloy system can be used up to 650°C, this will require: (1) a better understanding of the fundamentals of the corrosion/film formation process with current alloys and, (2) the development of advanced iron based alloys based on this understanding. The latest data from Russia indicates that the Fe-Si system is a promising one to explore. Additionally, work using Oxide Dispersion Strengthened (ODS) steels show promise for higher strength in the upper temperature range. At temperatures above 650°C the iron-based systems will be unsuitable from the corrosion as well as mechanical properties perspective. In this temperature range a completely new system will be required. Current thinking is that the use of active oxygen control to promote film formation will be inadequate as well. However, the basis for this contention comes from the iron-based system. New materials that form stable films at higher temperatures may allow for active oxygen control in this temperature range.

Protective film formation requires that sufficient oxygen be present in the system to raise the potential above the equilibrium potential for the formation of the film. In essentially all cases, the film is an oxide. As was mentioned above, it is important that the potential (free energy of formation for the film) be below that of PbO. If this is not the case then the oxide will also form and "sludge" will build up in the system. It is also important that the film be stable with respect to reduction by Pb or Bi.

While there has been extensive research in which materials have been exposed to Pb and Pb-Bi solutions at high temperature, followed by examination of the degree of degradation, much of the data has taken the form of penetration rate vs. time with very little detailed analysis which attempts to get to the fundamental phenomena. No systematic study has been performed as a part of a program to develop an alloy specifically designed for the application. At the same time, there is a wealth of knowledge regarding the scale formation process in steels in oxygen containing environments. To the first order, in the presence of oxygen, the Pb or Pb-Bi is inert with respect to scale formation. This means that the bulk of the literature and knowledge of high temperature scaling of steels can be used in the analysis. However, a very significant difference between the scale formation environment in oxygen containing Pb and the scale formation environment in oxygen containing atmospheres is the fact that most metals are soluble in the liquid metal environment and the dynamics of scale formation will be influenced by the removal of key elements (Cr for example) from the system by dissolution. Thus, for example, while nickel-containing alloys may be appropriate for oxygen containing atmospheres, it's solubility in liquid Pb may make it unsuitable as a material operating in Pb containing oxygen.

In this section we report the results of the FY-02 corrosion program conducted at MIT in collaboration with INEEL. During this past year the effort has been focused on the testing of selected refractory metals and initial testing of model Fe-Si alloys as part of an effort to develop a science-based alloy development program, the goal of which is to develop an advanced Fe based alloy specifically optimized for Pb and Pb-Bi service. In Section 4.2.2 we describe the experimental apparatus and overall test matrix. In Section 4.2.3 we discuss the experimental results for refractory metals tested in Pb. In Section 4.2.4 we present a description of the Fe-

based alloy development program and present results for Fe-Si alloys tested in both Pb and Pb-Bi. In Section 4.2.5 we discuss issues related to the development of advanced Fe-based alloys.

4.2.2. Experimental System Description & Test Matrix

4.2.2.1. System Description

Rotating Electrode System: The rotating electrode facilities at MIT have been built to conduct dynamic corrosion tests in Pb or Pb-Bi alloy coolants under isothermal conditions. The main design attributes of the system include: 1) the ability to perform high temperature corrosion tests (above 600°C), 2) the establishment of a well-known velocity distribution, and 3) vacuum tight boundaries which allow accurate oxygen pressure control.
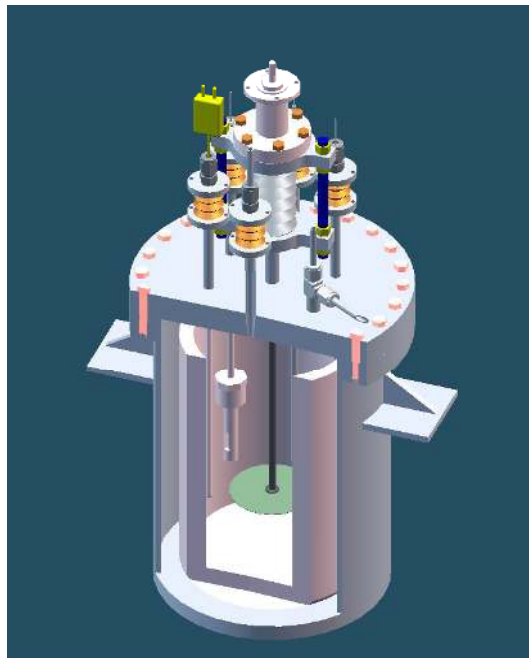
The system consists of two identical furnaces that contain separate rotating electrode test systems. The oxygen potential is controlled using a mixing and monitoring system. Figure 4.20 shows an overall view of two identical furnace systems. The systems are capable of operating at temperature up to 1000°C. Currently, a temperature limit of 650°C has been imposed due to vapor transport issues. These issues have been resolved and full temperature range operation is anticipated within the next quarter.

Figure 4.20. Overall views of the rotating electrode facilities (two identical systems).

The vessel arrangement consists of a stainless steel "catcher" vessel surrounding a Mg stabilized zirconia crucible. An external stainless steel vessel acts as a vacuum tight pressure boundary. Figure 4.21 shows the cross-sectional view of the vessel. Specimens can be either attached to a rotating shaft that feeds through the lid of the vessel or can be suspended in the crucible. Feed-throughs designed to allow measurement of temperature and oxygen potential, to rotate specimen in vacuum tight conditions, and to provide for environmental control pass through the vessel lid.

Figure 4.21. Cross-section view of the stainless steel vessel with feed-throughs.

Oxygen Control System: The control of the oxygen potential is a crucial part in the development of an understanding of the corrosion/film formation behavior of structural
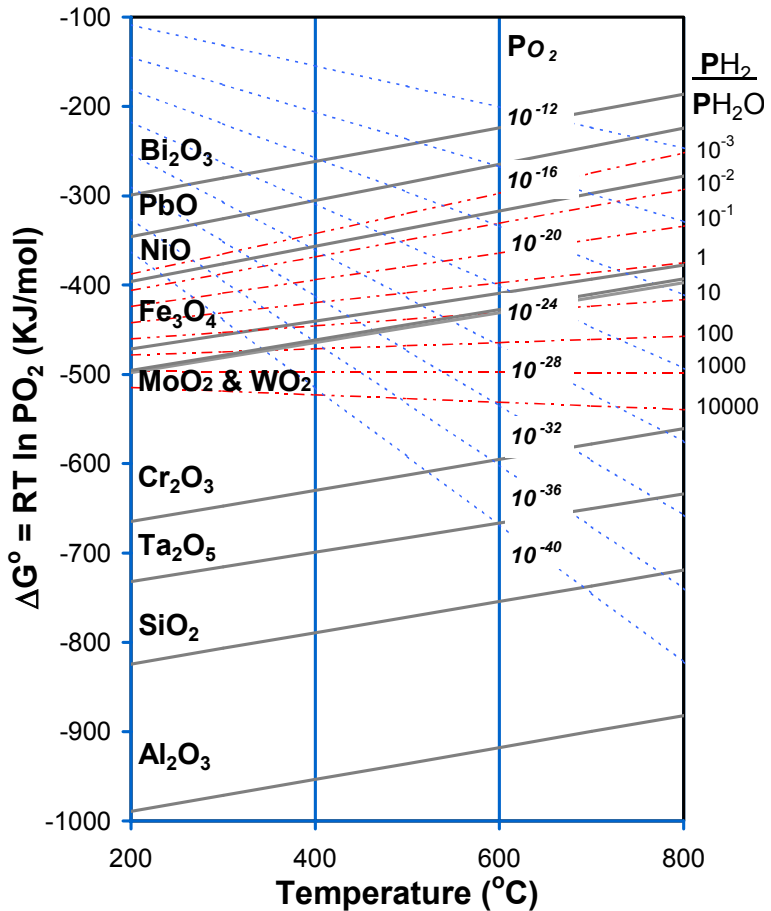
174

metals contacting Pb or Pb-Bi alloys. Since the required oxygen concentration is very low, instrumentation for direct measurement is not available. Instead, we make use of the equilibrium reaction between H_2, H_2O and O_2. In this way the partial pressure of oxygen can be maintained in the range of stability for oxides of relevant metal systems and thus control the selective reduction/oxidation of metal-metal oxide couples. Figure 4.22 shows an Ellingham diagram for

the equilibrium oxygen partial pressure of selected elements, along with the corresponding partial pressure ratios of H_2 and H_2O required to control the oxygen partial pressure. With the assumption of thermodynamic equilibrium conditions, one can use this diagram to determine the required partial pressure ratio of hydrogen and moisture to reduce/oxidize certain metal-oxide/metal systems.

Since lead and bismuth oxides form at higher oxygen partial pressures than the oxides of major alloying elements in steel, including nickel, chromium, and silicon, maintaining the oxygen partial pressure below the value for Pb or Bi oxide formation and above that of other oxides allows system operation in a region which promotes the formation of a surface oxide film –as a diffusion barrier –

Figure 4.22. Ellingham diagram for selected metal-metal oxide systems.

on the structural metals without generating PbO which degrades system performance through the formation of "sludge" which must be removed via the application of a reducing cycle for cleaning purposes. In order to study the film formation kinetics in alloys of engineering significance, accurate oxygen control and measurement is essential. To accomplish this a gas control system has been included as part of the test system.

Figure 4.23 shows a schematic diagram of the cover gas control/monitoring system. The system consists of two gas streams, an inert argon carrier gas stream and a hydrogen gas stream. However, while the purity of these gas streams is very high, this is still inadequate for our use. Thus, each starting gas stream is further purified prior to use. The argon passes through a gettering furnace to reduce its oxygen and moisture level from several ppm to several ppb, using the reaction between oxygen and titanium at high temperature. A measurement unit for monitoring oxygen and moisture concentrations is installed downstream of the oxygen gettering furnace to ensure its performance. Oxygen in the hydrogen stream is combined with hydrogen to form water vapor by passing the stream over a palladium catalyst, followed by a dryer to remove

moisture. The amount of hydrogen and argon flow is controlled by a mass flow controller and mixed to achieve the necessary hydrogen concentration. The mixed gas then passes through a constant temperature water bath to achieve the desired H_2/H_2O ratio for the desired oxygen potential in the gas stream. Figures 4.24 (a) and (b) show the gas monitoring/controlling system.
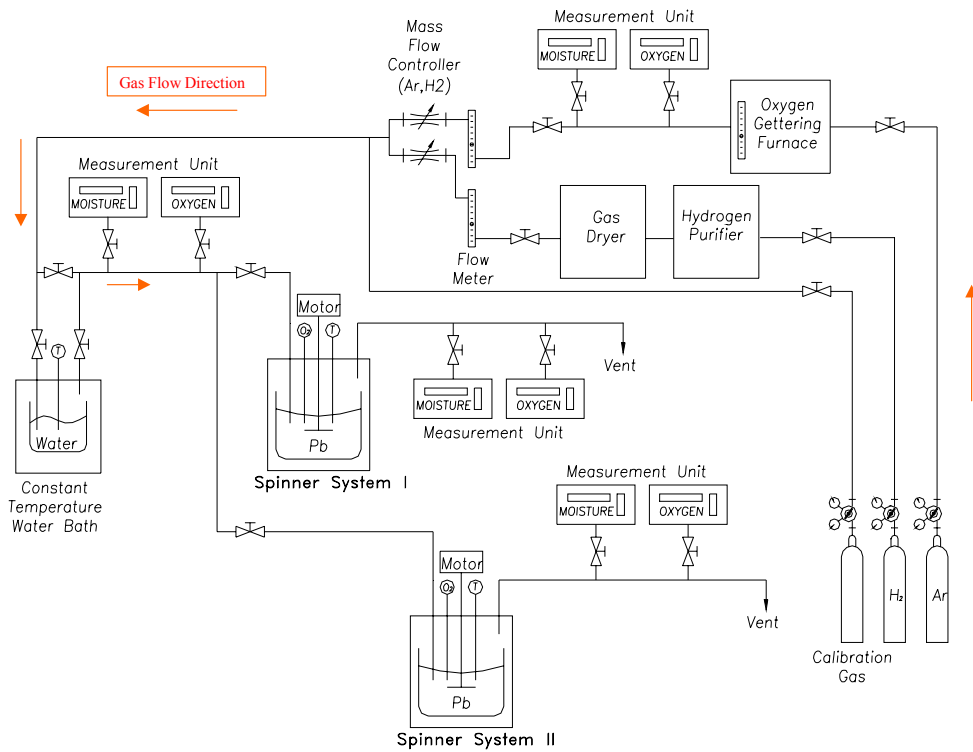
Figure 4.23. Schematic diagram of cover gas flow for experimental facilities.

Figure 4.24. (a) A built in gas monitoring /controlling system (b) Side view of (a) with constant temperature water bath.

4.2.2.2. Test Matrix and Materials

Using the rotating electrode system described above and developed in FY-01, selected refractory metals and Fe-Si alloys were tested in Pb and/or Pb-Bi eutectic during FY-02. Table 4.6 summarizes the material test matrix performed to date with key variables maintained during the tests. The oxygen conditions listed in Table 4.6 refer to the stability of the oxide of the major (or identified) element present. In the case of Molybdenum, the oxygen potential was maintained below the MoO_2 oxide formation potential-hence "Reducing". In the case of the Fe-1.24% Si alloy the oxygen potential was maintained below the iron oxide formation potential but above the silicon oxide formation potential. Since both tantalum (tested alone) and silicon (the alloying element of Fe-Si alloy group) oxides are stable at very low oxygen potentials the achievement of reducing oxygen potentials with respect to these oxides is not currently possible with our system. For the lead and bismuth, all the oxygen conditions were maintained reducing with respect to their oxides. As mentioned in our FY-00 report, this reducing condition was maintained using a H_2-H_2O-O_2 equilibrium by keeping the hydrogen to moisture ratio much greater than 100 at 600^oC. The rotational speed of the sample was 200 rpm, which is equivalent to a maximum flow velocity over the surface of 0.8 m/s. Nominal chemistries for the materials tested are shown in Table 4.7, including the Pb and Bi.

Table 4.6. Summary of MIT Pb/Pb-Bi corrosion test runs for FY-02.

Material		Melt	Test ID	Temp (^oC)	Time (hr)	Oxygen Condition	Rotating Speed (rpm)
Refractory Metals	Molybdenum	Pb	M1	600	100	Reducing	200
	Tungsten	Pb	W1	600	100	Reducing	200
	Tantalum	Pb	T1	600	100	Oxidizing	200
Iron/Iron-Silicon Alloys	Pure Iron	Pb	F1	600	100	Reducing	200
	Fe-1.24% Si	Pb	FA1	600	100	Re(Fe)/Ox(Si)	200
		Pb-Bi	FA1-b	600	100	Re(Fe)/Ox(Si)	200
			FA3-b	600	300	Re(Fe)/Ox(Si)	200
	Fe-2.55% Si	Pb	FB1	600	100	Re(Fe)/Ox(Si)	200
		Pb-Bi	FB1-b	600	100	Ox(Fe)/Ox(Si)	200
	Fe-3.82% Si	Pb	FC1	600	100	Re(Fe)/Ox(Si)	200

Table 4.7. Nominal Chemistries of Metal Samples with Pb and Bi.

a. Refractory metals														
Metal	Purity	Maximum Impurities (ppm)												
	(%)	C	Fe	W	Ta	Mo	Si	Nb	O	Ti	Ni	Co	Pb	Cr	Al
Mo	99.95	30	60	300	20	-	30	10	50	10	10	30	10	20	20
W	99.96	30	30	-	10	100	20	10	30	10	20	10	10	10	15
Ta	99.9	30	100	100	-	100	50	400	100	50	50	20	10	10	20

b. Composition of Fe-Si alloys												
Metal	Concentration (wt%)											
	Fe	Si	P	S	Mo	Cu	Cr	Al	Ti	C	Mn	Ni
Fe	Bal	0.05	0.007	0.016	0.017	0.03	0.04	0.031	0.002	0.02	0.31	0.03
Fe-1.24%Si	Bal	1.24	0.006	0.001	0.01	0.03	0.09	0.005	0.003	0.01	0.04	0.08
Fe-2.55%Si	Bal	2.55	0.003	0.001	0.10	0.03	0.08	0.003	0.006	0.017	0.12	0.15
Fe-3.82%Si	Bal	3.82	0.022	0.025	-	-	-	-	-	0.011	0.24	-

c. Impurities concentration in lead and bismuth											
Liquid metal	Purity (%)	Maximum Impurities (ppm)									
		Pb / Bi	Ag	Cu	Sn	As	Fe	Ni	Sb	Cd	Zn
Lead	99.99	2.7 (Bi)	< 1	< 1	< 5	< 1	< 1	-	< 5	4	< 1
Bismuth	99.99	2.8 (Pb)	3.3	0.9	-	-	< 0.6	< 0.9	< 3	< 0.2	< 0.2

4.2.3. Test Results-Refractory Metals

As listed in Table 4.6, refractory metals were tested in Pb for 100 hours at 600°C with a rotational speed of 200 rpm (0.8 m/s). Tested samples were analyzed using scanning electron microscopy (SEM), (FEI/Philips XL30 FEG ESEM) with Energy-Dispersive X-ray (EDX) analysis capability for a qualitative compositional analysis.

4.2.3.1. Molybdenum (Mo)

Figure 4.25 shows a secondary electron image of molybdenum exposed to
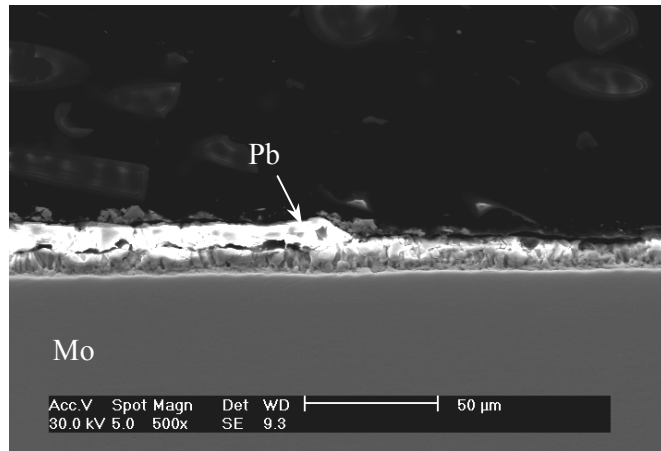
Figure 4.25. Secondary electron image of molybdenum sample tested in Pb (Test ID: M1).

reducing conditions for 100 hr at 600°C.   No attack by the lead is observed.   However, a columnar layer, identified by X-Ray analysis as being lead, develops on the surface during exposure.   The reason for the columnar structure of lead layer is not known at this time.

4.2.3.2. Tungsten (W)

Figure 4.26 shows a secondary electron image of a tungsten sample exposed at 600°C for 100 hours in Pb under reducing conditions. No apparent attack or wetting is present.
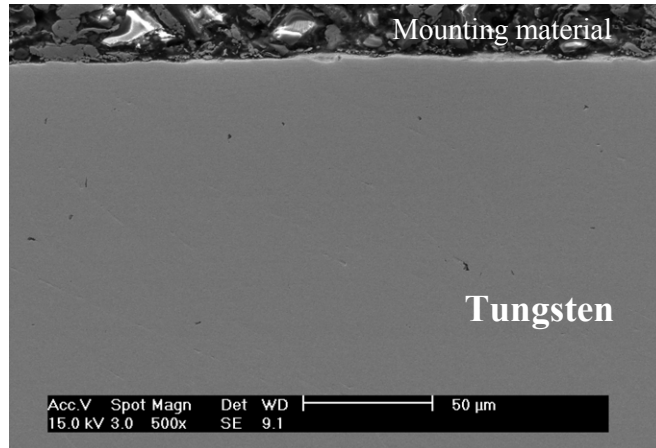
4.2.3.3. Tantalum (Ta)

As mentioned in Section 4.2.2.2, tantalum oxide is stable to very low oxygen potentials and is thus very hard to reduce with the current oxygen control system. Figure 4.27 shows a micrograph of a Ta sample exposed to Pb at 600°C for 100 hours.   A tantalum oxide layer is present on the surface after lead exposure. However, it is likely that an oxide layer was present prior to exposure also.
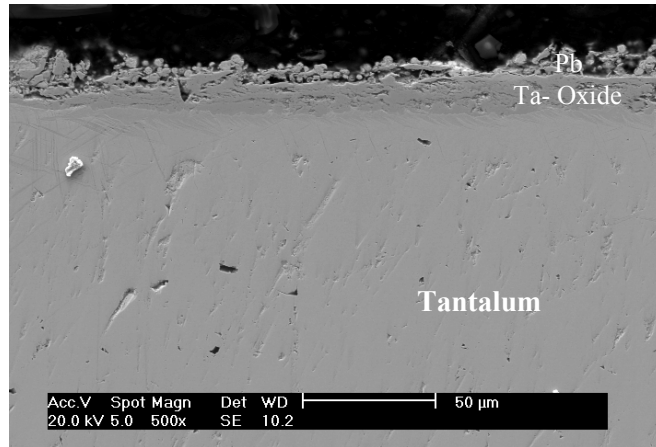
4.2.3.4. Conclusions-Refractory Metal Exposure

Figure 4.26. Secondary electron image of tungsten sample tested in Pb (Test ID:W1).

Figure 4.27. Secondary electron image of tantalum sample tested in Pb. (Test ID:T1)

The results of the test program have confirmed the results generated by others many years ago. The refractory metals exhibit very little degradation when exposed to liquid Pb or Pb-Bi. This is due to their very limited solubility as well as, in the case of Ta, the formation of a very stable oxide film. However, the use of these materials as a major structural component is not possible due to limitations other than resistance to corrosion in Pb or Pb-Bi alloys. Mechanical properties limitations, fabrication and processing limitations, as well as resource limitations effectively eliminate the use of these materials in large structures.
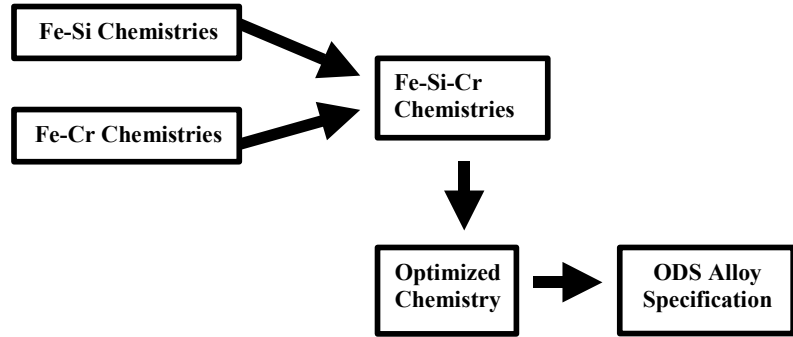
4.2.4. Iron-Based Program

The purpose of the Fe-based program is to develop a fundamental understanding of the role of Fe-alloy chemistry on the performance of materials in Pb and Pb-Bi environments and to apply this understanding to the development of Fe-based alloys optimized for Pb and Pb-Bi service.   The program takes a ground up approach by examining the role of individual elements in Fe first and then expanding the system to include multiple elements. Lastly, this understanding will be used to develop a new alloy that will be tailored to the application and will satisfy specific design requirements. The minimum design requirements will be:

1. Resistance to corrosion/dissolution in Pb and Pb-Bi over a range of oxygen concentrations from essentially zero to the PbO formation potential.
2. To maintain adequate strength for use as a structural material at temperatures up to 650°C.

Figure 4.28 shows a schematic of the overall development plan. The initial focus will be on Fe-Si alloys. The motivation for this focus is that: (1) Si has a low solubility in Pb and Pb-Bi, (2) Si has a very negative free energy for the formation of it's oxide, and (3) the Russian alloy EP823, which shows good resistance to corrosion in Pb and Pb-Bi, contains 1.3% Si. Initial results from the Fe-Si system are reported here. Upon completion of the study of

Figure 4.28 Schematic of Alloy Development Path

the Fe-Si system a series of Fe-Cr alloys will be melted and studied. There is some ambiguity as to the effectiveness of Cr in imparting resistance to Pb and Pb-Bi corrosion although it is clearly effective in the promotion of protective scale in oxygen containing atmospheres. High Cr (>15%) ferritic or martensitic stainless steels are known to be resistant to Pb and Pb-Bi corrosion. However, Cr has a relatively high solubility in Pb and Pb-Bi. At low Cr concentrations the Cr is incorporated into a spinel oxide structure. At higher Cr concentrations the formation of a Cr_2O_3 film is promoted. In the third phase of the program, the combination of Si and Cr in a base Fe alloy will be studied in an effort to produce an optimized chemistry for both resistance to dissolution in low oxygen environments and to scale formation in higher oxygen environments. Finally, the optimized alloy chemistry will be used as the base chemistry in the design of an ODS material similar to MA-956.

Table 4.6 shows the chemistry of the Fe-Si alloys tested. The chemistries were chosen to span the composition from pure Fe to Fe-3.82 wt% Si. At Si contents above 3.83wt% Si, the literature shows that these materials suffer from a loss of ductility. All the tests were conducted under reducing conditions with regard to the iron oxides.

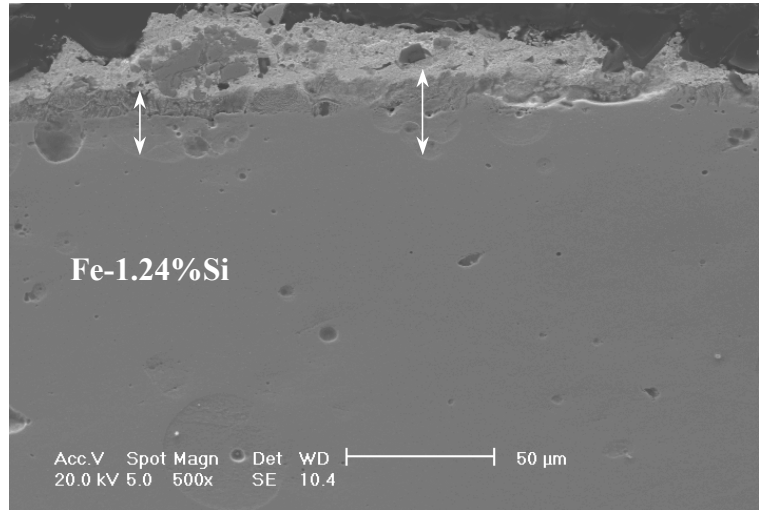### 4.2.4.1. Results: Pb Exposure

Pure Iron (Fe). Figure 4.29 shows an SEM micrograph of pure Fe exposed to Pb at 600°C for 100 hours. Pb both wets and penetrates the material as is indicated by the arrow in Figure 4.29. Considering the relatively short testing period of 100 hrs, the attack by lead is quite severe and thus confirms the need for protective measures for the iron when operating at
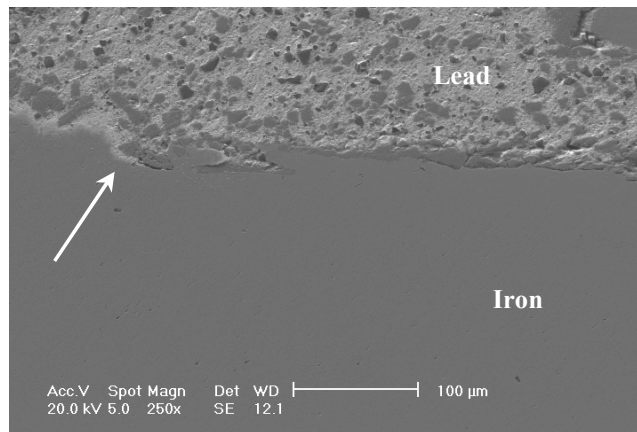
Figure 4.29. Secondary electron image of pure iron sample tested in Pb (Test ID:F1).

low oxygen potentials. These results serve as a benchmark from which we will compare results for Fe-Si compositions.

Fe-1.24% Si. Figure 4.30 shows a SEM micrograph of the Fe-1.24%Si alloy exposed to Pb for 100 hrs at 600°C under reducing conditions (Test ID: FA1). The depth of the interaction layer is in the 20~28 μm range. A more detailed analysis of the interaction layer is in progress. Figure 4.31 shows the same specimen but focuses only on the Pb/Fe alloy interface. The figure consists of an SEM micrograph (a) along with an X-Ray dot map (b) showing the location of the Si. Considering the relative intensity of the silicon signal, there appear to be some enrichment of the solid/liquid

Figure 4.30. Secondary electron image of Fe-1.24%Si sample tested in Pb (Test ID:FA1).

metal interface in Si, i.e. an apparent change in silicon concentration at the interface compared with that in the bulk metal.

(a)   (b)
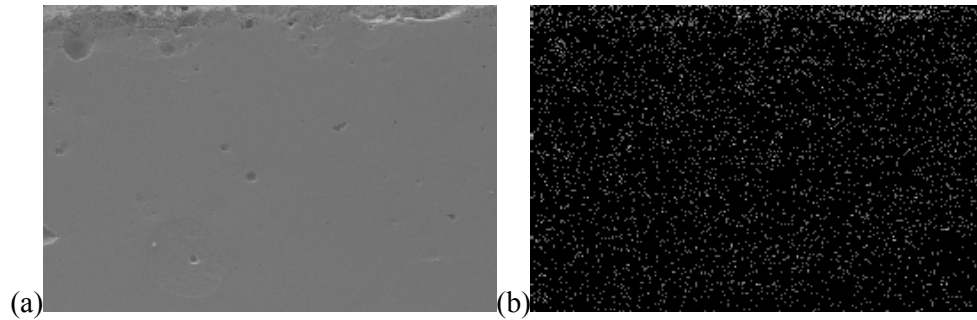
Figure 4.31. SEM picture with silicon K-α signal used to map silicon distribution (X-ray dot map) over Fe-1.24%Si sample tested in Pb (Test ID:FA1).

Fe-2.55% Si. The focus of the Fe-Si program has been on the Fe-2.25% Si alloy during this year. As such, more detail is presented here for this material. The Fe-2.25% Si alloy was exposed for 100 hours in molten lead at 600°C. Figures 4.32 and 4.33 show the as-received microstructure. The samples were mounted and polished using standard techniques and etched with 2% natal. The microstructure consists of ferrite grains with small inclusions. Figure 4.33 illustrates the effect of rolling with the pancaked grains oriented along the rolling direction.
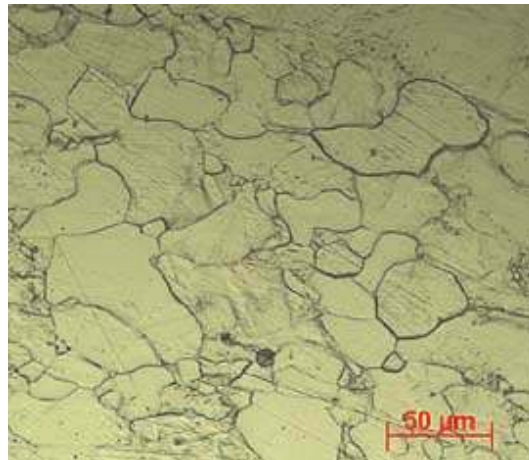
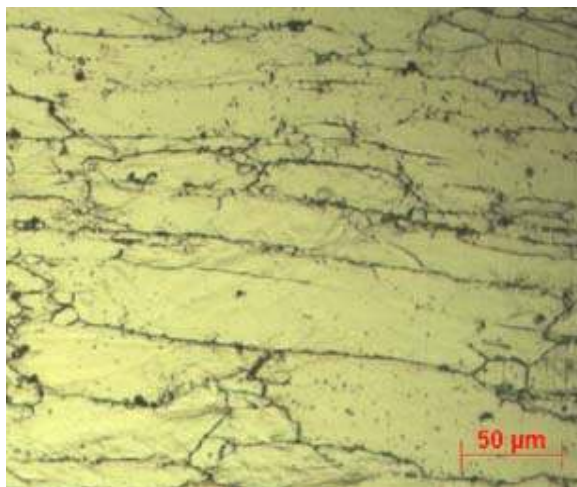**Figure 4.32. Optical micrograph of as received Fe-2.55wt% Si alloy-surface**

The H$_2$/H$_2$O ratio for this test was in the range 100-200 for the test, which placed the oxygen potential between the Fe$_3$O$_4$ and the Cr$_2$O$_3$ equilibrium. Note that this ratio also places the oxygen potential above the SiO$_2$ equilibrium.

Figure 4.34 shows a photograph of the sample after exposure. Analysis of the effect of velocity from the central region to the outer edge has not been completed at this time. The analysis has focused on optical and scanning electron microscopy thus far. Figures 4.35 and 4.36 show optical micrographs of the as-tested sample. As Figure 4.36 shows, the reaction with the Pb was very minor with no intergranular penetration observed. Exposure at 600°C has, however, resulted in recrystallization of the microstructure. Future tests will begin with recrystallized material.

Figures 4.37 and 4.38 show secondary electron and back scatter electron SEM micrographs of the as-exposed sample. The orientation is through-thickness.

The backscatter image is sensitive to atomic number. Thus, the lighter areas are material with a higher Z, in this case Pb. The lighter "islands" within the Pb are most likely Fe oxides that were formed on heatup and prior to establishment of the desired oxygen potential. At the oxygen potential of the experiment iron oxides are not stable. As with the optical micrographs, there is little surface dissolution and no intergranular penetration.

Figure 4.39 shows a series of X-Ray (EDX) generated elemental maps along with a secondary electron SEM image of the same region. The maps indicate that during exposure there is some amount of Fe dissolution, which results in an enrichment of Si in the surface due to its lower solubility in the Pb and Pb-Bi. At very low oxygen potentials, below the SiO$_2$ equilibrium we expect that the surface would continue to enrich in Si until an equilibrium is reached

Figure 4.33. Optical micrograph of as received Fe-2.55wt% Si alloy - through thickness direction.
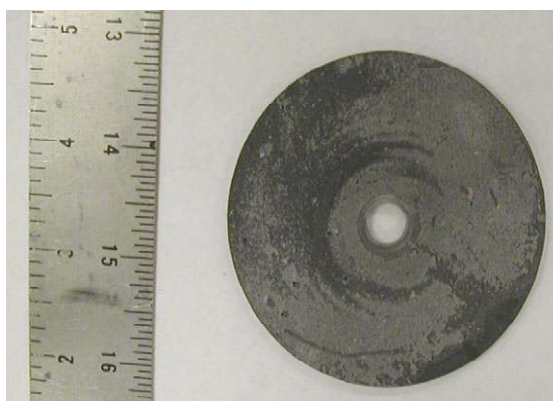
4.34. Fe-2.55Si alloy sample surface tested for 100 hrs in lead at 600°C.
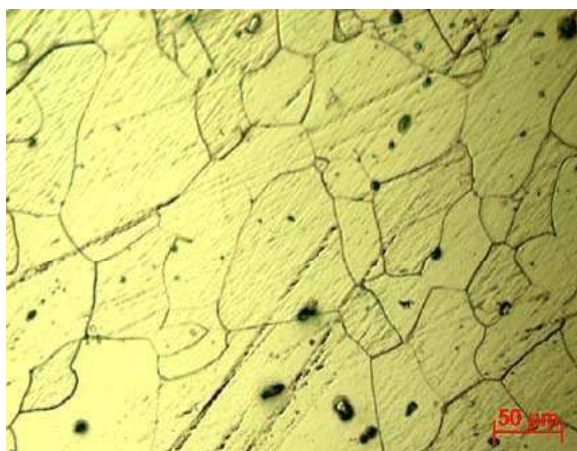

**Figure 4.35. Optical micrograph of tested Fe-2.55wt% Si alloy in lead for 100 hrs at 600°C-surface.**

whereby the lower solubility of Si limits the migration of Fe through the Si-rich layer. At oxygen potentials where SiO_2 is stable we expect that the concentration of Si will increase until its activity is sufficient, at the oxygen potential of the system, to form SiO_2 on the surface. At this point a protective film will form and limit further surface interaction. The results thus far are very promising but must remain preliminary until longer exposures are tested as well as tests at oxygen potentials where SiO_2 is encouraged.
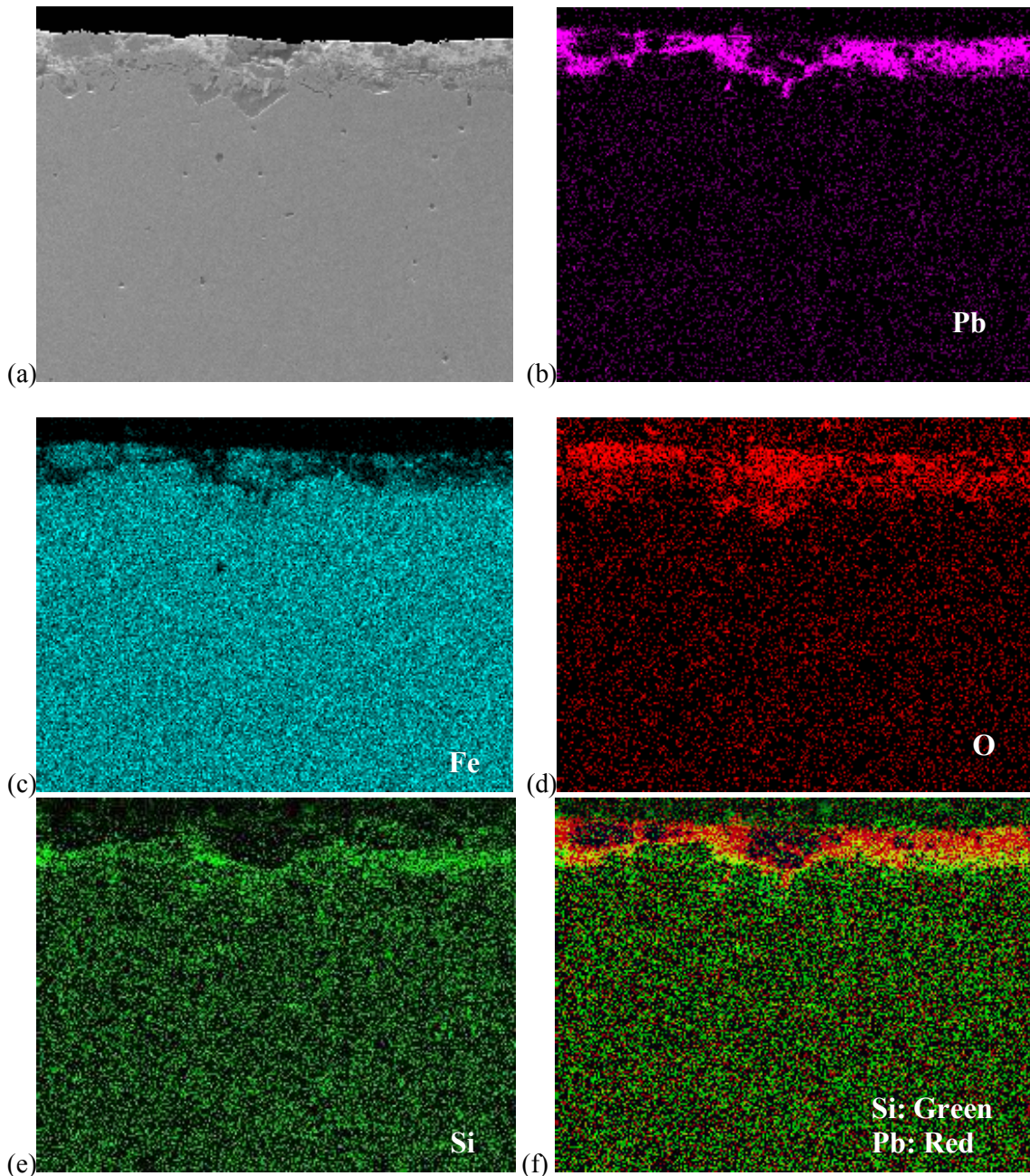

Figure 4.36. **Optical micrograph of tested Fe-2.55wt% Si alloy in lead for 100hrs at 600°C - through thickness direction.**
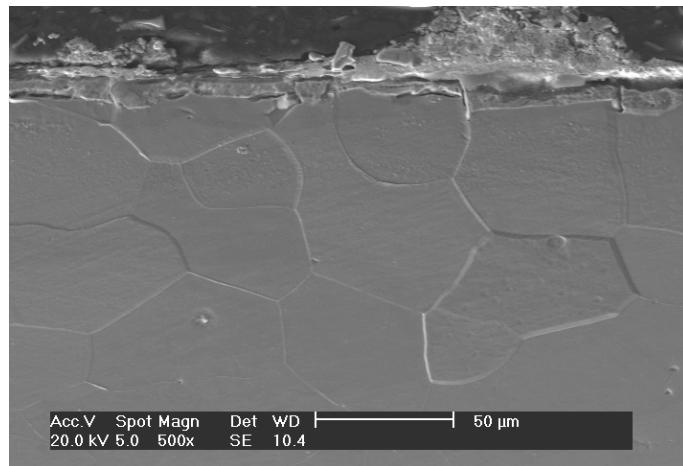
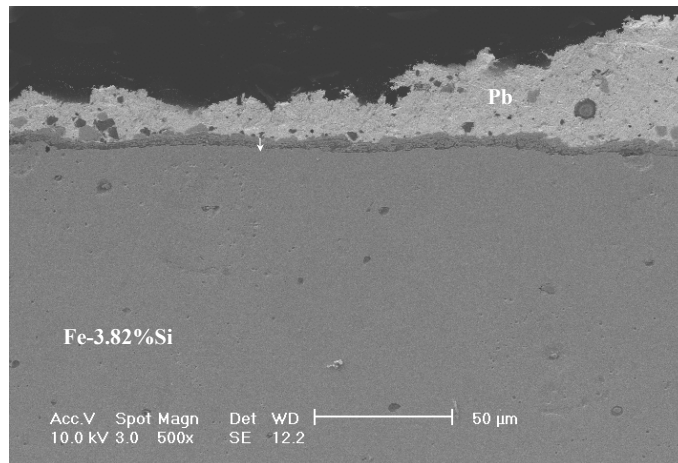**Figure 4.37. Secondary electron image of etched Fe-2.25wt% Si alloy.**
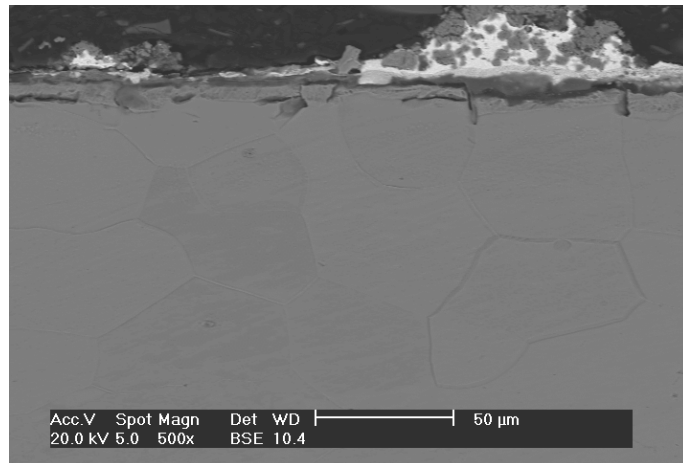
Figure 4.38 Back-scattered electron image of etched Fe-2.25wt% Si alloy.

183

Figure 4.39 (a) Secondary electron image of 500 times magnification Elements maps showing the distribution of (b) lead – Pb, (c) iron – Fe, (d) oxygen – O, (e) silicon – Si, (f) upper layer of lead (red) and lower layer of silicon (green).

Fe-3.82% Si. Figure 4.40 shows an SEM micrograph of the Pb-Fe-alloy interface after exposure. The surface layer for this level of Si shows a more compact interaction layer when compared with those with lower Si content. There is a very clear enrichment of Si in the surface region. Further testing is in progress to establish the details of the development of the enriched layer and its role in SiO_2 layer development at higher oxygen potentials.

Figure 4.40. Secondary electron image of Fe-3.82% sample tested in Pb (Test ID:FC1).

(a)   (b)
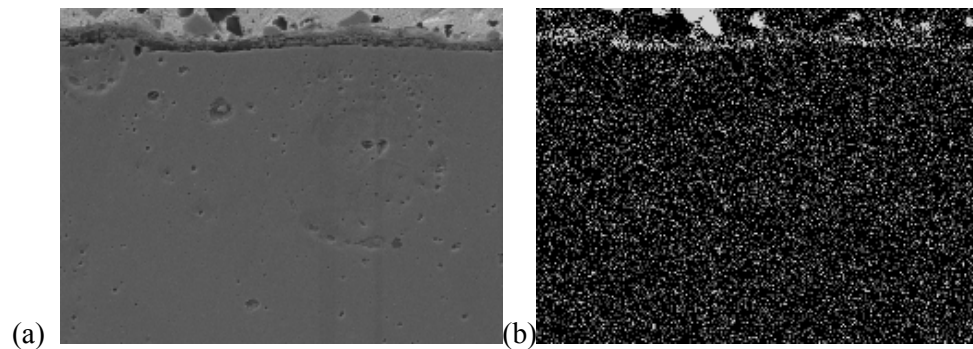
Figure 4.41. SEM picture with silicon K-α signal used to map silicon distribution (X-ray dot map) over Fe-3.82%Si sample tested in Pb (Test ID:FC1.)

4.2.4.2. Tested in Pb-Bi Eutectic

During this year the experimental program shifted from exposure in Pb to exposure in Pb-Bi.

Fe-1.24%Si. Figure 4.42 shows an SEM micrograph of a Fe-1.24% sample tested in Pb-Bi eutectic (44.5% Pb, 55.5% Bi) for 100 hours. Bulk materials (mainly iron oxide formed during the heat-up period) have been removed from surface and incorporated into the deposited Pb-Bi layer leaving compact but severely damaged interface between the Pb-Bi and bulk metal. The actual amount of the bulk metal removed by Pb-Bi attack is still under investigation.
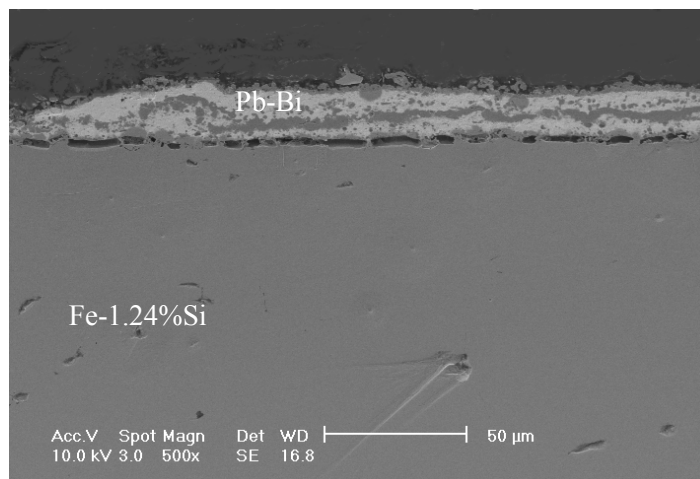
Figure 4.42. SEM micrograph of Fe-1.24% Si sample tested in Pb-Bi (Test ID:FA1-b).

185

Fe-2.55% Si. Figure 4.43 shows an SEM micrograph of the Fe-2.55% Si alloy after exposure to Pb-Bi eutectic at 600°C for 100 hours. The interaction layer consists of a detached iron oxide layer with Pb-Bi at the interface with the metal. We believe that the iron oxide formed during the heat process. Efforts are under way to pre-purge the system of oxygen prior to heatup to prevent this from happening in the future. The actual removal rate of material is still under investigation but, based on a comparison with the Pb case, it appears that the Pb-Bi is more aggressive than Pb alone.
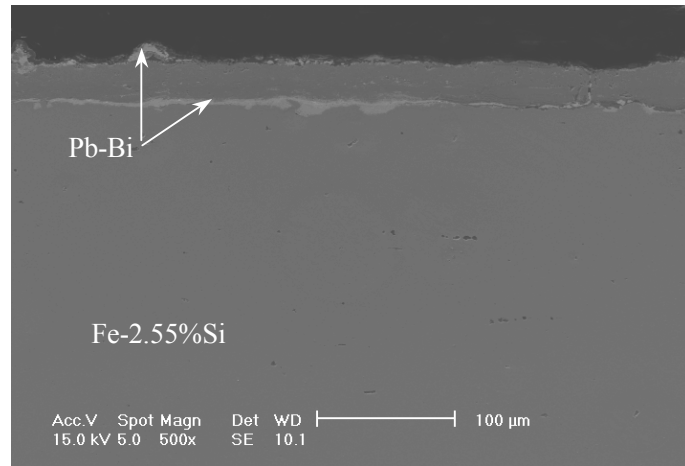
Figure 4.43. SEM image of Fe-2.55%Si sample tested in Pb-Bi Eutectic. (Test ID:FB1-b)

4.2.4.3. Discussion

The results of the Fe-Si series of tests show very promising behavior. It appears that, as expected, a Si rich layer is formed on the surface during exposure due to the selective dissolution of Fe. Since the solubility of Si is much lower than Fe in Pb and Pb-Bi, we expect that the enriched layer will continues to grow during exposure and will limit further dissolution. If the oxygen potential is high enough there will come a point where SiO_2 is stable and a protective oxide layer will form.

4.2.5. Future Work-Alloy Development

Work during FY-03 will focus in the following areas:

1. The completion of the Fe-Si alloy testing and analysis.
2. The procurement of Fe-Cr and Fe-Cr-Si alloys.
3. The completion of development of the oxygen probe.
4. The beginning of testing at intermediate oxygen potentials.
5. The procurement of and ODS alloy.

Table 4.8 shows the chemistries of the Fe-Cr and Fe-Cr-Si alloys that are currently being melted. Based on the initial promising results with the Fe-Si series, LANL has agreed to share in the cost of alloy production. The alloys will be melted and initially processed at the General Electric Corporate R&D Laboratory in Schenectady NY. Delivery of the Fe-Cr alloys is scheduled for the middle of October, 2002. Delivery of the Fe-Cr-Si alloys is scheduled for the first part of November 2002. Once the alloys are received they will be further processed at MIT to produce wrought material. Samples will then be prepared and sent to INEEL and LANL for testing.

With respect to the ODS material, initial discussions have been had with Special Metals (formally INCO Alloys International/Huntington Alloys International) and the Michigan Technological University powder metallurgy processing laboratory with the intent to procure an ODS material with base Fe-Cr-Si chemistry and Y_2O_3 dispersion as the strengthener. These discussions have been very positive and it is likely that we will be able to obtain the material once the optimized

chemistry has been determined. Initial thoughts are that the optimized chemistry will be in the range of 2.5-3.0 % Si, 18 Cr.

Table 4.8. Proposed alloy chemistry for the investigation of Si and Cr effects.

|		
Fe-Cr alloys	1	Fe-1% Cr
	2	Fe-2.25% Cr
	3	Fe-9% Cr
	4	Fe-12% Cr
	5	Fe-18% Cr
Fe-Cr-Si alloys	1	Fe-2.25% Cr-0.5%Si
	2	Fe-2.25% Cr-1.25%Si
	3	Fe-2.25% Cr-2.55%Si
	4	Fe-12% Cr-0.5%Si
	5	Fe-12% Cr-1.25%Si
	6	Fe-18% Cr-0.5%Si
	7	Fe-18% Cr-1.25%Si
	8	Fe-18% Cr-2.55%Si

5. Coolant Activation Studies

Lead-bismuth eutectic (LBE) nuclear reactors have been constructed and operated only in Russia, and several important technological issues (e.g., structural material corrosion, coolant chemistry control, filtration of impurities, and coolant activation) still need to be addressed. One of the most important issues is the radiological hazard associated with the activation of the LBE coolant upon neutron bombardment. Polonium-210, a toxic alpha-emitter of approximately 140 days half-life, is formed from ^{209}Bi by neutron capture according to the following reaction:

$$^{209}Bi + n \rightarrow ^{210}Bi \xrightarrow[t_{1/2}=5days]{\beta^-} ^{210}Po \xrightarrow[t_{1/2}=138days]{\alpha} ^{206}Pb \qquad (5.1)$$

In a typical LBE-cooled reactor the primary system is sealed and segregated from the secondary system by the steam generator. As a result, polonium is retained in the LBE coolant during normal operating conditions and can cause problems only if coolant leakage occurs. However, some polonium migrates to the cover gas in the reactor plenum and will diffuse outside the primary system when the reactor is opened for refueling and maintenance. Studies within the framework of the Los Alamos National Laboratory accelerator-driven facility project (Li et al. 1998) indicate that exposure of plant personnel to polonium can be maintained within tolerable limits even in the event of a massive release of the cover gas or coolant into the reactor room. Nevertheless, ^{210}Po will limit access to the surfaces on which it deposits, thus increasing maintenance costs and/or collective doses. Considerable experience in dealing with polonium-related issues has been gained in the past 30 years in Russia where several submarines were equipped with LBE-cooled nuclear reactors (Pankratov et al. 1992, Zrodnikov et al. 1999). A polonium technology was developed including special polonium filters for air cleaning, polonium-adsorbing adhesive films for decontamination of large surfaces, special respirators, and pressurized suits for maintenance of contaminated areas (Pankratov et al. 1992).

The polonium hazard (source term) can be significantly reduced by continuous online extraction from the reactor coolant because the rate of polonium release under any circumstances is proportional to its concentration in the LBE melt. Even small rates of extraction can result in a considerable reduction of the polonium concentration in the lead-bismuth, as shown in Figure 5.1 for a typical LBE-cooled fast reactor at several different fast flux levels (core and reactor pool characteristics from Buongiorno et al. 2001). However, it should be emphasized that, despite the construction of several submarine LBE reactors in the former Soviet Union, there is no industrially established and proven polonium extraction technology. The development of such technology is one of the objectives of this project.
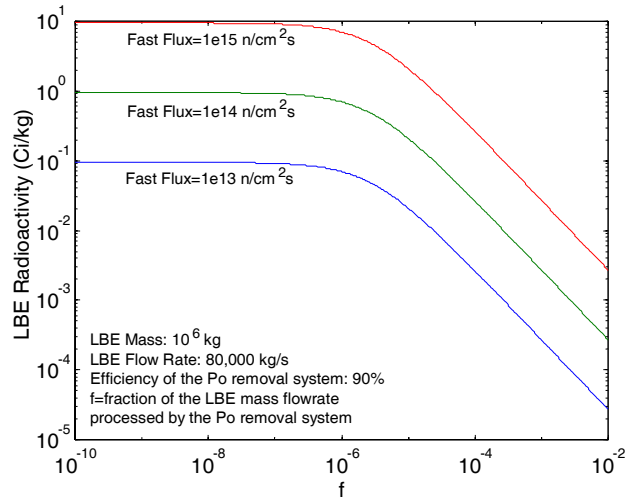
Figure 5.1. Effect of polonium extraction on the LBE radioactivity.

When generated in LBE, polonium forms a rather stable compound with lead, known as lead polonide, PbPo (Feuerstein et al. 1992, Gromov et al. 1996). Four chemical/physical mechanisms of PbPo removal from the LBE are being explored in this project:

1) <u>Polonium Hydride Stripping</u>. Formation of the volatile polonium hydride from the reaction of hydrogen gas with polonium-contaminated LBE:

$$PbPo + H_2 \rightarrow H_2Po + Pb \qquad (5.2)$$

2) <u>Formation of Rare-Earth Polonides</u>. Removal of polonium by formation of solid polonide species with Praseodymium or Thulium, e.g.,

$$PbPo + Pr \rightarrow Pb + PrPo \qquad (5.3)$$

3) <u>Alkaline Extraction</u>. Formation and separation of sodium polonide, Na_2Po, from the reaction of molten sodium hydroxide with polonium contaminated LBE:

$$PbPo + 4NaOH \leftrightarrow Na_2Po + Na_2PbO_2 + 2H_2O \qquad (5.4)$$

4) <u>Electro-deposition</u>. Deposition of polonium induced by the application of an electric field according to the following set of reactions:

$$PbPo \leftrightarrow Pb^{2+} + Po^{2-} \text{ (in LBE)} \qquad (5.5)$$
$$Po^{2-} \rightarrow Po + 2e^- \quad \text{(at the anode)} \qquad (5.6)$$
$$Pb^{2+} + 2e^- \rightarrow Pb \quad \text{(at the cathode)} \qquad (5.7)$$

The work on Mechanisms 1 and 2 was performed at MIT and is summarized in Section 5.1, while work on Mechanism 3 was performed at the INEEL and is summarized in Section 5.2. Electro-deposition (Mechanism 4) will be addressed at the INEEL in FY-2003.

5.1. Polonium Hydride Stripping and Formation of Rare-Earth Polonides (C. Larson, MIT)

Experiments on the removal of Po from a LBE melt were performed using two methods, hydride formation and sorption to lanthanides. For the hydride formation, kinetics as a function of temperature and H_2 concentration were examined. The lanthanide examined for sorption was Pr. The experiments were performed in a Parr pressure vessel using LBE containing activated Bi. The concentration of Po was determined using liquid scintillation counting and alpha spectroscopy. The use of the experimental results in a small scale Po extraction system is presented.

5.1.1. Kinetics of H₂Po Formation

In order to fully understand the chemical interactions between PbPo and H_2Po, experiments were performed to determine the release rate of Po for varying temperatures and concentrations of H_2 in an H_2-Ar gas mixture. Experiments were performed at 425°C and at 500°C, with concentrations of H_2 in the H_2-Ar gas mixture of 0, 1000, 5000, 10,000, 20,000, and 40,000 ppm H_2. Data was taken at time intervals of 5, 15, 30, 60, and 120 minutes. Experiments involving pure Ar gas were performed under a pressure of 1.0 MPa, while those with a mixture of Ar and H_2 were performed under a pressure of 0.4 MPa. The concentration of Po was evaluated using alpha spectroscopy or scintillation counting.

The relevant chemical and physical equations are used to find the equilibrium constants for the formation of H_2Po. Using the equilibrium constants from the reactions of PbPo with H_2O vapor and Pb with H_2O vapor, the equilibrium constant for the reaction in Equation 5.2, is found to be:

$$k = e^{-\frac{\Delta G(T)}{RT}} = \frac{[H_2Po][Pb]}{[PbPo][H_2]} = \frac{P'_{H2Po}a_{PbO}}{C_{PbO}P'_{H2O}} \tag{5.8}$$

with a Gibbs free energy of formation of:

$$\Delta G(T) = -7.56 + 0.074 \cdot T \tag{5.9}$$

The alpha activity in the Po traps is related to the Gibbs free energy. Using Raoult's Law and the molar fraction of H_2 in the H_2-Ar gas mixture, the following equation can be derived to determine the amount of H_2Po at equilibrium for a given temperature and mixture of H_2-Ar:

$$N_{H2Po} = \frac{C_{Po}}{\lambda_{dec}N_{av}}x_{H2}k\frac{V}{RT}(P_i - P_f) \tag{5.10}$$

The amount of H_2Po in the gaseous phase at equilibrium can be found using the experimentally determined activity due to Po and PbPo and the following equation:

$$[H_2Po]_g = [Po]_g + [PbPo]_g \tag{5.11}$$

The concentrations of the gaseous H_2Po and PbPo ($[Po]_{total}$) with respect to time are shown in Figure 5.2 and the concentration of the Po as a function of the concentration of the H_2 is shown in Figure 5.3.

As is evident from Figures 5.2 and 5.3, the total concentration of gaseous Po increases with increasing amounts of H_2, while more gaseous Po is formed at lower temperatures. From these concentrations, the kinetic constants of Equation 5.8 can be evaluated. Table 5.1 summarizes the results of the kinetic experiments, while Figures 5.4, 5.5 and 5.6 graphically represent the characteristics of the kinetic constants.
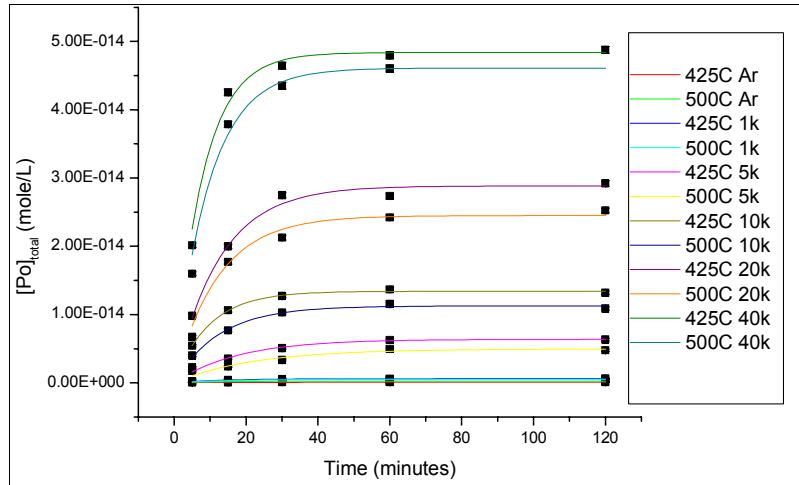
Figure 5.2. Concentration of Po vs. time for various [H₂] and temperature. The gases are argon (Ar), and different Ar gas mixtures with H₂ in ppm listed as k for 1000.
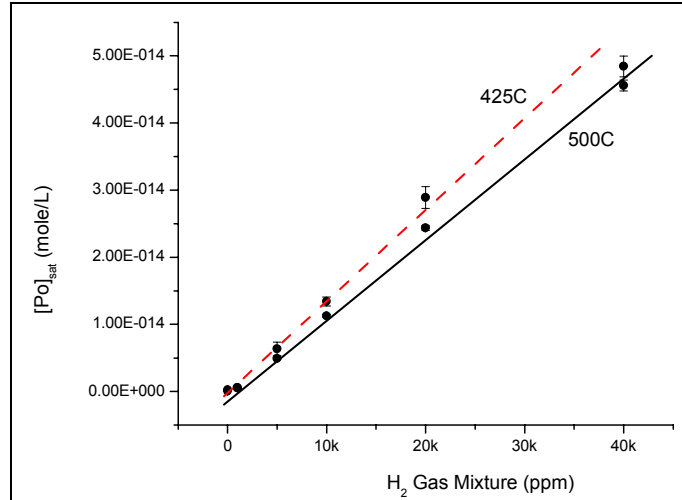
Figure 5.3. Concentration of Po vs. concentration of H_2.

Table 5.1. Concentrations and kinetic constants for formation of PbPo and H_2Po.

Temperature/ Gas Mixture	[Po]$_{max}$ (Obs.) (mol/L)	k_{H2Po} (M^{-1}*min^{-1})	R^2
425°C/Argon	8.703E-17	0.05185	0.961
425°C/1000ppm H_2	5.934E-16	0.07052	0.995
425°C/5000ppm H_2	6.346E-15	0.05824	0.983
425°C/10,000ppm H_2	1.340E-14	0.10382	0.847
425°C/20,000ppm H_2	2.892E-14	0.07720	0.968
425°C/40,000ppm H_2	4.844E-14	0.12228	0.916
500°C/Argon	2.421E-16	0.07551	0.984
500°C/1000ppm H_2	5.162E-16	0.06605	0.986
500°C/5000ppm H_2	4.919E-15	0.04664	0.966
500°C/10,000ppm H_2	1.125E-14	0.08017	0.970
500°C/20,000ppm H_2	2.438E-14	0.08556	0.983
500°C/40,000ppm H_2	4.560E-14	0.10517	0.980
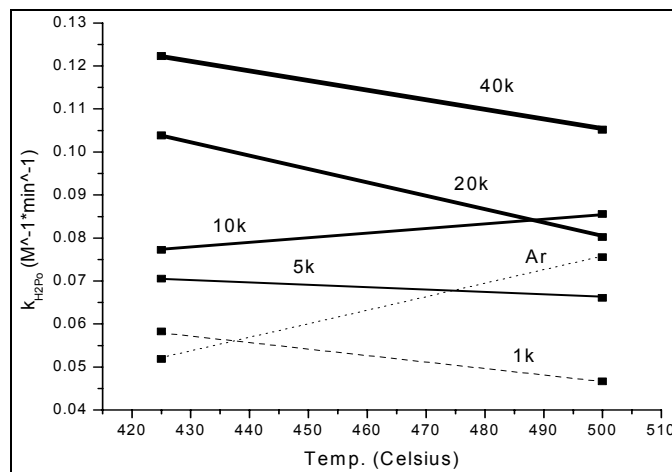
Figure 5.4. k_{H2Po} vs. temperature for various H_2-Ar gas mixtures.

191

Figure 5.4 shows the rate of release of H_2Po. It is obvious from the figure that the rate of release of H_2Po is faster with larger concentrations of H_2 and lower temperatures, except for pure Ar and for the gas mixture with $H_2 = 10,000$ ppm. The linear dependence of the kinetic constants of H_2Po is shown in Figures 5.5 and 5.6.
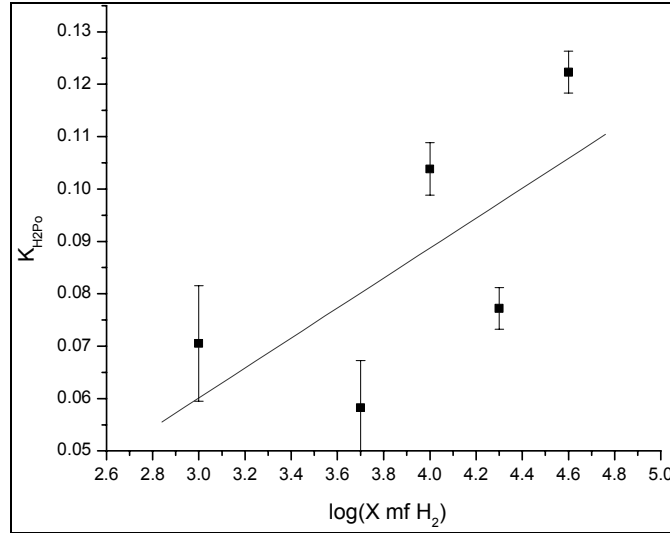
Figure 5.5. k_{H2Po} vs. concentration of H_2 at 425°C.
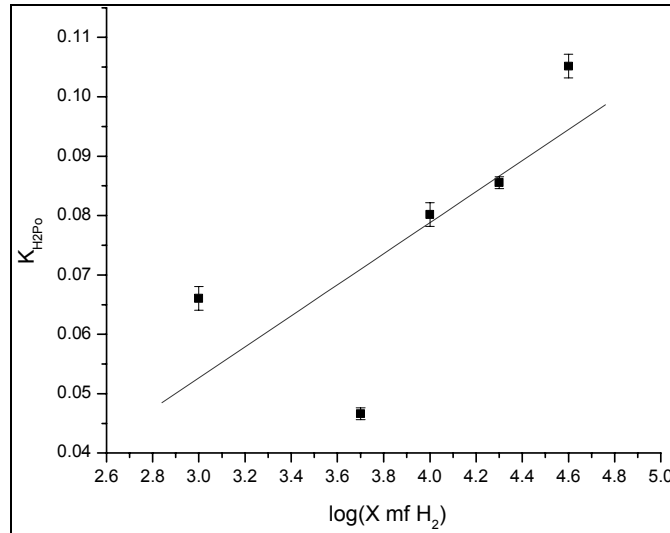
Figure 5.6. k_{H2Po} vs. concentration of H_2 at 500°C.

5.1.2. Interactions of PbPo and Pr

Rare earths form stable complexes with Po, so experiments were performed to evaluate the interaction of Pr with Po in order to remove Po from the LBE. The effect of temperature and oxygen on the sorption of Po to Tm and Pr foils was investigated. Additionally, the amount of Pr

left in the LBE was measured, as Pr has a relatively large capture cross-section and can degenerate the neutron economy of the core.

Initial experiments involved determining the adsorption rate of Po due to interactions of PbPo and Po gases with Pr or Pr_2O_3. Three Pr foils were exposed to PbPo gas for varied amounts of time, under a pressure of 1.4 MPa at 500°C. The resulting Po deposit is shown in Figure 5.7.

From Figure 5.7, it is obvious that the PbPo interacted with Foil #2 more than the other two foils. This is due to the fact that Foil #2 had less oxidation than Foils 1 and 3. This indicates that it is important to limit the exposure of Pr to air due to its rapid oxidation rate. A Pr_2O_3 coating inhibits interaction with Po.
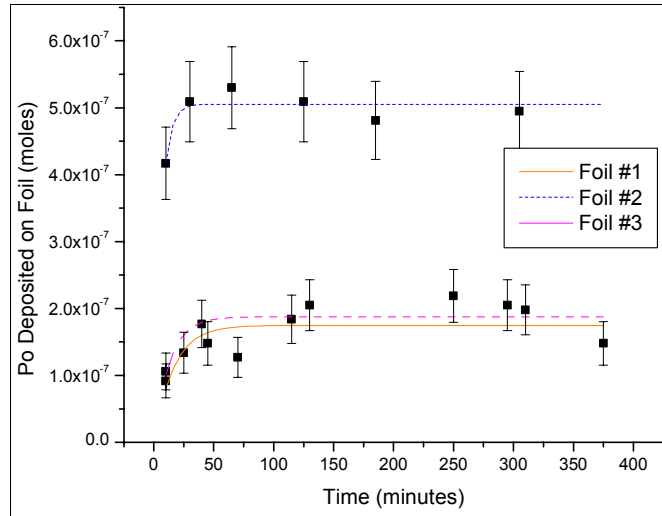

Figure 5.7. Po deposit on Pr foils.

5.1.3. Small-Scale Design of Extraction Systems

The purpose of a Po extraction system is to reduce the alpha-activity emanating from the lead-bismuth coolant. Two methods were evaluated for their performance and ease of reduction of Po in the coolant: an H_2Po mass exchanger and rare earth filtration.

H₂Po Stripping. It is assumed that the LBE is brought to 150°C and 40 atm, and falls against the H_2 stream. Subsequently, it passes through the mass exchanger and is directed back to the reactor pool. H_2 gas leaving the mass exchanger passes through an alkaline aqueous solution that traps the H_2Po. While in theory this system could reduce the amount of Po in the LBE by a factor of ~120, it has inherent dangers that make its use unlikely, namely the H_2 gas.

Rare Earth Filtering. Few technologies have been developed to filter LBE. There are various types of filters that may be employed and are discussed here. Rare earth incorporation into filters could be designed by suspension in a ceramic matrix by liquification or epitaxial growth, or electrodeposition or sputtering onto a fiberglass mesh. Any system must prevent release of the rare earth polonide into the LBE coolant, and any Pb captured in the filter must be reintroduced to the liquid metal. Currently, there are no pure rare earth filters, although forms of rare earths such as rods and foils can be used as filters. Rare earth metals are brittle and form oxide layers that prohibit the formation of polonides. For these reasons, a pure rare earth filter is doubtful.

Fiberglass filters have been utilized by the Russians for LBE filtration, demonstrating their effectiveness as a Po filter. Fiberglass filters can remove impurities with sizes down to 20 microns. Epitaxial growing of Pr_2O_3 films onto silicon has been successful, although the Pr_2O_3 degrades over time and the oxide form does not adequately absorb Po.
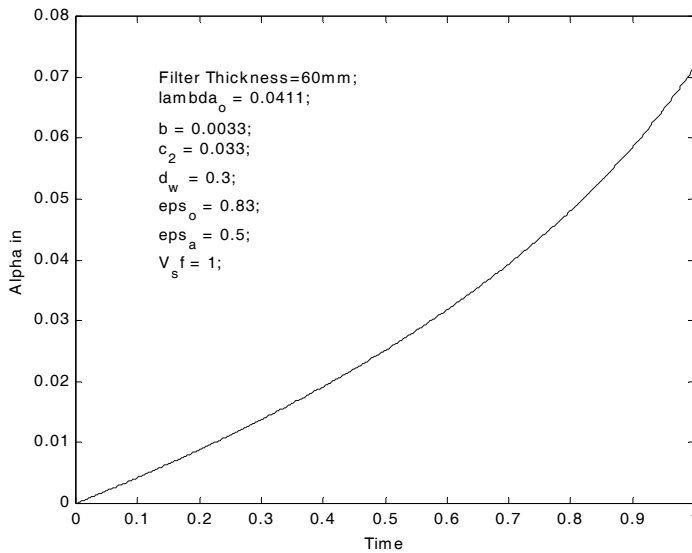
It may be possible to coat the surface of a ceramic filter system with a rare earth metal. This filter has three layers that provide the desired characteristics and performance. It was found that at

high fluid velocity, the probability that particles would attach to the filter increased. Additionally, the high number of particles would increase collisions between particles, which leads to a higher number of particles caught by the filter.

The performance of any given filter depends on the thermo-physical properties of the LBE. Chemical properties of the LBE such as chemical potential, diffusivity of components, and free energy of formation can be used to determine the effectiveness of a Po filter. For a filter with the characteristics in Table 5.2, the resulting Po capture can be estimated. Figure 5.8 shows the deposit of Po on the filter as a function of time. For this filter, the percent of polonium captured is 92%.

Table 5.2. Rare earth filter characteristics.

Parameter	Value
ε (porosity)	0.83
T (°C)	200
R_p (m)	1×10^{-6}
Re	0.1337
F (m^2/s^2)	5.6739
c_{in} ([Po]$_{in}$) (ppm)	10
u_s (m/s)	2
A (m^2)	1
Filter Thickness (mm)	60
Filter Efficiency (%)	92
F	~3030

Filter Thickness=60mm;
lambda$_o$ = 0.0411;

b = 0.0033;
c$_2$ = 0.033;
d$_w$ = 0.3;
eps$_o$ = 0.83;
eps$_a$ = 0.5;
V$_s$f = 1;

Figure 5.8. Estimated specific deposit of Po on filter.

5.2. Alkaline Extraction (J. Buongiorno, INEEL)

The alkaline extraction method was originally proposed by the Russians (Orlov et al. 1998). The reaction of Equation 5.4 occurs when a mass of lead-bismuth contaminated with polonium is put in contact with a NaOH melt. Because the melting point of NaOH is 318°C, the purification system must operate at relatively high temperature. Addition of KOH results in the formation of a low-melting NaOH-KOH eutectic, which would enable operating the system at a lower temperature (down to 250°C). On the basis of chemical similarities between KOH and NaOH and their respective thermodynamic data, it seems reasonable to assume that, if KOH is present, the following reaction will proceed in parallel with the NaOH reaction:

$$PbPo + 4KOH \leftrightarrow K_2Po + K_2PbO_2 + 2H_2O \tag{5.12}$$

However, we started our experimental investigation of alkaline extraction using NaOH only, which requires an operating temperature above >320°C, but enables to conduct a "cleaner" experiment where the effect of NaOH can be isolated.

Note that molten lead-bismuth (which acts as the polonium host metal) does not participate in the chemical reaction (Yefimov et al. 1998). The reaction was found to change with the concentration of oxygen and oxides in the lead-bismuth coolant, being enhanced at low concentrations and vice versa, probably due to kinetic reasons. Therefore, our experiments were performed in a reducing environment.

The Russians have not published detailed information on this polonium removal technology, and several issues are still open:

- The basic chemical characteristics of the alkaline extraction reaction are largely unexplored outside of Russia. These include the polonium removal efficiency as a function of the main process variables (e.g., temperature, polonium concentration, LBE/NaOH contact time), and the reaction equilibrium constant.
- The effect of alkaline extraction on the LBE quality (i.e., oxygen and oxides activity, residual impurity concentration) has not been quantified.
- A material that can safely contain high-temperature LBE and NaOH without affecting the reaction of interest needs must be determined or developed.

5.2.1. Justification of Tellurium as a Polonium Surrogate

There are no stable isotopes of polonium. Therefore, to meet the LDRD budget constraints on this project and to maximize the usage of existing facilities (which are not licensed for work with radioactive materials), it was decided to prove the feasibility of alkaline extraction using a stable chemical surrogate of polonium. Tellurium was identified as the most suitable metallic surrogate since:

- Tellurium and polonium are both Group VI elements.
- They are both solid and metallic at room temperature and pressure.
- Their most stable oxidation state is +4.
- Their atomic radii are comparable, i.e., 1.43 and 1.65 Å for Te and Po, respectively.
- There are similarities in their electrochemical behavior as indicated by their pH-potential diagrams, (Pourbaix 1966).

A key characteristic of polonium is that, when mixed with lead or bismuth, it forms relatively stable intermetallic compounds, i.e., PbPo with lead and Bi_2Po_3 with bismuth (Feuerstein et al. 1992, Gromov et al. 1996). Moreover, if both lead and bismuth are present, it preferentially forms PbPo (Yefimov et al. 1998), i.e., PbPo is more stable than Bi_2Po_3. Similarly, tellurium forms two intermetallic compounds with lead and bismuth (i.e., PbTe and Bi_2Te_3), of which the lead-based compound is more stable than the bismuth-based compound, i.e., $\Delta G_{PbTe}= -75$ kJ/mol$_{Te}$ vs. $\Delta G_{Bi2Te3}= -26$ kJ/mol$_{Te}$. As a result, when mixed with lead-bismuth eutectic, tellurium will also preferentially form PbTe. Figure 5.9 shows an SEM photo of the PbTe grains formed when 0.01wt% Te was mixed with LBE. The SEM is capable of providing the chemical composition of the grains, which were 49 at% Te, 51 at% Pb, 0 at.% Bi, i.e., practically the very definition of

PbTe. Therefore, the analogy between PbTe and PbPo is established, and it can be assumed that the alkaline extraction reaction for tellurium is:

$$PbTe+4NaOH \leftrightarrow Na_2Te+Na_2PbO_2+2H_2O \qquad (5.13)$$

Further, the solid PbTe and PbPo crystals share similar structures (i.e., the face-centered cubic structure typical of NaCl crystals) and lattice pitch, i.e., 6.34 and 6.59 Å, respectively (Bagnall 1966, Witteman et al. 1960). Furthermore, Na_2Po and Na_2Te, which are the products of reactions 5.4 and 5.13 respectively, also present similar characteristics. They share the same CaF_2-type crystalline cubic structure and comparable lattice pitch, i.e., 7.31 and 7.47 Å for Na_2Po and Na_2Te, respectively (Bagnall 1966).
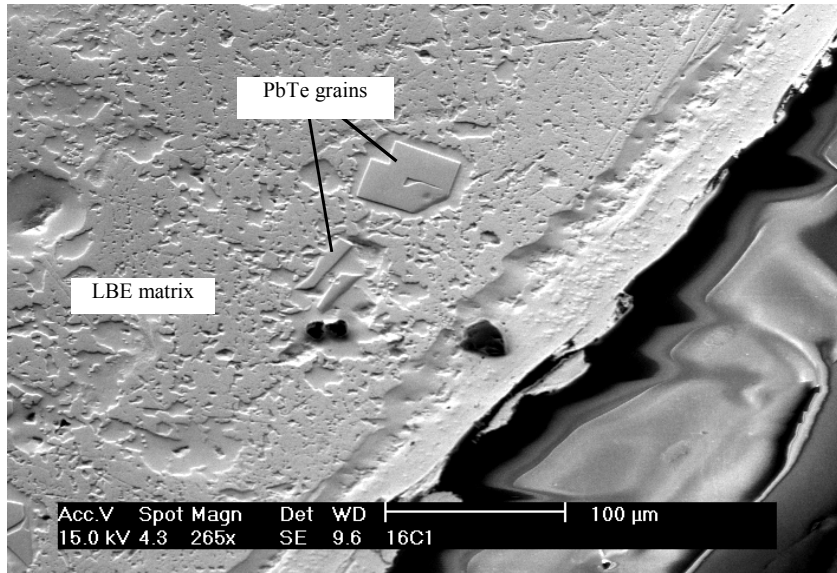
Figure 5.9. PbTe grains in LBE.

Finally, it should be emphasized that the scientists at the IPPE research center in Obninsk, Russia, also used tellurium in lieu of polonium for alkaline extraction experiments (Yefimov et al. 1998, Pankratov 2001) to reduce experimental cost and speed research efforts. A schematic of their apparatus is illustrated in Figure 5.10. Controlled quantities of molten LBE with known concentrations of tellurium were dropped (under inert gas atmosphere) in a NaOH bath at temperatures between 250 and 480°C, and then analyzed for residual tellurium. The specific data from these experiments is

1. Reaction Cell
2. Filter
3. LBE Tank
4. Te dispenser
5. LBE Discharge Tank
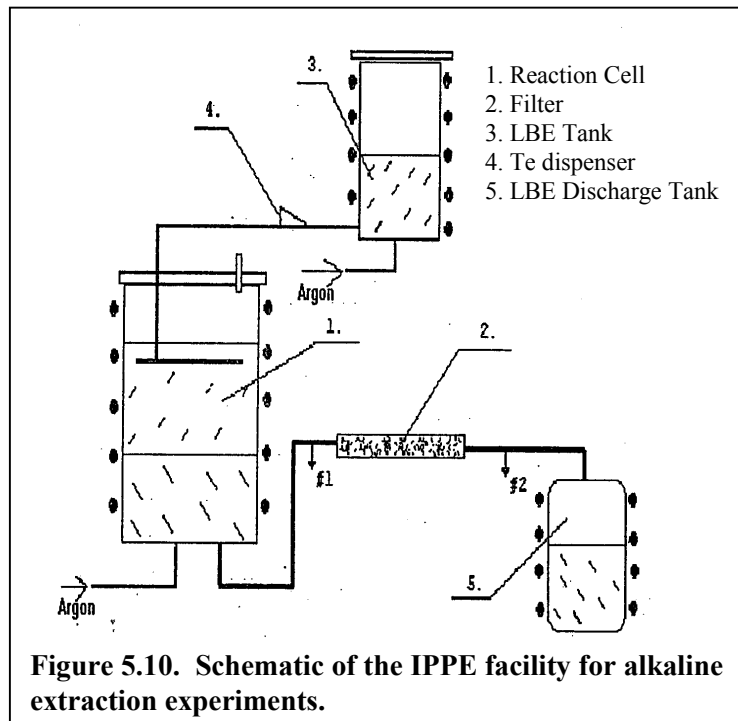
Figure 5.10. Schematic of the IPPE facility for alkaline extraction experiments.

not available in the open literature.

5.2.2. Reaction Cell and Preliminary Results

The reaction cell consists of a standard 10.16-cm (4″) pipe with welded flanges located in a 17.8-cm electric furnace. The cell can accommodate up to 4 crucibles of about 3.8 cm. Several penetrations through the cell top plate provide means of loading and extracting reaction materials prior to and during the experiments, as well as injecting and venting process gases during the experiments. The cell is shown in Figure 5.11.
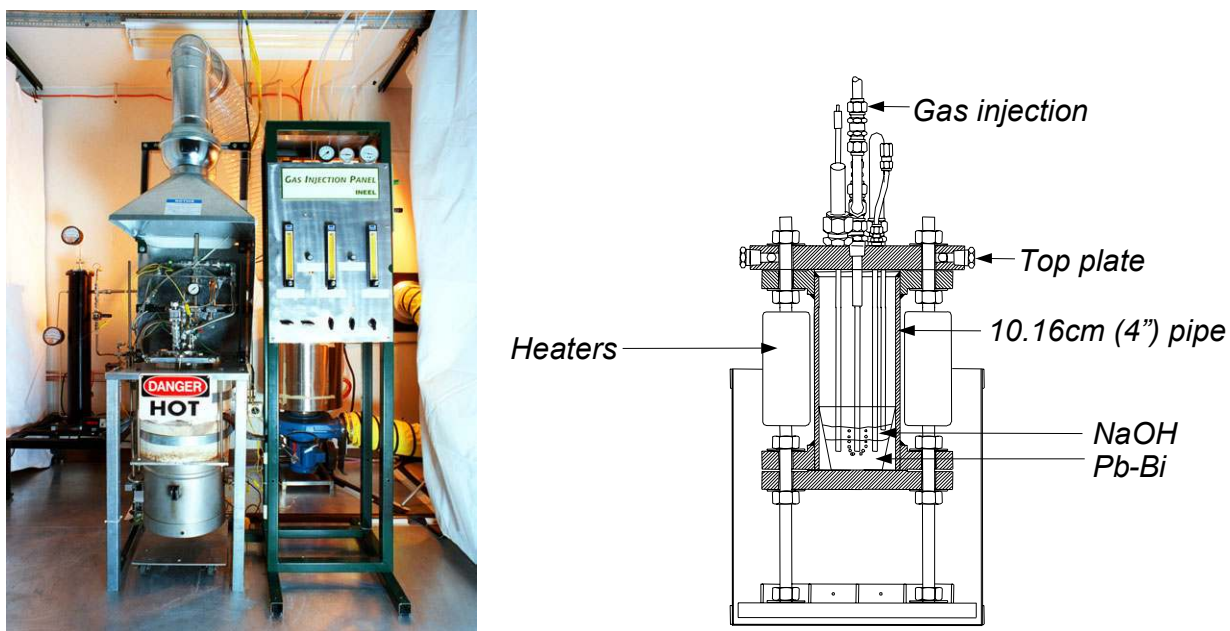
Figure 5.11. The INEEL apparatus for investigation of the alkaline extraction mechanism.

An Inductively Coupled Plasma (ICP) spectrometer was calibrated for analysis of the species of interest, i.e., lead, bismuth, tellurium and sodium. Calibration with samples of known composition demonstrated that the ICP measurements of Te in LBE or NaOH matrix are accurate within ±20%. In addition, a series of high-temperature preliminary experiments were conducted to assess the potential of the alkaline extraction technique and the suitability of two candidate materials for the crucible, i.e., alumina and graphite, which are known for their compatibility with lead and lead-bismuth. A detailed description of the apparatus, the preliminary experiments and the ICP measurement procedures can be found in Buongiorno (2002).

These preliminary experiments provided evidence that alkaline extraction might achieve very high separation efficiencies, *as a reduction of three to four orders of magnitude in the tellurium concentration in the metals was observed during the experiments, i.e., virtually all tellurium initially present in the lead or lead-bismuth melt migrated to the NaOH phase*.

ICP and Scanning Electronic Microscope (SEM) measurements confirmed that both graphite and alumina are completely compatible with the molten metals. However, alumina is severely attacked and embrittled by molten NaOH. Significant, albeit less aggressive, interaction was also

observed between graphite and NaOH. Therefore, these two crucible materials cannot be used in a Po removal system based on alkaline-extraction.

5.2.3. Crucible Materials

Selection of a suitable crucible material is key to ensuring the success of the experiments, and proving the feasibility of a full-scale polonium removal system based on alkaline extraction. Following the failure of graphite and alumina, we identified three candidate materials: nickel, nickel-chromium, and zirconium.

Nickel is known for its resistance to very concentrated NaOH at high temperature, i.e., Nelson (1987) reports a corrosion rate of only 0.23 mm/yr for wrought nickel in molten NaOH at 510°C, an order of magnitude lower than any other metal discussed by Nelson. On the other hand, nickel solubility in LBE is relatively high, i.e., 2.75 wt % at 500°C (Li 1999). Because our reaction cell is not a flow system, it was anticipated that the LBE in the crucible would rapidly saturate with nickel, and further dissolution of the crucible would not occur. However, high concentrations of nickel in the melt could affect the alkaline reaction. Therefore, attention was also given to nickel-chromium alloys (i.e., Inconel 600). Chromium, which has a much lower solubility in LBE (i.e., 10 wt ppm at 500°C, as reported by Li 1999), is key to minimizing the corrosion of ferritic steels in high-temperature molten LBE, as it forms a compact protective oxide layer (He et al. 2001). We expected that in a Ni-Cr alloy, nickel would provide resistance to the NaOH corrosion, while chromium would minimize dissolution of the crucible in the LBE. Good resistance of zirconium (Alloy 705) to corrosion by molten lead was observed in recent 100-hour experiments performed at the INEEL at temperatures up to 500°C (Loewen and MacDonald 2001). Moreover, a corrosion rate of 2.8 mm/yr is reported by Nelson (1987) for zirconium in molten NaOH at 540°C. While this corrosion rate would not be acceptable for long experiments, we deemed it acceptable for our relatively short experiments, i.e., <24 hours.

To evaluate the performance of these three materials, simple compatibility experiments with molten LBE and NaOH at high temperature were conducted. Crucibles of nickel, nickel-chromium, and zirconium containing LBE and NaOH were held at 500°C for 8 hours and then analyzed with the SEM. It was found that the most compatible material is zirconium, which exhibits little interaction with LBE and NaOH at that temperature, as illustrated in Figure 5.12. Zirconium is effectively protected by a thin compact zirconium-oxide layer. These results were confirmed by the ICP analysis
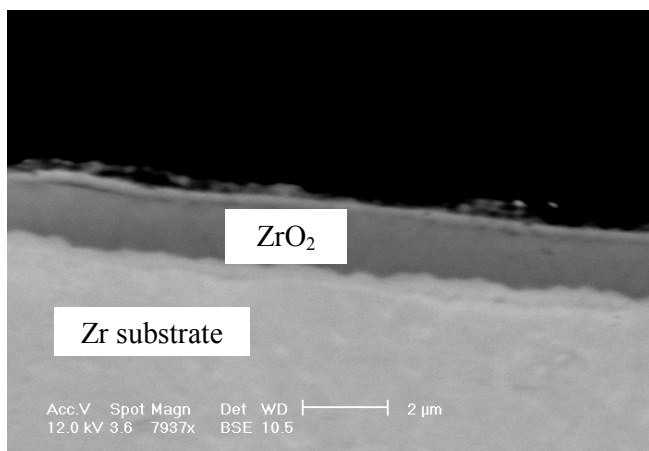
Figure 5.12. The Zr crucible surface.
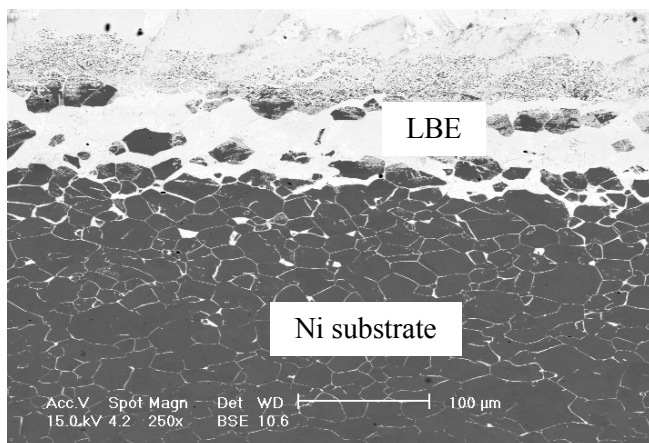
Figure 5.13. The nickel crucible surface.

revealing below-detection-limit zirconium concentrations in the LBE and NaOH melt. On the other hand, the nickel showed severe intergranular penetration by LBE (Figure 5.13), and nickel-chromium had a relatively thick interaction layer (Figure 5.14).
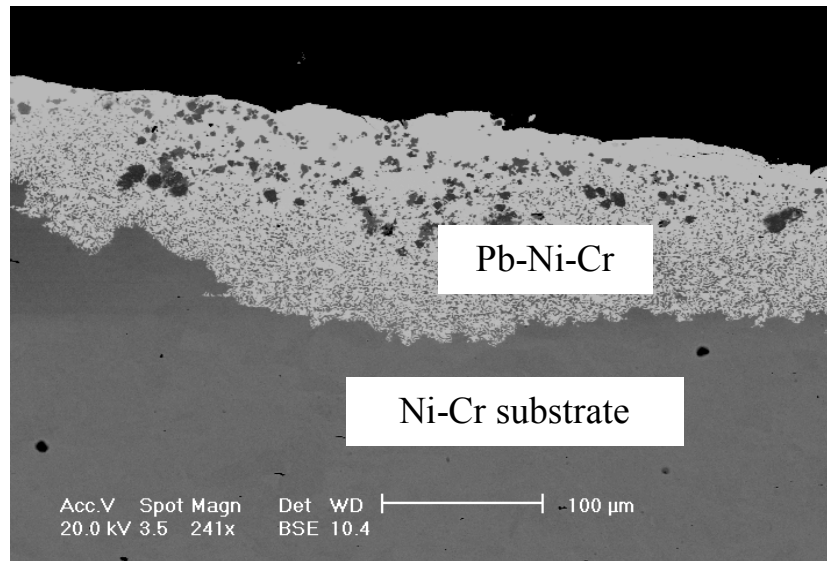
Figure 5.14. The Ni-Cr crucible surface.

5.2.4. Conclusions

During FY-2002 the reaction cell was constructed and tested. Several candidate materials for the crucible were tested and it was found that zirconium is the most compatible for operation in molten LBE and NaOH at temperatures around 500°C. The first experiments with tellurium indicate that alkaline extraction has a high potential for effective removal of tellurium from LBE. We are now ready to conduct the experiments with systematic variation of the important reaction parameters (e.g., temperature and initial tellurium concentration).

7. References

- Abdelrahman M.S. and Abdurrahman N.M., "UTXS: The University of Texas Neutron Cross Section Library: Generation and Validation," *Transactions of the American Nuclear Society*, Vol. 79, November 1998.
- Abramov, O.V., *Ultrasound in Liquid and Solid Metals*, CRC Press, Boca Raton, Florida, 1994.
- Adamov, A., et al, "Conceptual Design of Brest-300 Lead-Cooled Fast Reactor", RDIPE, Moscow, Russia, 1994.
- Anderko, K., *Constitution of Binary Alloys, Second Edition*, McGraw-Hill Book Co., New York, New York, pp. 178-180, 1958.
- ASME, 2001, *Rules for Construction of Nuclear Facility Components*, Vol. III, Division 1 - Appendices, July 1 2001.
- Bagnall, K., *The Chemistry of Selenium, Tellurium and Polonium*, Elsevier Publishing Company, 1966.
- Baker, R.S. and Tessier, M.J., *Handbook of Electromagnetic Pump Technology*, Elsevier Applied Science Publishing Co., Inc., Essex, England, 1987.
- Ballinger, R., Personal Communication, 15 April 2002.
- Beller D.E. et. al., "The U.S. Accelerator Transmutation of Waste Program," *Nuclear Instruments and Methods in Physics Research*, A 463 ,pp. 468-486, 2001.
- Boardman, C. E., A. E. Dubberly, D. G. Carroll, M. Hui, A. W. Fanning, and W. Kwant, "A Description of the S-PRISM Plant," ICONE-8168, *Proceedings of ICONE-8, Baltimore, Maryland*, April 2-6 2000.
- Boardman, C.E., 10 November 2001, Personal Communication.
- Branover, H., "Liquid Metal MHD Research and Development in Israel". Proceedings of the 1992 Symposium on Engineering Applications of MHD. Baltimore. June-July 1992.
- Briesmeister, J. F., Ed., *MCNP^{TM} - A General Monte Carlo Code N-Particle Transport Code, Version 4C*, Los Alamos National Laboratory, LA-13709-M, April 2000.
- Briesmeister, J. F., Ed., *MCNP - A General Monte Carlo Code for Neutron, Photon and Electron Transport, Version 3A/3B/4A/4B*, Los Alamos National Laboratory, LA-7396-M, 1986, Revised in 1988, 1991 and 1997.
- Buongiorno, J., "Conceptual Design of a Lead-Bismuth Cooled Fast Reactor with In-Vessel Direct-Contact Steam Generation", MIT PhD Thesis, 2001.
- Buongiorno, J. et al., *Conceptual Design of a Lead-Bismuth Cooled Fast Reactor with In-Vessel Direct-Contact Steam Generation*, Nuclear Engineering Department, MIT, Technical Report MIT-ANP-TR-079, 2001.
- Buongiorno, J., *Investigation of Polonium Removal Systems for Lead-Bismuth Cooled FBRs*, Idaho National Engineering and Environmental Laboratory, INEEL/EXT-2002-351, 2002.
- Carlson, K. E., P. A. Roth, and V. H. Ransom, *ATHENA Code Manual Vol. I: Code Structure, System Models, and Solution Methods*, EGG-RTH-7397, September 1986.
- Cho, S. M., H. L. Chou, and J. F.Cox, "Thermal-Hydraulic Design of A Supercritical, Once-Through Steam Generator for the Molten-Salt Breeder Reactor Plant", ASME paper JPGC-NE-9, 1976.
- Cohen, H., C. F. G. Rogers, H. I. H.Saravanamuttoo, *Gas Turbine Theory, 3rd edition, 5th Impression*, Longman Scientific & Technical, Co-published in the United States with John Wiley & Sons, Inc., New York, 1991.
- Corradini, M., Personal Communication with J. Buongiorno, September 2002

- Crawford, D. C., et al., "Large-Diameter, High-Plutonium Metallic Fuel Testing in EBR-II", *Transactions of the American Nuclear Society*, Vol.71, pp.178-179, 1994.
- Croff, A. G., *A User's Manual for the ORIGEN2 Computer Code*, Oak Ridge National Laboratory, ORNL/TM-7175, 1980.
- Davis, C. B., "Assessment of the ATHENA Code for Calculating the Void Fraction of a Lead-Bismuth/Steam Mixture in Vertical Upflow," *Nuclear Technology*, pp. 187-193, February 2001.
- Dean, J.A., editor, *Lange's Handbook of Chemistry: 15th Edition*, McGraw-Hill Handbooks, New York, 1999.
- Delene, et al., "Nuclear Energy Cost Data Base," DOE/NE-0095, 1988.
- Delene, J.G., and Hudson, C.R., "Cost Estimate Guidelines for Advanced Nuclear Power Technologies," ORNL/TM-10071/R3, 1993.
- Dostal, V., Personal Communication, 26 November 2001.
- Dostal, V., et al, "Plant Design and Cost Assessment of Forced Circulation Lead-Bismuth Cooled Reactors with Conventional Power Conversion Cycles", MIT-ANP-TR-082, 2001.
- Dostal, V., et al, "A Supercritical CO_2 Gas Turbine Power Cycle for Next-Generation Nuclear Reactors", ICONE10-22192, 10th International Conference on Nuclear Engineering, Arlington, Virginia, USA, 2002.
- Driscoll, M.J. and Kim, D., "The Need for Actinide Burner Reactor Fuel Cycle Cost Reduction," Transactions of the American Nuclear Society, Vol. 82, June 2000.
- Dostal, V., N. E. Todreas, P. Hejzlar, and M. S. Kazimi, *Power Conversion Cycle Selection for the LBE Cooled Reactor with Forced Circulation*, MIT-ANP-TR-085, February, 2002a.
- Dostal, V., M. J. Driscoll, P. Hejzlar, N. E. Todreas, "CO_2 Brayton Cycle Design and Optimization", MIT-ANP-TR-090, October, 2002b.
- Driscoll M.J. and Kim D., "The Need for Actinide Burner Reactor Fuel Cycle Cost Reduction," *Transactions of the American Nuclear Society*, Vol. 82, June 2000.
- Dunn F.E. et al., "The SASSYS-1 LMFBR Systems Analysis Code," *Proc. of Int. Meeting on fast Reactor Safety, Knoxville, Tennessee*, p. 999, 1985.
- El-Boher, A., S. Lesin, Y. Unger, H. Branover, "Experimental Studies of Liquid-Metal Two-Phase Flows in Vertical Pipes", *Proceedings of the 1st World Conference on Experimental Heat Transfer, Fluid Mechanics and Thermodynamics*, Dubrovnik, Yugoslavia, September 1988.
- Eriksson M. and Piaszczyk C., "Reliability Assessment of the LANSCE Accelerator System," NEA/OECD Workshop on Utilization and Reliability of High Power Accelerators in Mito, Japan, 13-15 October 1998.
- Feuerstein, H. et al., "Behavior of Po-210 in Molten Pb-17Li", *Journal of Nuclear Materials* 191-194, pp.288-291, 1992.
- Foust, O.J., 1976, "The Sodium-NaK Engineering Handbook: Volume 2" Gordon and Breach, New York.
- Forsberg C.W., Hopper C.M. and Vantine H.C., "What is Nonweapons-Usable U-233?" *Transactions of the American Nuclear Society*, Vol. 81, p. 62, Long Beach, California, November 14-18, 1999.
- Furuya, M., I. Kinoshita, Y. Nishi. "Vapor Explosions in the System of Water Droplet Impinging onto Melt Surface". Heat Transfer – Houston 1996. AIChE Symposium Series. Vol.92, n.310. pp.310-316. 1996.
- Generation IV Roadmap, "Report of the Fuel Cycle Crosscut Group (FCCG)", March 2002.
- GE, *PRISM, Preliminary Safety Information Document*, Vol. II, Chapter 5, page 5.4-34, 1986.

- Gokcek, O., et al., eds., "1994 ALMR Capital and Busbar Cost Estimates," GEFR-00940 UC-87Ta, 1995.
- Gromov, B.F., et al, "Nuclear Power Plants With Lead-Bismuth Coolant", Atomic Energy, Volume 8, No. 5, 1996.
- Gromov, B. F. et al., "Liquid-Metal Lead-Bismuth Target for High-Energy Protons as an Intense Source of Neutrons Controlled Systems", *Atomic Energy*, Vol.80, No.5, pp.378-384, 1996.
- He, Xiaoyi, Ning Li, and Mark Mineev. "A kinetic model for corrosion and precipitation in non-isothermal LBE flow loop*". Journal of Nuclear Materials,* Vol. 297, pp. 214-219, 2001.
- HEATRIC, Heatric official web page, www.heatric.com, 2002.
- Hejzlar, P., M. J. Driscoll and M. S. Kazimi, *Conceptual Reactor Physics Design of a Lead-Bismuth-Cooled Critical Actinide Burner*, Topical Report MIT-ANP-TR-069, Massachusetts Institute of Technology, Dep. of Nuclear Eng., January 2000.
- Hejzlar P., Driscoll M.J. and Kazimi M.S., "Conceptual Neutronic Design of a Lead-Bismuth-Cooled Actinide Burning Reactor," *Nuclear Science and Engineering*, Vol. 139, pp.1-18, 2001.
- Henry, R. E., J. D. Gabor, I. O. Winsch, D. J. Quinn, E. G. Erickson, J. J. Heiberger, G. T. Goldfuss. "Large Scale Vapor Explosions". Proc. Fast Reactor Safety Meeting, Argonne IL, Conf. 740 401-P2, p.922. 1974.
- Henry, R. E., H. K. Fauske. "Energetics of Vapor Explosions". Am. Soc. Mech. Eng. Paper 75-HT-66. 1975.
- Henry, R. E., L. M. McUmber. "Vapor Explosion Potential under LWR Hypothetical Accident Conditions". Proc. Light Water React. Saf. Meet., CONF-770708, p.414-425. Sun Valley, Idaho. 1977.
- Henry, R. E., "Test Plan: Large Scale Molten Salt-Water Vapor Explosion Studies to be Conducted at Ispra, Italy". NUREG/CR-0728, ANL-79-20. Argonne National Laboratory. 1978.
- Hesselgreaves, J. E., *Compact Heat Exchangers, Selection, Design and Operation*, 1st Edition, Pergamon, 2001.
- Hill R.N., Wade D.C. Liaw J.R. and Fujita E.K., "Physics Studies of Weapons Plutonium Disposition in the Integral Fast Reactor Closed Fuel Cycle," *Nuclear Science and Engineering,* Vol. 121, pp. 17-31, 1995.
- Hill R.N., Cahalan J.E., Khalil H.S. and Wade D.C., "Development of Small, Fast Reactor Core Design Using Lead-Based Coolant," *Proc. Global '99 Int. Conf. on Future Nuclear Systems, Jackson Hole, WY*, August 1999.
- Hunsbedt, A. and P. M. Magee, "Design and Performance of the PRISM Natural Convection Decay Heat Removal System," *Proceedings of the International Topical Meeting on Safety of Next Generation Power Reactors*, Seattle, Washington, May 1-5, 1988.
- Ilincev, G., "Research results on the corrosion effects of liquid heavy metals Pb, Bi and Pb-Bi on structural materials with and without corrosion inhibitors", *Nuclear Engineering and Design*, Vol. 217, pp. 167-177, 2002.
- Kakaç, S. and Yener, Y., *Convective Heat Transfer*, II Edition, CRC Press, Boca Raton, 1995.
- Kakaç, S. and Liu, H., *Heat Exchangers: Selection, Rating, and Thermal Design*, CRC Press, Boca Raton, Florida, 1998.
- Kang, C.M. and Mosteller R.O., "Incorporation of a Predictor-Corrector Depletion Capability into the CELL-2 Code," *Transactions of the American Nuclear Society*, Vol. 45, pp 729-731, 1983.

- Karasawa, et al., "Development of Under-Sodium Three-Dimensional Visual Inspection Technique Using Matrix-arrayed Ultrasonic Transducer," *Journal of Nuclear Science and Technology*, Vol. 37, No. 9, 2000.
- Karassik, I. J., et al, *Pump Handbook: Third Edition*, McGraw-Hill, New York, 2001.
- Kataoka, I. and M. Ishii, "Mechanistic Modeling of Pool Entrainment Phenomenon," *International Journal of Heat and Mass Transfer*, Vol. 27, No. 11, pp. 1999-2004, 1984.
- Kays, W.M., and London, A.L., *Compact Heat Exchangers: Second Edition*, McGraw-Hill Book Company, New York, 1964.
- Kim, D., et al, "Plant Design and Cost Estimation of a Natural Circulation Lead-Bismuth Reactor with Steam Power Conversion Cycle", MIT-ANP-TR-074, 2000.
- Kim D., Kazimi M.S., Todreas N.E., Driscoll M.J., *Economic Analysis of the Fuel Cycle of Actinide Burning Systems*, Topical Report MIT-NFC-TR-019, MIT, Dep. of Nuclear Engineering, February 2000.
- Kočiš, Š., and Figura, Z., *Ultrasonic Measurements and Technologies*, Chapman & Hall, London, 1996.
- Komai, M., Personal Communication. (masafumi.komai @toshiba.co.jp), 15 April 2002.
- Kuppan, T., *Heat Exchanger Design Handbook*, Marcel Dekker, Inc., New York, 2000.
- LaGuardia, T.S., "Nuclear Power-Reactor Decommissioning", *Nuclear Safety*, Vol. 20, No. 1, pp.15-23, January-February 1979.
- Lefevre, J.C., Personal Communication, 15 October 2001.
- Lefhalm, C. H., J. U. Knebel, and K. J. Mack, *J. Nucl. Mater.* Vol. 296, pp. 301-304, 2001.
- Li, N. et al., *Polonium Release from an ATW Burner System with Liquid Metal Lead-Bismuth Coolant*, LA-UR-98-1995, Los Alamos National Laboratory. (1998)
- Li, N., *Active Control of Oxygen in Molten Lead-Bismuth Eutectic Systems to Prevent Steel Corrosion and Coolant Contamination*, LA-UR-99-4696, Los Alamos National Laboratory. (1999)
- Li, Ning, LANL, personal communication with R, Herron, 2001.
- Li, N., *J. Nucl. Mater*. 300 (2002) 73-81.
- Loewen, E. P., and P. E. MacDonald, "Heavy Metal Coolant Corrosion Testing Using a Gas Lift Apparatus", *Transactions of the American Nuclear Society*, Vol. 85, 2001a.
- Loewen, E.P., and P.E. MacDonald, "Corrosion of Zr, 316, 410SS, F-22, and HT-9 Exposed to High Temperature Heavy Metal Coolant Under Extreme Conditions," *Transactions of the American Nuclear Society*, Vol. 85, pp. 296-297, 2001b.
- Lyon, R.N., *Liquid-Metals Handbook*, Navy Press, 1952.
- Mach, E.T., Personal Communication. (machet@westinghouse.com), 15 November 2001.
- MacDonald, P. E. and J. Buongiorno, 2001, *Design of an Actinide Burning, Lead or Lead-Bismuth Cooled Reactor That Produces Low Cost Electricity, FY-01 Annual Report*, INEEL/EXT-01-01376, MIT-ANP-PR-083, October.
- Mitenkov, F. M., et al. "Experience in Construction and Operation of OK-550 RP Equipment" Proceedings for HLMC-98, pp 80-83 (1999).
- Moore R.L., Schnitzler B.G., Wemple C.A., Babcock R.S., and Wessol D.E., *MOCUP: MCNP-ORIGEN2 Coupled Utility Program*, INEL-95/0523, Idaho National Engineering Laboratory, September 1995.
- Muller, G., et al., *J. Nucl. Mater*. Vol. 301, pp. 40-46 (2002).
- Nelson, J. K., "Corrosion by Alkalies and Hypochlorite", *Metals Handbook*, *9th Edition*, Volume 13, pp.1174-1178, ASM International. (1987)
- Oda, R. T., Editor, "ALMR Summary Plant Design Description," GE Nuclear Energy, GEFR-00909, March 1993.

- Oka, Y. and S. Koshizuka, "Design Concept of Once-Through Cycle Supercritical-Pressure Light Water Cooled Reactors," *Proceedings of the First International Symposium on Supercritical Water-cooled Reactors Design and Technology*, 101, University of Tokyo, Japan, 2000.
- Orlov, Y. et al., *LANL/IPPE/EDO-GP Collaboration Programs on Liquid Lead-Bismuth Technology*, Notes of the MIT ATW Technical Review, January 15-16, 1998. (1998)
- Pankratov, D. V. et al., "The Experience in Handling Lead-Bismuth Coolant Contaminated by Polonium-210", *Transactions of the American Nuclear Society*, Vol.67, Supplement No.1. p.256. (1992)
- Pankratov, D. V., "Polonium Problem for the Nuclear Power Installations with Lead-Bismuth Coolant", *Book of Presentations of the Japan-Russia LBE Coolant Workshop* (ISSN 0387-6144), Research Laboratory for Nuclear Reactors, Tokyo Institute of Technology, Tokyo, Feb 22-23, 2001. (2001)
- Park, C. S., and G. P. Sharp-Bette, *Advanced Engineering Economics*, John Wiley & Sons, Inc., New York, 1990.
- Poston D.I. and Trellue H.R., MONTEBURNS 1.0, An Automated, Multi-step Monte Carlo Burnup Code System," PSR-455, RSICC Peripheral Shielding Routine Collection, September 1999.
- Pourbaix, M., *Atlas of Electrochemical Equilibria in Aqueous Solutions*, pp.554-576, Pergamon Press. (1966)
- Royl P. H., Cahalan J.E., Friedel G., Kussmaul G., Moreau J., Perks M., and Wigeland R.A. , "Performance of Metal and Oxide Fuel Cores During Accidents in Large Liquid Metal-Cooled Reactors," *Nuclear Technology*, Vol. 97, February 1992.
- Salvatores M., "Fast Reactor Calculations," in <u>CRC Handbook of Reactors Calculations</u>, CRC Press, Boca Raton, 1986.
- Sekimoto, H., S. Makino, K. Nakamura, Y. Kamishima, and T. Kawakita, 2002, "Small LBE-Cooled Fast Reactor for Expanding Market," ICONE-22049, *Proceedings of ICONE-10*, Arlington, Virginia, April 14-18.
- Sienicky J.J. and Petkov P.V., "Passive Safety of the STAR-LMHLMC Natural Convection Reactor," ICONE10-22290, Proc. of ICONE10 – 10th Internatinal Conference on Nuclear Engineering, Arlington VA, April 14-18, 2002.
- Singh, K.P., and Soler, A.I., *Mechanical Design of Heat Exchangers*, Arcturus Publishers, Inc., Cherry Hill, New Jersey, 1984.
- Smith H.P., "The Relative Significance of Actinide Decay Heat for Nuclear Fuel Characterization," *Transactions of the American Nuclear Society*, Vol. 85, p. 320, Reno Nevada, November 11-15, 2001.
- Smith R.I., Shay M.R., Short S.M., Ehrman C.S., and Meyers T.J., *Estimated Cost of ATW System*, Report PNNL-13018, Pacific Northwest National Laboratory, September, 1999.
- Spencer, B.W., "The Rush to Heavy Liquid Metal Reactor Coolants – Gimmick or Reasoned", *Proceedings of the 8th International Conference on Nuclear Engineering (ICONE8), Baltimore, Maryland*, USA, 2000.
- Stepanoff, A.J., *Centrifugal and Axial Flow Pumps: 2nd Edition*, John Wiley & Sons, Inc., New York, 1957.
- Tentner A.M. et. al., "The SAS4A LMFBR Whole Core Accident Analysis Code," *Proc. of Int. Meeting on fast Reactor Safety, Knoxville, Tennessee*, p. 989, 1985.
- Todreas, N. E., and M. S. Kazimi, *Nuclear Systems I. Thermal Hydraulic Fundamentals,* Hemisphere Publishing Corporation, 1990.
- Tuzson, J., *Centrifugal Pump Design*, John Wiley & Sons, Inc., New York, 2000.
- Wade D.C. and Chang Y.I., "The Integral Fast Reactor Concept: Physics of Operation and Safety," *Nuclear Science and Engineering*, Vol. 100, pp. 507-524, 1988.

- Wade D.C. and Fujita E.K., "Trends Versus Reactor Size of Passive Reactivity Shutdown and Control Performance," *Nuclear Science and Engineering*, Vol. 103, pp. 182-195, 1989.
- Wade D.C. and Hill R.N., "The Design Rationale of the IFR," *Progress in Nuclear Energy*, Vol. 31, pp. 13-42, 1997.
- Wade D.C., R.A. Wigeland and Hill R.N., "The Safety of the IFR," Progress in Nuclear Energy, Vol. 31, pp. 63-82, 1997.
- Waltar A.E. and Reynolds A.B., Fast Breeder Reactors, Pergamon Press, New York, 1981.
- Weeks, J.R., and A.J. Romano. *"Liquidus Curves and Corrosion of Fe, Ti, Zr, and Cu in Liquid Bi-Pb Alloys"*. Corrosion, 25 (1969) 131-136.
- Wigeland R.A., and Moran T.J., "Radial Core Expansion Reactivity Feedback in Advanced LMRs: Uncertainties and their Effects on Inherent Safety," Proc. Conf. on Next Generation Power Reactors, Seattle, Washington, May 1-5, 1986.
- Wigeland R.A., "Effect of Detailed Radial Core Expansion Reactivity Feedback Model on ATWS calculations Using SASSYS/SAS4A," Trans. Am. Nucl. Soc., Vol. 53, p. 303, 1986.
- Wigeland R.A., "Comparison of the SASSYS/SAS4A Radial Core Expansion Reactivity Feedback Model and the Empirical Correlation for the FFTF," Trans. Am. Nucl. Soc., Vol. 55, p. 423, 1987.
- Witteman, W. et al., "The Preparation and Identification of Some Intermetallic Compounds of Polonium", *J. Phys. Chem.*, Vol.64, No.4, pp.434-440. (1960).
- www.eia.doe.gov, Department of Energy website, 2002.
- Xu Z., Hejzlar P., Driscoll M.J., and Kazimi M.S., "An Improved MCNP-ORIGEN Depletion Program (MCODE) and Its Verification for High-Burnup Applications," PHYSOR 2002, Seoul, Korea, October 7-10, 2002.
- Yan, X. L., Lidsky L. M., "Design of Closed-Cycle Helium Turbine Nuclear Power Plants", *International Gas Turbine and Aeroengine Congress and Exposition, Cincinnati, Ohio*, May 24-27, 1993, 93-GT-196
- Yefimov, E. et al., "Removal and Containment of High-Level Radioactive Polonium from Liquid Lead-Bismuth Coolant", *Materials Research Society Symposium Proceedings*, Vol.506, p.679-686. (1998)
- Zhao X., Hejzlar P., and Driscoll M.J., "Comparison of Code Results for PWR Thorium/Uranium Pin Cell Burnup," MIT-NFC-TR-027, Center for Advanced Nuclear Energy Systems, MIT (November 2000).
- Zrodnikov, A. V. et al. "Applications of Reactors Cooled by Lead-Bismuth Alloy in Nuclear Power Energy", *Proceedings of Global '99: International Conference on Future Nuclear Systems*, Jackson Hole, USA. (1999)
- Zrodnikov, A. V., et al., "Multi-Purposed Reactor Module SVBR-75/100", *Proceedings of the 8th International Conference on Nuclear Engineering (ICONE8)*, Baltimore, Maryland, USA, 2001.

Appendix A. Publication History Of The Lead-Cooled Actinide Burning Reactor Project

Theses

- J. Buongiorno, " Conceptual Design of a Lead-Bismuth Cooled Fast Reactor with In-Vessel Direct-Contact Steam Generation," Doctoral Thesis, Dept. of Nuclear Engineering, M.I.T., September 2000.
- R. Herron, *Component Design and Capital Cost Analysis of a Forced Circulation Lead-Bismuth Eutectic Cooled Nuclear Reactor*, Master's Thesis, Dept. of Nuclear Engineering, September 2002.

Topical Reports

- J. Buongiorno, P. Hejzlar, N. E. Todreas, M.J. Driscoll and M.S. Kazimi, "Actinide Transmutation by Lead-Bismuth Cooled Reactors," *MIT-ANP-TR-065*, MIT Nuclear Engineering Dept., June 1999.
- J. Buongiorno, N. E. Todreas and M. S. Kazimi, "Thermal Design of Lead-Bismuth Cooled Reactor for Actinide Burning and Power Production," *MIT-ANP-TR-066*, MIT Nuclear Engineering Dept., July 1999.
- P. Hejzlar, M. J. Driscoll and M. S. Kazimi, "Void Reactivity Performance in Lead-Bismuth Cooled Reactor for Actinide Transmutation," *MIT-ANP-TR-068*, MIT Nuclear Engineering Dept., August 1999.
- D. Kim, M. S. Kazimi, N. E. Todreas and M. J. Driscoll, "Economic Analysis of the Fuel Cycle of Actinide Burning Systems," *MIT-NFC-TR-019*, MIT Nuclear Engineering Dept., February 2000.
- P. Hejzlar, M. J. Driscoll, and M. S. Kazimi, "Conceptual Reactor Physics Design of a Lead-Bismuth-Cooled Critical Actinide Burner," MIT-ANP-TR-069, MIT Nuclear Engineering Dept., February 2000.
- P. E. MacDonald and J. Buongiorno, *Design of an Actinide Burning, Lead or Lead-Bismuth Cooled Reactor That Produces Low Cost Electricity, FY-00 Annual Project Status Report*, INEEL/EXT-2000-000994, MIT-ANP-PR-071, July, 2000.
- D. Kim, N. E. Todreas, M. S. Kazimi and M. J. Driscoll, "Plant Design and Cost Estimation of a Natural Circulation Lead-Bismuth Reactor with Helium Power Conversion Cycle," MIT-ANP-TR-074, MIT Nuclear Engineering Dept., November 2000.
- J. Buongiorno, N. E. Todreas, M. S. Kazimi and K. R. Czerwinski "Conceptual Design of a Lead-Bismuth Cooled Fast Reactor with In-Vessel Direct-Contact Steam Generation," MIT-ANP-TR-079, CANES/MIT Nuclear Engineering Dept., March 2001.
- R. G. Ballinger, J. Y. Lim and M. S. Kazimi "A Review of US Research Activities on Material Compatibility Issues in Nuclear Systems Using Heavy Liquid-Metal Coolant and Needs for Improved Materials," MIT-ANP-TR-080, CANES/MIT Nuclear Engineering Dept., June 2001.

- P. Hejzlar, N. E. Todreas, M. S. Kazimi and M.J. Driscoll, "Evaluation of a Once-Through lead-Bismuth-Cooled Reactor Concept," MIT-ANP-TR-081, MIT Nuclear Engineering Dept., July 2001.
- V. Dostal, N. E. Todreas, P. Hejzlar, and M. S. Kazimi, "Plant Design and Cost Assessment of a Forced Circulation Lead-Bismuth Cooled Reactor with Conventional Power Conversion Cycles", MIT-ANP-TR-082, MIT Nuclear Engineering Dept., August 2001.
- P. E. MacDonald and J. Buongiorno, *Design of an Actinide Burning, Lead or Lead-Bismuth Cooled Reactor That Produces Low Cost Electricity, FY-01 Annual Report*, INEEL/EXT-01-01376, MIT-ANP-PR-083, October, 2001.
- V. Dostal, M. J. Driscoll, P. Hejzlar, and N. E. Todreas, *Optimum Power Conversion Cycle Selection of a Forced Circulation Lead-Bismuth Cooled Reactor*, MIT-ANP-TR-084, MIT Nuclear Engineering Dept., September 2001.
- V. Dostal, M. S. Kazimi, P. Hejzlar, and N. E. Todreas, *Power Conversion Cycle Selection for the LBE Cooled Reactor with Forced Circulation*, MIT-ANP-TR-085, MIT Nuclear Engineering Dept., February 2002.
- R. Herron, N. E. Todreas, and P. Hejzlar**, *Component Design and Capital Cost Analysis of a Forced Circulation Lead-Bismuth Eutectic Cooled Nuclear Reactor*, MIT-ANP-TR-089, Dept. of Nuclear Engineering, September 2002.

Journal Papers

- K. D. Weaver, P. E. MacDonald, and J. S. Herring, "Reactivity and Isotopic Assessment of Fertile Fuels for Proliferation-Resistant, Actinide-Burning Lead or Lead-Bismuth Cooled Fast Reactors", Submitted to the *Journal of Nuclear Engineering and Design*, January 2001.
- C. B. Davis, "Assessment of the ATHENA Code for Calculating the Void Fraction of a Lead-Bismuth/Steam Mixture in Vertical Upflow", *Nuclear Technology*, Vol. 133, pp. 187-193, February 2001.
- J. Buongiorno, M. S. Kazimi, N. E. Todreas, "Heavy-Metal Aerosol Transport in a Lead-Bismuth Cooled Fast Reactor with In-Vessel Direct-Contact Steam Generation," Submitted to *Nuclear Technology*, April 2001.
- J. Buongiorno, and B. D. Hawkes, "Seismic Analysis of Heavy-Liquid-Metal-Cooled Reactor Vessels". Submitted to *Nuclear Technology*, June 2001.
- K. R. Czerwinski, J. Buongiorno, C. L. Larson. "Experimental Investigations on Vapor Pressure of Lead Polonide at Low Temperature & Thermodynamics of Polonium Hydride". Submitted to *Radiochimica Acta*. April 2001.
- P. Hejzlar, M. J. Driscoll, M. S. Kazimi, "Conceptual Neutronic Design of a Lead-Bismuth Cooled Actinide Burning Reactor," Accepted for publication in *Nuclear Science & Engineering*, Vol. 139, pp. 1-18, October 2001.
- J. Buongiorno, N. E. Todreas, M. S. Kazimi. "Heavy-Metal Aerosol Transport in a Lead-Bismuth Cooled Fast Reactor with In-Vessel Direct-Contact Steam Generation", *Nuclear Technology*, Vol.138, pp.30-43, April 2002.
- C. B. Davis, D. Kim, N. E. Todreas, and M. S. Kazimi, "Core power limits for a lead-bismuth natural circulation actinide burner reactor", *Nuclear Engineering and Design*, Vol. 213, pp.165-182, January 2002.
- K. R. Czerwinski, J. Buongiorno, C. L. Larson. "Experimental Investigations on Vapor Pressure of Lead Polonide at Low Temperature & Thermodynamics of Polonium Hydride". Resubmitted to *Radiochimica Acta*. October 2002.

- Eric Loewen and George Bisanz, "Comparison of Ultrasound and Micrographic Analysis of Liquid Metal Corrosion Samples", (Submitted to the *Journal of Materials Characterization*)
- Eric Loewen and George Bisanz, "Creation of a Thin Iron Arsenide (FeAs) film on a Stainless Steel Substrate Through Corrosion of a Lead-Bismuth Eutectic", (Submitted to the *Journal of Thin Solid Films*)
- Eric Loewen and Hannah Yount, "Comparison of the Corrosion Rate of Martensitic, Ferritic, and Carbon Steels in a Pb-Bi Eutectic at 550 and 650C", (Submitted to the *Journal of Nuclear Materials*)
- Eric Loewen, Keyna Riley and Hannah Yount, "Corrosion Testing of Zirconium Alloys in a Pb-Bi Eutectic at 550 and 650C", (Submitted to the *British Corrosion Journal*)
- Eric Loewen and Keyna Riley, "Tensile Tests of Stainless and Carbon Steels in Pb-Bi Eutectic at 550 and 650C", (Submitted to the *Journal of Nuclear Materials*)

Conference Papers

- P. Hejzlar, M. J. Driscoll and M. S. Kazimi, "Reactor Physics Design Challenges of a lead-bismuth Cooled Actinide Burner Reactor," *Transactions of the American Nuclear Society*, Vol. 80, pp. 192-194 June 1999.
- P. Hejzlar, M. J. Driscoll, and M. S. Kazimi, "Neutronic Design for a Pb-Bi-Cooled Actinide Burner Fast Reactor," *Transactions of the American Nuclear Society*, Vol. 81, pp. 271-273, 1999.
- J. Buongiorno, M. S. Kazimi and N. E. Todreas, "Natural Circulation Potential of lead-bismuth Cooled Reactors for Production and Actinide Burning," *Transactions of the American Nuclear Society*, Vol. 8, pp. 191-192, June 1999.
- J. Buongiorno, N. E. Todreas, M. S. Kazimi, M. J. Driscoll and P. Hejzlar, "Key Features of an Integrated Lead-Bismuth Cooled Reactor Based on Water/Liquid Metal Direct Heat Transfer," *Transactions of the American Nuclear Society, Vol 81, pp. 360*, Long Beach, CA, November 14-18, 1999.
- J. Buongiorno, N. E. Todreas, M. S. Kazimi. "Void Fraction Prediction for the Lead-Bismuth/Water Direct Contact Nuclear Reactor". *Proceedings of ICONE-8, 8th International Conference on Nuclear Engineering*, No. 8739, April 2-6, 2000, Baltimore, MD USA.
- C. B. Davis and A. S. Shieh, "Overview of the Use of ATHENA for Analysis of Lead-Bismuth Cooled Reactors", *Proceedings of the 8th International Conference on Nuclear Engineering (ICONE-8)*, April 2-6, 2000, Baltimore, MD.
- E. P. Loewen, C. B. Davis, and P. E. MacDonald, "A Technique for Dynamic Corrosion Testing in Liquid Lead Alloys" *Proceedings of the 8th International Conference on Nuclear Engineering (ICONE-8)*, April 2-6, 2000, Baltimore, MD.
- K. D. Weaver, J. S. Herring, and P. E. MacDonald, "Performance Modeling of Metallic and Nitride Fuels in Advanced Lead-Bismuth Cooled Fast Reactors," *Proceedings of the 8th International Conference on Nuclear Engineering (ICONE-8)*, April 2-6, 2000, Baltimore, MD.
- M. J. Driscoll and Dohyoung Kim, "The Need for Actinide Burner Reactor Fuel Cycle Cost Reduction," *Transactions of the American Nuclear Society*, Vol. 82, June 2000.
- J. Lim, and R. G. Ballinger "Development of a Facility for the Study of Liquid-Metal-Structural-Material Interaction", *Trans. Am. Nucl. Soc.* Vol. 83, pg. 310 November, 2000.

- J. Buongiorno, N. E. Todreas and M. S. Kazimi, "Thermal-Hydraulic Modeling of a Water/Liquid-Metal Direct Contact Heat Transfer Reactor," *Trans. Am. Nucl. Soc.* Vol. 83, pg. 395-397, November 2000.
- P. Hejzlar, M. J. Driscoll and M. S. Kazimi, "Consequence of Fuel Choice for Spent Fuel Characteristics for Once-Through Heavy Metal Cooled Fast Reactors," *Trans. Am. Nucl. Soc.* Vol. 83, pg. 39-41, November 2000.
- J. Buongiorno, N. E. Todreas, and M. S. Kazimi. "Thermal Design of a Lead-Bismuth Cooled Fast Reactor with In-Vessel Direct-Contact Steam Generation". ICONE-9772. *Proceedings of ICONE-9, the 9th International Conference on Nuclear Engineering. Nice, France.* April 8-12, 2001.
- P. Hejzlar, M. J. Driscoll, M. S. Kazimi and N. E. Todreas, "Minor Actinide Burning in Dedicated Lead-Bismuth Cooled Fast Reactors," Track 8 - #336, *The Proceedings of ICONE 9, April 8-12, 2001-Nice, France.*
- K. D. Weaver, J. S. Herring and P. E. MacDonald. "Performance Comparison of Metallic, Actinide Burning Fuel in Lead-Bismuth and Sodium Cooled Fast Reactors," ICONE-409 *Proceedings of ICONE-9, the 9th International Conference on Nuclear Engineering. Nice, France.* April 8-12, 2001.
- M. J. Driscoll, and P. Hejzlar, "A Negative Reactivity Feedback Device for Actinide Burner Cores," *Trans. Am. Nucl. Soc.*, Vol. 84, pg. 241-242, June 2001
- J. Buongiorno, B. D. Hawkes. "Seismic Response of Lead- and Lead-Bismuth-Cooled Reactor Vessels". Proceedings of the SMiRT-16 Conference. Washington D.C., August 12-17, 2001.
- J. Buongiorno, C. L. Larson, and K. R. Czerwinski. "Discussion on Polonium Extraction Systems for Pb-Bi-Cooled Nuclear Reactors". *Proceedings of the Global 2001 International Conference. Paris (France)*, September 9-13, 2001.
- J. Buongiorno, "Temperature Limits for the Fuel and Cladding of Heavy-Liquid-Metal-Cooled Reactors". *Proceedings of the Global 2001 International Conference. Paris (France)*, September 9-13, 2001.
- K. D. Weaver, J. S. Herring and P. E. MacDonald. "A Comparison of Long-Lived, Proliferation Resistant Fast Reactors," *Proceedings of the Global 2001 International Conference. Paris (France)*, September 9-13, 2001.
- J. Buongiorno, "Temperature Limits for Heavy-Liquid-Metal Reactor Vessels". Summary submitted for the ANS Winter Meeting, Reno, NV, November 2001.
- P. Hejzlar, N.E. Todreas, M.S. Kazimi, M.J. Driscoll, "Challenges of Minor Actinide Burning in Critical Lead-Bismuth Cooled Reactors," Track #2, Article 2, pg. 41-42, *Transactions of the ANS Winter Meeting, Reno, NV*, November 2001.
- V. Dostal, P. Hejzlar, M.J. Driscoll, N.E. Todreas, "A Supercritical CO2 Brayton Cycle for Advanced Reactor Applications" Track #2, Article 5, pg. 110-111, *Transactions of the ANS Winter Meeting, Reno, NV*, November 2001.
- J. Lim, P. W. Stahle and R.G. Ballinger, "A Test System for Experimental Studies of Liquid-Metal-Structural-Material Interaction", Summary submitted for the ANS Winter Meeting, Reno, NV, November 2001.
- J. Buongiorno. "Temperature Limits for Heavy-Liquid-Metal Reactor Vessels". *Proceedings of the 2001 ANS Winter Meeting, Reno, Nevada*, Nov. 11-15, 2001.
- J. Buongiorno, N. E. Todreas, M. S. Kazimi. "An Oxygen Control Strategy for Corrosion Minimization in Direct-Contact Lead-Bismuth/Water Systems", Proceedings of the International Congress on Advanced Nuclear Power Plants (ICAPP), Hollywood, FL, June 2002.

- J. Buongiorno, A. Barak, E. Greenspan. "Irradiation Performance of the Metal Fuel for the Encapsulated Nuclear Heat Source (ENHS)", *Proc. 2002 ANS Annual Meeting, Hollywood FL*, June 2002.
- V. Dostal, P. Hejzlar, M.J. Driscoll, N.E. Todreas, "A Supercritical CO_2 Gas Turbine Power Cycle for Next-Generation Nuclear Reactors" *Proceedings of the Tenth International Conference on Nuclear Engineering, ICONE10*, Arlington, VA, Track 22192, April 14-18, 2002.
- P. Hejzlar, P. E. MacDonald, J. Buongiorno, M. J. Driscoll, N. E. Todreas, "Design Strategies for Lead-Bismuth-Cooled Reactor for Actinide Burning and Low Cost Electricity", *Proceedings of the Tenth International Conference on Nuclear Engineering, ICONE10*, Arlington, VA, Track 22377, April 14-18, 2002.
- J. Buongiorno, M. S. Kazimi, and N. E. Todreas, " An Oxygen Control Strategy for Corrosion Minimization in Lead-Bismuth/Water Direct-Contact Systems ", Proceedings of the International Congress on Advanced Nuclear Power Plants (ICAPP), Hollywood, FL, Track 7 - #1107, June 2002.
- P. Hejzlar, N. E. Todreas, M. S. Kazimi, "Actinide Burning in a Lead-Bismuth-Cooled Critical Fast Reactor with Economic Electricity Generation," 7th Information Exchange Meeting on Actinide and Fission Product Partitioning and Transmutation, Jeju, South Korea, October 14-16, 2002.
- Eric Loewen and George Bisanz, "Ultrasonic Examination versus Scanning Electron Microscopy for Analyzing Lead Corrosion in Stainless Steel", *Proceedings of the American Nuclear Society 2002 Winter Meeting, November 17-21*, 2002.
- Eric Loewen and Hannah Yount, "HT-9 Corrosion Growth in Flowing Pb-Bi at 550 and 650C", *Proceedings of the American Nuclear Society 2002 Winter Meeting, November 17-21*, 2002.
- Eric Loewen and Keyna Riley, "Tensile Testing of 410 Stainless Steel Exposed to Pb-Bi Eutectic", *Proceedings of the American Nuclear Society 2002 Winter Meeting, November 17-21*, 2002.
- Hannah Yount, "Corrosion of Metals in Pb-Bi Eutectic at 550 and 650C", Submitted to ICONE-11 Tokyo, Japan, April 2003.
- Keyna Riley, "Tensile Performance of Martensitic and Ferritic Steels in Pb-Bi Eutectic at 550 and 650C" Submitted to ICONE-11 Tokyo, Japan, April 2003.

Awards

- J. Buongiorno received the ANS Mark Mills national award in recognition of the "best original technical paper contributing to the advancement of science and engineering related to the atomic nucleus", September 2001.
- "Void Fraction Prediction for the Lead-Bismuth/Water Direct Contact Nuclear Reactor" by J. Buongiorno, N. Todreas and M. Kazimi received the Best Technical Paper of the Thermal-Hydraulic Track award at the 8th International Conference on Nuclear Engineering (ICONE-8), Baltimore MD, April 2000.

<u>Invited Presentations and Seminars</u>

- J. Buongiorno. "Evaluation of Polonium Extraction Technology for Lead-Bismuth Cooled Fast Reactors", presentation at the Russia-Japan LBE Workshop held at the Tokyo Institute of Technology in Tokyo (Japan). February 2001.
- J. Buongiorno. "Conceptual Design of a Lead-Bismuth Cooled Fast Reactor with In-Vessel Direct-Contact Steam Generation". Seminar held at the Department of Engineering Physics of the University of Wisconsin at Madison. February 2001.
- E. Loewen, "Dynamic Corrosion Testing at the INEEL", Limited distribution proceedings, Dec. 13, 2000, Lead-Bismuth Technology International Meeting, Japan Nuclear Cycle Development Institute, Tokyo and Mito, Japan
- P. E. MacDonald, "Design of an Actinide Burning, Lead or Lead-Bismuth Cooled Reactor That Produces Low Cost Electricity", Limited distribution proceedings, Dec. 12, 2000, Lead-Bismuth Technology International Meeting, Japan Nuclear Cycle Development Institute, Tokyo and Mito, Japan
- P. Hejzlar, M. J. Driscoll, and N. E. Todreas, "Impact of Fuel Choices On Spent Fuel Characteristics for Once-Through Heavy Metal Cooled Reactors", Proceedings are not yet published, Nov. 23-Dec. 1, IAEA Technical Meeting, IAEA, ANL, Argonne, IL
- D. Kim, M. S. Kazimi, M. J. Driscoll, and N. E. Todreas, "The Economics of Transmutation Fuel Cycles", Proceedings not yet published, Nov. 23-Dec. 1, IAEA Technical Committee Meeting, IAEA, ANL, Argonne, IL

Appendix B. Cost Analysis Terminology

Inflation is the erosion of the real value of money with time. The inflation rate is defined as the rate of change in the general price level as measured by the Gross Domestic Product Implicit Price Deflator. Escalation is based on the same concept as inflation, but applies to a particular good or service and can be greater or less than the inflation rate. Inflation applies to the economy as a whole while escalation applies to specific items [Delene and Hudson 1993].

There is an important distinction between constant and nominal dollars. The value of a constant dollar is defined as the value of a dollar at some reference date. Inflation generally lessens the value (buying power) of the dollar over time; the use of constant dollars factors out inflation. For example, because the ALMR capital cost analysis was performed in 1994, values are provided in constant 1994 dollars. In contrast, nominal dollars include the effects of inflation. The nominal dollar cost is the cost measured in as-spent dollars. Nominal dollars may also be thought of as "current" dollars, "year of expenditure" dollars, or "as-spent" dollars [Delene and Hudson 1993].

The direct costs are the costs of equipment, site labor, and site materials. Indirect costs include various services and owner's costs. Owner's costs typically include engineering and quality assurance, taxes and insurance, spare parts, staff training, and other overhead.   The general assumption is that owner's costs equal 10% of the sum of the direct and other indirect costs [Delene et al. 1988].

To allow for uncertainty in the capital cost analysis a contingency allowance is added.   The contingency allowance adjusts for costs that may arise during the construction process that were not included in the cost estimate. It basically provides a buffer and adds conservatism to the capital cost estimate. The contingency allowance is a percentage of each component's cost and varies depending on the component. Well-developed technologies have low contingency factors, while newer technologies have higher factors to account for uncertainty.   For example a pressurized water reactor might have a composite contingency factor of 10%, but a liquid metal reactor, which is a newer technology, would have a higher contingency factor, possibly 15% [Delene et al. 1988].

The base construction cost is the most likely nuclear power plant cost based on direct and indirect costs only. This value will be lower than the total capital cost because contingency, interest, and escalation are not included [Delene and Hudson 1993].

The overnight cost is the sum of the base construction costs and contingency allowances. As the name suggests, it is the cost of the power plant if it could be built overnight. The overnight cost ignores the time value of money and does not include inflation, escalation, or interest [Delene et al. 1988].

The acronyms FOAK and NOAK represent the terms "first of a kind" and "n[th] of a kind," respectively. As the names suggest, they represent the properties associated with the first of a series of reactors (FOAK) or the properties associated with the nth version of a reactor (NOAK). The total costs of FOAK and NOAK reactors will differ based on the learning curve for construction. With more experience reactor components can be built more quickly and cheaply. For the ALMR capital cost analysis the FOAK total cost is the average of the projected total cost of the first and second power plants, while the NOAK total cost is the average of the fourteenth and fifteenth power plants.

Various capital components of a nuclear reactor are divided into categories that make it easy to identify different cost areas as well as a consistent format used by all cost engineers. Different plant systems are identified by what is known as an "account number." The one digit account number identifies a broad cost category. For example, the account number 2 represents direct costs, while the account number 9 represents indirect costs. A second digit to the account number indicates a further differentiation. Table B.1 is a summary of the major cost accounts, to the two-digit level, used in the analysis of a nuclear power plant.

Each of these accounts is subdivided further. For example, account number 22, reactor plant equipment, is further divided into nine, three-digit accounts. Table B.2 provides a summary of account number 22 to the three-digit level. The "A" in the 220A cost account distinguishes the nuclear steam supply system of the ALMR from other varieties of nuclear steam supply systems.

Three-digit accounts can be further broken down into lower level accounts. These accounts are identified by the three-digit account number and followed by a decimal point and three more account numbers. The typical format for these account numbers is XXX.XXX. For this cost analysis, which scales an existing analysis, this level of detail was not used, except in the nuclear steam supply steam (NSSS). The NSSS account includes most major reactor components (Table B.3).

This cost analysis was completed at the two-digit level except for the NSSS, which was analyzed in greater detail. The NSSS account was given close attention because it was the major source of differences between the ALMR and the proposed LBE power plant.

Table B.1. Summary of major two-digit accounts [Delene and Hudson 1993].

Account Number	Account Description
2	**Total Direct Costs**
20	Land and Land Rights
21	Structures and Improvements
22	Reactor Plant Equipment
23	Turbine Plant Equipment
24	Electric Plant Equipment
25	Miscellaneous Plant Equipment
26	Heat Rejection System
9	**Total Indirect Costs**
91	Construction Services
92	Home Office Engineering & Services
93	Field Office and Services
94	Owner's Costs

Table B.2. Reactor plant equipment accounts

Account Number	Account Description
22	**Reactor Plant Equipment**
220A	Nuclear Steam Supply System (NSSS)
221	Reactor Equipment
222	Main Heat Transport System
223	Safeguards System
224	Radwaste Processing
225	Fuel Handling
226	Other Reactor Plant Equipment
227	Reactor Instrumentation and Control
228	Reactor Plant Miscellaneous Equipment

Table B.3. Account numbers for the NSSS

Account Number	Account Description
220A	Nuclear Steam Supply System
220A.2	Distributed NSSS Price
220A.211	Reactor Vessels
220A.212	Reactor Vessel Internals
220A.213	Control Rod Drives
220A.214	Transport to Site
220A.22	Heat Transport System
220A.221	Primary Heat Transport System
220A.222	Intermediate Heat Transport System
220A.223	Steam Generator System
220A.23	Safeguards System
220A.231	Backup Heat Removal System
220A.25	Fuel Handling and Storage
220A.26	Other Equipment
220A.27	Instrumentation and Control
220A.3	Undistributed NSSS Cost
220A.31	Support Engineering

Design of an Actinide Burning, Lead or Lead-Bismuth Cooled Reactor That Produces Low Cost Electricity

FY-02 Annual Report, October, 2002

Report compiled and edited by
P. E. MacDonald and J. Buongiorno